

**DEVELOPMENT OF POLYMER BASED MULTI-FUNCTION
NANOCOMPOSITE COATING SYSTEM**

AMMAR SHAFAMRI

**FACULTY OF SCIENCE
UNIVERSITY OF MALAYA
KUALA LUMPUR**

2018

**DEVELOPMENT OF POLYMER BASED MULTI-
FUNCTION NANOCOMPOSITE COATING SYSTEM**

AMMAR SHAFAMRI

**THESIS SUBMITTED IN FULFILMENT OF THE
REQUIREMENTS FOR THE DEGREE OF
DOCTOR OF PHILOSOPHY**

**DEPARTMENT OF PHYSICS
FACULTY OF SCIENCE
UNIVERSITY OF MALAYA
KUALA LUMPUR**

2018

UNIVERSITY OF MALAYA
ORIGINAL LITERARY WORK DECLARATION

Name of Candidate: **AMMAR SHAFAMRI**

Matric No: **SHC 150036**

Name of Degree: **DOCTOR OF PHILOSOPHY**

Title of Project Paper/Research Report/Dissertation/Thesis ("this Work"):

**DEVELOPMENT OF POLYMER BASED MULTI-FUNCTION
NANOCOMPOSITE COATING SYSTEM**

Field of Study: **EXPERIMENTAL PHYSICS**

I do solemnly and sincerely declare that:

- (1) I am the sole author/writer of this Work;
- (2) This Work is original;
- (3) Any use of any work in which copyright exists was done by way of fair dealing and for permitted purposes and any excerpt or extract from, or reference to or reproduction of any copyright work has been disclosed expressly and sufficiently and the title of the Work and its authorship have been acknowledged in this Work;
- (4) I do not have any actual knowledge nor do I ought reasonably to know that the making of this work constitutes an infringement of any copyright work;
- (5) I hereby assign all and every rights in the copyright to this Work to the University of Malaya ("UM"), who henceforth shall be owner of the copyright in this Work and that any reproduction or use in any form or by any means whatsoever is prohibited without the written consent of UM having been first had and obtained;
- (6) I am fully aware that if in the course of making this Work I have infringed any copyright whether intentionally or otherwise, I may be subject to legal action or any other action as may be determined by UM.

Candidate's Signature

Date:

Subscribed and solemnly declared before,

Witness's Signature

Date:

Name:

Designation:

DEVELOPMENT OF POLYMER BASED MULTI-FUNCTION NANOCOMPOSITE COATING SYSTEM

ABSTRACT

In this study, polymer-based nanocomposite coating systems were developed based on the utilization of a hybrid acrylic–silicone polymeric matrix and two types of nanoparticles, namely, SiO₂ and ZnO, at different loading rates of 1 wt. %, 3 wt. %, 5 wt. % and 8 wt. %. Then, by modifying the base acrylic–silicone polymeric matrix with various loadings of epoxy resin and epoxidized soybean oil, fully organic coating system were prepared and investigated. All developed coating systems were subjected to the same conditions in the curing process, using polyisocyanate (NCO) as the curing agent. The brush method was used to apply the developed coating system onto the surface of the pretreated cold-rolled mild steel substrates. To fully cure and dry, all prepared samples were kept at room temperature for seven days and all the coated films were controlled to have a dry-film thickness of 75 ± 5 mm. The ability of the developed single-layer coating system for use in multifunctional coating films was confirmed via the utilization of various characterization techniques in order to evaluate different properties of the developed coating systems. The properties investigated included the chemical structure, surface morphology, wettability, transparency, thermal stability, adhesion performance and corrosion protection ability. The obtained results reveal that a nanoparticle loading ratio of 3 wt. % for both SiO₂ and ZnO can be considered to be the optimum ratio as it provides the most pronounced enhancement of the overall coating performance especially for the corrosion protection and barrier properties. Also, a significant improvement was obtained by introducing 9 wt. % of epoxy resin and 1 w. % of epoxidized soybean oil to the acrylic–silicone polymeric blend. These results conclusively confirm that the coating system with 3 wt. % SiO₂ nanoparticles (AS 3) demonstrates the best overall performance and successful multifunctionality.

Keywords: Corrosion; Polymer Coatings; Nanocomposites; Multifunctionality, Steel Protection.

University of Malaya

PENGEMBANGAN SISTEM LAPISAN NANOKOMPOSIT KEPELBAGAIAN FUNGSI BERASASKAN POLIMER

ABSTRAK

Dalam kajian ini, sistem nanokomposit berasaskan polimer berasaskan penggunaan matriks polimerik hibrid silikon-akrilik dan dua jenis nanopartikel iaitu, nanopartikel SiO_2 dan ZnO , pada kadar pemuatan yang berbeza secara khusus, 1 wt. %, 3 wt. %, 5 wt. %, dan 8 wt. %, telah dibangunkan. Tambahan lagi, dengan mengubahsuaikan matriks polimer asas silikon-akrilik dengan pelbagai jumlah resin epoksi dan minyak kacang soya yang dioksidakan, sistem salutan organik yang lengkap telah disediakan dan diselidik. Semua sistem salutan yang telah campurkan dilengkapi dengan proses pengerasan dengan kehadiran polyisocyanate (NCO) sebagai agen pengeras. Kaedah memberus telah digunakan untuk menerapkan semua sistem salutan yang telah disediakan pada permukaan keluli besi sejuk. Semua sampel yang telah disiapkan disimpan sepenuhnya untuk dikeringkan pada suhu bilik selama 7 hari dan semua salutan filem dikawal untuk mempunyai ketebalan filem kering dalam lingkungan 75 ± 5 mm. Untuk mengesahkan keupayaan salutan yang telah disiapkan untuk berfungsi sebagai salutan pelbagai fungsi, pelbagai teknik pencirian telah dijalankan untuk menilai ciri-ciri sistem salutan yang telah disempurnakan. Sehubungan itu, sifat-sifat lain termasuk struktur kimia, morfologi permukaan, keadaan kebolehbagaian, ketelusan, kestabilan haba, sifat lekatan dan keupayaan perlindungan kakisan telah diselidik. Hasil yang diperoleh menunjukkan bahawa, 3 wt. % nisbah nanopartikel, untuk kedua-dua SiO_2 dan ZnO , boleh dianggap sebagai jumlah yang optimum dan mempunyai peningkatan yang paling ketara untuk keseluruhan prestasi salutan. Juga, memperkenalkan 9 wt. % resin epoksi dan 1 wt. % minyak kacang soya epoxidized kepada campuran polimerik silikon akrilik memperoleh peningkatan yang ketara. Kajian-kajian ini telah mengesahkan bahawa sistem salutan AS

3, dengan 3 wt. % nanopartikel SiO₂, menunjukkan prestasi keseluruhan yang terbaik dan berjaya memperoleh pelbagai fungsi.

Kata kunci: Pengkaratan; Penyaduran Polimer; Komposit Nano; Multi-kefungsian; Pelindung Besi

University of Malaya

ACKNOWLEDGEMENTS

In the name of Allah, the Most Gracious and the Most Merciful

Alhamdulillah, all praises to Allah for the strengths and His blessing in completing this work. First and foremost, my most sincere and profound appreciation to my supervisors, Associate Professor Dr. Ramesh Kasi and Professor Dr. Ramesh T. Subramaniam, who have supported me throughout my thesis with their patience and knowledge. I attribute the level of my PhD degree to their encouragement and effort and without them this work would not have been completed. One simply could not wish for better or friendlier supervisors.

A special word of thanks goes to Dr. Vengadaesvaran V. Balakrishnan. The smooth running of the laboratory work is much more a testament to his efforts than my own. Many thanks also go my lab mate Iling Ma for the great support.

I would also to take the opportunity to express my appreciation and thanks to my friends, namely Suhaib, Said, Ehab, Maher, Yamen, Hassan, and my cousins Moutasem and Ramez.

Last but not least, my deepest gratitude goes to my beloved mother, sisters and my brother for their endless love, prayers and encouragement. Also, not forgetting my brothers in law for supporting me in countless ways.

To those who indirectly contributed in this research, your kindness means a lot to me

Thank you very much.

TABLE OF CONTENTS

| | |
|--|--------------|
| ABSTRACT | iii |
| ABSTRAK | v |
| ACKNOWLEDGEMENTS..... | vii |
| TABLE OF CONTENTS..... | viii |
| LIST OF FIGURES | xii |
| LIST OF TABLES | xviii |
| LIST OF SYMBOLS AND ABBREVIATIONS | xxi |
| CHAPTER 1: INTRODUCTION..... | 1 |
| 1.1 Introduction..... | 1 |
| 1.2 Research Objectives..... | 2 |
| 1.3 Thesis Outline | 3 |
| CHAPTER 2: LITERATURE REVIEW..... | 5 |
| 2.1 Introduction..... | 5 |
| 2.2 Corrosion | 5 |
| 2.2.1 Definition and Mechanism of Corrosion..... | 5 |
| 2.2.2 Corrosion Classifications | 6 |
| 2.2.2.1 Uniform Corrosion..... | 7 |
| 2.2.2.2 Pitting Corrosion..... | 7 |
| 2.2.2.3 Stress Corrosion Cracking | 8 |
| 2.2.2.4 Fatigue Corrosion | 9 |
| 2.2.2.5 Intergranular corrosion | 11 |
| 2.2.2.6 Filiform Corrosion..... | 12 |
| 2.2.2.7 Crevice Corrosion..... | 12 |
| 2.2.2.8 Galvanic or Bi-Metallic Corrosion | 14 |

| | | |
|------------------------------------|---|-----------|
| 2.2.2.9 | Fretting corrosion..... | 14 |
| 2.2.2.10 | Erosion corrosion..... | 15 |
| 2.2.2.11 | High-temperature corrosion..... | 16 |
| 2.2.3 | Corrosion protection methods | 17 |
| 2.3 | Coating..... | 19 |
| 2.3.1 | Coating Selection | 21 |
| 2.3.2 | Coating Composition..... | 21 |
| 2.3.2.1 | Binder | 22 |
| a) | Acrylic Polyol Resin | 22 |
| b) | Silicone | 24 |
| c) | Soybean Oil..... | 25 |
| 2.3.2.2 | Solvents | 26 |
| 2.3.2.3 | Pigments | 26 |
| 2.3.3 | Nanocomposite Coatings..... | 27 |
| CHAPTER 3: METHODOLOGY..... | | 30 |
| 3.1 | Introduction..... | 30 |
| 3.2 | Materials | 30 |
| 3.3 | Methods | 33 |
| 3.3.1 | Preparation of Acrylic-Silicone Hybrid Polymeric Matrix | 33 |
| 3.3.2 | Preparation of SiO ₂ Nanocomposite Coating Systems..... | 34 |
| 3.3.3 | Preparation of ZnO Nanocomposite Coating Systems..... | 35 |
| 3.3.4 | Preparation of Epoxy-Soybean Oil Modified Organic Coating System..... | 35 |
| 3.3.5 | Sample Preparation and Coatings Application..... | 36 |
| 3.4 | Characterization | 37 |
| 3.4.1 | Fourier Transform Infrared Spectroscopy (FTIR)..... | 38 |
| 3.4.2 | Field Emission Scanning Electron Microscopy (FESEM)..... | 38 |
| 3.4.3 | Contact Angle Measurements (CA) | 38 |
| 3.4.4 | Ultraviolet-Visible (UV-Vis) Spectroscopy | 40 |

| | | |
|-------|--|----|
| 3.4.5 | Cross Hatch Test (CHT)..... | 40 |
| 3.4.6 | Thermogravimetric analysis (TGA) | 41 |
| 3.4.7 | Electrochemical Impedance Spectroscopy (EIS) | 43 |

CHAPTER 4: RESULTS AND DISCUSSIONS OF SiO₂ NANOCOMPOSITE

COATING SYSTEMS.....45

| | | |
|-----|--|----|
| 4.1 | Introduction..... | 45 |
| 4.2 | Fourier Transform Infrared Spectroscopy (FTIR) | 45 |
| 4.3 | Surface Morphology | 46 |
| 4.4 | Contact angle measurements (CA) | 48 |
| 4.5 | UV-Visible Spectroscopy | 51 |
| 4.6 | Cross Hatch Test (CHT) | 52 |
| 4.7 | Thermogravimetric Analysis (TGA)..... | 54 |
| 4.8 | Electrochemical impedance spectroscopy (EIS)..... | 59 |
| 4.9 | Summary | 79 |

CHAPTER 5: RESULTS AND DISCUSSION OF ZnO NANOCOMPOSITE

COATING SYSTEMS.....84

| | | |
|-----|--|-----|
| 5.1 | Introduction..... | 84 |
| 5.2 | Surface Morphology of ZnO Nanocomposite Coating Systems..... | 84 |
| 5.3 | Contact Angle Measurements (CA)..... | 86 |
| 5.4 | UV-Visible Spectroscopy | 87 |
| 5.5 | Cross Hatch Test (CHT) | 88 |
| 5.6 | Thermogravimetric Analysis (TGA)..... | 90 |
| 5.7 | Electrochemical impedance spectroscopy (EIS)..... | 94 |
| 5.8 | Summary | 110 |

**CHAPTER 6: RESULTS AND DISCUSSIONS OF EPOXY-SOYBEAN OIL
MODIFIED ORGANIC COATING SYSTEM..... 114**

| | | |
|-----|--|-----|
| 6.1 | Introduction..... | 114 |
| 6.2 | Fourier Transform Infrared Spectroscopy (FTIR) | 114 |
| 6.3 | Contact angle measurements (CA) | 115 |
| 6.4 | UV-Visible Spectroscopy | 117 |
| 6.5 | Cross Hatch Test (CHT) | 118 |
| 6.6 | Thermogravimetric Analysis (TGA)..... | 119 |
| 6.7 | Electrochemical impedance spectroscopy (EIS)..... | 125 |
| 6.8 | Summary | 147 |

CHAPTER 7: CONCLUSIONS AND SUGGESTIONS FOR FUTURE WORK 150

| | | |
|-----|-----------------------------------|-----|
| 7.1 | Conclusions..... | 150 |
| 7.2 | Suggestions for Future Work | 156 |

REFERENCES..... 157

LIST OF PUBLICATIONS AND PAPERS PRESENTED 165

LIST OF FIGURES

| | | |
|-------------|---|----|
| Figure 2.1 | : Uniform corrosion | 7 |
| Figure 2.2 | : Pitting corrosion | 8 |
| Figure 2.3 | : Stress corrosion cracking | 9 |
| Figure 2.4 | : The general mechanism of fatigue corrosion | 9 |
| Figure 2.5 | : Fatigue corrosion | 10 |
| Figure 2.6 | : Intergranular corrosion | 11 |
| Figure 2.7 | : Filiform corrosion | 12 |
| Figure 2.8 | : Crevice corrosion | 13 |
| Figure 2.9 | : Galvanic corrosion | 14 |
| Figure 2.10 | : Fretting corrosion | 15 |
| Figure 2.11 | : Erosion corrosion | 16 |
| Figure 2.12 | : High temperature corrosion | 17 |
| Figure 3.1 | : Shapes of water drop on solid surfaces of different wettability with its corresponding contact angle values | 39 |
| Figure 3.2 | : The classic three-electrode cell used for EIS characterizations | 44 |
| Figure 4.1 | : FTIR spectra of (a) neat silicone and (b) neat acrylic and (c) AS 0 coating system | 47 |
| Figure 4.2 | : FESEM micrographs at scale 100 000× of magnification of (a) AS 1, (b) AS 3, (c) AS 5, and (d) AS 8 SiO ₂ nanocomposite coating systems | 48 |
| Figure 4.3 | : UV-Vis spectra for A 100, AS 0 and all prepared SiO ₂ nanocomposite coating systems | 52 |
| Figure 4.4 | : Results of cross hatch test for A 100, AS 0 and all prepared SiO ₂ nanocomposite coating systems | 53 |
| Figure 4.5 | : TGA thermogram of A 100 coating system | 55 |
| Figure 4.6 | : TGA thermogram of AS 0 coating system | 56 |
| Figure 4.7 | : TGA thermogram of AS 1 coating system | 56 |
| Figure 4.8 | : TGA thermogram of AS 3 coating system | 57 |
| Figure 4.9 | : TGA thermogram of AS 5 coating system | 57 |

| | | |
|-------------|--|----|
| Figure 4.10 | : TGA thermogram of AS 8 coating system | 58 |
| Figure 4.11 | : The equivalent circuit models | 60 |
| Figure 4.12 | : Bode plots for AS 0 and all prepared SiO ₂ nanocomposite coating systems after 1 day of immersion time | 63 |
| Figure 4.13 | : Nyquist plot for AS 0 coating system after 1 day of immersion time. | 63 |
| Figure 4.14 | : Nyquist plots for all prepared SiO ₂ nanocomposite coating systems after 1 day of immersion time | 64 |
| Figure 4.15 | : Bode plots for AS 0 and all prepared SiO ₂ nanocomposite coating systems after 30 days of immersion time | 66 |
| Figure 4.16 | : Nyquist plot for AS 0 coating system after 30 days of immersion time | 66 |
| Figure 4.17 | : Nyquist plots for all prepared SiO ₂ nanocomposite coating systems after 30 days of immersion time | 67 |
| Figure 4.18 | : Bode plots for AS 0 and all prepared SiO ₂ nanocomposite coating systems after 60 days of immersion time | 68 |
| Figure 4.19 | : Nyquist plot for AS 0 coating system after 60 days of immersion time | 69 |
| Figure 4.20 | : Nyquist plots for all prepared SiO ₂ nanocomposite coating systems after 60 days of immersion time | 69 |
| Figure 4.21 | : Bode plots for AS 0 and all prepared SiO ₂ nanocomposite coating systems after 90 days of immersion time | 72 |
| Figure 4.22 | : Nyquist plot for AS 0 coating system after 90 days of immersion time | 73 |
| Figure 4.23 | : Nyquist plots for all prepared SiO ₂ nanocomposite coating systems after 90 days of immersion time | 73 |
| Figure 4.24 | : Bode plots of AS 0 coating system after (a) 1 day and (b) 90 days of immersion along with the determining the breakpoint frequency and the corresponding capacitive (A1) and resistive (A2) regions... | 76 |
| Figure 4.25 | : Bode plots of AS 1 coating system after (a) 1 day and (b) 90 days of immersion along with the determining the breakpoint frequency and the corresponding capacitive (A1) and resistive (A2) regions... | 76 |
| Figure 4.26 | : Bode plots of AS 3 coating system after (a) 1 day and (b) 90 days of immersion along with the determining the breakpoint frequency and the corresponding capacitive (A1) and resistive (A2) regions... | 77 |
| Figure 4.27 | : Bode plots of AS 5 coating system after (a) 1 day and (b) 90 days of immersion along with the determining the breakpoint frequency and the corresponding capacitive (A1) and resistive (A2) regions... | 77 |

| | | |
|-------------|--|-----|
| Figure 4.28 | : Bode plots of AS 8 coating system after (a) 1 day and (b) 90 days of immersion along with the determining the breakpoint frequency and the corresponding capacitive (A1) and resistive (A2) regions... | 78 |
| Figure 5.1 | : FESEM micrographs at scale 100 000× of magnification of (a) AZ 1, (b) AZ 3, (c) AZ 5, and (d) AZ 8 ZnO nanocomposite coating systems | 85 |
| Figure 5.2 | : UV-Vis spectra for A 100, AS 0 and all prepared ZnO nanocomposite coating systems | 88 |
| Figure 5.3 | : Results of cross hatch test for A 100, AS 0 and all prepared ZnO nanocomposite coating systems | 89 |
| Figure 5.4 | : TGA thermogram of AZ 1 coating system | 92 |
| Figure 5.5 | : TGA thermogram of AZ 3 coating system | 92 |
| Figure 5.6 | : TGA thermogram of AZ 5 coating system | 93 |
| Figure 5.7 | : TGA thermogram of AZ 8 coating system | 93 |
| Figure 5.8 | : Bode plots for AS 0 and all prepared ZnO nanocomposite coating systems after 1 day of immersion time | 96 |
| Figure 5.9 | : Nyquist plot for AS 0 coating system after 1 day of immersion time. | 96 |
| Figure 5.10 | : Nyquist plots for all prepared ZnO nanocomposite coating systems after 1 day of immersion time | 97 |
| Figure 5.11 | : Bode plots for AS 0 and all prepared ZnO nanocomposite coating systems after 30 days of immersion time | 99 |
| Figure 5.12 | : Nyquist plot for AS 0 coating system after 30 days of immersion time | 99 |
| Figure 5.13 | : Nyquist plot for AZ 1 nanocomposite coating system after 30 days of immersion time | 100 |
| Figure 5.14 | : Nyquist plot for AZ 3 and AZ 5 nanocomposite coating systems after 30 days of immersion time | 101 |
| Figure 5.15 | : Nyquist plot for AZ 8 nanocomposite coating system after 30 days of immersion time | 101 |
| Figure 5.16 | : Bode plots for AS 0 and all prepared ZnO nanocomposite coating systems after 60 days of immersion time | 104 |
| Figure 5.17 | : Nyquist plot for AS 0 coating system after 60 days of immersion time | 104 |
| Figure 5.18 | : Nyquist plot for AZ 1 and AZ 5 nanocomposite coating systems after 60 days of immersion time | 105 |

| | | |
|-------------|--|-----|
| Figure 5.19 | : Nyquist plot for AZ 3 nanocomposite coating system after 60 days of immersion time | 105 |
| Figure 5.20 | : Nyquist plot for AZ 8 nanocomposite coating system after 60 days of immersion time | 106 |
| Figure 5.21 | : Bode plots of AZ 1 coating system after (a) 1 day and (b) 90 days of immersion along with the determining the breakpoint frequency and the corresponding capacitive (A1) and resistive (A2) regions... | 108 |
| Figure 5.22 | : Bode plots of AZ 3 coating system after (a) 1 day and (b) 90 days of immersion along with the determining the breakpoint frequency and the corresponding capacitive (A1) and resistive (A2) regions... | 108 |
| Figure 5.23 | : Bode plots of AZ 5 coating system after (a) 1 day and (b) 90 days of immersion along with the determining the breakpoint frequency and the corresponding capacitive (A1) and resistive (A2) regions... | 109 |
| Figure 5.24 | : Bode plots of AZ 8 coating system after (a) 1 day and (b) 90 days of immersion along with the determining the breakpoint frequency and the corresponding capacitive (A1) and resistive (A2) regions... | 109 |
| Figure 6.1 | : FTIR spectra of AS 0 and all prepared epoxy-epoxidized soybean oil hybrid organic coating systems | 115 |
| Figure 6.2 | : UV - Vis spectra for A 100, AS 0 and all prepared epoxy-epoxidized soybean oil hybrid organic coating systems | 117 |
| Figure 6.3 | : Results of cross hatch test for A 100, AS 0 and all prepared epoxy-epoxidized soybean oil hybrid organic coating systems | 119 |
| Figure 6.4 | : TGA thermogram of ES 0 coating system | 121 |
| Figure 6.5 | : TGA thermogram of ES 1 coating system | 122 |
| Figure 6.6 | : TGA thermogram of ES 2 coating system | 122 |
| Figure 6.7 | : TGA thermogram of ES 4 coating system | 123 |
| Figure 6.8 | : TGA thermogram of ES 6 coating system | 123 |
| Figure 6.9 | : TGA thermogram of ES 8 coating system | 124 |
| Figure 6.10 | : TGA thermogram of ES 10 coating system | 124 |
| Figure 6.11 | : Bode plots for AS 0 and all prepared epoxy-epoxidized soybean oil hybrid organic coating systems after 1 day of immersion time | 128 |
| Figure 6.12 | : Nyquist plot for AS 0 coating system after 1 day of immersion time. | 128 |
| Figure 6.13 | : Nyquist plots ES 0, ES4 and ES 6 hybrid organic coating systems after 1 day of immersion time | 129 |

| | | |
|-------------|--|-----|
| Figure 6.14 | : Nyquist plots ES 1 and ES 2 hybrid organic coating systems after 1 day of immersion time | 129 |
| Figure 6.15 | : Nyquist plots ES 8 and ES 10 hybrid organic coating systems after 1 day of immersion time | 130 |
| Figure 6.16 | : Bode plots for AS 0 and all prepared epoxy-epoxidized soybean oil hybrid organic coating systems after 30 day of immersion time | 133 |
| Figure 6.17 | : Nyquist plot for AS 0 coating system after 30 days of immersion time | 133 |
| Figure 6.18 | : Nyquist plots ES 0 and ES 2 hybrid organic coating systems after 30 day of immersion time | 134 |
| Figure 6.19 | : Nyquist plots ES 1 hybrid organic coating system after 30 day of immersion time | 134 |
| Figure 6.20 | : Nyquist plots ES 4 and ES 6 hybrid organic coating systems after 30 day of immersion time | 135 |
| Figure 6.21 | : Nyquist plots ES 8 and ES 10 hybrid organic coating systems after 30 day of immersion time | 135 |
| Figure 6.22 | : Bode plots for AS 0 and all prepared epoxy-epoxidized soybean oil hybrid organic coating systems after 60 day of immersion time | 138 |
| Figure 6.23 | : Nyquist plot for AS 0 coating system after 60 days of immersion time | 138 |
| Figure 6.24 | : Nyquist plots ES 0, ES 4 and ES 6 hybrid organic coating systems after 30 day of immersion time | 139 |
| Figure 6.25 | : Nyquist plots ES 1 hybrid organic coating system after 60 day of immersion time | 139 |
| Figure 6.26 | : Nyquist plots ES 2 hybrid organic coating system after 60 day of immersion time | 140 |
| Figure 6.27 | : Nyquist plots ES 8 and ES 10 hybrid organic coating systems after 60 day of immersion time | 140 |
| Figure 6.28 | : Bode plots of AS 0 coating system after (a) 1 day and (b) 90 days of immersion along with the determining the breakpoint frequency and the corresponding capacitive (A1) and resistive (A2) regions... | 143 |
| Figure 6.29 | : Bode plots of ES 0 coating system after (a) 1 day and (b) 90 days of immersion along with the determining the breakpoint frequency and the corresponding capacitive (A1) and resistive (A2) regions... | 143 |
| Figure 6.30 | : Bode plots of ES 1 coating system after (a) 1 day and (b) 90 days of immersion along with the determining the breakpoint frequency and the corresponding capacitive (A1) and resistive (A2) regions... | 144 |

| | | |
|-------------|---|-----|
| Figure 6.31 | : Bode plots of ES 2 coating system after (a) 1 day and (b) 90 days of immersion along with the determining the breakpoint frequency and the corresponding capacitive (A1) and resistive (A2) regions... | 144 |
| Figure 6.32 | : Bode plots of ES 4 coating system after (a) 1 day and (b) 90 days of immersion along with the determining the breakpoint frequency and the corresponding capacitive (A1) and resistive (A2) regions... | 145 |
| Figure 6.33 | : Bode plots of ES 6 coating system after (a) 1 day and (b) 90 days of immersion along with the determining the breakpoint frequency and the corresponding capacitive (A1) and resistive (A2) regions... | 145 |
| Figure 6.34 | : Bode plots of ES 8 coating system after (a) 1 day and (b) 90 days of immersion along with the determining the breakpoint frequency and the corresponding capacitive (A1) and resistive (A2) regions... | 146 |
| Figure 6.35 | : Bode plots of ES 10 coating system after (a) 1 day and (b) 90 days of immersion along with the determining the breakpoint frequency and the corresponding capacitive (A1) and resistive (A2) regions... | 146 |

LIST OF TABLES

| | | |
|-----------|--|----|
| Table 3.1 | : Specification of acrylic polyol resin | 30 |
| Table 3.2 | : Specification of silanol functional phenyl silicone intermediate resin | 30 |
| Table 3.3 | : Specification of epoxy resin | 30 |
| Table 3.4 | : Specification of aliphatic polyisocyanate (NCO) curing agent | 32 |
| Table 3.5 | : Composition and nomenclature of the reference samples and all prepared SiO ₂ nanocomposite coating systems | 34 |
| Table 3.6 | : Composition and nomenclature of the reference samples and all prepared ZnO nanocomposite coating systems | 35 |
| Table 3.7 | : Composition and nomenclature of the reference samples and all prepared epoxy-soybean oil modified coating systems | 36 |
| Table 3.8 | : Classification of coating adhesion according to ASTM D3359 B | 42 |
| Table 4.1 | : Contact angles values of A 100, AS 0 and all prepared SiO ₂ nanocomposite coating systems | 50 |
| Table 4.2 | : The parameters gained from TGA studies of A 100, AS 0 and all prepared SiO ₂ nanocomposite coating systems | 59 |
| Table 4.3 | : The resistance values from EIS studies, along with the equivalent circuit model used to fit the data, of AS 0 and all prepared SiO ₂ nanocomposite coating systems after 1 day of immersion time | 64 |
| Table 4.4 | : The constant phase element values from EIS studies of AS 0 and all prepared SiO ₂ nanocomposite coating systems after 1 day of immersion time | 65 |
| Table 4.5 | : The resistance values from EIS studies, along with the equivalent circuit model used to fit the data, of AS 0 and all prepared SiO ₂ nanocomposite coating systems after 30 days of immersion time ... | 67 |
| Table 4.6 | : The constant phase element values from EIS studies of AS 0 and all prepared SiO ₂ nanocomposite coating systems after 30 days of immersion time | 68 |
| Table 4.7 | : The resistance values from EIS studies, along with the equivalent circuit model used to fit the data, of AS 0 and all prepared SiO ₂ nanocomposite coating systems after 60 days of immersion time | 70 |
| Table 4.8 | : The constant phase element values from EIS studies of AS 0 and all prepared SiO ₂ nanocomposite coating systems after 60 days of immersion time | 70 |

| | | |
|------------|--|-----|
| Table 4.9 | : The resistance values from EIS studies, along with the equivalent circuit model used to fit the data, of AS 0 and all prepared SiO ₂ nanocomposite coating systems after 90 days of immersion time ... | 74 |
| Table 4.10 | : The constant phase element values from EIS studies of AS 0 and all prepared SiO ₂ nanocomposite coating systems after 90 days of immersion time | 74 |
| Table 5.1 | : Contact angles values of A 100, AS 0 and all prepared ZnO nanocomposite coating systems | 86 |
| Table 5.2 | : The parameters gained from TGA studies of A 100, AS 0 and all prepared ZnO nanocomposite coating systems | 91 |
| Table 5.3 | : The resistance values from EIS studies, along with the equivalent circuit model used to fit the data, of AS 0 and all prepared ZnO nanocomposite coating systems after 1 day of immersion time | 97 |
| Table 5.4 | : The constant phase element values from EIS studies of AS 0 and all prepared ZnO nanocomposite coating systems after 1 day of immersion time | 98 |
| Table 5.5 | : The resistance values from EIS studies, along with the equivalent circuit model used to fit the data, of AS 0 and all prepared ZnO nanocomposite coating systems after 30 days of immersion time ... | 102 |
| Table 5.6 | : The constant phase element values from EIS studies of AS 0 and all prepared ZnO nanocomposite coating systems after 30 days of immersion time | 102 |
| Table 5.7 | : The resistance values from EIS studies, along with the equivalent circuit model used to fit the data, of AS 0 and all prepared ZnO nanocomposite coating systems after 60 days of immersion time | 106 |
| Table 5.8 | : The constant phase element values from EIS studies of AS 0 and all prepared ZnO nanocomposite coating systems after 60 days of immersion time | 107 |
| Table 6.1 | : Contact angles values of A 100, AS 0 and all epoxy-epoxidized soybean oil hybrid organic coating systems | 116 |
| Table 6.2 | : The parameters gained from TGA studies of A 100, AS 0 and all epoxy-epoxidized soybean oil hybrid organic coating systems | 125 |
| Table 6.3 | : The resistance values from EIS studies, along with the equivalent circuit model used to fit the data, of AS 0 and all prepared epoxy-epoxidized soybean oil hybrid organic coating systems after 1 day of immersion time | 130 |
| Table 6.4 | : The constant phase element values from EIS studies of AS 0 and all prepared epoxy-epoxidized soybean oil hybrid organic coating systems after 1 day of immersion time | 131 |

| | | | |
|-----------|---|--|-----|
| Table 6.5 | : | The resistance values from EIS studies, along with the equivalent circuit model used to fit the data, of AS 0 and all prepared epoxy-epoxidized soybean oil hybrid organic coating systems after 30 days of immersion time | 136 |
| Table 6.6 | : | The constant phase element values from EIS studies of AS 0 and all prepared epoxy-epoxidized soybean oil hybrid organic coating systems after 30 days of immersion time | 137 |
| Table 6.7 | : | The resistance values from EIS studies, along with the equivalent circuit model used to fit the data, of AS 0 and all prepared epoxy-epoxidized soybean oil hybrid organic coating systems after 60 days of immersion time | 141 |
| Table 6.8 | : | The constant phase element values from EIS studies of AS 0 and all prepared epoxy-epoxidized soybean oil hybrid organic coating systems after 60 days of immersion time | 142 |

LIST OF SYMBOLS AND ABBREVIATIONS

| | | |
|-----------------------|---|--|
| θ | : | Contact Angle |
| A | : | Acrylic Resin |
| ASTM | : | American Society for Testing and Materials |
| CA | : | Contact Angle |
| CHT | : | Cross Hatch Test |
| CPE_{diff} | : | Constant Phase Element of Diffusion Capacitance |
| CPE_{dl} | : | Constant Phase Element of Double Layer Capacitance |
| CPE_{po} | : | Constant Phase Element of Pore Capacitance |
| E | : | Epoxy Resin |
| EIS | : | Electrochemical Impedance Spectroscopy |
| ESO | : | Epoxidized Soybean Oil |
| FESEM | : | Field Emission Scanning Electron Microscopy |
| FTIR | : | Fourier transform infrared spectroscopy |
| IDT | : | Initial Degradation Temperature |
| NCO | : | Polyisocyanate |
| PVC | : | Polyvinyl chloride |
| R_{po} | : | Charge Transfer Resistance |
| R_{po} | : | Diffusion Resistance |
| R_{po} | : | Electrolyte Resistance Through the Pores |
| R_s | : | Solution Resistance |
| S | : | Silicone Resin |
| SCE | : | Saturated Calomel Electrode |
| SiO_2 | : | Silicon Dioxide Nanoparticles |
| $T_{50\text{ wt.\%}}$ | : | The Temperature Where 50 % Weight Loss Occurred |
| TGA | : | Thermogravimetric Analysis |

| | | |
|--------|---|----------------------------------|
| UV | : | Ultra Violet |
| UV-Vis | : | Ultraviolet-Visible Spectroscopy |
| Wt. % | : | Weight Percentage |
| ZnO | : | Zinc Oxide nanoparticle |

University of Malaya

CHAPTER 1: INTRODUCTION

1.1 Introduction

Corrosion is a worldwide phenomenon with huge economic consequences. Metals are used in the products, equipment, and machinery of all industries, including the oil and gas, chemical, food, fertilizer, marine and construction industries. Unless carefully designed and managed, storage and workplace environments can make the metals used vulnerable to corrosion. As such, cost effective methods must be designed and employed to protect metal surfaces (Ramesh et al., 2013; Sharmin et al., 2004).

The application of protective coatings is an efficient and cost-effective way to prevent metal corrosion. Current coating techniques focus on enhancing the overall performance of organic materials. One rapidly growing area in the development of protective coatings is the combined use of inorganic and organic materials, which capitalizes on the advantages of both to prevent corrosion. Coatings must be having excellent mechanical, thermal and anticorrosive properties to withstand adverse corrosive environments (Heidarian et al., 2010; Huttunen-Saarivirta et al., 2013).

Polymeric nano-reinforced coatings, in particular, have attracted much research interest as they offer good metal-surface protection from corrosion and fouling, especially with respect to steel. Nanoscale materials feature unique mechanical, physical and chemical properties that can increase the level of corrosion protection in bulk materials. Also, the miscibility of nano-sized particles in a polymer matrix results in decreased porosity and zigzagging in the diffusion pathways against the penetration of the electrolyte and the corrosive agents (Shi et al., 2009).

The performance of organic-coating barriers can be improved by the utilization of nanocomposites in protective coatings. There are also many other advantages associated with the use of advanced nano-structured coatings, including improvements in the optical,

mechanical, hydrophobic, tribological and electrochemical properties of the materials used to protect industrial components (Pourhashem et al., 2017; Zvonkina & Soucek, 2016).

1.2 Research Objectives

In recent years, the use of nanotechnology in the coating industry has become one of the smartest choices in the development of new coating systems that can meet advanced industrial requirements and facilitate the fabrication of intelligent and multifunctional coating systems. The objective of this study is to develop a multifunctional nanocomposite coating system that provides more than a physical barrier layer or decorative function, as well as serves many other functions that can facilitate industrial-scale production and the application of the coating system. The main objectives of this study can be summarized as follows:

1. Develop nanocomposite coating systems that consist of a polymeric matrix and inorganic nanofillers.
2. Study the impact of the developed binder and paint systems to realize anti-corrosion, hydrophobic, transparent nanocomposite coatings.
3. Determine the role of the utilized nanoparticles in enhancing the functional properties of coatings and identify the best type, size and loading ratio that ensure multifunctionality.
4. Evaluate the corrosion protection ability, hydrophobicity, transparency, and overall performance after the introduction of epoxidized soybean oil (ESO) to the hybrid polymeric matrix with regard to achieving intact organic coatings with multifunctional features.

1.3 Thesis Outline

This thesis comprises seven chapters, as follows:

- ❖ Chapter 1: This introductory chapter, which briefly describes the research background, primary research objectives and this thesis outline.
- ❖ Chapter 2 reviews previous investigations of corrosion, including corrosion types, effects and corrosion protection techniques. It also presents a detailed literature review on corrosion protection coatings in term of their composition, application and improvement approaches, especially the incorporation of inorganic nanoparticles within hybrid polymeric matrices (nanocomposite coatings).
- ❖ Chapter 3 describes the materials and preparation methods used to develop the proposed coating systems. In addition, it provides a description of all the characterization techniques, parameters and testing procedures utilized in the tests.
- ❖ Chapter 4 discusses the influence of modifying acrylic resin with 30 wt. % silicone resin (AS 0 coating system). In addition, it presents the results of SiO₂ nanocomposite coating systems and discusses the influence of utilizing different loading rates of SiO₂ nanoparticles on the overall performance of the hybrid polymeric matrix. Practically speaking, this performance is evaluated regarding the success it achieves with respect to multifunctionality along with superior corrosion protection ability, hydrophobicity and transparency.
- ❖ Chapter 5 presents an analysis of the collected results of ZnO nanocomposite coatings and discusses changes in the overall performance and the resulting multifunctionality after modifying the acrylic–silicone host matrix with different loading ratios of ZnO nanoparticles.
- ❖ Chapter 6 presents the results for coating systems that contain epoxidized soybean oil (ESO). It discusses in detail the effectiveness of utilizing natural oil to modify the previously developed acrylic–silicone hybrid polymeric matrix with respect to its

multifunctionality, corrosion protection performance and physical, thermal and structural properties.

- ❖ Chapter 7 presents the conclusions, based on the obtained results and makes suggestions for future work that could bring this research work to the next level.

University of Malaya

CHAPTER 2: LITERATURE REVIEW

2.1 Introduction

Material degradation due to its chemical interaction with the surrounding environment, usually referred to as corrosion, has been observed by humans for many years. There have been many attempts to study, analyse and understand the corrosion of metallic surfaces and to develop durable and efficient methods to prevent its occurrence. The application of protective coatings is one of the most suitable methods for preventing metal corrosion, in which the metal surface is prevented from making direct contact with the surrounding environment. However, corrosion continues to have a costly and harmful impact on many industries worldwide. To minimize the effects, costs, risks and hazards of corrosion, it is essential to better understand and investigate its effects while developing new prevention approaches and techniques (Hou et al., 2017).

2.2 Corrosion

2.2.1 Definition and Mechanism of Corrosion

Many definitions have been given to describe the corrosion process. According to the International Union of Pure and Applied Chemistry (IUPAC), corrosion is defined as “an irreversible interfacial reaction of a material (metal, ceramic, polymer) with its environment which results in consumption of the material or in dissolution into the material of a component of the environment. Often, but not necessarily, corrosion results in effects detrimental to the usage of the material considered. Exclusively physical or mechanical processes such as melting or evaporation, abrasion or mechanical fracture are not included in the term corrosion” (Sriharsha et al., 2017).

However, the above definition of the corrosion process has been considered to be too general and to be more specific, the ISO 8044-1986 defined corrosion as “the physico-

chemical interaction between a metal and its environment, which results in changes in the properties of the metal and which may often lead to impairment of the function of the metal, the environment, or the technical system of which these form a part” (Montemor, 2014).

Despite the fact that the term "corrosion" is typically used to describe the degradation of metallic-based materials, it also covers other materials, including those that are polymeric and ceramic. The prevalence of corrosion in the natural environment involves the transformation of iron to rust, oxidation of copper, tarnishing of silver and so on. In this study, cold-rolled mild steel substrates were utilized as a metallic substrate, and the investigations were designed to examine and analyse the ability of the chosen corrosion protection method (application of protective coating) to withstand and resist the initiation of the corrosion process. The selection of steel substrates was based on the consideration of steel as a vital commodity metal with a wide variety of applications in so many industrial sectors, i.e., buildings, bridges, power stations. Also, steel was chosen based on the fact of the significant worldwide economic impact of corrosion on steel, i.e., one-quarter of the world's steel annual production is destroyed by corrosion, which corresponds to a loss of five tons of steel per second or up to 150 million tons per year (Landolt, 2007).

2.2.2 Corrosion Classifications

The analysis of various types and classifications of corrosion can provide a better understanding of this destructive phenomenon. The extent and impact of corrosion in the natural environment is classified as either uniform, pitting or stress corrosion cracking, as described below.

2.2.2.1 Uniform Corrosion

Uniform corrosion, also called general corrosion, is the most common form of corrosion and occurs in response to chemical attack. When metal experiences this kind of corrosion, the substrate appears dull, loses thickness and finally collapses. Figure 2.1(a) shows a sectional schematic of steel metal subjected to uniform corrosion. Several methods could be used to obtain a proper surface protection against this type of corrosion, including increasing the metal thickness, the application of protective coatings, utilization of corrosion inhibitors or alteration of the surrounding environment. Generally, this type of corrosion attacks metallic surfaces that cannot form a passive protection layer after having been in direct contact with the surrounding atmosphere, as illustrated in Figures 2.1(b) and (c).

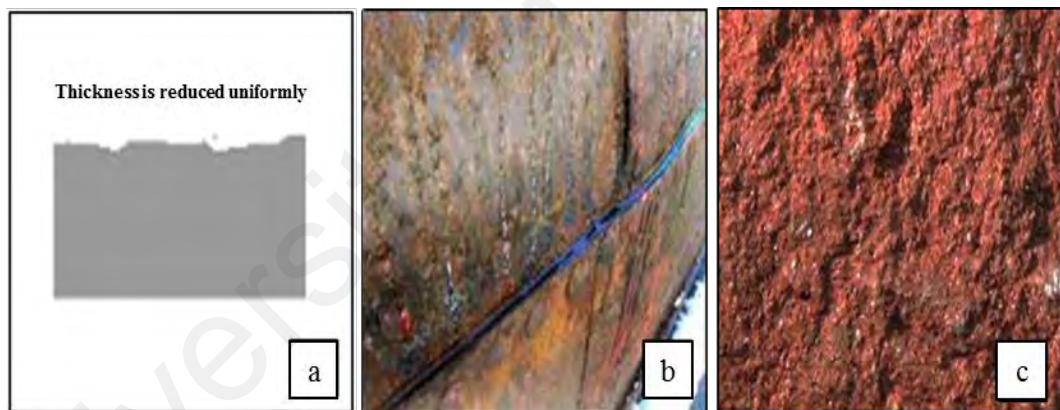


Figure 2.1: Uniform corrosion (Photo sourced from www.corrosion-doctors.com).

2.2.2.2 Pitting Corrosion

In this form of corrosion attack, metal surfaces are subjected to localized failure that results in small pits or holes, which lead to a rapid degradation in the metal properties. The dissimilarity in the size and shape of the resulting holes produces a rough surface with a heterogeneous morphology, as shown in Figure 2.2. Pitting corrosion is usually observed when a metallic surface can avert uniform corrosion, due to the application of corrosion protective coatings or other corrosion protection method. However, when there

is a defect in the coating layer or a loss of adhesion on some parts of the coating–substrate interface, pitting corrosion attack can occur (Xu et al., 2012).

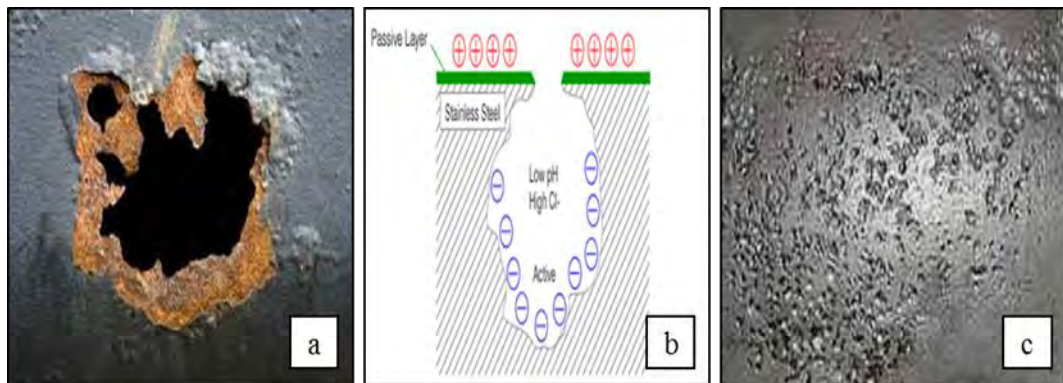


Figure 2.2: Pitting corrosion (Photo sourced from www.corrosion-doctors.com).

2.2.2.3 Stress Corrosion Cracking

This kind of corrosion is usually observed in the manufactured parts used in various mechanical operations. The simultaneous impact of static tensile stresses on these metallic components is considered to be the main factor accounting for the initiation of stress corrosion cracking. Figure 2.3(a) shows a sectional schematic of a corroded metal part after its exposure to stress corrosion. The stresses applied to metals can arise from internal sources such as welding, heat treatment or cold work. However, external forces can also contribute to this kind of corrosion whereby operations like bending, annealing and hammering can be primary sources of the mechanical stresses and crack propagation. It is worth mentioning that the cracking usually occurs perpendicular to the applied stresses as illustrated in Figure 2.3(b) and (c).

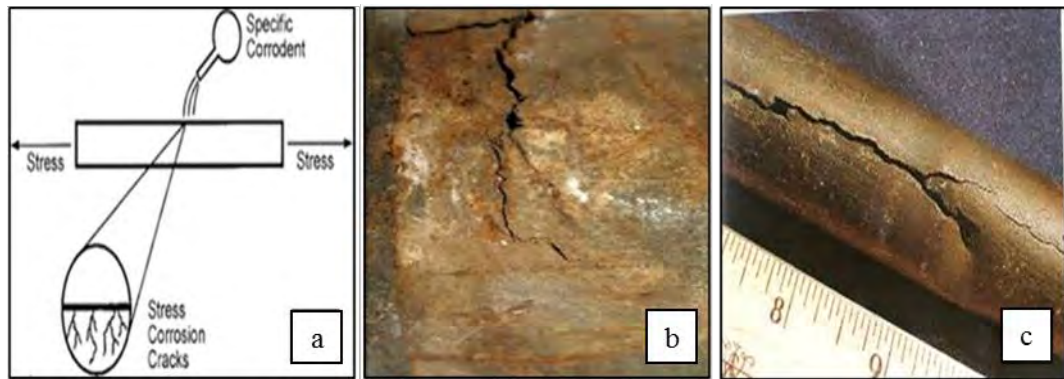


Figure 2.3: Stress corrosion cracking (Photo sourced from www.corrosion-doctors.com).

2.2.2.4 Fatigue Corrosion

Fatigue corrosion, a type of stress corrosion, occurs due to the effect of cyclic stress in an environment that is corrosive. For instance, in response to being folded and straightened numerous times, a wire will eventually break, as the metal becomes fatigued. As shown in Figure 2.4, fracture occurs due to the increasing stress associated with the repetitive bending.

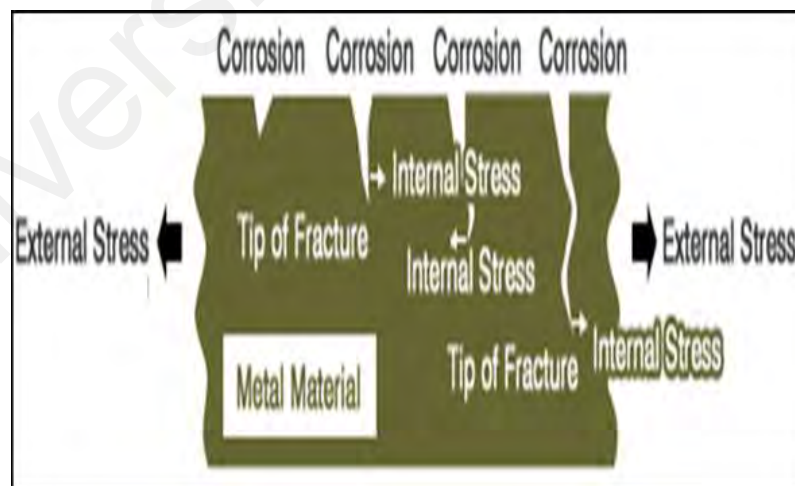


Figure 2.4: The general mechanism of fatigue corrosion (Photo sourced from www.misumi-techcentral.com).

Many things on Earth are exposed to repetitive stresses. Railway lines experience stress whenever a train passes, and aquatic structures such as bridges and platforms experience significant cyclic stress in response to wave action. Aircraft pressure bulkheads, which experience extreme air-pressure differentials, are also subject to stress fatigue. Metal fatigue is common in the atmosphere, in the marine environment, and in vacuum conditions. As shown in Figure 2.5(a), fatigue cracks can propagate through metal and cyclic stress can result in extensive fractures to the point of brittle fracture, as illustrated in Figure 2.5(b). Stress corrosion can only occur in the presence of both stresses and corrosion.

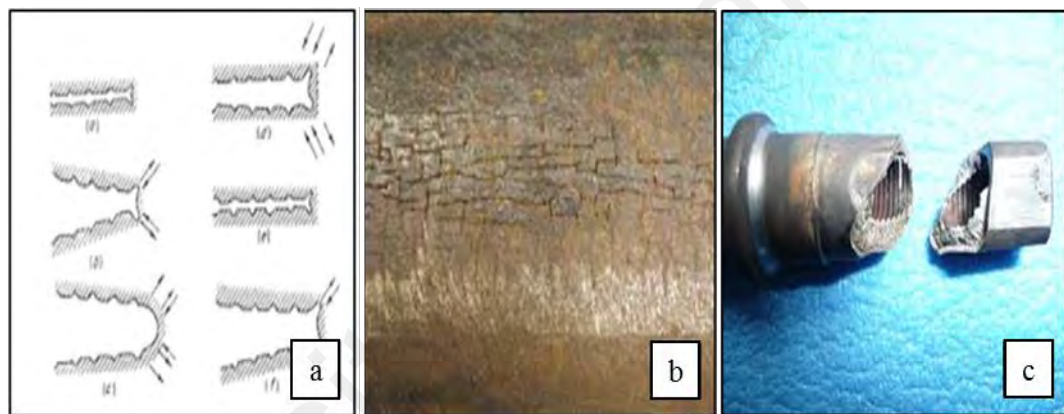


Figure 2.5: Fatigue corrosion (Photo sourced from www.corrosion-doctors.com).

When the stress experienced is below the fatigue limit of a metal, it will not fracture despite repeated stress exposure. On this basis, there are critical indexes used in machinery and equipment design for equipment that is exposed to repetitive stress. However, fractures from repetitive stress can occur in metals even when those stresses are below the fatigue limit if that stress occurs in a corrosive environment. In addition, these fractures can take place after fewer repetition cycles at given stress levels.

As such, the fatigue limit is a term that can become irrelevant, as metals can fracture, as illustrated in Figure 2.5(c), irrespective of repetitive stress levels and number of cyclic stress repetitions. This phenomenon is known as "fatigue corrosion" (Gangloff, 1995). It

is possible to control fatigue by reducing the amount of cyclic stress experienced or by employing a corrosion controller. A roughened metal brittle-fracture surface is illustrated in Figure 2.5.

2.2.2.5 Intergranular corrosion

Intergranular corrosion in metals and alloys occurs at the grain boundaries, i.e., where the crystal surfaces are in contact. Crystals are characterized by orderly atomic alignment, although the atomic alignments in adjacent crystals can differ as shown in Figure 2.6(a). Atoms located in grain boundary areas must interact with those of crystals having different alignments. As such, these atoms have mixed orientations and high energy levels. This can be observed microscopically in specimens etched with a corrosive solution, as shown in Figure 2.6(b), in which the grain boundaries have dissolved and the crystals are distinctly visible (Ziegler et al., 2005). Intergranular corrosion is a surface phenomenon and advances no deeper. However, when heated in certain conditions, crystal grain boundaries do not exhibit the chemical composition changes described above and selective corrosion can occur.

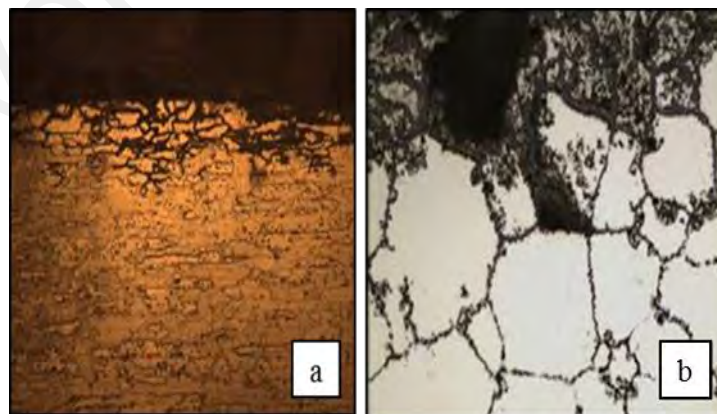


Figure 2.6: Intergranular corrosion (Photo sourced from www.corrosion-doctors.com).

2.2.2.6 Filiform Corrosion

Filiform corrosion, also referred to as "filamentary" or underfilm corrosion, is associated with magnesium (Mg), aluminium (Al) and iron alloys that are typically coated with organic materials (McMurray et al., 2010). This corrosion type can be identified with the naked eye and requires no microscope.

The filiform corrosion mechanism involves the migration of water and oxygen molecules beneath painted surfaces as illustrated in Figure 2.7(a). This corrosion type tends to occur in very humid conditions. Figure 2.7(b) is a sectional schematic of filiform corrosion on a coated metal substrate. Anions containing halides have been identified as being associated with filiform corrosion (McMurray et al., 2010). In corroded areas, a thread-like filament forms under the coating as shown in the Figure 2.7(c). Various methods are used to reduce the effects of filiform corrosion, one of which is to apply multiple protective-coating layers and reduce the relative humidity.

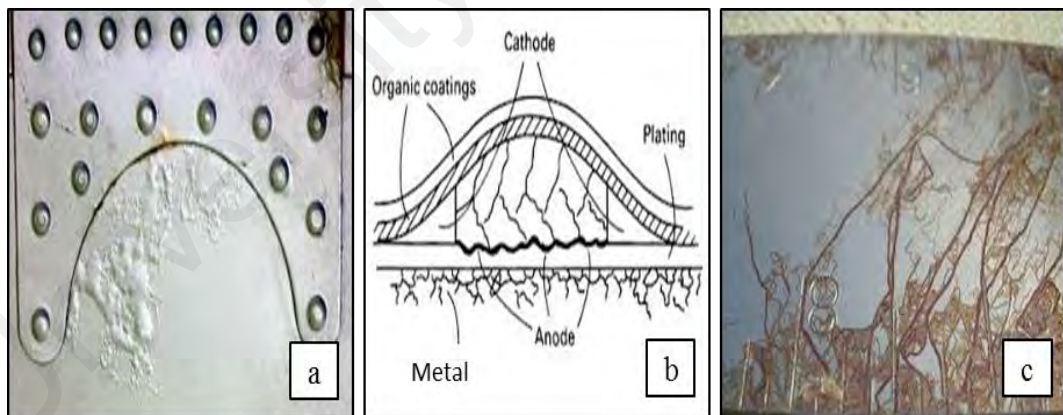


Figure 2.7: Filiform corrosion (Photo sourced from www.corrosion-doctors.com).

2.2.2.7 Crevice Corrosion

A crevice or narrow opening can occur between two pieces of metal or two strongly adhered materials such as plastic. Crevice or contact corrosion occurs at the contact area of two metals that form a geometric structure, such as riveted plates, welded materials or

threaded joints as illustrated in Figure 2.8(a) and (b). Contact can also occur between metallic and non-metallic solids, such as plastics, glass and rubber with dirt, sand or permeable-corrosion products on the metal surfaces.

Crevice corrosion is localized in crevices or on affixed surfaces that are subject to a stagnant solution. Many metals and alloys are vulnerable to crevice corrosion, which occurs first and most typically in stainless steel (Wika, 2012). This corrosion type is the most common localized corrosion type as well as one of the most harmful, as it occurs in alloys that typically have excellent corrosion resistance, e.g., stainless steel. Moreover, it takes place in areas that are not immediately obvious (Rashidi et al., 2007). As such, crevice corrosion can result in the sudden failure of a metal in use. Crevice corrosion typically occurs around washers, barnacles and sand grains, under protective films or coatings and in the pockets of threaded joints as shown in the Figure 2.8(c).

The simplest way to prevent crevice corrosion is to reduce the number of crevices in the overall structural design. When this is not possible, other strategies are to minimize the amount of retained moisture by ensuring effective drainage, sealing metal edges or widening crevice openings as much as possible.

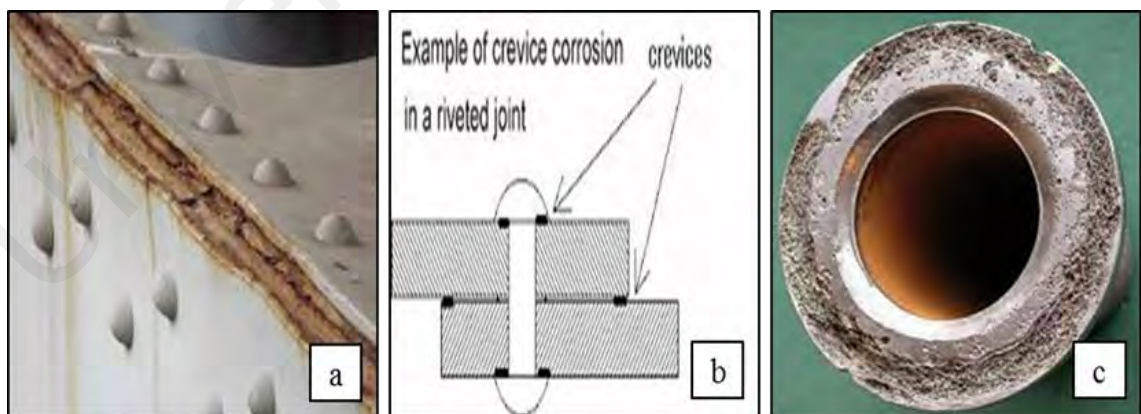


Figure 2.8: Crevice corrosion (Photo sourced from www.corrosion-doctors.com).

2.2.2.8 Galvanic or Bi-Metallic Corrosion

Galvanic corrosion occurs when two different metals are joined in the presence of an electrolyte. As shown in Figure 2.9, in the formation of a galvanic couple, one of the two metals becomes the anode and corrodes more quickly than it would alone and the other becomes the cathode and corrodes more slowly than it would alone. The joint between these metal pairs is where the most severe attacks occur. Farther away from this bi-metallic joint, the acceleration of the attack slows. Each metal has a characteristic potential that is unique when submerged in an electrolyte. These metals can be represented in a relational series.

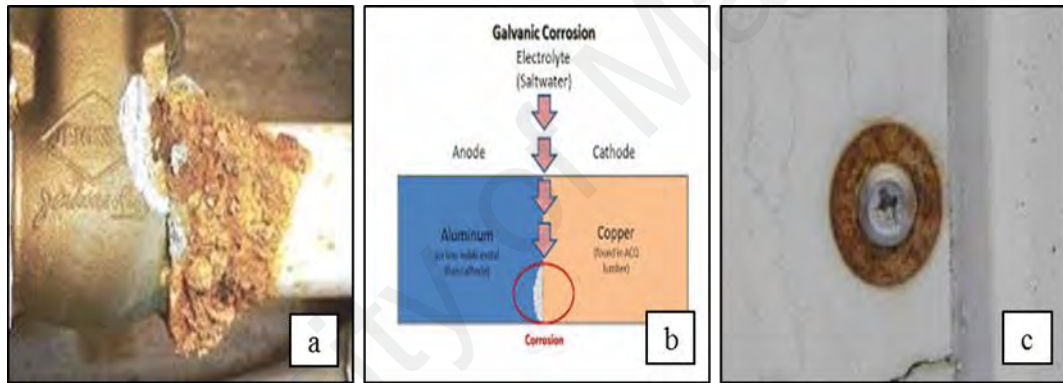


Figure 2.9: Galvanic corrosion (Photo sourced from www.corrosion-doctors.com).

2.2.2.9 Fretting corrosion

Fretting corrosion occurs rapidly at the interface between surfaces in contact, whereby the contacting interface of these bodies is under load or in relative motion sufficient to produce surface deformation as shown in Figure 2.10. This corrosion often results in fatigue failure and most commonly occurs in machinery bearing surfaces, e.g., connecting rods, bearing supports and splined shafts.

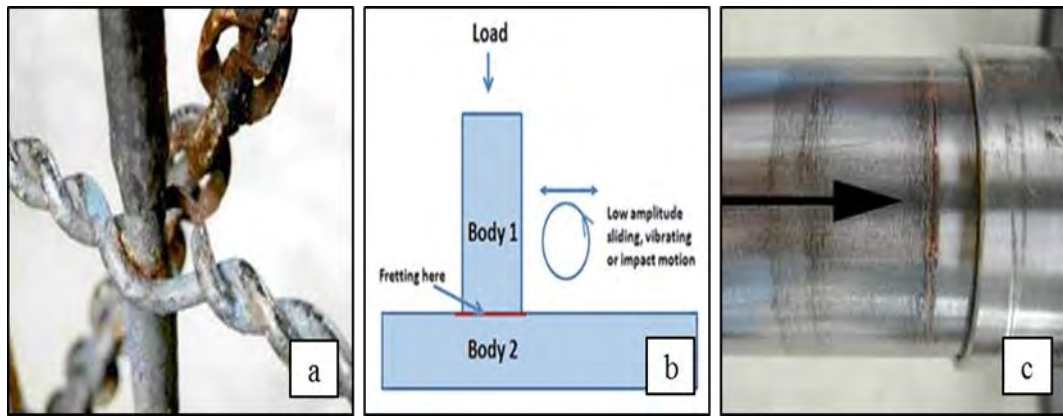


Figure 2.10: Fretting corrosion (Photo sourced from www.samtec.com).

Fixing the problems caused by fretting corrosion is an expensive undertaking. No standard test method exists for fretting corrosion. For this corrosion type, the mechanical design is a more important consideration than material selection (Ramis Rao, 2016). While it is not possible to completely eliminate fretting corrosion, it can be minimized by reducing the relative movement between materials or increasing hardness by utilizing materials that are not vulnerable to fretting corrosion. One simple and inexpensive approach is to use a contact lubricant and seal to minimize vibrations.

2.2.2.10 Erosion corrosion

Erosion corrosion involves both erosion and corrosion along with a moving corrosive fluid or a metal component, whereby there is a rapid degeneration of the protective layer on a metal surface. This corrosion type can be made worse by poor quality workmanship when fluid flow is improperly directed (El Rayes et al., 2013).

Erosion corrosion is thought to be the result of entrained air bubbles, particulates and suspended matter at a sufficient flow rate. Erosion, much like impingement attack, is found most often at elbows and tees or in areas in which the water direction is altered sharply as shown in Figure 2.11. Copper (Cu) and brass and other soft metals are more vulnerable than steel to erosion corrosion. Careful consideration of the design and selection of materials can minimize erosion corrosion.

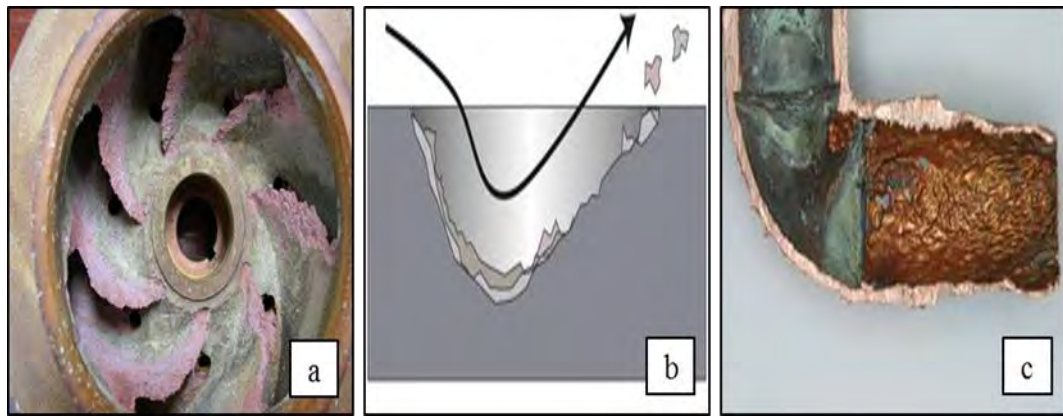


Figure 2.11: Erosion corrosion (Photo sourced from www.corrosion-doctors.com).

2.2.2.11 High-temperature corrosion

High-temperature corrosion, which occurs by the oxidation of a metal at elevated temperatures, does not depend on the presence of a liquid electrolyte. This is a non-galvanic type of corrosion that occurs when a metal is in a high-temperature atmosphere that contains oxygen, sulphur or other compounds that can oxidize the metal of interest. For example, the materials often used in aerospace applications, power generation stations and car engines must be resistant for prolonged high-temperature periods during which they are exposed to an atmosphere containing highly corrosive combustion products. Typically, this damage occurs in the exhaust manifold and is known as “dry corrosion” or “scaling” as shown in Figure 2.12.

The oxidation reaction is the most critical in high-temperature corrosion. For example, oxide formation on stainless steels can provide a protective layer that prevents further atmospheric assault, thus permitting the use of the steel for long periods in the otherwise hostile room- and high-temperature conditions (Lang, 2012). By examining the plentiful metal corrosion deposits following corrosion, the corrosion mechanism can be determined, i.e., metal-oxide oxidation, metal-carbide carburization, metal-sulphide sulfidation, sulfidation or oxidation by mixtures of sulphides and oxides or metal-chloride chlorination (Marcus, 2011).

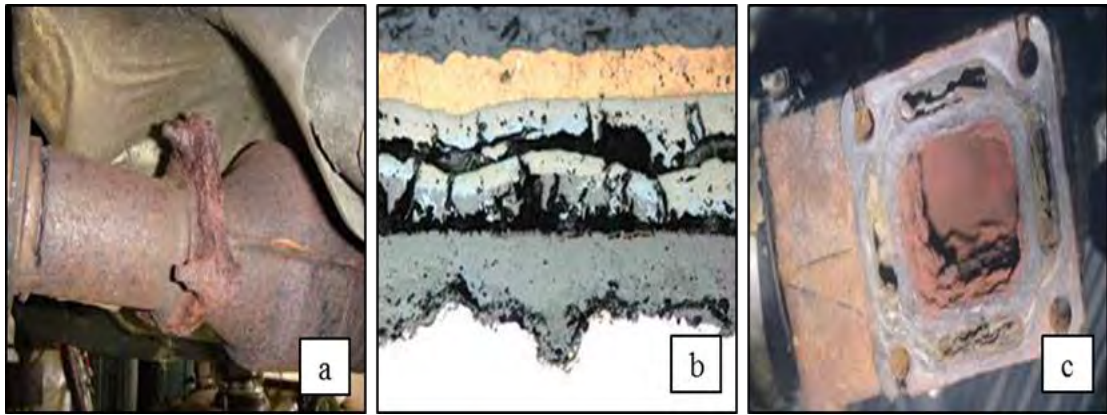


Figure 2.12: High temperature corrosion (Photo sourced from www.corrosion-doctors.com).

2.2.3 Corrosion protection methods

Four approaches can be used to reduce and protect steel from corrosion (Mohamed et al., 2015; Sriharsha et al., 2017; Zhang et al., 2016).

1. Selecting corrosion-resistant materials:

In addition to cost, material availability, and other factors, corrosion resistance is an important consideration in the overall material selection process. In our system, we select materials for specific locations based on previous industry analyses and corrosion testing data. Essentially, we look for a metal that is less likely to oxidize in the conditions specific to our system. Generally, we prefer a metal with a high standard electric potential for hydrogen oxidation in the electromotive series.

2. Corrosion inhibitors:

These inhibitors help modify the system environment to prevent or slow the corrosion process. By forming a deposit on the metal surface, they slow the rate of corrosion by increasing the polarizations of the anode and cathode as well as the electrical resistance. Corrosion control can be achieved by modifying structures to improve drainage and using inhibitors in power plants and engine cooling systems.

3. Cathodic protection:

In this method, an electric current is supplied from an external source to reduce the difference between the anode and cathode. This method is used to effectively protect underground structures and those in contact with water, such as pipelines and underground storage tanks, in which the natural electrochemical cell action is inhibited.

The external current can be delivered in one of two ways:

- a) **Sacrificial Anode:** In this approach, the active metal corrodes, thus sacrificing itself and protecting the vulnerable surface. The corrosion of an active metal, such as zinc (Zn), produces a standard electric potential. To quantify this method, we use the natural corrosion potential to select the sacrificial metal.
- b) **Impressed current:** This method involves supplying a direct electric current from an external source (even a rectifier can be used to convert AC to DC) and the use of an inert anode material to complete the circuit.

4. Protective coatings:

This approach is currently the one most widely used worldwide. The use of protective coatings becomes even more effective in combination with the methods described above. Three basic mechanisms are used to enhance the degree of corrosion control provided by protective coatings:

- a) **Barrier protection:** This mechanism makes the protective coating impermeable to moisture and other electrolytes by forming a barrier between surfaces that are vulnerable to corrosion and the environmental factors that promote corrosion. As such, it retards or completely thwarts the approach of oxygen to the metal surface.
- b) **Cathodic protection of steel:** Some protective coatings are characterized by a high Zn (or any other active metal) particle loading, whereby the particles are themselves in electric contact as well as with the metal they coat. As a result, a protective film provides cathodic protection.

- c) **Inhibitive pigments:** The pigments present in protective coatings can also function as corrosion inhibitors at the metal–coating interface.

5. Other methods:

Metals that form a stable oxide layer: By forming a stable surface oxide layer, further corrosion can be prevented. With this approach, we first select a metal that generates a stable oxide layer and then enhance the oxidation resistance of certain metals (typically alloys) by adding alloying elements such as silicon (Si), chromium (Cr), aluminium (Al) or other element. Upon reacting with oxygen, these elements tend to form a stable oxide layer that serves as a protective coating on metals exposed to certain application environments.

2.3 Coating

The corrosion-prevention coating technique involves the application of a layer of film onto a metal substrate both to provide primary protection and to prevent environmental contact with the metal surface (Rau et al., 2012). In the manufacturing process, the coatings produced must have flexibility, good adhesion and cohesion, as well as physical resistance to impact and moisture permeation and chemical resistance to corrosive environments (Wicks et al., 2007). These coatings can be metallic (electroplating or galvanizing metals), organic (polymer) or inorganic (ceramics, glass). The most commonly used coating material is paint, which contains organic binders and inorganic pigments. Some paints also have corrosion-inhibiting ingredients that hinder the corrosion of steel substrates and generate a galvanic action (Rau et al., 2012).

The appearances (clear, pigmented, metallic or glossy) and functions (corrosion protective, abrasion protective, decorative or photosensitive) of these coatings vary and can be categorized into three groups: organic, inorganic and hybrid.

- a) **Organic Coatings:** Lowest in cost and the most widely used, these coatings include paints, varnishes and lacquers. The resins used to produce these

coatings typically include organic polyurethanes, acrylics, epoxies, polyesters and alkyds.

b) **Inorganic Coatings:** The metallic and ceramic particles in inorganic coatings provide effective corrosion barriers. Typical examples include cladding, electroplating, vapour deposition and flame spraying, all of which resist heat and radiation, are biologically inert, and provide electrical conductivity.

c) **Hybrid Coatings:** Some protective coatings today may contain an organic–organic or organic–inorganic resin to enhance their effectiveness. These coatings are used as a single layer rather than the multiple layers that are widely used.

In general, inexpensive coatings are used on low-cost structural materials to minimize the expense and maximize the economic viability of this corrosion-control option. However, in general, the lifetime of paints and coating materials is shorter than the materials they protect, so it is vital that a routine maintenance schedule be employed to ensure coating effectiveness (Revie, 2008).

The critical concern in the surface preparation of organic coatings is the selection of the primer and top coats. Poorly prepared surfaces can lead to coating system failure and 70 % coating failure is due to improper surface preparation. With a properly prepared metal substrate, the applied coating system spreads and solidifies in the surface crevices and holes, allowing the coating to mechanically bond to the substrate to further ensure its adhesion to the substrate.

When using a hybrid organic coating, there is no need to apply multiple layers to the substrate, which indirectly prevents the incorporation of impurities like dust and air bubbles. The longer drying times needed for multilayer coatings means that higher-level strata cure first, which can trap solvents inside, resulting in lower resistance to abrasion

and poorer adherence to the substrate. As such, newer protective coatings that utilize a hybrid coating mixture can enhance coating performance.

2.3.1 Coating Selection

When selecting a coating system, there may be a number of acceptable options, so consideration must be given to factors related to corrosion control and cost. The main factors include the following:

- Certain projects may warrant high-performance high-quality materials if they involve high cost, high status, or will engender serious consequences should failure occur.
- Expectation of an excellent system track record regarding environmental and operational conditions.
- Relative ease of access to high-quality equipment and contractor for substrate work-surface application.
- Legal and environmental regulatory compliance.
- Conditions of maintenance and compatibility with existing materials.
- Coating life expectancy to time of first required maintenance.
- Substrate to be coated and delivery considerations.

2.3.2 Coating Composition

Coating is essentially a pigmented liquid that protects and enhances the surface appearance of a substrate. To produce these pigmented liquids, manufacturers utilize a variety of raw materials comprising liquid (binder and solvent) and solid (pigment) components. The three components of a typical coating system are the binder, solvent and pigments. The binder forms the paint's film that adheres the components and affixes the

paint to the substrate. The solvent thins or disperses the binder to enable easy paint application. Pigments provide colour and aid in corrosion control.

2.3.2.1 Binder

The binder in a paint forms the film that adheres the components and affixes the paint to the substrate. It is a vital aspect of a system's adhesion performance. Anticorrosive coatings employ a wide variety of binders. In fact, any relatively inert and durable binder can be utilized, and resins (liquid plastics, i.e., epoxies, acrylics, polyesters, polyurethane, and vinyl esters) are a typical choice for many applications.

Organic-resin binders can be classified as either thermosetting or thermoplastic polymers. Thermosetting polymers are uncured and irreversible polymers that are liquid at room temperature. Most are routinely used as adhesives and are characterized by a chemical bond formation that affixes the coating to the substrate. Practically speaking, thermoset coating systems are stronger and more durable than those using thermoplastic polymers due to their polymer cross-linkages and higher heat resistance. Polyester, epoxy and urethane are typical examples of thermosetting polymers (Knudsen & Forsgren, 2017; Lyon et al., 2017). Thermoplastic polymers, in contrast, can be formed into any shape, provide no reinforcement strength, and have no adhesion property, although their resistance to impact is comparable to that of thermosets. Polycarbonate, acrylic and vinyl are typical examples of thermoplastics.

In this study, several organic resins were utilized in order to develop the optimum hybrid polymeric matrix.

a) Acrylic Polyol Resin

Acrylic polyols, by and large, involve free-radical polymerization by an initiator, such as a compound with an azo link ($R-N \equiv N-R'$) or a peroxy link ($R-O-O-R'$) (Knudsen

& Forsgren, 2017). The term 'polyol' refers to the numerous hydroxyl functionality groups comprising its structure.

Acrylics are produced by dissolving polymers of acrylic and methacrylic acids. Generally, these mixtures have an acrylic polyol structure. The hydroxyl group residue in these monomers can incorporate additional functional groups and improve the performance of resin products. Acrylics can be either solid in form or a solution in organic or inorganic solvents, emulsions, dispersions or water.

Acrylic resins are very durable, transparent and non-yellowing. They are resistant to hydrolysis and inert to aliphatic cleaners, solvents and polish. Thermoplastic and thermosetting acrylic resins are used in the manufacturing and automotive industries and they can be cross-linked with polyisocyanate and melamine formaldehyde resins (Jones et al., 2017). To successfully cross-link these resins, for every molecule or chain, one species must have at least two and the other species at least three reactive sites (Jones et al., 2017).

The acrylic component can be designed for the desired degree of flexibility, weathering characteristics, and gloss in a car finish, esp. a metallic finish. Acrylic resins are characterized by high gloss, gloss retention and resistance to hydrolysis. Today, aqueous acrylic coatings are used more often in wood and corrosion-protection coatings. Typically, these paint types are not baked; rather their mechanical properties are enhanced by the formation of cross-linkages at room temperature. Acrylic resins can also be cured at elevated temperatures and require no additional external hardeners. Methyl methacrylates are known for their excellent weather resistance and gloss retention and their compatibility with other organic polymers such as epoxy, polyester and silicone.

To enhance the mechanical and electrochemical properties of acrylic, 10–20 wt. % of epoxy can be added to the blend, but the enhancement abruptly decreases with any further increase in the epoxy percentage (Ramis et al., 2013). Researchers have shown that the

properties of stiffness and barrier formation in acrylic coatings can be enhanced by the addition of solid phenyl silicone. Experimental analyses on a mild steel substrate have revealed that a blend of 30 wt. % silicone resin and 70 wt. % acrylic resin exhibits good adhesion and impact resistance (Vengadaesvaran et al., 2010).

b) Silicone

Polydimethylsiloxanes, more commonly called silicones, are produced by the hydrolysis and condensation of methylchlorosilanes. These semiorganic synthetic polymers are characterized by a spine of repeating silicone–oxygen units with organic groups hanging from the polymer chain.

Silicone's properties can be changed using different organic substituents, but methyl groups yield the most desirable characteristics. According to their molecular structures and weights, the main silicone classifications include silicone fluids, resins and elastomers. Silicone-derived products have a variety of applications, including emulsions, adhesives, greases, sealants, elastomers, coatings and special chemicals (Andriot et al., 2007; Hou, et al., 2000).

The physical properties of silicones endure over a wide range of temperatures and weather conditions. Silicones are resistant to ozone, corona discharge and ageing; they exhibit good dielectric strength and ability to form films, and are characterized by high oxidation and thermal stability, good hydrophobic behaviour and release action, low surface tension and superb physiological inertness. In combination, these attributes make silicones useful in a wide range of engineering and industrial applications, including biomaterials and aerospace (Pouget et al., 2009).

The application of silicone fluids extends to hydraulics, water-repellent finishes for textiles, antifoaming products, surfactants, lubricants and greases. Varnishes, paints, electrical insulation, moulding compounds, laminates, adhesives and release coatings all use silicone resins. Elastomer applications include caulks, sealants, gaskets, adhesives,

hoses, tubing, belts and electrical insulations in automobile ignition cables, fabric coatings, encapsulation and moulding applications, encapsulants and various medical applications, including anti-flocculants, pacemakers encasements, heart valves, contact lenses, prosthetics and plasma-bottle coatings to prevent blood coagulation (Selvaganapathi, 2013).

c) Soybean Oil

The increasing demand for petroleum-based products and the associated negative environmental impact, in addition to diminishing non-renewable resources are factors that are moving scientists to identify more environmentally sustainable and responsible solutions. With respect to the manufacture of bioplastics, there is growing interest in the use of renewable starting materials, such as starches, vegetable oils and proteins (Baştürk et al., 2013).

Soybean oils are a cheap and abundant biological feedstock option and are available in large quantities. As starting materials, they offer many advantages, including low toxicity and biodegradability. They have double bonds, which serve as reactive sites in coatings and can be functionalized by epoxidation. For industrial applications, epoxidized vegetable oils have great potential as inexpensive and renewable starting materials (Sharma et al., 2006; Tehfe et al., 2010).

Composites of soybean oil-based hybrid materials with good mechanical properties have been produced using acrylate-modified soybean oil, as have organic–inorganic hybrid coatings from plant oils. Using silicium oxides, researchers have developed transparent organic–inorganic hybrid networks. In addition, a new class of green hybrid materials has been reported, which incorporates a silica network into a soybean-oil polymer matrix (Ahn et al., 2011; Hong et al., 2011).

2.3.2.2 Solvents

Solvents are liquids that are utilized to dissolve other materials. In paint manufacturing, solvents are liquids or liquid mixtures that dissolve resins and carry pigments and other components. In water-based paints, water is the solvent, but the resin (or latex) is not dissolved but emulsified in the water. Small quantities of other solvents are also added to water-based paints. In the paint industry, solvents have three major uses:

- As cleaning agents, solvents are used to remove oily deposits from a substrate during paint preparation and to clean equipment and remove paint splatters and spills after paint application.
- As an integral component of paint formulations.
- As paint thinners added after paint is produced to adjust its application properties.

In paint formulations, the solvent carries the paint from its container to the substrate in a condition that permits the paint to be uniformly sprayed, rolled or brushed. Solvents are also used to realize a certain gloss level and dry-film thickness to meet the performance specifications listed on the product data sheet. Without a solvent to extend the drying time, paint can dry too quickly after application and become too thick and stringy to achieve the desired finish. The careful selection of a solvent can also enhance the balance of a paint's application properties, including its viscosity, spreading rate, flow, drying time and ability to maintain a wet edge (Salihoglu & Salihoglu, 2016).

2.3.2.3 Pigments

Pigments, the solid component in paints, not only provide colour, finish and opacity, but also protect the underlying surface from corrosion and weathering and help hold the paint together. Solid pigment particles are finely ground, insoluble and well dispersed. They can be natural or synthetic, inorganic or organic. Generally, both inorganic and

organic pigments are used and inorganic pigments are typically less expensive and provide colours that are less clear (Freitag & Stoye, 2008; Kalendová et al., 2008).

Pigments can also serve as fillers, property modifiers and reinforcements. To be effective, the pigment must be evenly dispersed and in contact with the solvent. A layer of moist air, or in some cases other gases, surround pigment particles. To establish contact between the pigment and solvent, this surrounding layer must be displaced, a process known as wetting. If the pigment in paint is not properly wetted, colour streakiness may occur in the paint. As such, solvents and pigments must be carefully selected to produce a well-wetted pigment and must also be compatible with the binders in a given paint system. Inorganic pigments do not bleed and are heat and light stable, so they are widely used. They are utilized in specialized pigments (e.g., anti-corrosion pigments) and in black and white pigments, since there are no pure black or white organic pigments (Ahmed et al., 2016; Kalendová et al., 2014).

2.3.3 Nanocomposite Coatings

Materials with at least one nanoscale dimension are referred to as nano-sized or nano-structured materials. In nanoscale materials or nanocomposites that have a component in the nano domain, the size and distribution of this nano component (grain, particle, nanorod etc.) in the given matrix are very important parameters that determine the overall nanomaterial performance (Saji & Cook, 2012).

There is burgeoning scientific interest in polymeric nano-reinforced coatings as they offer a convenient way to prevent the corrosion and fouling of metal surfaces. The unique physical, chemical and mechanical properties of nanoscale materials play important roles in improving the corrosion protection of bulk materials. In addition, improved barrier performance leads to the miscibility of nano-sized particles in the polymer matrix by reducing porosity and zigzagging in the diffusion pathway (Shi et al., 2009).

Currently, the inorganic nanoparticles used most often are silicon dioxide and zinc oxide nanoparticles. Used in the production of multifunctional nano coatings, these multi-purpose nanoparticles are characterized by their hardness, hydrophobic enhancement, low refractive index and excellent dispersion (Dolatzadeh et al., 2011a). However, there is a major problem of microscopic-phase separation, which occurs due to the inhomogeneous dispersion of inorganic nanoparticles in organic matrixes. This aggregation can also occur during curing despite there being a good particle distribution in the polymer matrix during blending. In addition, a viscosity increment has been observed with higher nanoparticles percentages, which could pose difficulties in coating applications (Amerio et al., 2008).

Silica or silicon dioxide, SiO_2 an inorganic nanoparticle, is often used as additives to enhance the properties of many organic base resins (Islam et al., 2015; Kasturibai & Kalaiganan, 2013; Zhao et al., 2016). High mechanical strength, good thermal and chemical stability and high surface area make SiO_2 nanoparticles gain the trust as a useful tool to enhance the mechanical properties and reduce its thermal degradation at high temperature of the polymeric films (Ray & Okamoto, 2003; Ribeiro et al., 2014). Moreover, many researchers have confirmed the capability of SiO_2 nanoparticles in enhancing the barrier properties and the hydrophobicity of the coatings system by zigzagging the diffusion pathways against the penetrating corrosive agents and producing new levels of surface roughness respectively.

Islam et al. (2015) have successfully reduced the surface porosity of Ni-P- SiO_2 nanocomposite coatings and further enhanced the corrosion protection ability (Islam et al., 2015). Moreover, Pourhashemet al., (2017) studied the effect of utilizing SiO_2 particles on the corrosion protection performance of the epoxy coatings via fabricating SiO_2 – graphene oxide (GO) nanohybrids via a facile one-step method (Pourhashem et al., 2017). The finding of this study revealed that utilizing SiO_2 nanoparticles along with GO nanosheets led to enhance the overall performance of the epoxy coatings via

increasing the hydrophobicity of the resulting surface, significantly improving the adhesion of the epoxy coating to the metallic substrate, and by giving strong interfacial bonding with the matrix.

However, homogenous mixture of silica and organic resin are considered difficult to be achieved since the nanoparticles aggregates strongly and easily. This is due to the H-bonding formations between the nanoparticles through the silanol group presents at the surface (Ribeiro et al., 2014).

Zinc oxide (ZnO) has great potential for a wide variety of applications, due to its stability, ultraviolet absorption efficiency, environmental friendliness and low cost. Potential applications include emission displays, ultraviolet light emitters, gas sensors, dye-sensitized solar cells, piezoelectric devices and photocatalysts (John et al., 2015). To improve the mechanical characteristics and anticorrosion performance of organic paints, nanoparticles such as nano-ZnO have been used. Studies have found ZnO nanoparticles to be non-toxic and suitable for use in the production of environmentally friendly coatings (Ramezanzadeh et al., 2011).

Due to zinc oxide's unique optical, chemical, electrical, biological and non-toxic properties, this pigment is widely used to improve the organic-coating properties of carbon steels (Shen & Zuo, 2014). As a semiconductor material, zinc oxide increases the light-degradation resistance of coatings by blocking and absorbing UV radiation. In addition, studies show that a certain number of zinc oxide particles, specifically 3.5 wt. %, can improve the adhesion of organic coatings on carbon steel, thereby prolonging the life of zinc-rich primers (Wang et al., 2016; Ramezanzadeh et al., 2011).

CHAPTER 3: METHODOLOGY

3.1 Introduction

This chapter describes the materials utilized in the development of the polymer-based multi-function nanocomposite coating systems and the methods and procedures employed in the fabrication of the proposed coating systems. In addition, this chapter describes the characterization techniques used to evaluate the fabricated coating systems, as well as the testing procedure and experimental parameters.

3.2 Materials

The following chemicals were used as received without any further purification to fabricate the hybrid polymeric coatings and develop the nanocomposite coating systems:

- Acrylic polyol resin, denoted as (A), was obtained from Synthese Malaysia Sdn. Bhd (Malaysia) and utilized as the base resin. Table 3.1 lists the material specifications and other chemical properties of this acrylic resin.

Table 3.1: Specification of acrylic polyol resin.

| Specification property | Value | Unit of measurement |
|--|--------------------|---------------------|
| Product name | Desmophen A 870 BA | |
| Non-volatiles (Solid content wt. %) | 70 ± 1 | % |
| Hydroxyl content | 2.95 ± 0.15 | % |
| Viscosity at 23 °C | 3500 ± 700 | mPa.s |
| Density at 20 °C | 1.09 | g/ml |
| Solvent | Butyl acetate | |

- Silanol functional phenyl silicone intermediate resin in the solid flake form, denoted as (S), was supplied by Wacker Silicone (Germany) and used as a modifier resin. Table 3.2 lists the material specifications and other chemical properties of this silicone resin.

Table 3.2: Specification of silanol functional phenyl silicone intermediate resin.

| Specification property | Value | Unit of measurement |
|--|----------------|---------------------|
| Product name | SILRES® IC 836 | |
| Non-volatiles (Solid content wt. %) | 100 | % |
| Hydroxyl content | 3 – 4.5 | % |
| Average molecular weight | 1500 | g/mol |

- Epoxy resin, denoted as (E), was obtained from World Wide Resin A.C.R Tech. Co. LTD, Taipei, Taiwan and employed as a modifier resin. Table 3.3 lists the material specifications and other chemical properties of this epoxy resin.

Table 3.3: Specification of epoxy resin.

| Specification property | Value | Unit of measurement |
|--|--------------|---------------------|
| Product name | NPSN-901X75 | |
| Non-volatiles (Solid content wt. %) | 74 – 76 | % |
| Epoxy Equivalent weight | 450 – 500 | g/eq |
| Viscosity at 25 °C | 8000 – 15000 | mPa.s |
| Density at 25 °C | 1.1 | g/cm ³ |
| Solvent | Xylene | |

- Epoxidized soybean oil, denoted as (ESO), with an epoxy value of 6.76 %, was used as a modifier. This oil was supplied by Eagle Chemicals Sdn Bhd (Malaysia).
- Aliphatic polyisocyanate resin, designated as NCO, was used as the curing agent and was obtained from Bayer Material Science (Germany). Table 3.4 lists the material specifications and other chemical properties of this NCO curing agent.

Table 3.4: Specification of aliphatic polyisocyanate (NCO) curing agent.

| Specification property | Value | Unit of measurement |
|--|--|---------------------|
| Product name | Desmodur [®] N 75 MPA/X | |
| Non-volatiles (Solid content wt. %) | 75 ± 1 | % |
| NCO content | 16.5 ± 0.3 | % |
| Viscosity at 23 °C | 250 ± 75 | mPa.s |
| Density at 20 °C | 1.07 | g/cm ³ |
| Solvent | 1-methoxypropylacetate- 2/xylene 1 : 1 | |

- Silicon dioxide nanoparticles, denoted as (SiO₂), with diameters ranging from 10 nm to 20 nm and a density ranging from 2.2–2.6 g/mL at 25 °C, were purchased from Sigma-Aldrich (Malaysia) and used as reinforcing nanofillers.
- Zinc oxide nanoparticles, denoted as (ZnO), with a mean diameter of 100 nm and density of 1.7 g/mL at 25 °C, were purchased from Sigma-Aldrich (Malaysia) and used as reinforcing nanofillers.
- Butyl acetate, obtained from Sigma-Aldrich (Malaysia), was used as a solvent.
- Dibutyltindilaurate was used as a catalyst and was supplied from Sigma–Aldrich (Malaysia).

3.3 Methods

In this study, the methods used to prepare the investigated coating systems can be classified as follows:

3.3.1 Preparation of Acrylic-Silicone Hybrid Polymeric Matrix

To fabricate a hybrid matrix to host the nanoparticles in a polymeric matrix, acrylic resin (A) was chosen as the base resin and silicone resin (S) as the modifier. NCO resin was used as the curing agent and butyl acetate as the solvent. The mixing ratio of the acrylic and silicone resins for all prepared coating systems was set as 70 wt. % acrylic resin (A) and 30 wt. % silicone resin (S). This ratio was chosen based on the results of previous studies investigating the overall performance of acrylic–silicone coating systems at different mixing ratios, which concluded that a blend comprising 70 wt. % acrylic resin and 30 wt. % silicone resin demonstrated the greatest durability against degradation from corrosion with significantly enhanced heat resistance (Vengadaesvaran et al., 2013; Vengadaesvaran et al., 2010). Prior to mixing, to obtain a solid content similar to that in acrylic polyol resin, 70 g of solid flake silicone resin was dissolved in 30 g of butyl acetate. The stoichiometric amount of the NCO resin curing agent was calculated for all the developed coating systems using the following formula:

$$NCO = \frac{2.47 \times \% OH}{\% NCO} \times \text{amount of resin (g)} \quad (3.1)$$

where the % OH content in the acrylic resin used was determined to be 2.95 % with a % NCO content of 19.6 % in the NCO resin. However, it is noted that this acrylic–silicone blend was used to develop an AS 0 coating system to serve as a reference system for the reported experiments. Moreover, a neat acrylic coating system (A 100) was also prepared and used as a reference system to illustrate the role of silicone resin in enhancing some properties of the coating systems.

3.3.2 Preparation of SiO₂ Nanocomposite Coating Systems

The solution intercalation method was used to develop the SiO₂ reinforced nanocomposite coating systems, in which different weight ratios of SiO₂ nanoparticles were introduced to the developed hybrid acrylic–silicone (AS) polymeric matrix (Reddy, 2011). Loading rates of 1 wt. %, 3 wt. %, 5 wt. % and 8 wt. % of SiO₂ nanoparticles were used to prepare four different nanocomposite coating systems. Table 3.5 details the compositions of the reference samples and the prepared SiO₂ nanocomposite coating systems, along with their corresponding notations. The SiO₂ nanoparticles were dispersed in butyl acetate for 30 minutes with continuous stirring at 800 rpm, followed by sonication. Then, the AS blend and dissolved nanoparticles were mixed for 20 min at 1000 rpm. Following 60 minutes of sonication, the percentage (w/w) of the NCO curing agent was calculated.

Table 3.5: Composition and nomenclature of the reference samples and all prepared SiO₂ nanocomposite coating systems.

| System | Acrylic wt. % | Silicone wt. % | SiO ₂ wt. % | Designation |
|--------|---------------|----------------|------------------------|-------------|
| 1 | 100 | 0 | 0 | A 100 |
| 2 | 70 | 30 | 0 | AS 0 |
| 3 | 70 | 30 | 1 | AS 1 |
| 4 | 70 | 30 | 3 | AS 3 |
| 5 | 70 | 30 | 5 | AS 5 |
| 6 | 70 | 30 | 8 | AS 8 |

Sonication was performed using a sonication probe with a frequency of 20 kHz and a power supply of 120 W. The sonicator was operated at 60 % amplitude. Before application of the coating films onto the steel substrates, the prepared blend and curing agent were constantly stirred for 5 min, followed by the application of a vacuum pump to remove any trapped air bubbles.

3.3.3 Preparation of ZnO Nanocomposite Coating Systems

Following the same procedure utilized to prepare the SiO₂ reinforced nanocomposite coating systems, four different ZnO nanocomposite coatings were developed. Table 3.6 details the compositions of the reference samples and the prepared ZnO nanocomposite coating systems, along with their corresponding notations.

Table 3.6: Composition and nomenclature of the reference samples and all prepared ZnO nanocomposite coating systems.

| System | Acrylic wt. % | Silicone wt. % | ZnO wt. % | Designation |
|--------|---------------|----------------|-----------|-------------|
| 1 | 100 | 0 | 0 | A 100 |
| 2 | 70 | 30 | 0 | AS 0 |
| 3 | 70 | 30 | 1 | AZ 1 |
| 4 | 70 | 30 | 3 | AZ 3 |
| 5 | 70 | 30 | 5 | AZ 5 |
| 6 | 70 | 30 | 8 | AZ 8 |

3.3.4 Preparation of Epoxy-Soybean Oil Modified Organic Coating System

A hybrid organic–inorganic nanocomposite coating system was developed by the incorporation of an acrylic–silicone polymeric matrix with SiO₂ or ZnO nanoparticles. The multifunctionality of these fabricated coating systems was determined, as was the influence of the incorporated nanoparticles of different types, sizes and loading rates on the overall coating performance. However, the development of an entirely organic coating system that can fulfil the multifunctionality requirement remains an important goal. Therefore, this work was extended to develop and analyse an organic hybrid coating system comprising the same base hybrid acrylic–silicone hybrid blend with the addition of E and ESO at different loading ratios. In this experiment, the various loading ratios of E and ESO were added dropwise to the acrylic–silicone blend while being continuously

stirred. Table 3.7 details the compositions of the reference samples and the prepared epoxy–soybean oil modified coating systems with their corresponding notations.

Table 3.7: Composition and nomenclature of the reference samples and all prepared epoxy-soybean oil modified coating systems.

| System | Acrylic wt. % | Silicone wt. % | Epoxy wt. % | Epoxidized soybean oil wt. % | Designation |
|--------|---------------|----------------|-------------|------------------------------|-------------|
| 1 | 100 | 0 | 0 | 0 | A 100 |
| 2 | 70 | 30 | 0 | 0 | AS 0 |
| 3 | 63 | 27 | 10 | 0 | ES 0 |
| 4 | 63 | 27 | 9 | 1 | ES 1 |
| 5 | 63 | 27 | 8 | 2 | ES 2 |
| 6 | 63 | 27 | 6 | 4 | ES 4 |
| 7 | 63 | 27 | 4 | 6 | ES 6 |
| 8 | 63 | 27 | 2 | 8 | ES 8 |
| 9 | 63 | 27 | 0 | 10 | ES 10 |

3.3.5 Sample Preparation and Coatings Application

To examine the developed coating systems, samples were prepared in four different shapes to make each suitable for the characterization technique utilized. Cold-rolled steel panels with the dimensions 75.0 mm (length) \times 50.0 mm (width) \times 0.5 mm (thickness), purchased from GT Stainless (Melaka, Malaysia), were coated on both sides using the brushing method. Samples with the above dimensions were used in the contact angle (CA), cross hatch test (CHT) and electrochemical impedance spectroscopy (EIS) experiments. The field emission scanning electron microscopy (FESEM) test used the same type of steel panels with the dimensions 10.0 mm (length) \times 10.0 mm (width) \times 0.5 mm (thickness). It is noted that all steel coated substrates were subject to a surface preparation process prior to the application of the coating films. These substrates were first cleaned and washed with acetone to remove any dust, oil or any specks of dirt that

could affect the adhesion properties of the coating–metal interface. After ensuring the dryness of the cleaned substrates, a sandblasting technique was employed to achieve Sa 2½ surface profile according to the ASTM D609 standard. The samples used in the Fourier transform infrared spectroscopy (FTIR), and thermogravimetric analysis (TGA) experiments were in the form of free films cast onto Teflon plates. For the ultraviolet-visible (UV-Vis) spectroscopy test, glass plates (2.54 x 7.62 x 0.12 cm) were used, which were first coated using the brushing method. All prepared samples were kept fully cured and dry at room temperature for seven days. All the coated films were controlled at a dry-film thickness of $75 \pm 5 \mu\text{m}$. An Elcometer 456 thickness gauge was used to measure the thickness at five different points on each sample.

3.4 Characterization

To investigate the overall performance of the developed coating systems, several characterization techniques were utilized in this study. The chemical structure of the developed hybrid polymeric matrix was investigated using FTIR, and the morphology, wettability and adhesion properties of the developed coating films were determined using FESEM, CA and CHT, respectively. Further investigations were conducted to analyse the transparency of the developed coating systems, via UV-Vis spectroscopy. The thermal properties including the initial degradation temperature (IDT), the temperature where 50 % weight loss occurred ($T_{50 \text{ wt. \%}}$), and the residue yields at 700 °C were determined by the thermogravimetric analysis (TGA). In addition, detailed EIS studies were conducted to evaluate the corrosion protection performance and barrier properties of the developed coating systems.

3.4.1 Fourier Transform Infrared Spectroscopy (FTIR)

As one of the most fundamental methods used in the coating industry, FTIR has been widely applied in qualitative analysis and to trace the cross-linking process, which has helped to gain a fuller understanding of the bonding state between organic functional groups. To investigate the effectiveness of the room-temperature curing process and to confirm the achievement of an excellently bonded structure between the acrylic and silicone resins in the presence of the NCO curing agent, an ATR Nicolet iS10 Spectrometer (Thermo Fisher Scientific, Waltham, MA, USA) was used in the transmittance mode. For all the recorded spectra, 32-scan data in a wavenumber range of 400–4000 cm^{-1} at a resolution of 4.0 cm^{-1} was acquired. OMNIC spectra software, obtained from Thermo Scientific, was used to analyse the recorded spectra.

3.4.2 Field Emission Scanning Electron Microscopy (FESEM)

Surface morphological analysis, as well as the investigation of the dispersion state of the utilized nanoparticles within the hybrid polymeric matrix were performed utilizing FESEM. To do so, an FEI Quanta450 FEG at 10 kV was used as the accelerating voltage in low vacuum (LVSEM) conditions. It is noted that, to obtain clear evidence that nanoparticles can alter the surface morphology of the hybrid polymeric matrix, the FESEM test was performed only on the coating systems containing nanoparticles. We found the manipulation of surface characteristics in the nano domain to yield a significant reduction in the surface wettability and to contribute to the achievement of a hydrophobic coating system.

3.4.3 Contact Angle Measurements (CA)

The wettability of the developed coated surface is one of the most important characteristics to consider in the fabrication of intact anticorrosion coating systems.

Montemor (2014) reported the hydrophobicity of surfaces to be a key surface property that plays a vital role in the development of coating systems that ensure minimal contact between the surface and the aqueous electrolyte as well as anti-fouling and anti-icing characteristics (Montemor, 2014).

In general, depending on their wettability, surfaces can be classified into four main categories: superhydrophilic, hydrophilic, hydrophobic and superhydrophobic. This classification mainly depends on the CA (θ) values, as shown in Figure 3.1, where $\theta < 10^\circ$ indicates a surface with superhydrophilicity, whereas a CA in the range $10^\circ < \theta < 90^\circ$ is typically recorded as a hydrophilic surface. Hydrophobic surfaces are characterized by CA values in the range $90^\circ < \theta < 150^\circ$ and those with CA values of $\theta > 150^\circ$ are known as superhydrophobic (Mohamed et al., 2015).

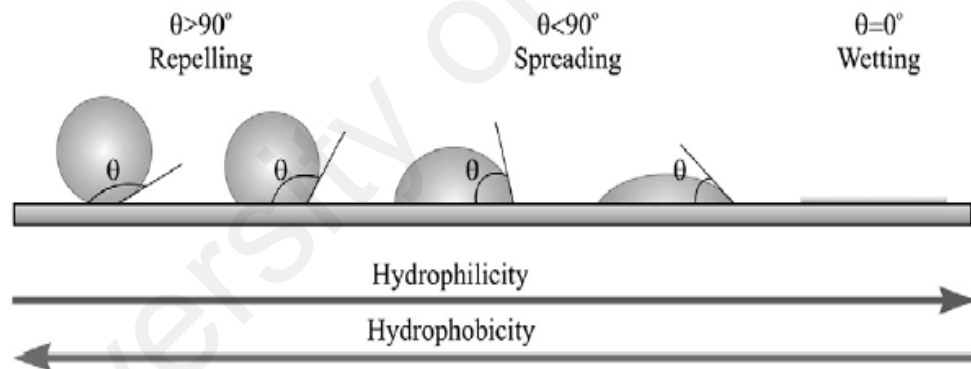


Figure 3.1: Shapes of water drop on solid surfaces of different wettability with its corresponding contact angle values (Krasowska et al., 2009).

The surface wettability of all the prepared coating systems was evaluated by measuring the water CAs. The CAs of five droplets of distilled water at different points on each sample were recorded using an Optical Contact Angle 15EC instrument. To determine the static CA, images were captured instantly after the gentle deposition of a 5 μL distilled water droplet. The CA values reported here represent the average of five measurements.

3.4.4 Ultraviolet-Visible (UV-Vis) Spectroscopy

To evaluate changes in the coating-film transparency of all the fabricated coating systems, the systems were examined via UV-Vis spectroscopy. As one of the primary functions proposed for developed multifunctional coating systems, changes in transparency were investigated in the presence of different loading ratios of either SiO₂ or ZnO nanoparticles. Moreover, the influence of modifying the polymeric matrix with epoxy and ESO on the transparency was determined.

A UV-3101PC (Shimadzu, Kyoto, Japan) UV-Vis spectrometer in transmission mode was used, with a wavelength range of 300–800 nm. A 2-nm slit width and medium speed were set as parameters. To perform this test, glass plates (2.54 cm x 7.62 cm x 0.12 cm) were coated and then cured and dried at room temperature for seven days. The fundamental principle of UV-Vis spectroscopy can be summarized as the detection by an optical spectrometer of light waves that pass through tested samples and recording of the transmission percentage at each wavelength. As such, the obtained results show the percentage of transmitted waves at each corresponding wavelength.

3.4.5 Cross Hatch Test (CHT)

One of the most important properties to be studied when developing anticorrosion coating systems is the adhesion of the coating layer to the pretreated substrate surface, which was investigated utilizing the CHT, as per the ASTM D3359 B standard. In this regard, a cross-hatch cutter (ELCOMETER 107) was placed gently on the top of the coated surface, then, with a little pressure applied to the coating layer, the substrate surface was pulled steadily to form a series of parallel cuts approximately 20 mm long. To obtain a lattice pattern on the coating surface, the cutting tool was again placed on the sample, but this time at a 90° angle to the first cut, and this process was repeated to create a series of parallel cuts. After lightly brushing the surface to remove any detached flakes

or ribbons, a selective special tape was applied at the centre over the lattice. To ensure excellent adhesion, a typical pencil eraser was used to rub the tape firmly onto the lattice. Removing the tape can only be done after 90 seconds by pulling the tape in single action at an angle of 180° along the sample surface. The adhesion properties of all the developed coating systems were evaluated using a digital polarized microscope (Dino-Lite, AM413ZT) to capture images of the lattice cuts on the sample surfaces after performing the above test. The ASTM D3359 B standard was applied and Table 3.8 shows the recorded results classified according to the surface state.

3.4.6 Thermogravimetric analysis (TGA)

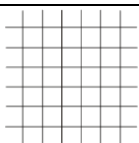
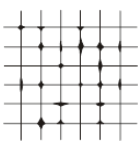
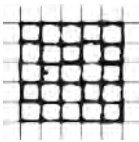
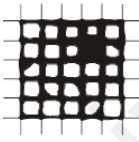
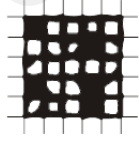
The influence on the thermal stability of the hybrid acrylic–silicon polymeric matrix of utilizing two types of nanoparticles, specifically SiO₂ and ZnO, was examined at different loading ratios using the thermogravimetric analysis (TGA) technique. In addition, the impact of introducing E and ESO to the acrylic–silicon polymeric blend was also investigated. TGA is a robust method for investigating the thermal properties of coating systems in which the changes in the mass of a tested sample are examined over a wide range of temperatures (Patel & Mannari, 2014; Tao et al., 2017).

From the obtained thermographs, the progression of the coating-film degradation was investigated based on the initial degradation temperature (IDT), the temperature at which 50 % of the weight loss occurred ($T_{50 \text{ wt. \%}}$) and the residue yields at 700 °C as the main factors that can provide a better understanding of the thermal stability.

The TGA tests were performed using a Mettler Toledo TGA Q500 (Columbus, USA). The tested samples were heated from 30 °C to 700 °C at a heating rate of 50 °C/min under nitrogen gas with a flow rate of 60 mL/min. The tested samples were prepared in the form of free films casted in Teflon plates and left to dry and fully cure for seven days at room

temperature. The obtained results were then evaluated utilizing the STARE software version TA Universal Analysis V4.7A. The mass of the tested samples was 10 ± 2 mg.

Table 3.8: Classification of coating adhesion according to ASTM D3359 B.

| Surface state | Description | Classification |
|---|--|----------------|
|  | The edges of the cuts are completely smooth; none of the squares of the lattice is detached. | 5 B |
|  | Detachment of flakes of the coating at the intersections of the cuts. A cross cut area not significantly greater than 5 % is affected. | 4 B |
|  | The coating has flaked along the edges and/or at the intersections of the cuts. A cross cut area significantly greater than 5 %, but not significantly greater than 15 % is affected. | 3 B |
|  | The coating has flaked along the edges of the cuts partly or wholly in large ribbons, and/or it has flaked partly or wholly on different parts of the squares. A cross cut area significantly greater than 15 %, but not significantly greater than 35 %, is affected. | 2 B |
|  | The coating has flaked along the edges of the cuts in large ribbons and/or some squares have detached partly or wholly. A cross cut area significantly greater than 35 %, but not significantly greater than 65 %, is affected. | 1 B |
| | Any degree of flaking that cannot be classified even by classification 4 (1B). | 0 B |

3.4.7 Electrochemical Impedance Spectroscopy (EIS)

Several testing methods have been utilized by the coating industry to evaluate the corrosion protection ability of paint systems. Some of the widely used test procedures depend primarily on simulating natural conditions that lead to initial corrosion and metal degradation. For instance, salt spray, weathering and immersion tests are some of the tests typically used to induce the accelerated deterioration of coating systems. However, the continuous development of more durable coating systems has led to the need for short-term testing methods that generate more reliable information about the response of the coating layer to the corrosion process. Moreover, as corrosion is an electrochemical process, it was worthwhile to utilize an electrochemical base test method to evaluate the corrosion protection performance, which can be obtained by EIS.

The electrochemical properties and corrosion behaviour of the developed coating systems were investigated using EIS techniques. A standard three-electrode cell with a 3.5 wt. % NaCl solution was used to perform these studies over 60 days of immersion. To prepare the electrochemical cell, a polyvinyl chloride (PVC) tube with a 2.0-cm inner diameter was vertically fixed to the surface of the coated substrate with epoxy adhesive glue. With respect to the adhesive joint, a sample with a 3.0 cm² exposed area served as the working electrode, a saturated calomel electrode (SCE) was the reference electrode and a platinum electrode was the counter electrode. All measurements were performed after placing the tested sample in a Faraday cage to minimize noise levels during measurement. A Gamry PC14G300 potentiostat with a frequency range of 100 kHz–10 mHz at the open circuit potential was used to perform all the EIS tests. A Gamry Echem Analyst, Version 6.03 was used to analyse the obtained EIS data. Figure 3.2 shows the electrochemical cell that was fabricated and used in all the EIS studies.

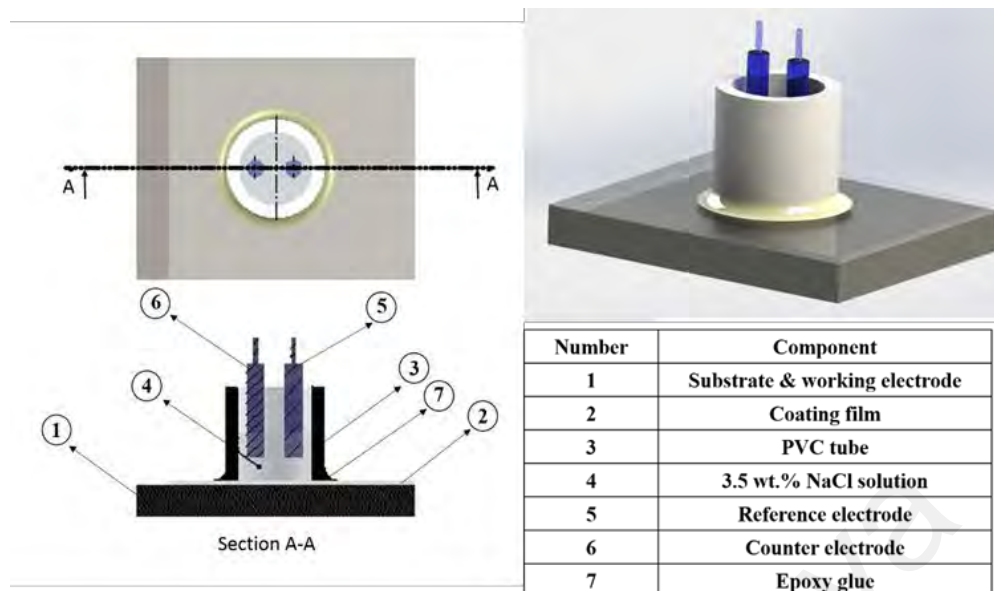


Figure 3.2: The classic three-electrode cell used for EIS characterizations.

CHAPTER 4: RESULTS AND DISCUSSIONS OF SiO₂ NANOCOMPOSITE COATING SYSTEMS

4.1 Introduction

In this chapter, the influence of embedding SiO₂-nanoparticle at loading ratios of 1 wt. %, 3 wt. %, 5 wt. % and 8 wt. % on the overall performance of the hybrid acrylic–silicone polymeric matrix is reported. The investigated properties include the surface morphology, wettability, transparency, thermal stability, adhesion performance and corrosion protection ability. Also investigated was the multifunctionality of the single-layer coating systems.

In this research, it was essential to determine the most appropriate acrylic–silicone polymeric matrix to be used as the host polymeric matrix for the developed coating systems. Therefore, a neat acrylic coating system (A 100) and an acrylic–silicone coating system (AS 0) were prepared and used as reference samples for comparison. The acrylic–silicone polymeric matrix was investigated using FTIR to determine its chemical structure and to confirm the efficacy of the curing process.

4.2 Fourier Transform Infrared Spectroscopy (FTIR)

In this study, the main component of the developed coating systems was the hybrid acrylic–silicone polymeric matrix, which was utilized as a host matrix in the SiO₂ and ZnO nanocomposite coating systems and as the base blend in the epoxy–soybean-modified coating systems. Therefore, to fabricate the proposed multifunctional coating systems, an essential factor was the excellent crosslinking between the acrylic and silicone resins, with NCO as the curing agent.

In this regard, Figure 4.1 shows the FTIR spectra of the neat silicone resin, cured neat acrylic coating system (A 100) and AS 0 coating systems. The bands at 1244 cm⁻¹ and

1525 cm^{-1} were attributed to C–N and N – H stretching modes, respectively (Ramesh et al., 2013; Ramesh et al., 2008; Vengadaesvaran et al., 2010). The presence of these bands is clear evidence of crosslinking between the NCO resin with both the A 100 and AS 0 coating systems, which is the result of an effective curing process. C–H bending-mode bands at 760 cm^{-1} and 1430 cm^{-1} were observed in the spectra of the AS 0 hybrid coating system (Figure 4.1(c)), but not in that of the neat acrylic coating system or neat silicone resin. This is a clear indication that crosslinking between the acrylic–silicone resins has occurred. In addition, the observable shift in the C–H stretching band in the 2800–3000 cm^{-1} range and the O–H band in the 3300–3600 cm^{-1} range confirms the occurrence of blending of the acrylic and silicone resins. This blending occurs because both the silanol functional phenyl silicone and the acrylic polyol resin have –OH end groups. Also, aliphatic NCO resin has two NCO functional groups. An interaction is expected between the functional groups of the acrylic polyol resin, silicone resin, and NCO resin via their hydroxyl end groups and the NCO functional groups; hence the formation of –NH bonds. Furthermore, bands were observed between 1000 cm^{-1} and 1200 cm^{-1} , which are attributed to Si–O–Si and Si–O–C stretching modes (Duo et al., 2008; Kapridaki & Maravelaki-Kalaitzaki, 2013) in the neat silicone resin and in the AS 0 hybrid coating system, but not in the spectra of the neat acrylic resin. There was a wide band in this range, which made it difficult to clearly observe the changes.

4.3 Surface Morphology

The solution intercalation method was used to introduce different loading ratios of SiO_2 nanoparticles into the acrylic–silicone polymeric matrix. On this basis, the surface morphology of the resulting coating systems differed in different coating systems according to the loading ratio of SiO_2 nanoparticles, whereby a higher amount of nanoparticles increased the likelihood for these nanoparticles to be agglomerated. Hence,

the dispersion of the nanoparticles within the polymeric matrix could be affected (Khan et al., 2016; Ramezanzadeh et al., 2011).

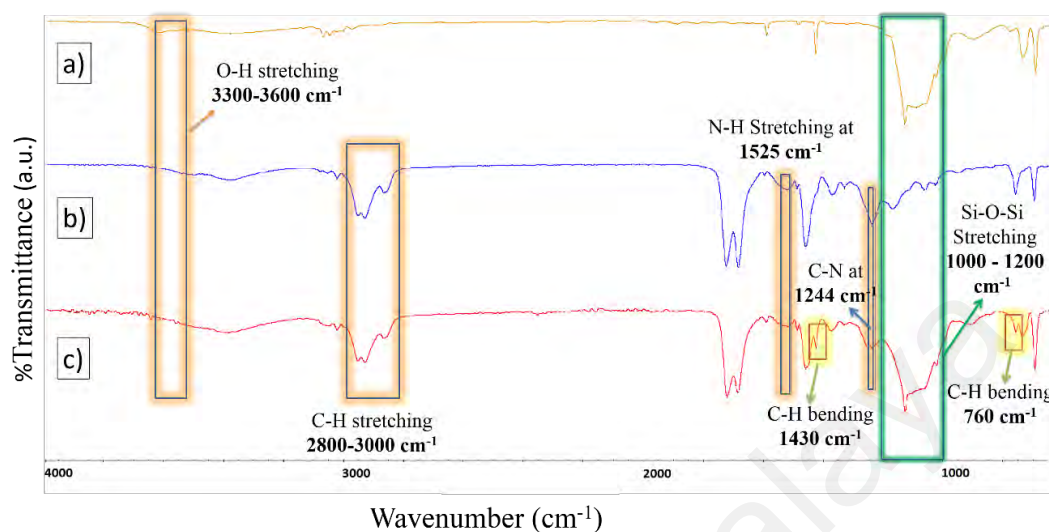


Figure 4.1: FTIR spectra of (a) neat silicone and (b) neat acrylic and (c) AS 0 coating system.

Figure 4.2 shows FESEM micrographs of the prepared SiO₂ nanocomposite coating systems. The uniform dispersion of nano SiO₂ particles in the hybrid acrylic–silicone matrix was confirmed by these images, which is evidence of the efficiency of the sonication process in developing an acceptable dispersion level of SiO₂ nanoparticles in the polymeric matrix.

However, it is noted that as the nanoparticles loading ratio increased, the agglomeration also increased due to the increases in the number of nanoparticles in the unit area, which was most pronounced in the AS 8 coating system with the highest loading ratio of SiO₂ nanoparticles (8 wt. %), as shown in Figure 4.2(d). Therefore, the ability of the nanoparticles to attract each other increased, thereby forming relatively larger agglomerations. Furthermore, the heterogeneous morphology of nanosized particles that can be observed on the surface area after incorporation during the second inorganic phase led to higher surface roughness, which in turn ensured a more hydrophobic surface

(Zhang et al., 2016). In addition, it was also observed that the optimum curing of polymeric nanocomposite films at room temperature is an important factor for achieving coating films without any micro cracks. This reveals the strong interaction between the binder and SiO₂ nanoparticles that support the superior barrier performance of the developed coating systems.

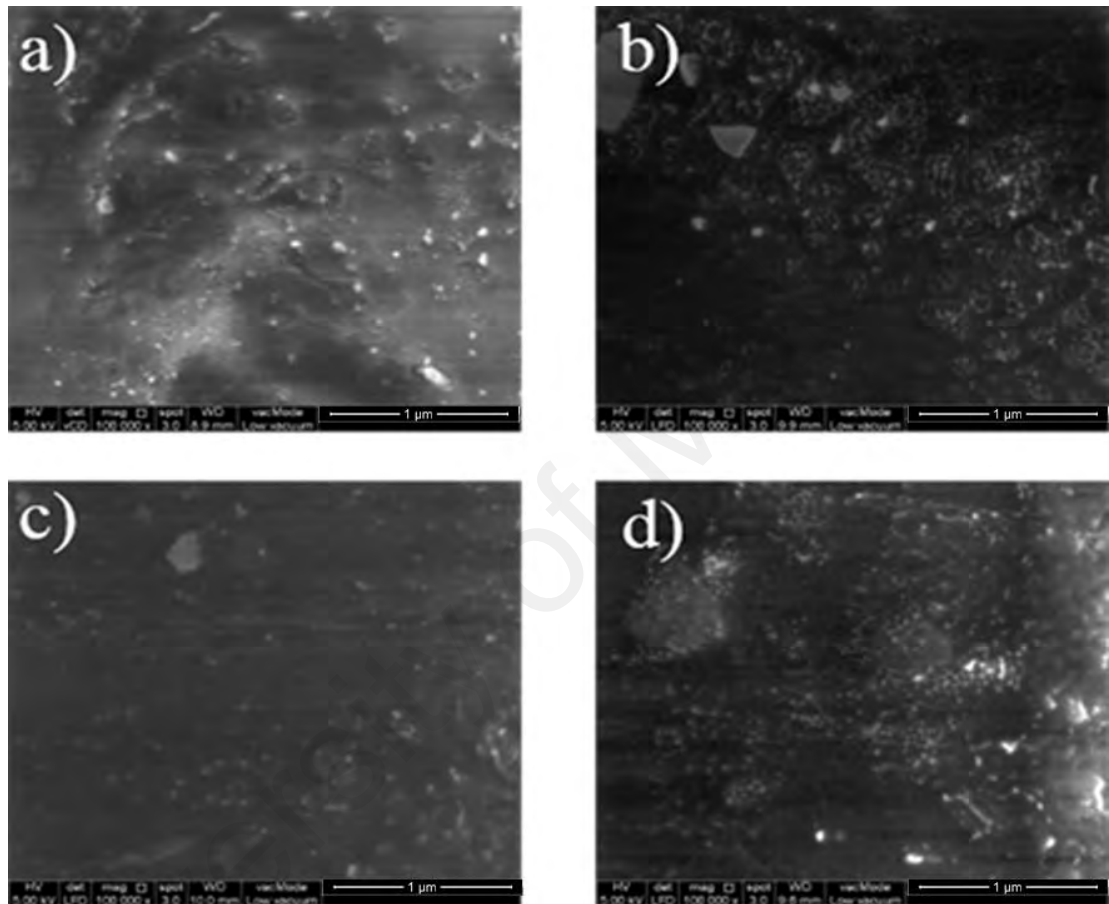


Figure 4.2: FESEM micrographs at scale 100 000× of magnification of (a) AS 1, (b) AS 3, (c) AS 5, and (d) AS 8 SiO₂ nanocomposite coating systems.

4.4 Contact angle measurements (CA)

Water CA measurements were conducted to investigate the hydrophobic character of the developed SiO₂ nanocomposite coatings and to determine the influence of embedded SiO₂ nanoparticles on the wettability of the resulting coated surfaces.

The morphology of the surface and the surface energy of the materials used to develop the coating system are considered to be the two main factors that directly influence surface

wettability (Mohamed et al., 2015). Therefore, the CA results for the neat acrylic, A 100 and AS 0 coating systems are also included here to highlight the contribution of the silicone resin, as a modifier of the acrylic resin, in enhancing the wettability of the coating surface toward greater hydrophobicity. Table 4.1 lists the recorded CA values for the reference coating systems, namely the A 100 and AS 0 and SiO₂ nanocomposite coating systems.

As shown in Table 4.1, the incorporation of silicone intermediate resin into the acrylic resin results in an increase in the CA at 78.5° compared to the A 100 coating system, which consists of neat acrylic resin and exhibited a CA of 52.3°. Although the abovementioned coating systems are in a hydrophilic state, it was observed that the existence of the silicone resin in the polymeric coating further enhanced the hydrophobicity.

In contrast, introducing SiO₂ nanoparticles to the polymeric matrix transformed the hydrophilic surface into a hydrophobic surface with a CA > 90° in all the SiO₂ nanocomposite coating systems. However, of the developed coating systems, the most pronounced effect was observed when 3 wt. % of SiO₂ nanoparticles was introduced to the hybrid polymeric matrix with a corresponding CA of 97.3°. It is noted that similar observations have been previously reported with respect to the introduction of SiO₂ nanoparticles into a polymeric matrix (Bravo et al., 2007; Ogihara et al., 2012; Su et al., 2006; Wang et al., 2011)

Many researchers, including Zhang et al. (2016), have correlated two main factors with the development of hydrophobic surfaces by the application of hybrid organic–inorganic coating systems. First, some materials possess a significantly low surface energy and have the ability to produce hydrophobic surfaces. As such, it was found that after the incorporation of a silicone resin, which is well-known to have a relatively low surface energy at 22 mN/m, the CA value increased by approximately 26°. This can be attributed

to changes in the chemical composition due to the presence of (–Si–O–Si–) silicone, as was confirmed by previously reported FTIR studies (Zhang et al., 2016).

The second main factor that was identified in the fabrication of a hydrophobic surface is the manipulation of surface roughness. In this regard, developed coating systems containing SiO₂ nanoparticles have been recorded to have CA values higher than 90°, which means that these surfaces are approaching hydrophobicity. The CA results reported by Bravo et al. (2007) and Wang et al. (2011) have shown that surfaces with different roughness levels have higher water repellence than surfaces characterized by single-domain roughness (Bravo et al., 2007; Wang et al., 2011). Moreover, according to Ogihara et al. (2012), all hydrophobic surfaces must have high surface roughness and low surface energy. Also, the authors reported that when a water droplet settles on a rough surface, it will be in contact with both the constituent materials and the air trapped within the rough surface. This then contributes to an increase in surface hydrophobicity because air is an absolutely hydrophobic material (Ogihara et al., 2012). In addition, Ogihara et al. (2012) explained that when the agglomeration of nanoparticles increases, the hydrophobicity of the coating decreases. A similar effect was observed in our studies, whereby a slight drop in the CA values occurred when the SiO₂ nanoparticle loading ratio was greater than 5 wt. %.

Table 4.1: Contact angles values of A 100, AS 0 and all prepared SiO₂ nanocomposite coating systems.

| System | Contact angle (θ°) |
|--------|----------------------------------|
| A 100 | 52.3 \pm 0.9 |
| AS 0 | 78.5 \pm 0.7 |
| AS 1 | 95.3 \pm 0.3 |
| AS 3 | 97.3 \pm 0.4 |
| AS 5 | 93.7 \pm 1.1 |
| AS 8 | 90.6 \pm 0.3 |

4.5 UV-Visible Spectroscopy

Figure 4.3 shows the light transmittance spectra of the cured neat acrylic (A100), acrylic/silicone (AS0) and nanocomposite acrylic/silicone (AS1–AS8) films of uniform thickness. As shown in the figure, the neat acrylic film has the highest light transmittance percentage of 90 % at 550 nm, and thus the highest transparency. The addition of silicone resin to the acrylic matrix does not influence the transparency of the neat acrylic film. However, in the nanocomposite acrylic/silicone films, the transmittance value decreased with increases in the loading ratio of SiO₂ nanoparticles. The light transmission of the AS1 and AS3 films were about 87 % at a wavelength of 550 nm, which indicates a relatively uniform dispersion of SiO₂ nanoparticles in the hybrid polymer matrices. Further additions of SiO₂ nanoparticles in the AS5 and AS8 films reduced the light transmittance to 86 % and 84 %, respectively, which is attributed to the suppression of transparency due to higher levels of agglomeration. As reported by Ou and Shiu (2010), the transparency of a nanocomposite incorporated with 7 wt. % of SiO₂ nanoparticle still has higher than 80 % light transmittance (Ou & Shiu, 2010). Many factors can affect the degree of transparency in a nanocomposite coating, including the dispersion of nanoparticles in the polymer matrix and the intercalation of the network chains.

Nevertheless, the results also show a sudden decline in transmittance in the ultraviolet region (300–400 nm), which is attributed to the lack of optical activity in this region. Despite this, all the films are considered to be transparent with high transmittance values in the visible region. This suggests that the SiO₂ nanocomposite will have a role in future optical studies due to its promising optical properties in polymer matrices.

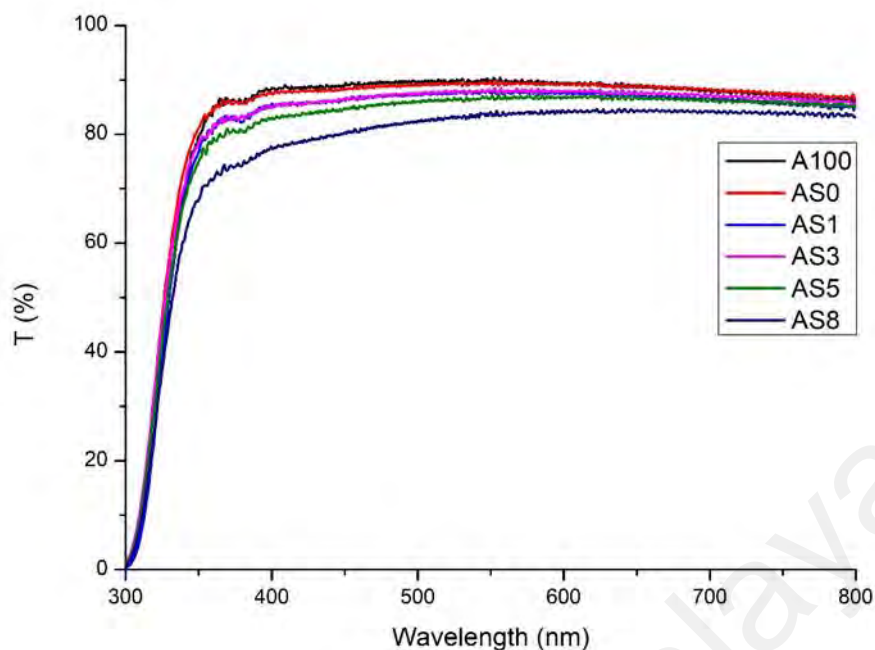


Figure 4.3: UV-Vis spectra for A 100, AS 0 and all prepared SiO₂ nanocomposite coating systems.

4.6 Cross Hatch Test (CHT)

Another important property to be studied when developing anticorrosion coating systems is the adhesion of the coating layer to the pretreated substrate surface, as determined by CHT investigations (Aneja et al., 2015; Lakshmi et al., 2014). In this study, the classification of the obtained results was made by comparing the captured images of the surfaces, after being subjected to cross cut and tape removal, with the standard damage images obtained by ASTM D3359 method B, as shown above in Table 3.8.

The adhesion behaviours of the A100, AS 0 and the prepared SiO₂ nanocomposite coating films to the steel substrate were investigated and the results are shown in Figure. 4.4. The surface image of the A 100 coating system shows no loss of adhesion in that all the edges of the cuts were smooth, which is clear evidence of excellent adhesion of the acrylic resin to the pretreated cold-rolled mild steel substrate, and which is classified as 5B grade.

The same observation was recorded after the application of the AS 0 coating systems, which further confirms that the incorporation of the silicone and acrylic resins showed no effects on the excellent adhesion properties of acrylic resin. The surface of the AS 0 coating system was recorded as 5B grade, as shown in Figure 4.4. A similar observation was reported by Vengadaesvaran et al. (2006), where the modification of acrylic resin with 30 wt. % silicone resin exhibited the best adhesion properties, which the authors attributed to the existence of Si-C bonds (Vengadaesvaran et al., 2010).

Moreover, it was interesting to note that, according to the ASTM D3359 method B standard, the CHT results of all developed nanocomposite coating systems demonstrated a 5B adhesion grade, as the edges of the cuts were completely smooth and none of the lattice squares had detached. These findings again confirm the excellent adhesion behaviour of the nanocomposite coating systems.

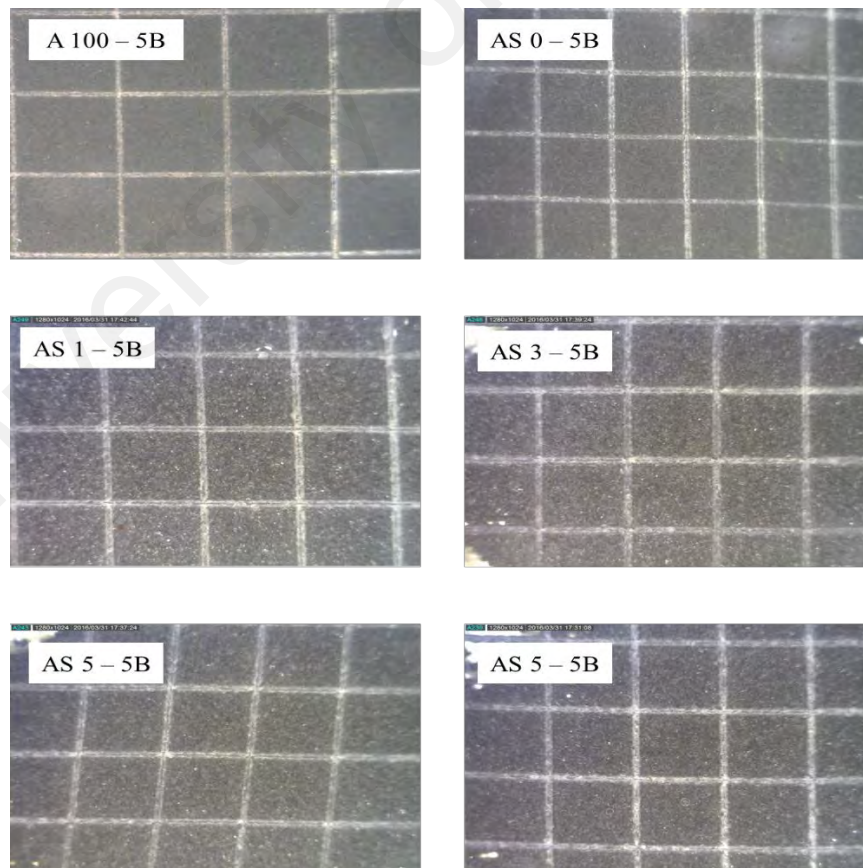


Figure 4.4: Results of cross hatch test for A 100, AS 0 and all prepared SiO₂ nanocomposite coating systems.

4.7 Thermogravimetric Analysis (TGA)

The thermal stability of all the developed SiO₂ nanocomposite coating systems was investigated by TGA, which examines the changes in the mass of tested samples over a wide range of temperatures from 30–700 °C. However, it is noted the TGA results of the A 100 and AS 0 coating systems distinguish between the effect of each component in the SiO₂ nanocomposite coating systems on the enhancement of thermal stability of the coating film against continuous changes in temperature. From the TGA results, reliable and detailed information can be obtained regarding the thermal degradation, residual values and decomposition temperatures of the hybrid polymeric-based coating systems.

Figures 4.5 – 4.10 show the TGA thermograms of the A 100, AS 0 and prepared SiO₂ nanocomposite coatings. Different stages of weight loss can be observed, which may correspond to the degradation of one component or more in the hybrid polymeric-based coating systems. From the TGA thermogram of Figure 4.5, it is evident that the thermal degradation of the A 100 coating system occurred in three main stages. The first stage began at approximately 120 °C and the loss of mass showed a linear rate up to 280 °C. This could be attributed to the loss of the residual solvent, butyl acetate, which, according to the datasheet obtained from the manufacturer, boils between temperatures of 124–128 °C. The second degradation stage occurred in the temperature range of 280–390 °C, where the loss in mass could be correlated to the loss of the NCO resin, which has a boiling point of 280 °C, according to its datasheet. As the acrylic resin has a boiling point of approximately 370 °C, the third stage of thermal degradation that occurred between 390–485 °C can be attributed to the loss of acrylic resin.

Figure 4.6 shows the TGA thermogram of the AS 0 coating system, in which can be seen that the mass loss of the AS 0 coating system occurred in four stages of thermal degradation. The first three stages matched with those recorded for the neat acrylic coating system, A100, for which the first stage could be attributed to the loss of residual

butyl acetate. The second stage correlates to the degradation of the intercalation agent, NCO resin. The decomposition of the acrylic resin was observed in the third degradation stage. The fourth stage in the TGA curve occurred when the temperature exceeded 500 °C, which indicates the loss of silicone resin, which is known to have ignition temperature higher than 400 °C. However, it is noted that the TGA thermograms shown in Figures 4.7 – 4.10 for the developed SiO₂ nanocomposite coating systems could be described as similar.

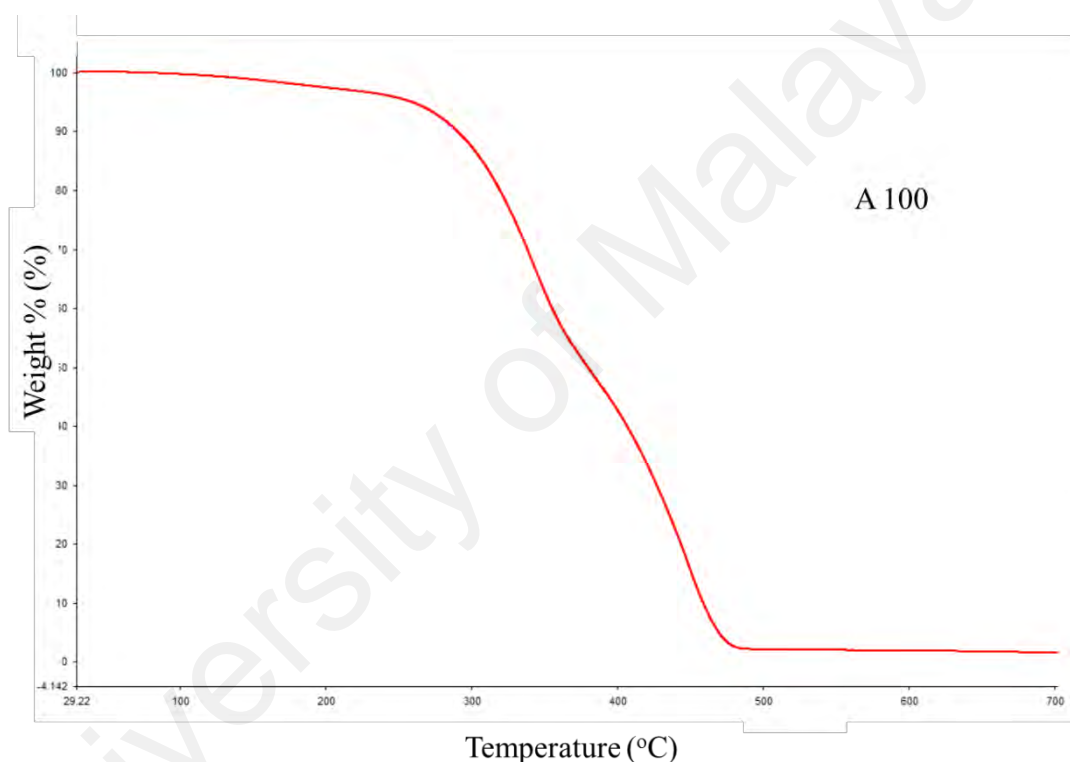


Figure 4.5: TGA thermogram of A 100 coating system.

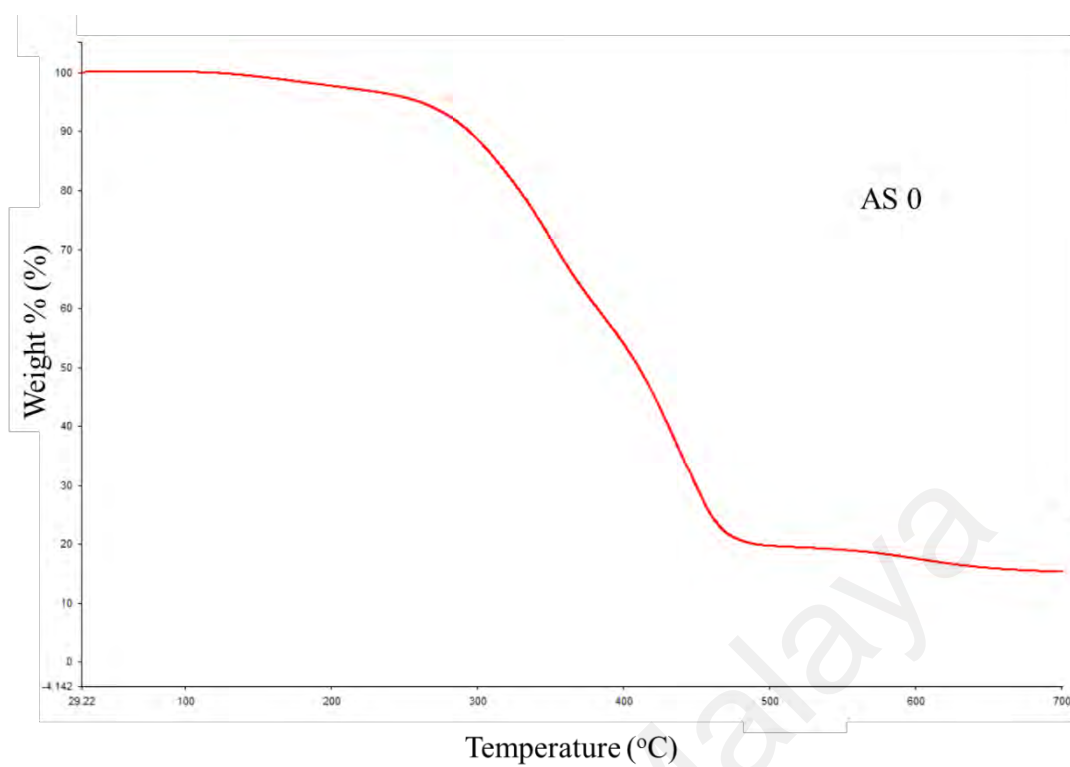


Figure 4.6: TGA thermogram of AS 0 coating system.

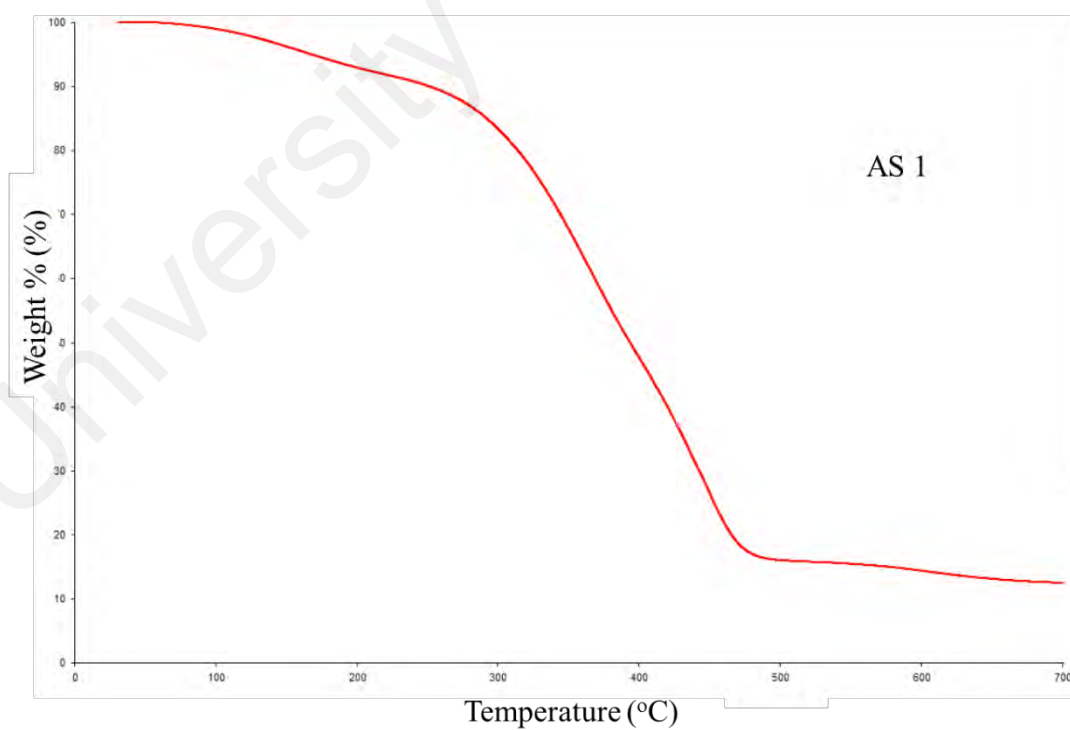


Figure 4.7: TGA thermogram of AS 1 coating system.

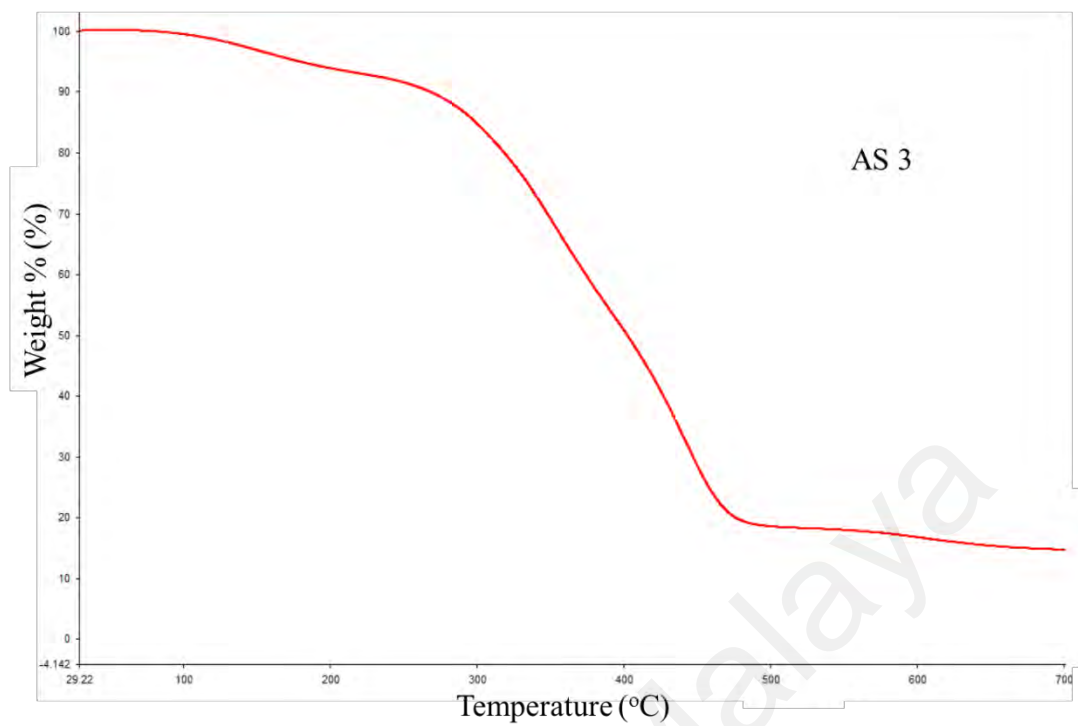


Figure 4.8: TGA thermogram of AS 3 coating system.

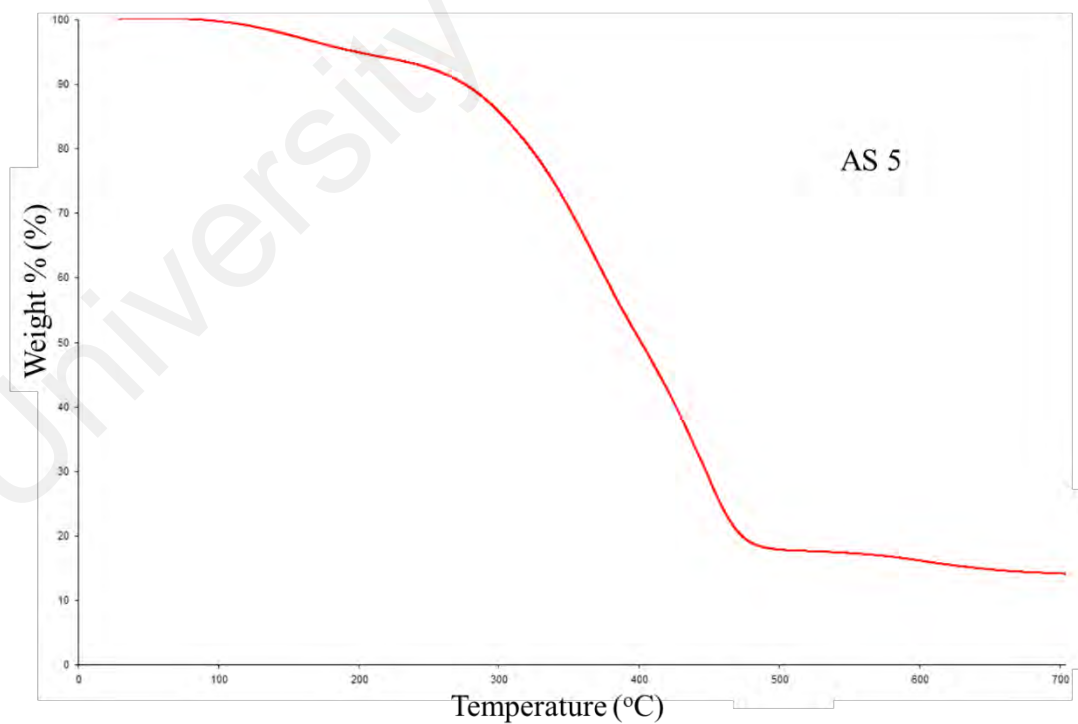


Figure 4.9: TGA thermogram of AS 5 coating system.

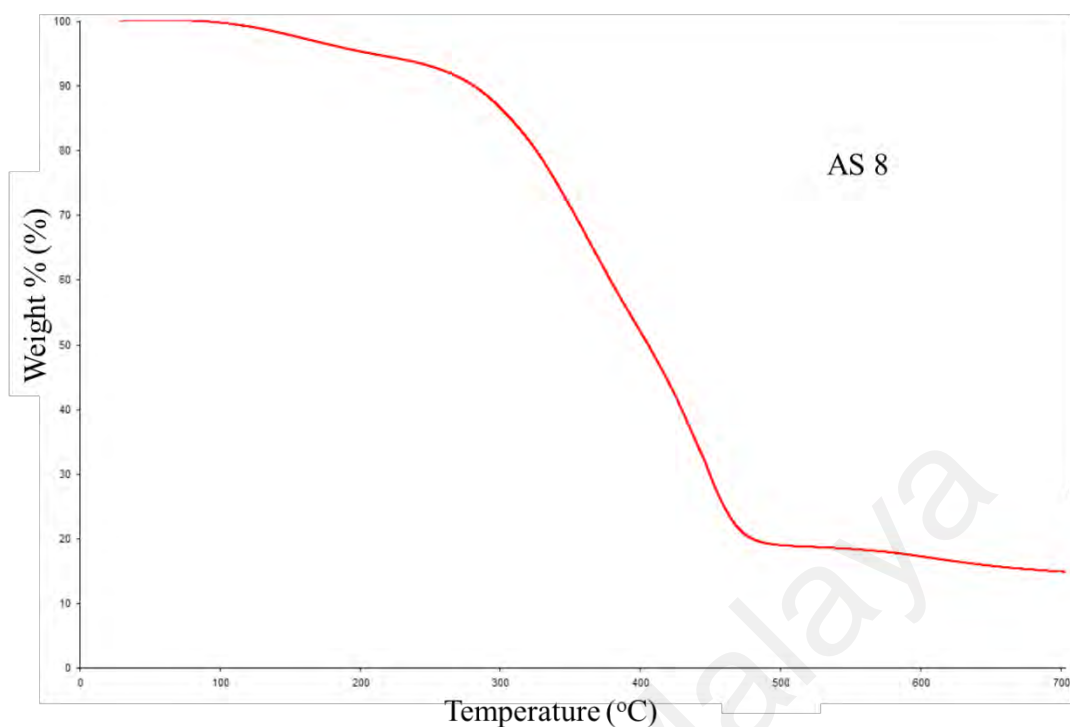


Figure 4.10: TGA thermogram of AS 8 coating system.

Moreover, to investigate the influence of the silicone resin in enhancing the thermal stability of acrylic resin and to determine the effects of the embedded SiO₂ nanoparticles at different loading ratios in the hybrid polymeric matrix, the IDT, the temperature at which 50 % weight loss occurred ($T_{50 \text{ wt. } \%}$) and the residue yields at 700 °C were recorded and are listed in Table 4.2.

The IDT, which is defined as the temperature corresponding to a weight loss of 10 %, was used as a thermal stability indicator. From Table 4.2, it can be seen that as 30 wt. % of the silicone resin was incorporated with the acrylic resin, higher thermal stability was realized by the coating film with the higher IDT, $T_{50 \text{ wt. } \%}$ and residue values. This can be interpreted as being due to the presence of Si–O–Si bonds in the silicone structure, which are inorganic and could be responsible for the enhancement of thermal stability (Ananda Kumar & Sankara Narayanan, 2002; Vengadaesvaran et al., 2013). However, embedding the SiO₂ nanoparticles within the acrylic–silicone hybrid polymeric matrix yielded slightly lower IDT and $T_{50 \text{ wt. } \%}$ values, which indicates a slight decrease in the thermal

stability of the developed SiO₂ nanocomposite coatings. This, in turn, could be explained by the influence of the nanoparticles in reducing the mobility of the chains in the polymeric matrix near the surfaces of the dispersed nanoparticles (Ma & Zhang, 2009; Tomić et al., 2014).

Table 4.2: The parameters gained from TGA studies of A 100, AS 0 and all prepared SiO₂ nanocomposite coating systems.

| System | IDT (°C) | T _{50 wt. %} (°C) | Residue at 700 °C |
|--------|----------|----------------------------|-------------------|
| A 100 | 290 | 380 | 1.52 |
| AS 0 | 295 | 411 | 15.28 |
| AS 1 | 251 | 394 | 12.45 |
| AS 3 | 268 | 402 | 14.12 |
| AS 5 | 275 | 402 | 14.69 |
| AS 8 | 281 | 405 | 14.85 |

4.8 Electrochemical impedance spectroscopy (EIS)

In this section, the electrochemical response and anti-corrosion properties of the developed SiO₂ nanocomposite coating systems are reported, based on their EIS analysis results. EIS measurements were performed periodically after exposing the coated substrates to 3.5 wt. % NaCl solution and the results are expressed graphically in Nyquist and Bode plots. According to the electrochemical behaviour of the various prepared coating systems, Figure 4.11 shows three different equivalent circuit models, which were proposed to obtain the best numerical fittings during the study periods.

When the coating system acts as a perfect capacitor with superior barrier properties, model A of the equivalent circuit was used to fit the obtained data, which consists of the following elements: a resistor (R_s), i.e., indicating solution resistance, which has no important technical or theoretical information regarding the coating system so was not

included in this study; a resistor (R_{po}) and a constant phase element (CPE_{po}), which represents the electrolyte resistance through the pores, and its associated CPE_{po} . Model B was used to fit the EIS data after the electrolyte had started to penetrate the coating film and the corrosion reaction had been initiated. In addition, this model contains a parallel combination of a constant phase element and resistor, which represents the parameters of the corrosion reaction, specifically, the constant phase elements of double-layer capacitance (CPE_{dl}) and charge-transfer resistance (R_{ct}). The high degree of coating degradation and the reduction in the barrier properties can be perfectly described by model C of the equivalent circuit, which has been used to describe the diffusion process in the presence of corrosion products. This model introduces a new constant phase element and resistor, which enables the identification of new parameters, namely, the constant phase elements of diffusion capacitance (CPE_{diff}) and diffusion resistance (R_{diff}). It is noted that the constant phase element (CPE) has been used to replace the capacitance element by Meng et al., (2015) and others (Meng et al., 2015; Balaskas et al., 2011; Hirschorn et al., 2010; Jie et al., 2013), due to the “scattering effect” arising from the heterogeneity of the coating surface and to simulate deviations from non-ideal capacitive behaviour.

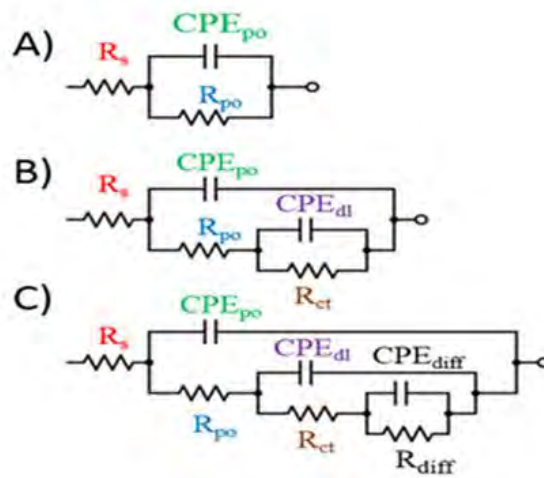


Figure 4.11: The equivalent circuit models.

Furthermore, Montemor and Ferreira (2007) attributed the necessity of utilizing constant phase elements instead of capacitance to the distributed surface reactivity, surface heterogeneity, electrode porosity, roughness, or fractal geometry and the current and potential distributions related to electrode geometry (Montemor & Ferreira, 2007).

To investigate the vital role of the utilized SiO₂ nanoparticles in enhancing the barrier properties of the fabricated acrylic–silicone polymeric matrix, and to determine the influence of changing the nanoparticle loading rates on the corrosion protection performance of the coating film, the EIS results of the acrylic–silicone coating systems (AS 0) and the prepared SiO₂ nanocomposite coating systems are reported after 1 day, 30 days, 60 days and 90 days of immersion time.

The EIS results after one day of immersion are illustrated in the form of a Bode plot in Figure 4.12 and Nyquist plots in Figures 4.13 and 4.14. At this stage of immersion, the AS 0 coating system shows an obvious bend in the low-frequency region of the Bode plot, Figure 4.12, and a full semi-circle is observed in the Nyquist plot, Figure 4.13, which is clear evidence that the electrolyte has begun penetrating the coating film and a corrosion reaction has been initiated. This observation further confirms the fact that pure organic resins cannot behave as intact coating layers with superior barrier performance due to the existence of free volume and porosity, which serve as direct diffusion pathways for electrolytes to the coating–metal interface (Zhou et al., 2014). The electrochemical behaviour of the AS 0 system at this level of degradation is perfectly described using model B of the equivalent circuit.

In contrast, the EIS results after one day of immersion of the prepared SiO₂ nanocomposite coating systems demonstrate capacitive behaviour in a straight line with a slope of -1 in the Bode plot, Figure 4.12, and one capacitive loop in the Nyquist plot, Figure 4.14, which is clear evidence of the efficiency of these coating systems in preventing any penetration of the electrolyte and the complete isolation of the metal

surface from the surrounding corrosion medium. As there was no charge transfer or diffusion of the electrolyte within the coating films, model A with just R_s , R_{po} and CPE_{po} was used to fit the EIS diagrams at this stage of immersion.

Moreover, the values of all parameters that have been obtained by fitting the EIS data according to the proposed equivalent circuit models after 1 day of immersion time are tabulated in Tables 4.3 and 4.4.

As the exposure time elapsed, the most significant degradation was observed on the substrate coated with the AS 0 coating system. As shown in Figures 4.15 and 4.16, a Bode plot with two time constants and a Nyquist plot with two full semi-circuits, respectively, were observed for the AS 0 coating systems after 30 days of immersion, which indicates poor corrosion resistance of the coating film. These changes in the EIS diagrams for the AS 0 coating system reveal the weakness of this system in withstanding the penetration of electrolytes to the coating–substrate interface, which leads to the initiation of a corrosion reaction and degradation in the coating film barrier. The electrochemical behaviour of the AS 0 system at this level of degradation is perfectly described by model C of the equivalent circuit. It is important to note that similar observations without significant changes were recorded for the acrylic–silicone coating system, AS 0, after 60 and 90 days of exposure, as shown in Figures 4.18, 4.19, 4.21 and 4.22, respectively.

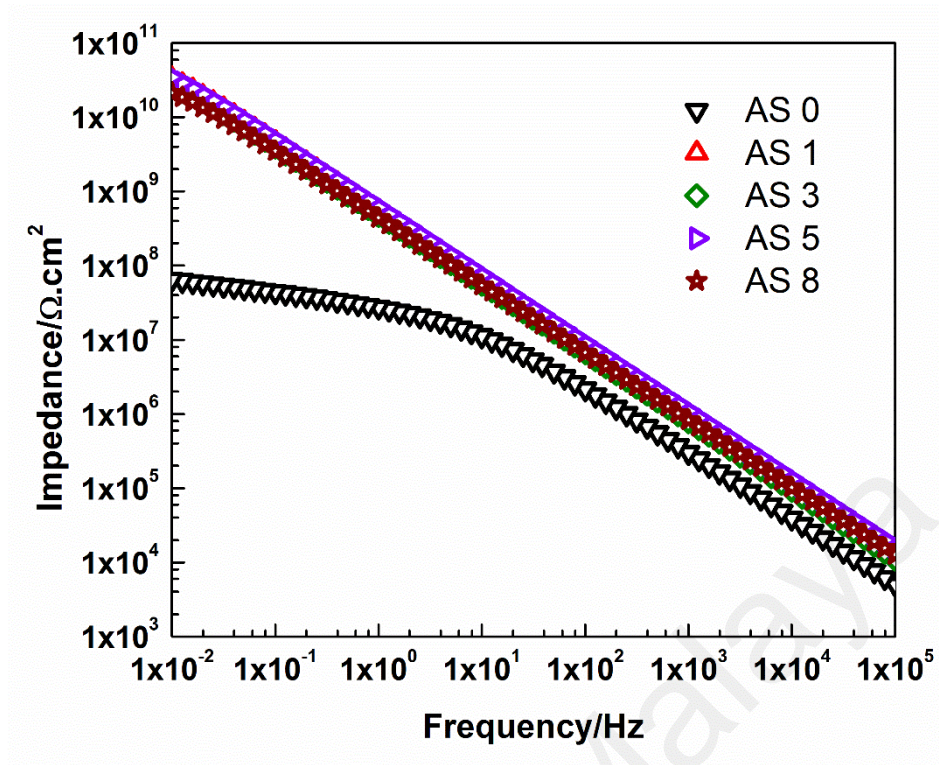


Figure 4.12: Bode plots for AS 0 and all prepared SiO_2 nanocomposite coating systems after 1 day of immersion time.

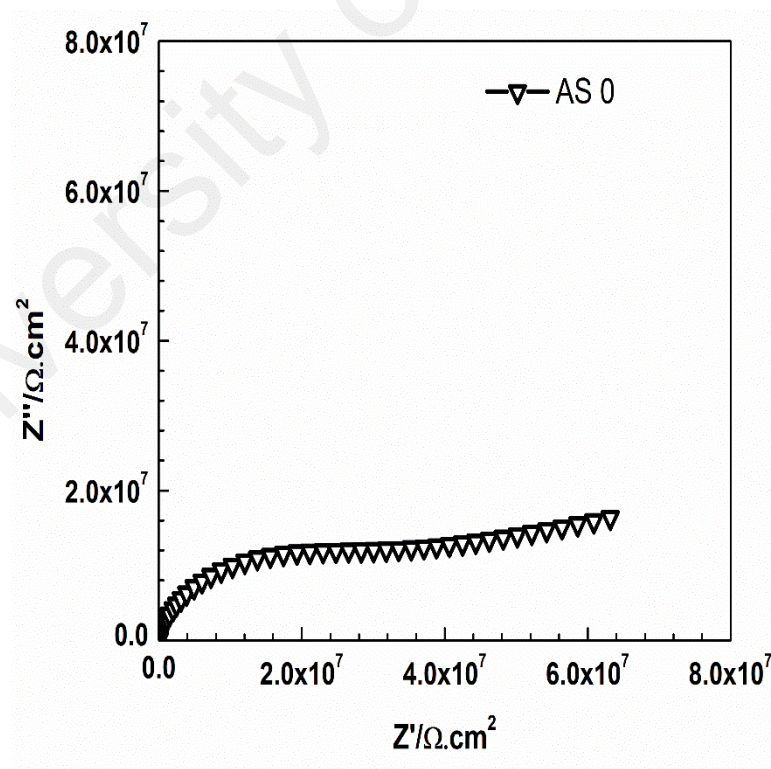


Figure 4.13: Nyquist plot for AS 0 coating system after 1 day of immersion time.

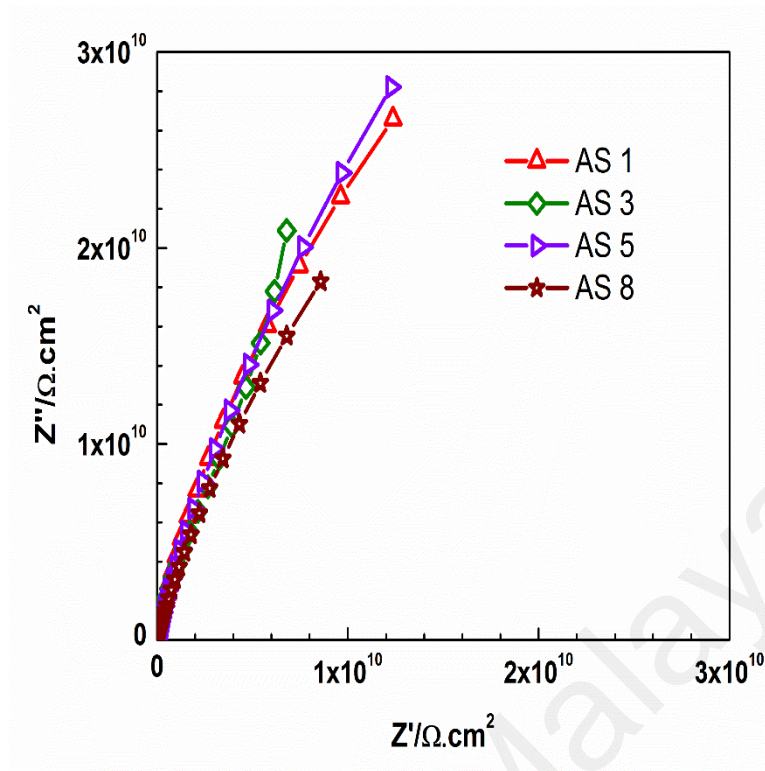


Figure 4.14: Nyquist plots for all prepared SiO₂ nanocomposite coating systems after 1 day of immersion time.

Table 4.3: The resistance values from EIS studies, along with the equivalent circuit model used to fit the data, of AS 0 and all prepared SiO₂ nanocomposite coating systems after 1 day of immersion time.

| System | R_{po} ($\Omega \text{ cm}^2$) | R_{ct} ($\Omega \text{ cm}^2$) | R_{diff} ($\Omega \text{ cm}^2$) | Model used |
|--------|------------------------------------|------------------------------------|--------------------------------------|------------|
| AS 0 | $(7.94 \pm 0.06) \times 10^6$ | $(2.38 \pm 0.02) \times 10^9$ | - | B |
| AS 1 | $(7.08 \pm 0.08) \times 10^{10}$ | - | - | A |
| AS 3 | $(5.69 \pm 0.02) \times 10^{10}$ | - | - | A |
| AS 5 | $(7.55 \pm 0.07) \times 10^{10}$ | - | - | A |
| AS 8 | $(3.73 \pm 0.01) \times 10^{10}$ | - | - | A |

Table 4.4: The constant phase element values from EIS studies of AS 0 and all prepared SiO₂ nanocomposite coating systems after 1 day of immersion time.

| System | CPR _{po} | | CPE _{dl} | | CPE _{diff} | |
|--------|---|------|---|------|---|---|
| | Y ₀ (Ω ⁻¹ cm ⁻² s ⁿ) | n | Y ₀ (Ω ⁻¹ cm ⁻² s ⁿ) | n | Y ₀ (Ω ⁻¹ cm ⁻² s ⁿ) | n |
| AS 0 | $(1.31 \pm 0.01) \times 10^{-9}$ | 0.89 | $(1.98 \pm 0.10) \times 10^{-8}$ | 0.14 | - | - |
| AS 1 | $(3.34 \pm 0.02) \times 10^{-10}$ | 0.93 | - | - | - | - |
| AS 3 | $(3.81 \pm 0.02) \times 10^{-10}$ | 0.93 | - | - | - | - |
| AS 5 | $(3.03 \pm 0.01) \times 10^{-10}$ | 0.92 | - | - | - | - |
| AS 8 | $(4.28 \pm 0.02) \times 10^{-10}$ | 0.91 | - | - | - | - |

On the other hand, after 30 days of immersion, the EIS results reveal that the incorporation of SiO₂ nanoparticles in the acrylic–silicone polymeric matrix resulted in a remarkable enhancement of the anti-corrosion performance as there were no significant changes observed in the Bode and Nyquist plots shown in Figure 4.15 and Figure 4.17, respectively. Moreover, the developed coating films that contained SiO₂ nanoparticles at different loading rates remained intact, thereby demonstrating superior anti-corrosion performance and optimal properties for up to 60 days of exposure of the coated substrates to 3.5 % NaCl solution. Figures 4.18 and 4.20 show Bode and Nyquist plots of the developed SiO₂ nanocomposite coatings, respectively.

Moreover, the values of all parameters that have been obtained by fitting the EIS data according to the proposed equivalent circuit models after 30 and 60 days of immersion time are tabulated in Tables 4.5, 4.6, 4.7 and 4.8.

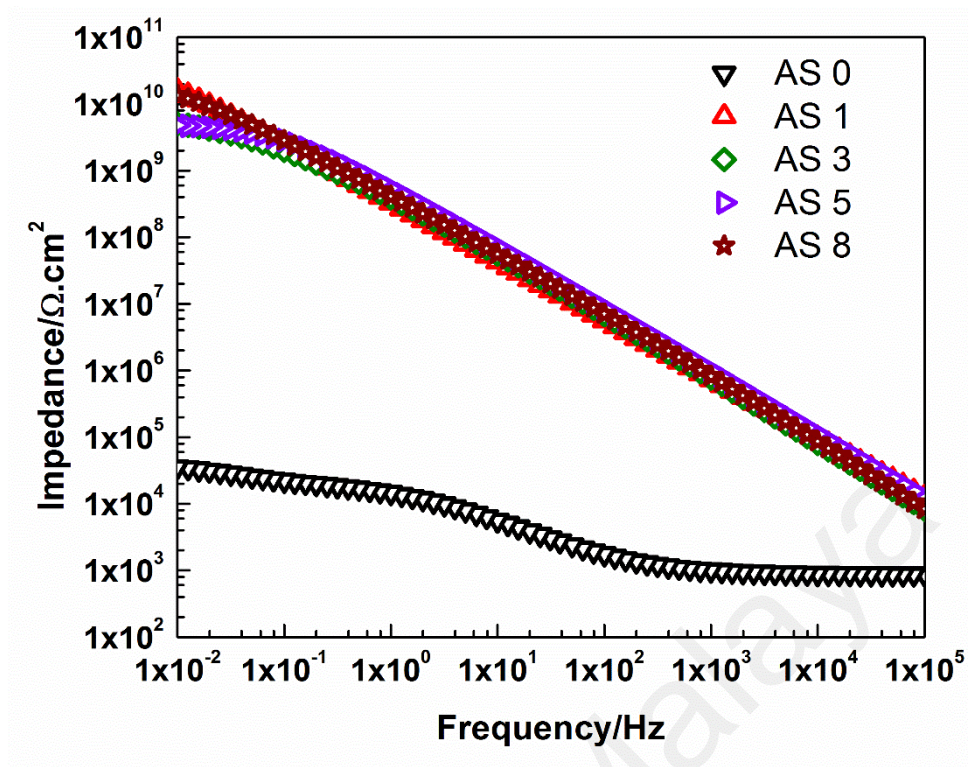


Figure 4.15: Bode plots for AS 0 and all prepared SiO_2 nanocomposite coating systems after 30 days of immersion time.

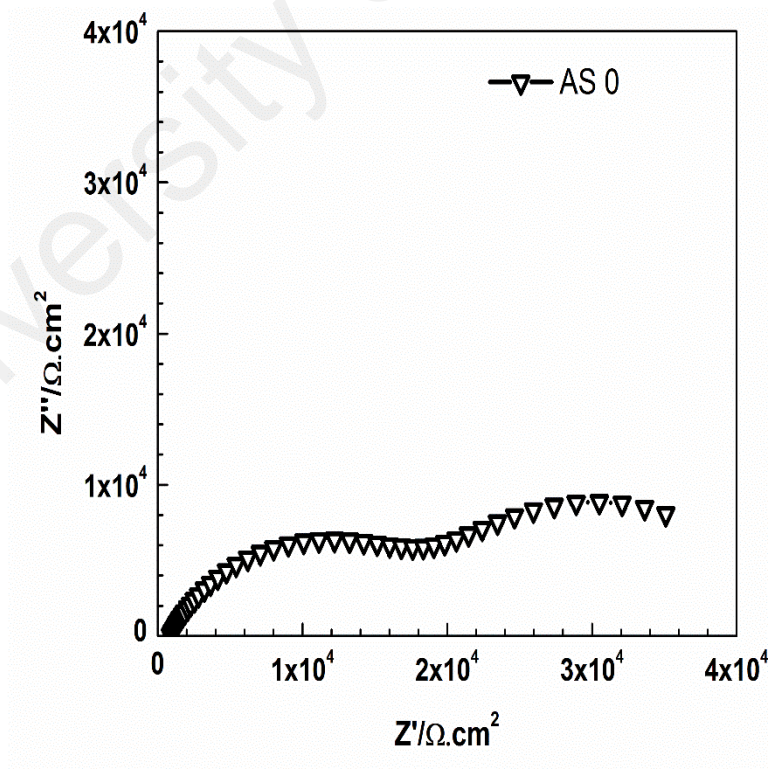


Figure 4.16: Nyquist plot for AS 0 coating system after 30 days of immersion time.

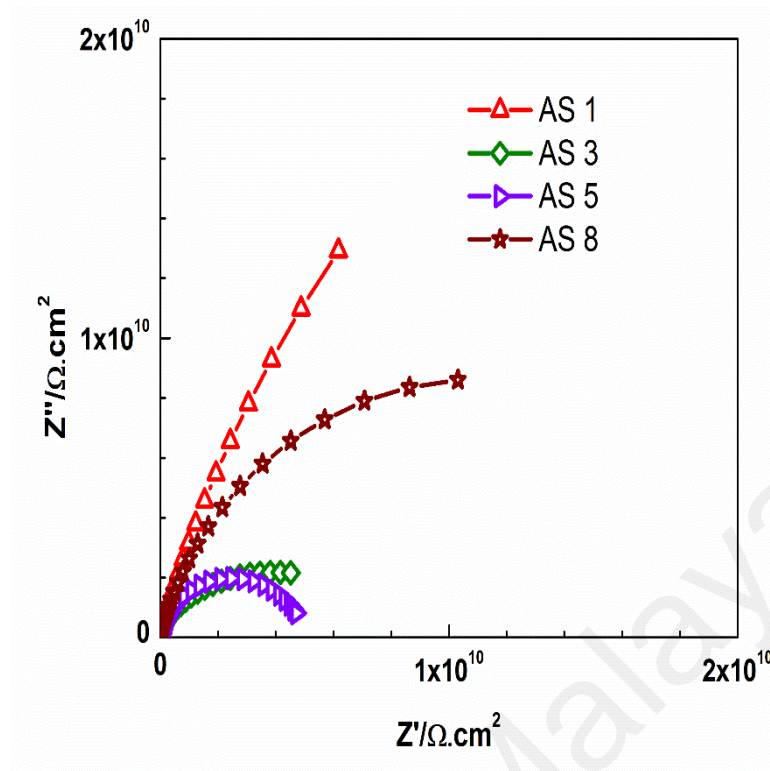


Figure 4.17: Nyquist plots for all prepared SiO₂ nanocomposite coating systems after 30 days of immersion time.

Table 4.5: The resistance values from EIS studies, along with the equivalent circuit model used to fit the data, of AS 0 and all prepared SiO₂ nanocomposite coating systems after 30 days of immersion time.

| System | $R_{po} (\Omega \text{ cm}^2)$ | $R_{ct} (\Omega \text{ cm}^2)$ | $R_{diff} (\Omega \text{ cm}^2)$ | Model used |
|--------|----------------------------------|--------------------------------|----------------------------------|------------|
| AS 0 | $(1.37 \pm 0.13) \times 10^3$ | $(1.27 \pm 0.09) \times 10^5$ | $(1.04 \pm 0.06) \times 10^4$ | C |
| AS 1 | $(3.66 \pm 0.09) \times 10^{10}$ | - | - | A |
| AS 3 | $(3.97 \pm 0.03) \times 10^9$ | - | - | A |
| AS 5 | $(4.46 \pm 0.04) \times 10^9$ | - | - | A |
| AS 8 | $(1.58 \pm 0.00) \times 10^{10}$ | - | - | A |

Table 4.6: The constant phase element values from EIS studies of AS 0 and all prepared SiO₂ nanocomposite coating systems after 30 days of immersion time.

| System | CPR _{po} | | CPE _{dl} | | CPE _{diff} | |
|--------|---|------|---|------|---|------|
| | $Y_0 (\Omega^{-1} \text{ cm}^{-2} \text{ s}^n)$ | n | $Y_0 (\Omega^{-1} \text{ cm}^{-2} \text{ s}^n)$ | n | $Y_0 (\Omega^{-1} \text{ cm}^{-2} \text{ s}^n)$ | n |
| AS 0 | $(3.82 \pm 0.15) \times 10^{-5}$ | 0.20 | $(2.90 \pm 0.09) \times 10^{-6}$ | 0.85 | $(6.40 \pm 0.07) \times 10^{-6}$ | 0.18 |
| AS 1 | $(5.96 \pm 0.02) \times 10^{-10}$ | 0.88 | - | - | - | - |
| AS 3 | $(4.56 \pm 0.02) \times 10^{-10}$ | 0.92 | - | - | - | - |
| AS 5 | $(3.23 \pm 0.02) \times 10^{-10}$ | 0.93 | - | - | - | - |
| AS 8 | $(4.59 \pm 0.02) \times 10^{-10}$ | 0.91 | - | - | - | - |

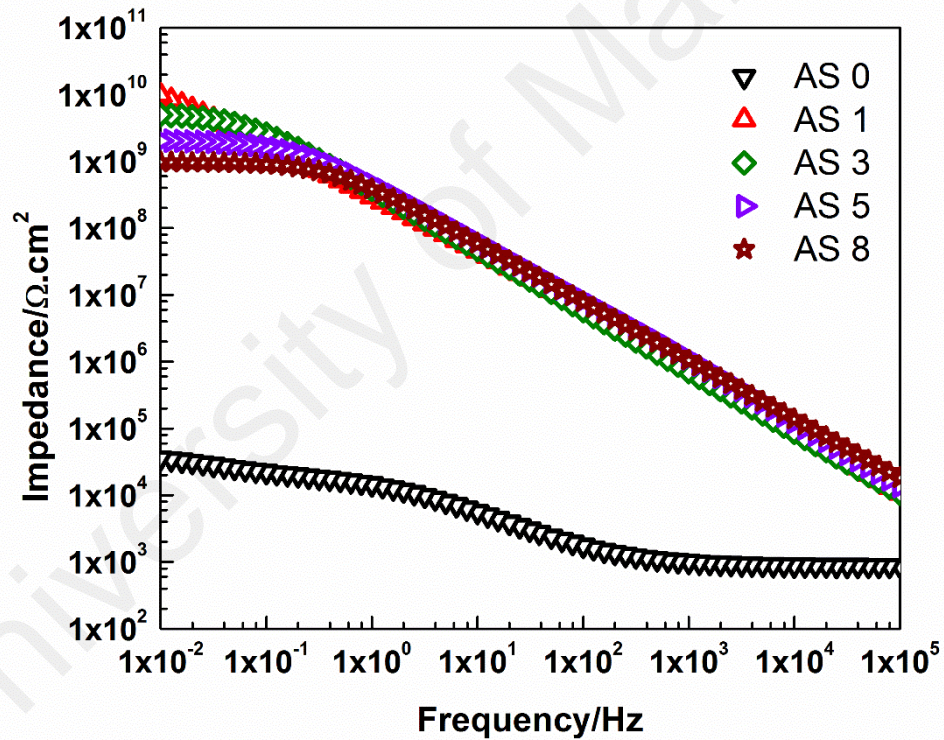


Figure 4.18: Bode plots for AS 0 and all prepared SiO₂ nanocomposite coating systems after 60 days of immersion time.

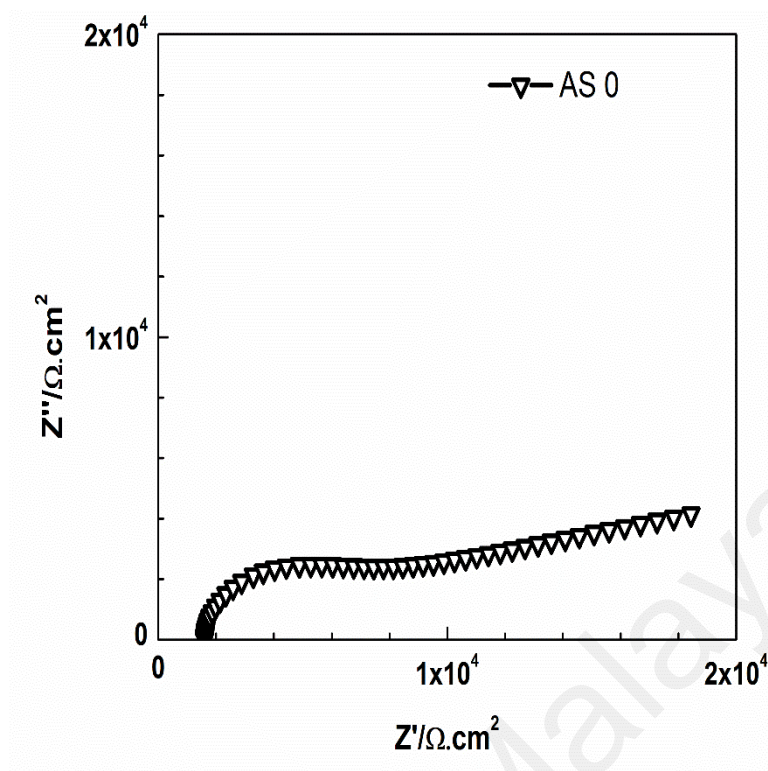


Figure 4.19: Nyquist plot for AS 0 coating system after 60 days of immersion time.

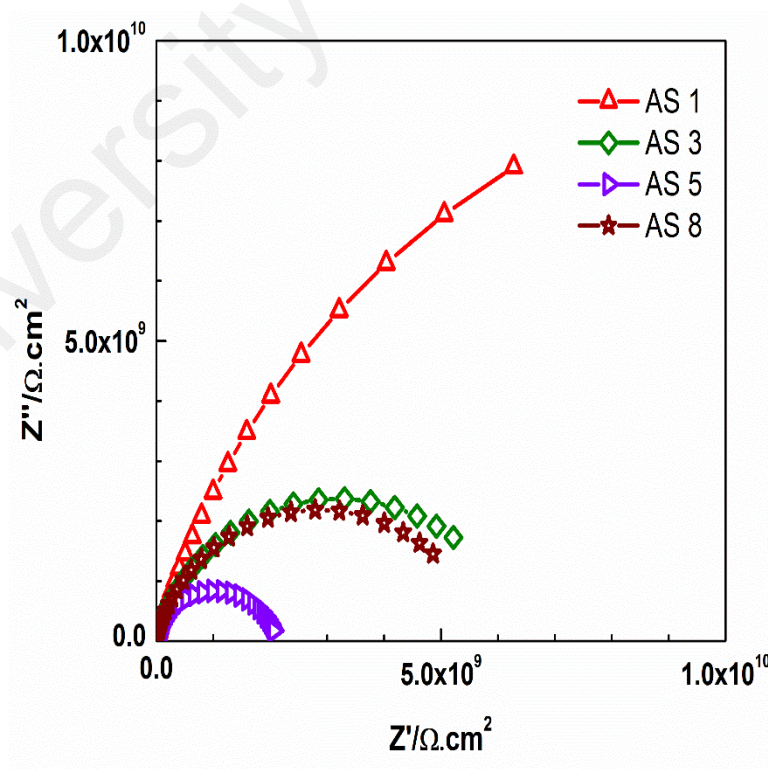


Figure 4.20: Nyquist plots for all prepared SiO₂ nanocomposite coating systems after 60 days of immersion time.

Table 4.7: The resistance values from EIS studies, along with the equivalent circuit model used to fit the data, of AS 0 and all prepared SiO₂ nanocomposite coating systems after 60 days of immersion time.

| System | R _{po} (Ω cm ²) | R _{ct} (Ω cm ²) | R _{diff} (Ω cm ²) | Model used |
|--------|--------------------------------------|--------------------------------------|--|------------|
| AS 0 | $(6.38 \pm 0.04) \times 10^3$ | $(7.80 \pm 0.02) \times 10^4$ | $(1.49 \pm 0.05) \times 10^5$ | C |
| AS 1 | $(1.71 \pm 0.03) \times 10^{10}$ | - | - | A |
| AS 3 | $(5.15 \pm 0.05) \times 10^9$ | - | - | A |
| AS 5 | $(1.42 \pm 0.02) \times 10^7$ | - | - | A |
| AS 8 | $(4.93 \pm 0.05) \times 10^9$ | - | - | A |

Table 4.8: The constant phase element values from EIS studies of AS 0 and all prepared SiO₂ nanocomposite coating systems after 60 days of immersion time.

| System | CPR _{po} | | CPE _{dl} | | CPE _{diff} | |
|--------|---|------|---|------|---|------|
| | Y ₀ (Ω ⁻¹ cm ⁻² s ⁿ) | n | Y ₀ (Ω ⁻¹ cm ⁻² s ⁿ) | n | Y ₀ (Ω ⁻¹ cm ⁻² s ⁿ) | n |
| AS 0 | $(1.63 \pm 0.08) \times 10^{-6}$ | 0.71 | $(5.90 \pm 0.03) \times 10^{-7}$ | 0.94 | $(8.33 \pm 0.01) \times 10^{-11}$ | 0.87 |
| AS 1 | $(7.03 \pm 0.03) \times 10^{-10}$ | 0.87 | - | - | - | - |
| AS 3 | $(4.71 \pm 0.02) \times 10^{-10}$ | 0.91 | - | - | - | - |
| AS 5 | $(1.90 \pm 0.01) \times 10^{-10}$ | 0.96 | - | - | - | - |
| AS 8 | $(5.05 \pm 0.03) \times 10^{-10}$ | 0.90 | - | - | - | - |

However, as the electrochemical responses of the SiO₂ nanocomposite coatings were relatively similar, to determine the best loading ratio of SiO₂ nanoparticles to be added to the acrylic–silicone polymeric matrix to achieve the best corrosion protection ability, EIS was performed after 90 days of immersion and Figures 4.21 and 4.23 show the resulting Bode and Nyquist plots, respectively.

Even after such a long period of time, the prepared nanocomposite coating systems continued to perform as intact coating layers and demonstrated high pore resistance.

However, the incorporation of 1 wt. % SiO₂ nanoparticles resulted in the AS 1 coating system suffering some penetration of the electrolyte after long periods of exposure. This was observed in the Bode plot of the AS 1 coating system, which shows a bend in the low-frequency region and one full semi-circle in the Nyquist plot. It is noted that this electrochemical behaviour can be perfectly described by fitting the EIS data using model B of the equivalent circuit. On the other hand, of the prepared SiO₂ nanocomposite coatings, the AS 3 coating system with 3 wt. % SiO₂ nanoparticles demonstrated the best performance, with almost no changes observed in the Bode and Nyquist plots, as it can be fitted using model A of the equivalent circuit. A straight line in the Bode plot with a slope of -1 and one capacitive loop in the Nyquist plot indicate the total capacitive behaviour of the coating film.

This result can be attributed to the role of the SiO₂ nanoparticles in zigzagging the diffusion pathways in response to corrosive agents, which causes these agents to travel a longer and more tortuous distance to reach the surface of the substrate (Ramezanzadeh et al., 2011; Yuan et al., 2015; Zhou et al., 2014).

Furthermore, the presence of SiO₂ nanoparticles can enhance the barrier performance of the polymeric matrix by ensuring a higher degree of crosslinking between the polymeric matrix and the embedded nanoparticles. These SiO₂ nanoparticles, with significantly large specific areas and -OH groups on their surfaces, can react with the -NCO groups from the NCO curing agent. Therefore, a stronger interaction occurs between the organic and inorganic components in the coating film (Zhou et al., 2002). Dolatzadeh et al. also demonstrated that the presence of SiO₂ nanoparticles in a polymeric matrix rearranges and modifies the structure so that the resulting nanocomposite coating exhibits enhanced barrier properties (Dolatzadeh et al., 2011b). Apart from this fact, the intact corrosion protection performance realized by utilizing SiO₂ nanoparticles can also be explained by the fact that the dual nature (physical–chemical) of the interactions

between the SiO₂ nanoparticles and the polymeric matrix provides efficient resistance to hydrolytic degradation compared to the resistance gained by the chemical interaction of hybrid resin chains (Bravo et al., 2007; Ogiwara et al., 2012; Su et al., 2006; Wang et al., 2011). It is noted that no further corrosion protection was obtained once the SiO₂ loading ratio exceeded 3 wt. %. As a full semi-circle in the Nyquist plot and an obvious bend in the low-frequency region in the Bode plot were observed with the AS 5 and AS 8 coating systems, models B and A were utilized to perform the numerical fitting, respectively.

This result could be attributed to the tendency of the nanoparticles to form agglomerations at high loading ratios as the number of nanoparticles increases in the unit area. Thus, the formation of larger particles will affect the barrier properties of the utilized reinforcing particles, which will impede their dispersion throughout the polymeric matrix and in filling all the pores. Moreover, the values of all parameters that have been obtained by fitting the EIS data according to the proposed equivalent circuit models after 90 days of immersion time are tabulated in Tables 4.9 and 4.10.

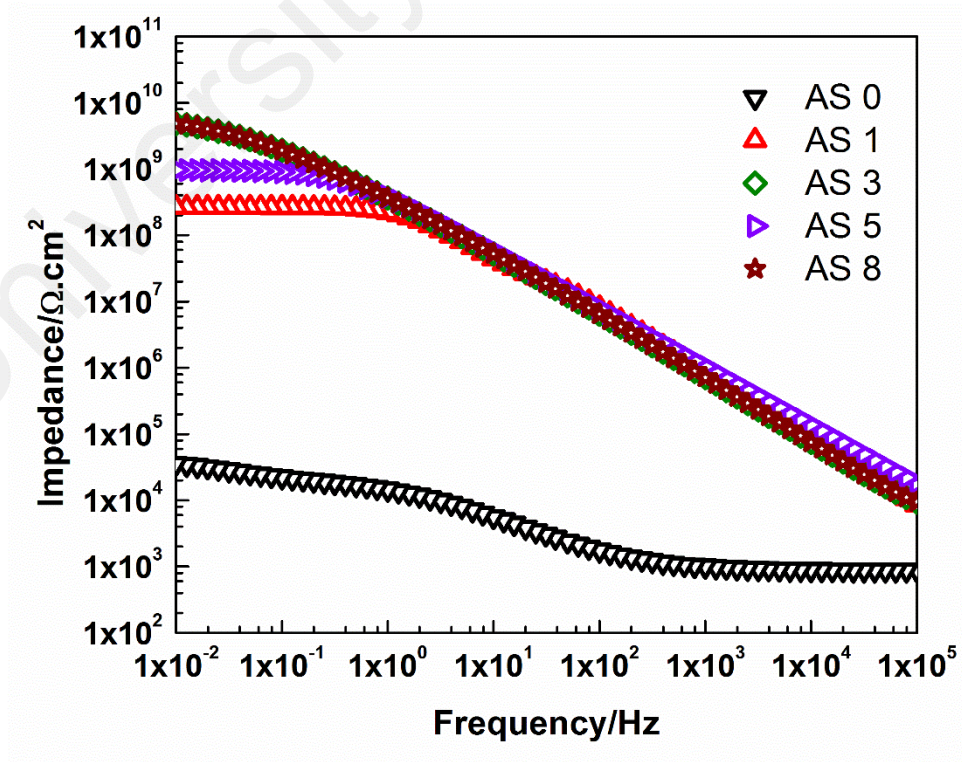


Figure 4.21: Bode plots for AS 0 and all prepared SiO₂ nanocomposite coating systems after 90 days of immersion time.

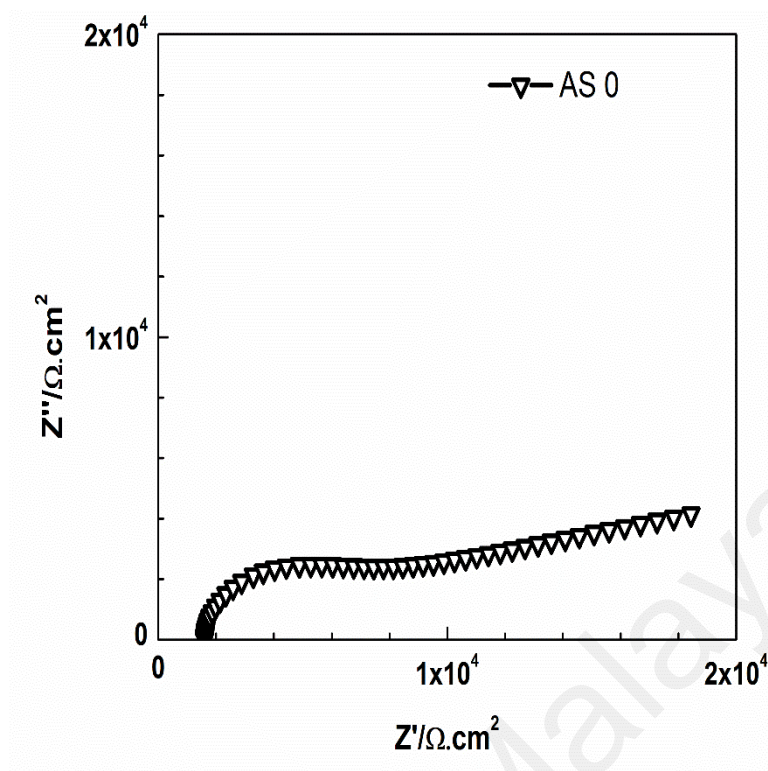


Figure 4.22: Nyquist plot for AS 0 coating system after 90 days of immersion time.

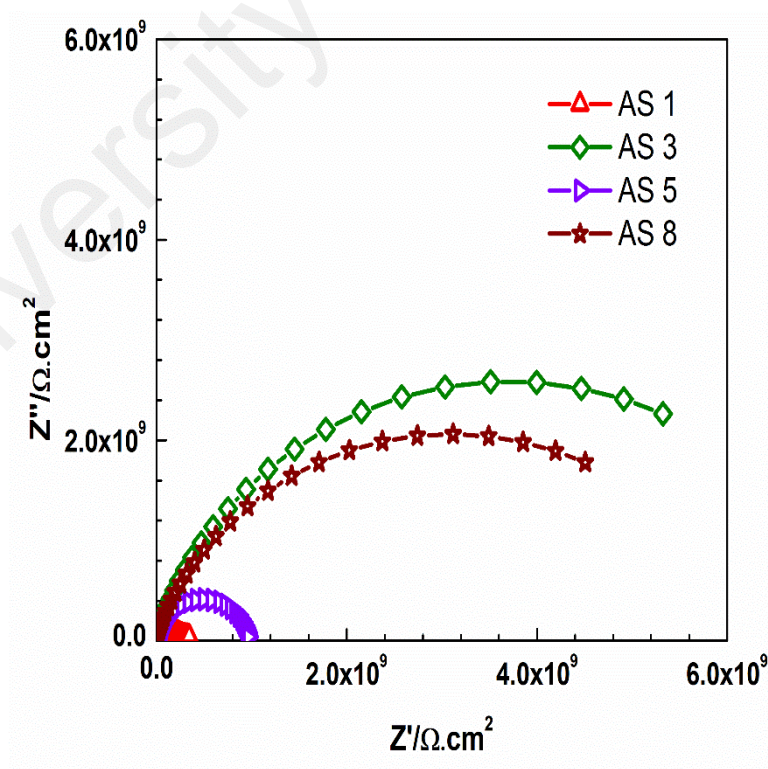


Figure 4.23: Nyquist plots for all prepared SiO₂ nanocomposite coating systems after 90 days of immersion time.

Table 4.9: The resistance values from EIS studies, along with the equivalent circuit model used to fit the data, of AS 0 and all prepared SiO₂ nanocomposite coating systems after 90 days of immersion time.

| System | $R_{po} (\Omega \text{ cm}^2)$ | $R_{ct} (\Omega \text{ cm}^2)$ | $R_{diff} (\Omega \text{ cm}^2)$ | Model used |
|--------|--------------------------------|--------------------------------|----------------------------------|------------|
| AS 0 | $(1.52 \pm 0.13) \times 10^3$ | $(2.61 \pm 0.08) \times 10^4$ | $(1.06 \pm 0.07) \times 10^5$ | C |
| AS 1 | $(1.43 \pm 0.09) \times 10^8$ | $(3.49 \pm 0.06) \times 10^7$ | - | B |
| AS 3 | $(5.10 \pm 0.05) \times 10^9$ | - | - | A |
| AS 5 | $(1.03 \pm 0.02) \times 10^9$ | $(3.18 \pm 0.07) \times 10^7$ | - | B |
| AS 8 | $(3.88 \pm 0.03) \times 10^9$ | - | - | A |

Table 4.10: The constant phase element values from EIS studies of AS 0 and all prepared SiO₂ nanocomposite coating systems after 90 days of immersion time.

| System | CPR_{po} | | CPE_{dl} | | CPE_{diff} | |
|--------|---|------|---|------|---|------|
| | $Y_0 (\Omega^{-1} \text{ cm}^{-2} \text{ s}^n)$ | n | $Y_0 (\Omega^{-1} \text{ cm}^{-2} \text{ s}^n)$ | n | $Y_0 (\Omega^{-1} \text{ cm}^{-2} \text{ s}^n)$ | n |
| AS 0 | $(7.76 \pm 0.09) \times 10^{-5}$ | 0.19 | $(8.87 \pm 0.01) \times 10^{-7}$ | 1.00 | $(7.63 \pm 0.03) \times 10^{-11}$ | 0.88 |
| AS 1 | $(2.09 \pm 0.01) \times 10^{-10}$ | 0.98 | $(9.33 \pm 0.04) \times 10^{-10}$ | 0.50 | - | - |
| AS 3 | $(4.97 \pm 0.03) \times 10^{-10}$ | 0.91 | - | - | - | - |
| AS 5 | $(4.45 \pm 0.05) \times 10^{-10}$ | 0.87 | $(5.41 \pm 0.08) \times 10^{-8}$ | 1.00 | - | - |
| AS 8 | $(4.68 \pm 0.02) \times 10^{-10}$ | 0.93 | - | - | - | - |

To investigate the stability of the coating films against damage by the electrolyte and to evaluate the state of the interfacial adhesion bonds at the coating–substrate interface for different immersion periods, the EIS method was used in the Bode-plot format (impedance and phase angle as a function of the frequency). With the assistance of breakpoint frequency values, which indicate the frequency at a -45° phase angle, the region below the Bode plot can be divided into capacitive and resistive regions. Subsequently, by recording and analysing the changes that occur in these regions for each

coating system over the whole immersion period, a fuller understanding and detailed information can be obtained regarding the electrochemical behaviour, barrier properties, coating delamination and electrolyte diffusion state (Ghasemi et al., 2016; Ramezanzadeh et al., 2016).

Figures 4.24(a) and 4.24(b) show Bode plots of the AS 0 coating system after 1 and 90 days of immersion, respectively. It can be clearly seen that the AS 0 coating system has two regions under the Bode plot after the first day of immersion, namely, a resistive region in the low-frequency domain and a capacitive region in the high-frequency domain. These regions could indicate the weakness of the corrosion protection ability of the coating film and the poor barrier properties at this early stage of exposure to 3.5 % NaCl solution.

However, after 90 days of immersion, the whole area under the Bode plot was classified as resistive, which indicates the failure of the coating system as the diffusion of the electrolyte occurred within the coating film. Thus, coating delamination and loss of adhesion occurred at the substrate surface.

In contrast, after the incorporation of different loading ratios of SiO₂ nanoparticles in the hybrid polymeric material, better performance was observed for all the nanocomposite coating systems. As can be clearly observed in Figures 4.25(a), 4.26(a), 4.27(a) and 4.28(a) of the Bode plots of the developed SiO₂ nanocomposite coating systems after one day of immersion, significant enhancement in the corrosion protection performance and barrier properties was observed, in that the coating films demonstrated a capacitive behaviour over the entire tested frequency range and there was only a capacitive region under the Bode plots at this stage of immersion.

Moreover, as the EIS studies extended up to 90 days of immersion, Figures 4.25(b), 4.26(b), 4.27(b) and 4.28(b) show the Bode plots (impedance and phase angle as a function of the frequency) of AS 1, AS 3, AS 5 and AS 8, respectively, after 90 days of

immersion. It is interesting to note that the incorporation of SiO₂ nanoparticles in the acrylic–silicone polymeric matrix enhanced the barrier properties, as observed in the lower breakpoint frequencies. Therefore, relatively smaller resistive regions in the low-frequency domain and larger capacitive regions in the AS 0 coating system were observed.

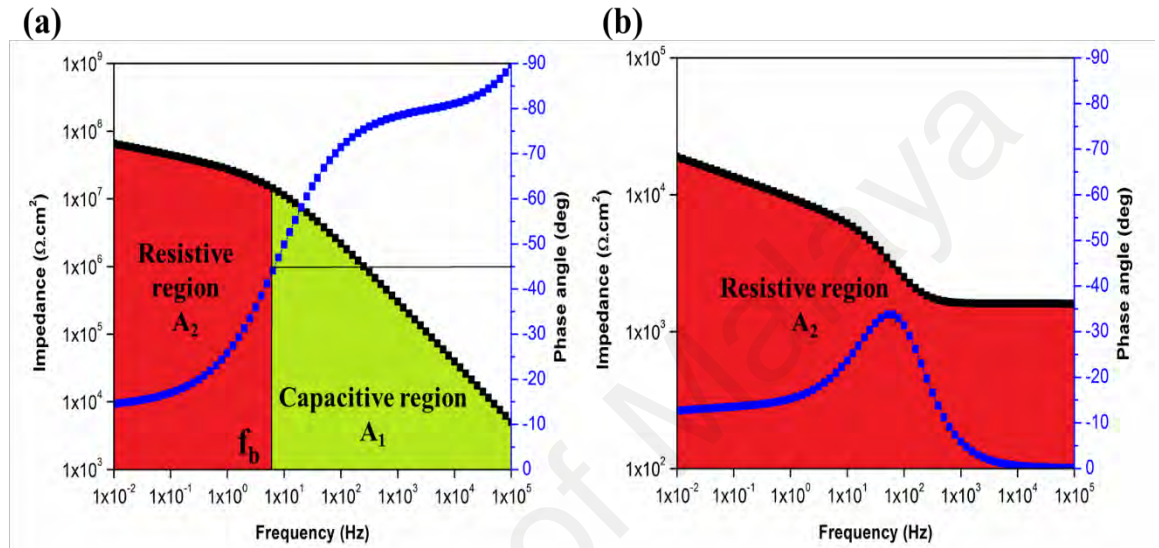


Figure 4.24: Bode plots of AS 0 coating system after (a) 1 day and (b) 90 days of immersion along with the determining the breakpoint frequency and the corresponding capacitive (A1) and resistive (A2) regions.

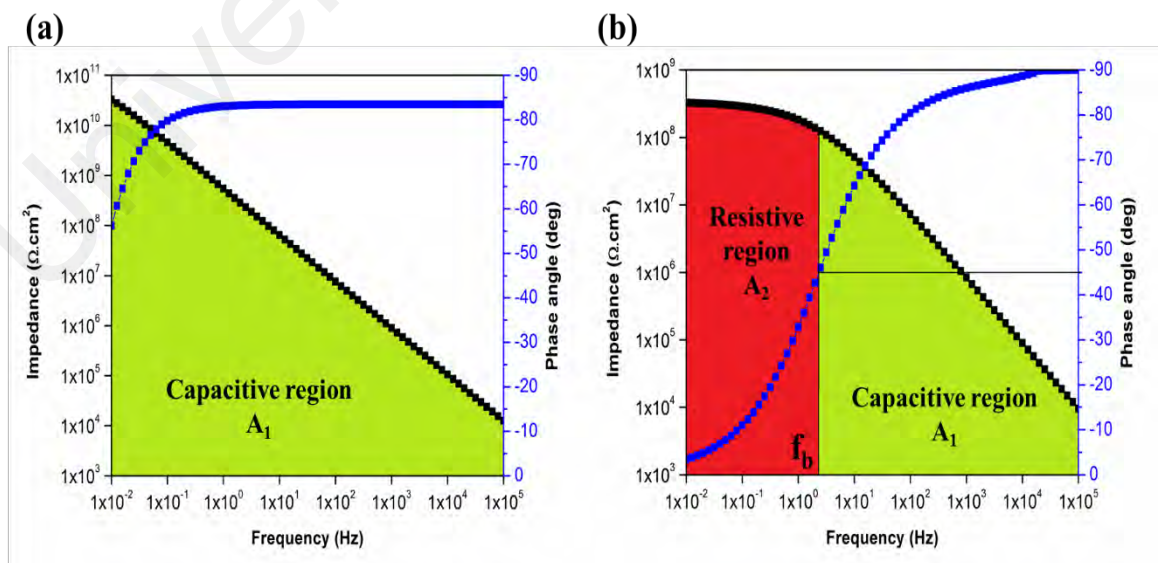


Figure 4.25: Bode plots of AS 1 coating system after (a) 1 day and (b) 90 days of immersion along with the determining the breakpoint frequency and the corresponding capacitive (A1) and resistive (A2) regions.

However, it is noted that, based on the results of the breakpoint frequency method, it can be further confirmed that the AS 3 coating system demonstrated the best corrosion protection performance and provided the best barrier properties of the developed SiO₂ nanocomposite coatings.

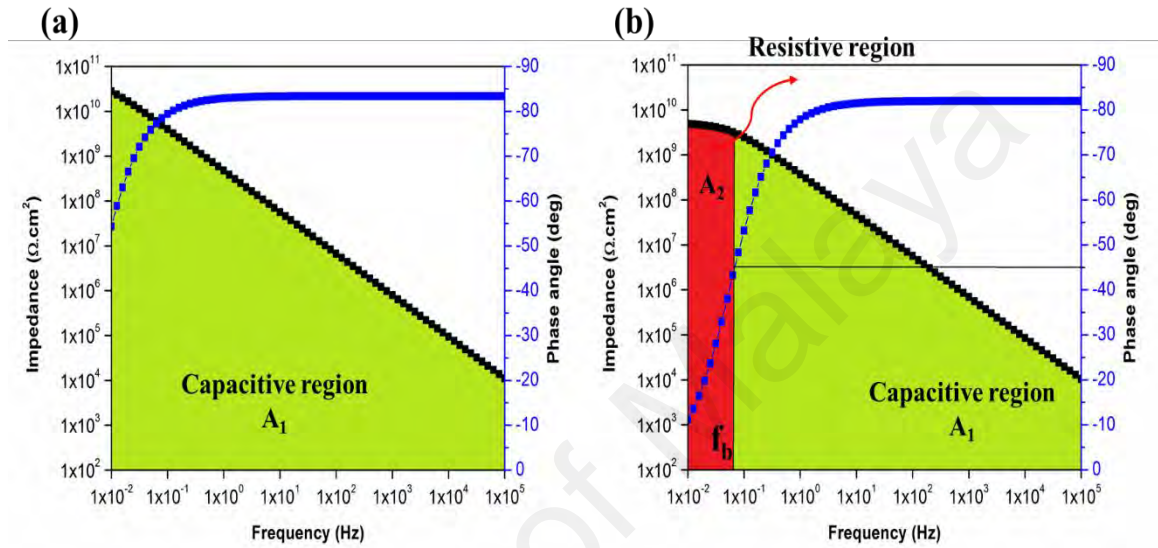


Figure 4.26: Bode plots of AS 3 coating system after (a) 1 day and (b) 90 days of immersion along with the determining the breakpoint frequency and the corresponding capacitive (A1) and resistive (A2) regions.

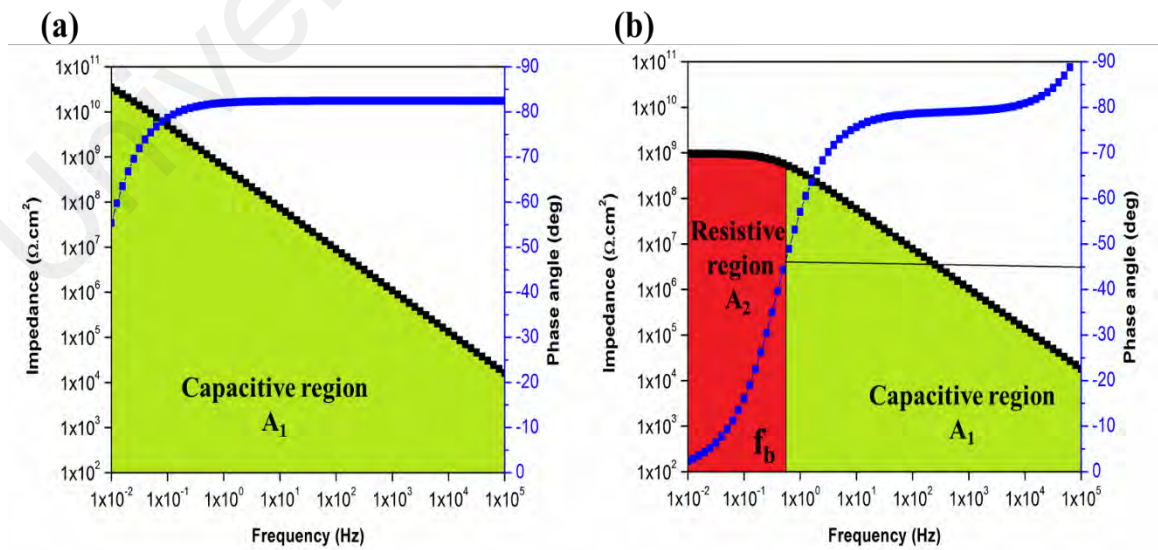


Figure 4.27: Bode plots of AS 5 coating system after (a) 1 day and (b) 90 days of immersion along with the determining the breakpoint frequency and the corresponding capacitive (A1) and resistive (A2) regions.

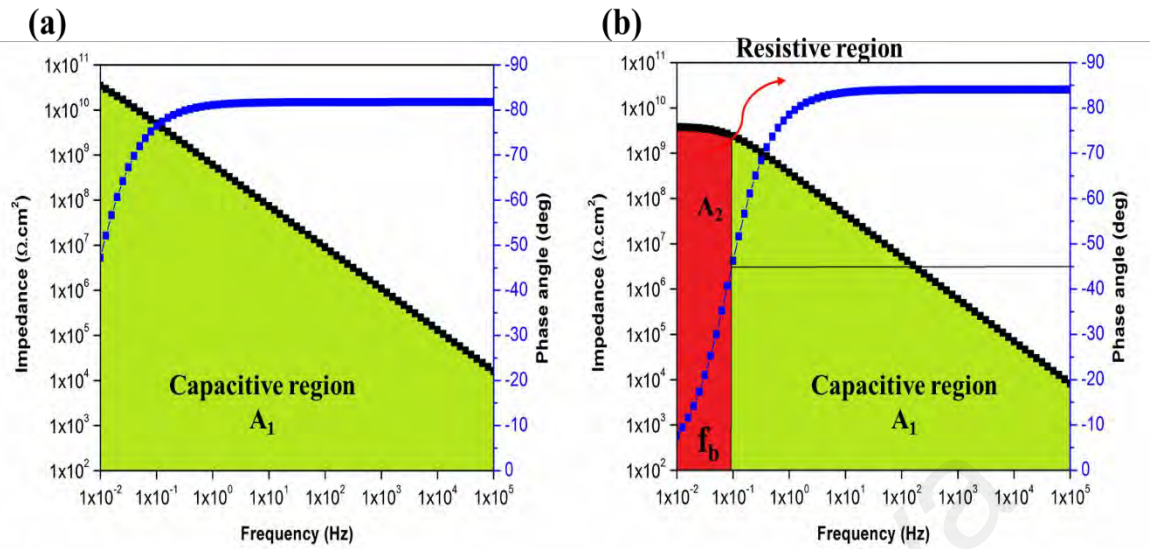


Figure 4.28: Bode plots of AS 8 coating system after (a) 1 day and (b) 90 days of immersion along with the determining the breakpoint frequency and the corresponding capacitive (A_1) and resistive (A_2) regions.

4.9 Summary

The application of organic coatings is considered to be one of the best methods for effectively protecting metals from corrosion. By acting as a physical barrier layer, organic coating films play a vital role in isolating metal surfaces that would otherwise be in direct contact with the surrounding environment, hence, they prevent the onset of the corrosion process. However, there are many shortcomings associated with the application of organic coating systems e.g., weak barrier performance, hydrophilic surfaces, low thermal and UV stability, poor chemical resistance and a high affinity between water and polymer polar groups.

Therefore, in this study, the objective was to introduce a second aspect to the polymeric matrix in the form of inorganic nanoparticles to overcome the various limitation of purely organic coating systems. Using the solution intercalation method, different loading ratios of SiO₂ nanoparticles were embedded into the hybrid acrylic–silicon polymeric matrix, specifically, 1 wt. %, 3 wt. %, 5 wt. % and 8 wt. %.

To determine the influence of the addition of SiO₂ nanoparticles in enhancing the overall performance of the acrylic–silicone polymeric matrix and the ability of the developed nanocomposite coating systems to act as multifunctional coating layers, several characterization techniques were employed to examine the different properties and functions of the developed single-layer nanocomposite coatings.

Prior to testing the developed nanocomposite coating systems, it was essential to investigate the effective achievement of the acrylic–silicone polymeric matrix to be used as the host polymeric matrix for the developed coating systems in this study.

In this regard, FTIR was employed to investigate the chemical structure and the attained curing level. The FTIR findings revealed the compatibility between the acrylic and silicone resins and confirmed the ability of the NCO curing agent to yield an excellent crosslinked structure. The appropriateness of using a room-temperature curing process

with the utilization of a single curing agent was confirmed by the existence of new bands in the AS 0 spectra, with the respect to the neat acrylic and neat silicone FTIR spectra, and the interaction between the functional groups of the acrylic polyol resin, silicone resin and NCO resin via the hydroxyl end groups and NCO functional groups.

After confirming the ability of the NCO curing agent to obtain a good curing level of the acrylic–silicone polymeric blend, it was essential to confirm the efficacy of the solution intercalation method in the development of excellent particle distribution of the SiO₂ nanoparticles within the hybrid polymeric matrix. Therefore, FESEM was performed on the developed SiO₂ nanocomposite coating systems. The FESEM micrographs confirmed the optimal curing of the polymeric nanocomposite films at room temperatures, as the coated surface was crack-free and no phase separation was observed. Moreover, a good dispersion of the SiO₂ nanoparticles observed in the polymeric matrix proved the efficiency of the sonication process. However, as the loading ratio of the nanoparticles increased, particularly with the application of the AS 8 coating system, the agglomeration increased due to increases in the number of nanoparticles in the unit area.

Surface hydrophobicity is considered to be a key surface property that plays a vital role in the development of coating systems that ensure minimal contact between the surface and aqueous electrolytes. In this study, the wettability of the developed coated surfaces, one of the main characteristics, and the influence of the loading ratio of SiO₂ nanoparticles on the CA value were investigated.

Two main factors can directly affect the wettability of a given surface, i.e., the surface energy of the utilized materials and the surface morphology. As such, experiments were conducted to determine the CA values of the A 100 and AS 0 coating systems. The results reveal that the incorporation of silicone resin with acrylic resin can shift the wettability of the resulting surface toward greater hydrophobicity. This can be attributed to the

changes in the chemical composition due to the presence of the (–Si–O–Si–) silicone, as has been confirmed in previously reported FTIR studies.

On the other hand, further enhancement of the hydrophobicity of the resulting surfaces was confirmed by the CA results of the SiO₂ nanocomposite coating systems, which were observed to have CA > 90°. This, in turn, confirms the ability of SiO₂ nanoparticles, especially at a 3 wt. % loading ratio, to alter the surface morphology of the hybrid polymeric matrix to obtain hydrophobic coating films.

Another desired function of the developed SiO₂ nanocomposite coatings is film transparency, which changes after the incorporation of different loading ratios of SiO₂ nanoparticles, and which were investigated using UV-Vis measurement. To distinguish the effect of each component involved in developing the SiO₂ nanocomposite coating systems, it was necessary to analyse the light transmittance spectra of the A 100 and AS 0 coating systems. It was interesting to note that the introduction of silicone resin to acrylic resin did not significantly affect the transparency of the coating film. On the other hand, the obtained results reveal that as the loading ratio of the SiO₂ nanoparticles increased in the hybrid acrylic–silicone polymeric matrix, the light transmittance decreased. This was attributed to the tendency of the nanoparticles to form larger agglomerated particles, especially with the application of the AS 5 and AS 8 coating systems. Despite this fact, all films were still considered to be transparent, based on their high transmittance values in the visible region.

Next, the adhesion properties of the developed SiO₂ nanocomposite coating systems were evaluated by CHT. It is interesting to note that the addition of the different loading amounts of SiO₂ nanoparticles did not alter the excellent adhesion properties of the hybrid acrylic–silicone polymeric matrix. The application of the AS 0 coating system was recorded as 5B grade, according to the ASTM D3359 standard, as were the developed SiO₂ nanocomposite coating systems. Hence, these observations again confirm the

successful development of multifunctional nanocomposite coating systems based on a hybrid acrylic–silicone polymeric material and SiO₂ nanoparticles.

The thermal stability of the A 100, AS 0 and prepared SiO₂ nanocomposite coatings were investigated by performing TGA. In addition to analysing the thermogram results, the IDT, the temperature at which 50 % weight loss occurs ($T_{50 \text{ wt. \%}}$) and the residue yields at 700 °C were utilized as main factors in obtaining a better understanding of thermal stability. The results reveal that introducing silicone resin to acrylic resin enhances thermal stability due to the presence of Si–O–Si bonds in the silicone structure, which is inorganic in nature. However, embedding SiO₂ nanoparticles in the acrylic–silicone hybrid polymeric matrix reduces the chain mobility of the polymeric matrix near the surfaces of the dispersed nanoparticles, thus slightly lowering the observed IDT and $T_{50 \text{ wt. \%}}$ values.

In this study, the main functions desired in the developed coating system were the ability to withstand corrosion and the formation of an intact barrier layer to prohibit the penetration of the electrolyte into the coating film. In this regard, the EIS technique was employed to investigate the corrosion protection performance and barrier properties of the developed SiO₂ nanocomposite coating systems over a long period of exposure of the coated substrates to 3.5 % NaCl solution.

The EIS results, in the form of Bode and Nyquist plots, were analysed after 1 day, 30 days, 60 days and 90 days of immersion. In addition, the concept of breakpoint frequency was used to gain a better understanding of the changes occurring to the coating films over the exposure period. To demonstrate the vital role of the embedded SiO₂ nanoparticles, the performance of AS 0 coating system was examined as a reference sample. Enhancement of the anticorrosion properties was observed from the first day of immersion as the AS 0 coating system showed poor barrier properties, whereas, the coating films of all the SiO₂ nanocomposite coating systems demonstrated capacitive

behaviour. However, of the nanocomposite coatings, the AS 3 coating system, which was loaded with 3 wt. % of SiO₂ nanoparticles, exhibited the best barrier properties and continued to exhibit intact behaviour for up to 90 days of immersion. These findings are in strong agreement with the results of the breakpoint frequency tests, as a weak corrosion protection ability of AS 0 was observed as two regions under the Bode plot after the first day of immersion, i.e., both a resistive and a capacitive region. In contrast, the superiority the AS 3 nanocomposite coating system was further confirmed since this system exhibited the lowest breakpoint frequency value after 90 days of immersion.

CHAPTER 5: RESULTS AND DISCUSSION OF ZnO NANOCOMPOSITE COATING SYSTEMS

5.1 Introduction

In this chapter, the influence of embedding different loading ratios of ZnO nanoparticles of 1 wt. %, 3 wt. %, 5 wt. % and 8 wt. % on the overall performance of the hybrid acrylic–silicone polymeric matrix is presented. Properties including the surface morphology, wettability, transparency, thermal stability, adhesion, and corrosion protection ability were investigated, as was the multifunctionality of single-layer coating systems.

5.2 Surface Morphology of ZnO Nanocomposite Coating Systems

The influence of different loading ratios of ZnO nanoparticles on the surface morphology of the hybrid acrylic–silicone polymeric matrix was investigated by FESEM. The FESEM micrographs indicate the nature of the surface, nanoparticle distribution, phase distribution and surface failure.

Figure 5.1 shows FESEM micrographs of the prepared ZnO nanocomposite coating systems, specifically AZ 1, AZ 3, AZ 5 and AZ 8. Good dispersion of ZnO nanoparticles was observed in the hybrid polymeric matrix without any cracks or phase separation, which is in agreement with the FTIR results of the hybrid polymeric matrix reported in Chapter 4, and further confirms the efficacy of the curing process (Ananda Kumar & Sankara Narayanan, 2002).

Moreover, FESEM findings can provide evidence regarding the competence of the sonication process in developing a good nanoparticle dispersion in the polymeric matrix. Under the same conditions during the sonication process, increasing the loading ratio of the nanoparticles resulted in an increasing amount of nanoparticles in the unit area. Hence,

the ability of the particles to be attracted to each other was increased, thereby producing relatively larger agglomerated particles.

Of the prepared nanocomposite coating systems, the AZ 3 coating system with a ZnO nanoparticle loading ratio of 3 wt. % was found to have the most uniform dispersion of ZnO nanoparticles, as illustrated in Figure 5.1(b). When the loading ratio of the ZnO nanoparticles was greater than 3 wt. %, the agglomeration of the nanoparticles becomes increasingly pronounced, with relatively larger particles, as shown in Figures 5.1(c) and 5.1(d) for the AZ 5 and AZ 8 coating systems, respectively. This can be attributed to the fact that, as the number of the nanoparticles increases within the unit area, the distance between the nanoparticles decreases and that nanoparticles tend to agglomerate at high loading rates (Chen et al., 2015; Zhou et al., 2014).

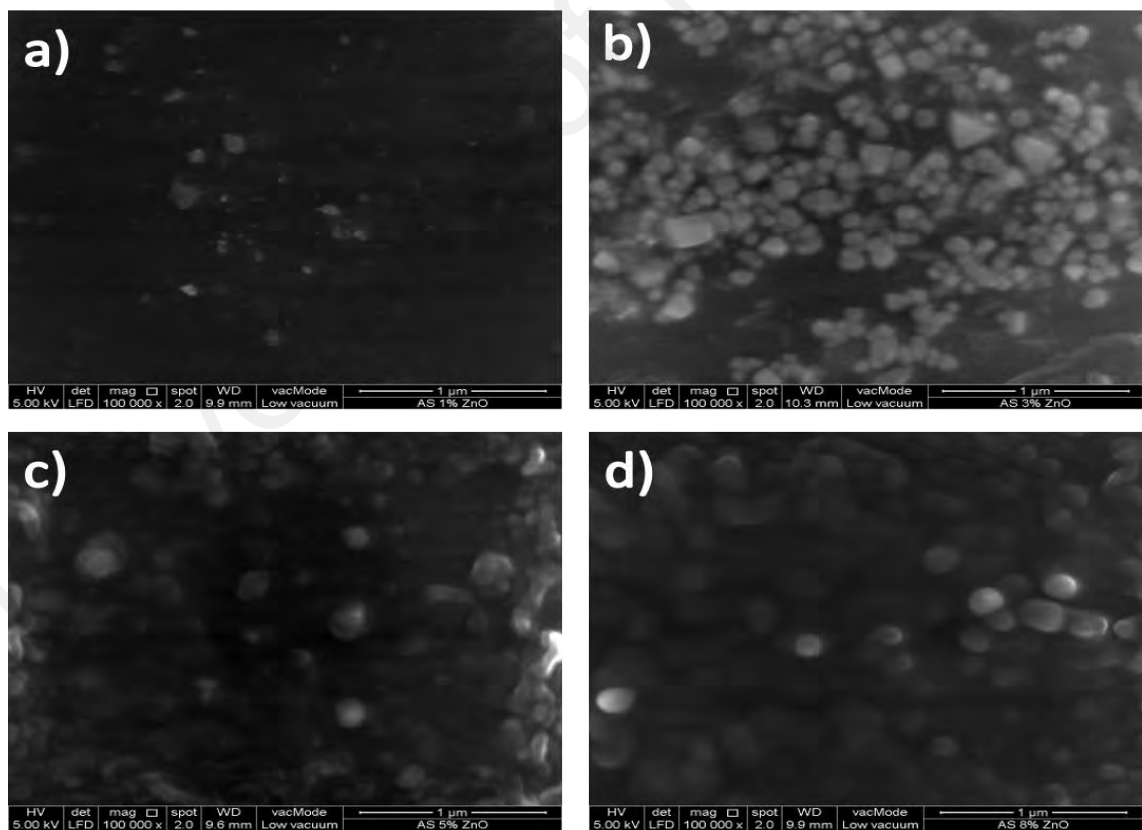


Figure 5.1: FESEM micrographs at scale 100 000× of magnification of (a) AZ 1, (b) AZ 3, (c) AZ 5, and (d) AZ 8 SiO₂ nanocomposite coating systems.

5.3 Contact Angle Measurements (CA)

In this study, water CA measurements were conducted to investigate the hydrophobic character of the developed ZnO nanocomposite coatings and to determine the influence of the embedded ZnO nanoparticles on the wettability of the resulting coated surfaces.

Table 5.1 lists the CA values recorded for the reference coating systems, including A 100 and AS 0, and the developed ZnO nanocomposite coating systems. As the effect of silicone resin in enhancing the water repellency of the neat acrylic coating system was discussed in the previous chapter, in this section, only the influence of ZnO nanoparticles at different loading ratios is presented.

Table 5.1: Contact angles values of A 100, AS 0 and all prepared ZnO nanocomposite coating systems

| System | Contact angle (θ°) |
|--------|----------------------------------|
| A 100 | 52.3 ± 0.9 |
| AS 0 | 78.5 ± 0.7 |
| AZ 1 | 91.4 ± 0.3 |
| AZ 3 | 95.6 ± 0.2 |
| AZ 5 | 94.1 ± 0.4 |
| AZ 8 | 92.0 ± 0.6 |

However, the CA results of the ZnO nanocomposite coatings further confirm that the incorporation of a second inorganic phase, in the form of nanoparticles, can significantly affect the usability of the resulting surface and enhance its hydrophobic properties. The most pronounced improvement in surface hydrophobicity was recorded after the addition of the 3 wt. % of ZnO nanofillers, AZ 3, which had the highest CA value at 95.6° .

As the loading ratio of ZnO nanoparticles exceeded 3 wt. %, no further increase in the CA values was observed. This can be attributed to the strong tendency of the nanoparticles

to form aggregates at high loading ratios, as noted above, which can result in a reduction in the surface roughness. Chen et al. (2015) discussed in detail the tendency of nanoparticles to agglomerate at high loading ratios. The authors reported that for each combination of nanoparticles and polymeric matrix, there is a specific loading ratio of nanoparticles that can be considered to be the optimum concentration, at which the nanoparticles can significantly affect the surface morphology of the resulting surfaces. Exceeding this critical concentration results in the nanoparticles gathering more at the bottom of the coating film rather than the surface area, therefore affecting the bulk properties more than the surface properties (Chen et al., 2015).

5.4 UV-Visible Spectroscopy

Nanocomposite films were prepared from the transparent acrylic–silicone polymeric matrix and ZnO nanoparticles. The UV–Vis transmittance spectra of the neat acrylic and acrylic/silicone were ~90 % at 550 nm, as shown in Figure. 5.2. As the loading ratio of ZnO nanoparticle increases, the transmittance percentage generally decreases. The nanocomposite AZ1 exhibits light transmission in the range of 88 % to 85 % in the visible wavelength ranges. The characteristic peak at ~350 nm demonstrates that the UV-light shielding efficiency of AZ1 is about 21 %. According to Li et al., the UV spectra of zinc oxide nanoparticles consist of UV light absorption and light scattering, which contribute to their high-UV shielding efficiency (Li et al., 2006). The characteristic peaks ranging from 300–400 nm also confirm the formation of the nanocomposite (Quadri et al., 2017).

Hence, as the loading ratio of ZnO nanoparticles increased in the nanocomposite coating systems, the transparency of AZ3, AZ5 and AZ8 at 550 nm decreased to 79 %, 66 % and 43 %, respectively. However, they continued to exhibit UV-light shielding properties despite their poor transparency. Huang and Hsieh (2010) studied the optical properties of the ZnO/acrylic nanocomposite and found that the reduced light

transmission intensity in a composite sample is influenced by the size and dispersion of nanoparticles in the system (Huang & Hsieh, 2010).

As observed in the UV-Vis spectra, AZ8 exhibits a very high UV-light shielding efficiency of 97 % at 350 nm, followed by AZ5 and AZ3, which are 78 % and 47 %, respectively. Therefore, the lower visible light transmittance of nanocomposites compared to neat acrylic and acrylic/silicone is mainly influenced by the scattering of agglomerated ZnO nanoparticles, whereas the increased UV-light shielding efficiency are attributed to the natural optical properties of ZnO nanoparticles. This also indicates that ZnO nanoparticles are a promising material for future use as an optical enhancing agent.

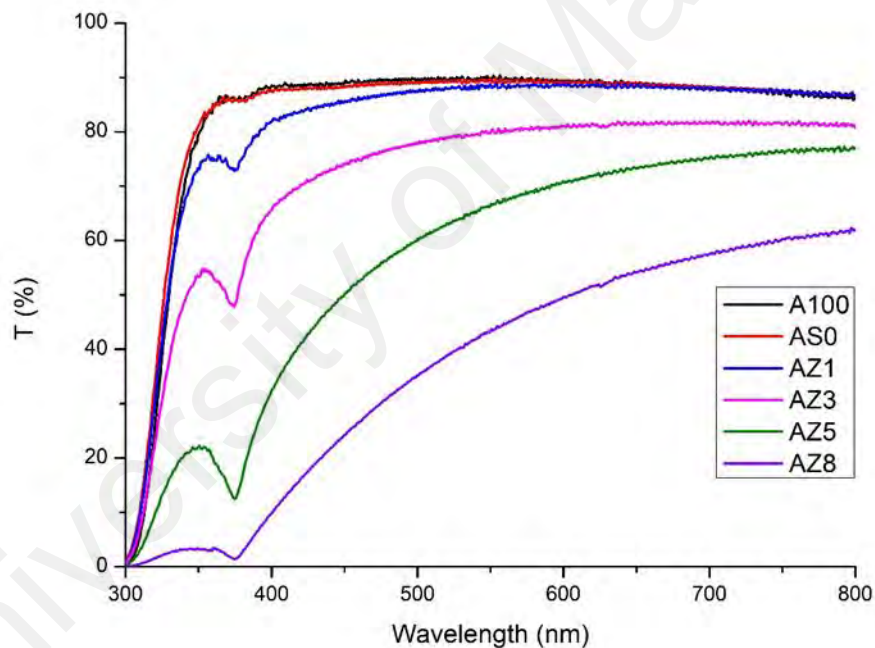


Figure 5.2: UV-Vis spectra for A 100, AS 0 and all prepared ZnO nanocomposite coating systems.

5.5 Cross Hatch Test (CHT)

To develop an intact coating system with superior overall performance, the adhesion of the coating film to the metallic substrate is considered to be an essential factor. Therefore, in this study, the adhesion properties of the ZnO nanocomposite coating

systems were investigated by CHT and the collected results were analysed with respect to the ASTM D3359 method B standard.

Figure 5.3 shows the CHT results as images for the reference coating systems, namely, A 100 and AS 0, and the developed ZnO nanocomposite coating systems. As discussed above, both the A 100 and AS 0 coating systems showed superior adhesion performance and were found to have a 5B grade ranking.

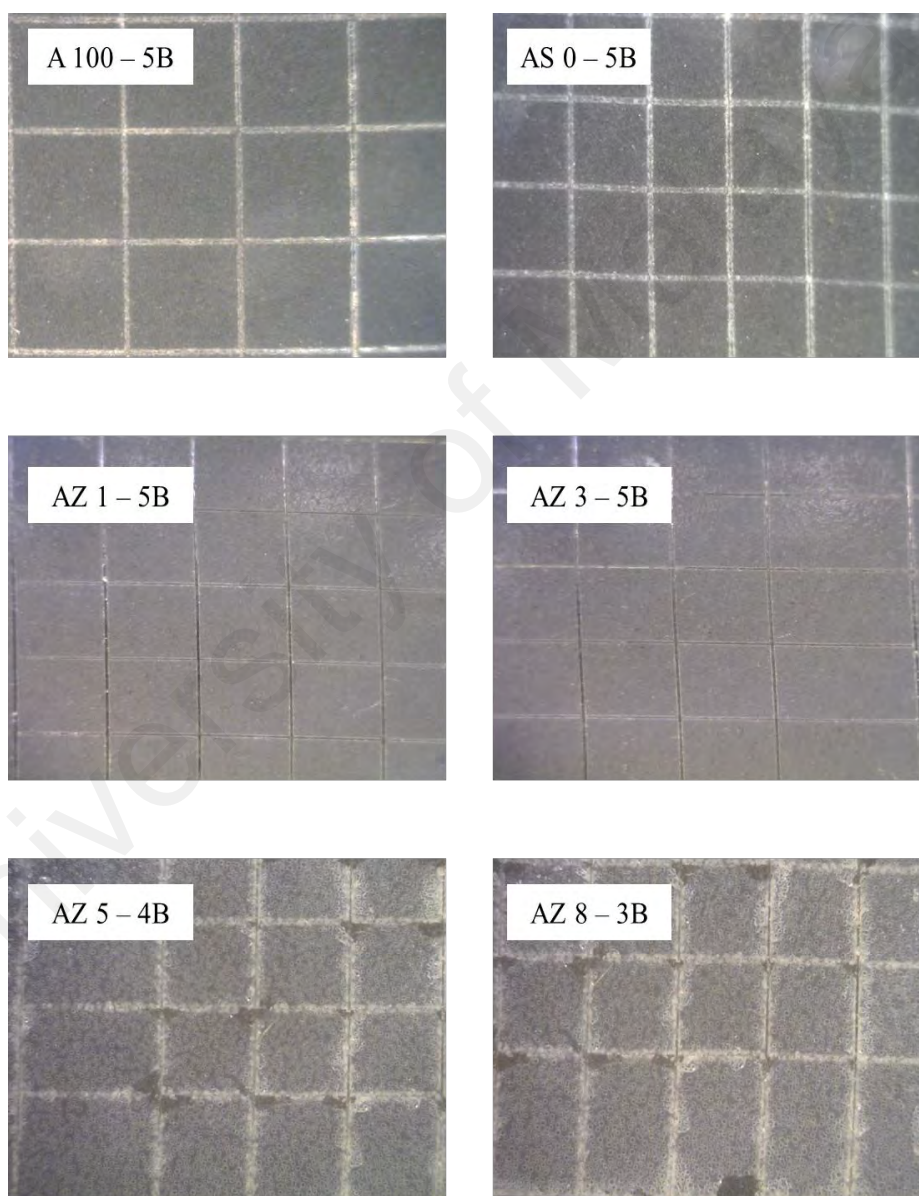


Figure 5.3: Results of cross hatch test for A 100, AS 0 and all prepared ZnO nanocomposite coating systems.

The incorporation of 1 wt. % and 3 wt. % loading rates of ZnO nanoparticles within the hybrid polymeric matrix of acrylic and silicone resins did not result in any significant changes in the adhesion behaviour of the coating films. CHT results with 5B adhesion grade were recorded for both the AZ 1 and AZ 3 coating systems in which there were cuts with smooth edges without any loss of adhesion or detachment of the lattice squares. These observations further confirm the proper dispersion of the ZnO nanoparticles and the good curing state of the applied coating films. On the other hand, it is noted that as the ZnO nanoparticles loading ratio increased above 3 wt. %, a slight decrease in the adhesion properties was observed for the AZ 5 coating system and a more obvious decrease for the AZ 8 coating system where grades 4B and 3B surfaces were observed after performing the CHT, respectively. This could be attributed to the tendency of the nanoparticles to agglomerate and affect the bulk properties of the coating film rather than the surface properties, which is in strong agreement with the FESEM and CA findings.

5.6 Thermogravimetric Analysis (TGA)

The thermal stability and decomposition temperatures of the prepared ZnO nanocomposite coating systems were evaluated by TGA analysis. Figures 5.4-5.7 show thermograms of the ZnO nanocomposite coating systems and Table 5.2 lists the obtained IDT values, the temperature at which 50 % weight loss occurred ($T_{50 \text{ wt. \%}}$) and the residue yields at 700 °C. However, to distinguish the changes in the thermal stability that occurred due to the incorporation with ZnO nanoparticles, Table 5.2 also shows the values of reference samples A 100 and AS 0.

As the effect of silicone resin in enhancing the thermal stability of the neat acrylic coating system was discussed in the previous chapter, this section reports only the role of ZnO nanoparticles at different loading rates in altering the thermal stability of the hybrid acrylic–silicone polymeric matrix.

From Figures 5.4–5.7, it is interesting to note that the ZnO nanocomposite coating systems showed the same four main stages of decomposition as was observed in the AS 0 coating system. The first stage is correlated to the loss of the residual butyl acetate and the second stage to the degradation of the intercalation agent, NCO resin. Decomposition of the acrylic resin was observed at the third stage of degradation and the fourth stage in the TGA curve is observed when the temperature exceeds 500 °C. This indicates the loss of silicone resin, which is known to have an ignition temperature above 400 °C.

Different loading rates of the ZnO nanoparticles led to some changes in the temperature ranges at each stage of degradation, and the data in Table 5.2 was utilized to investigate these changes. It is interesting to note that none of the loading ratios of the ZnO nanoparticles resulted in any significant change to the IDT and T_{50 wt. %} values, for which the maximum difference was less than 10 °C in all the developed systems, as compared to the AS 0 coating systems.

However, a slight decrease in the thermal stability could be observed, which could be attributed to the influence of the nanoparticles in reducing the chain mobility of the polymeric matrix near the surfaces of the dispersed nanoparticles (Ma & Zhang, 2009; Tomić et al., 2014).

Table 5.2: The parameters gained from TGA studies of A 100, AS 0 and all prepared ZnO nanocomposite coating systems.

| System | IDT (°C) | T _{50 wt. %} (°C) | Residue at 700 °C |
|--------|----------|----------------------------|-------------------|
| A 100 | 290 | 380 | 1.52 |
| AS 0 | 295 | 411 | 15.28 |
| AZ 1 | 287 | 405 | 16.78 |
| AZ 3 | 290 | 408 | 15.39 |
| AZ 5 | 286 | 404 | 15.02 |
| AZ 8 | 288 | 405 | 15.88 |

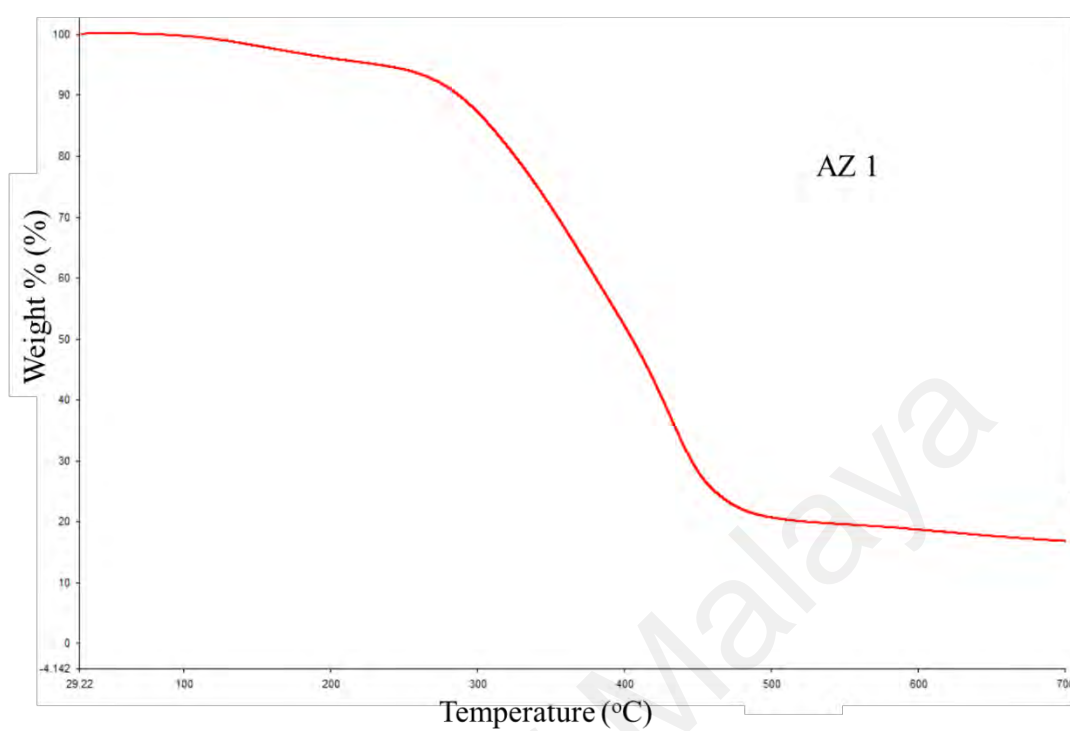


Figure 5.4: TGA thermogram of AZ 1 coating system.

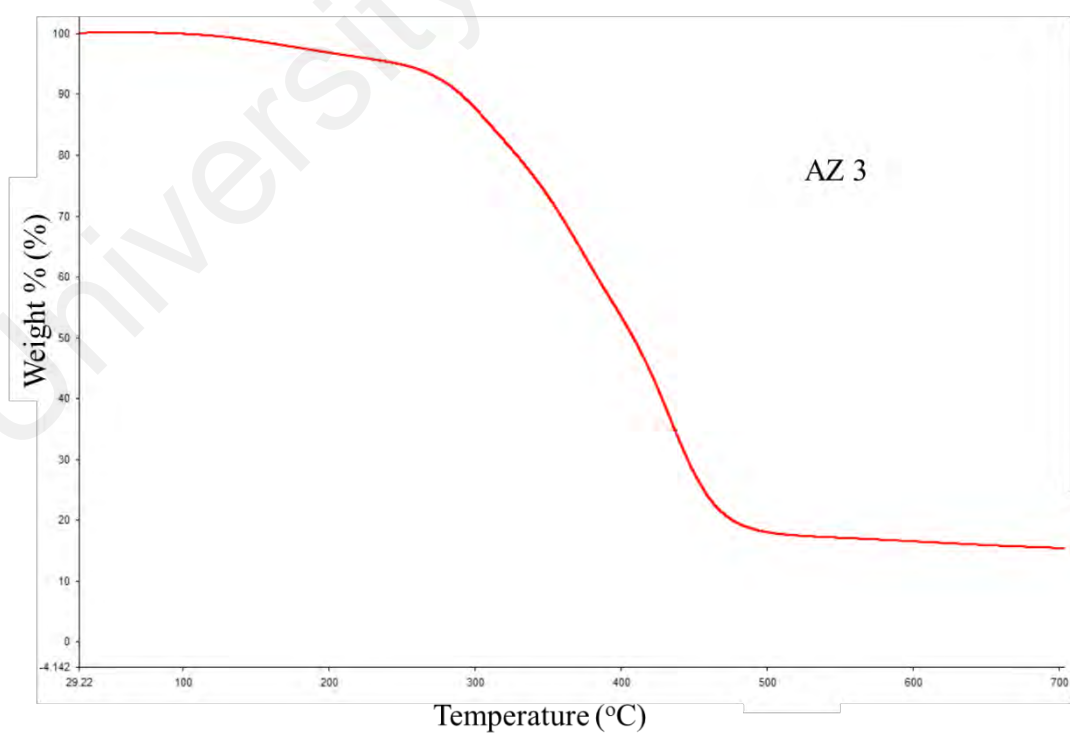


Figure 5.5: TGA thermogram of AZ 3 coating system.

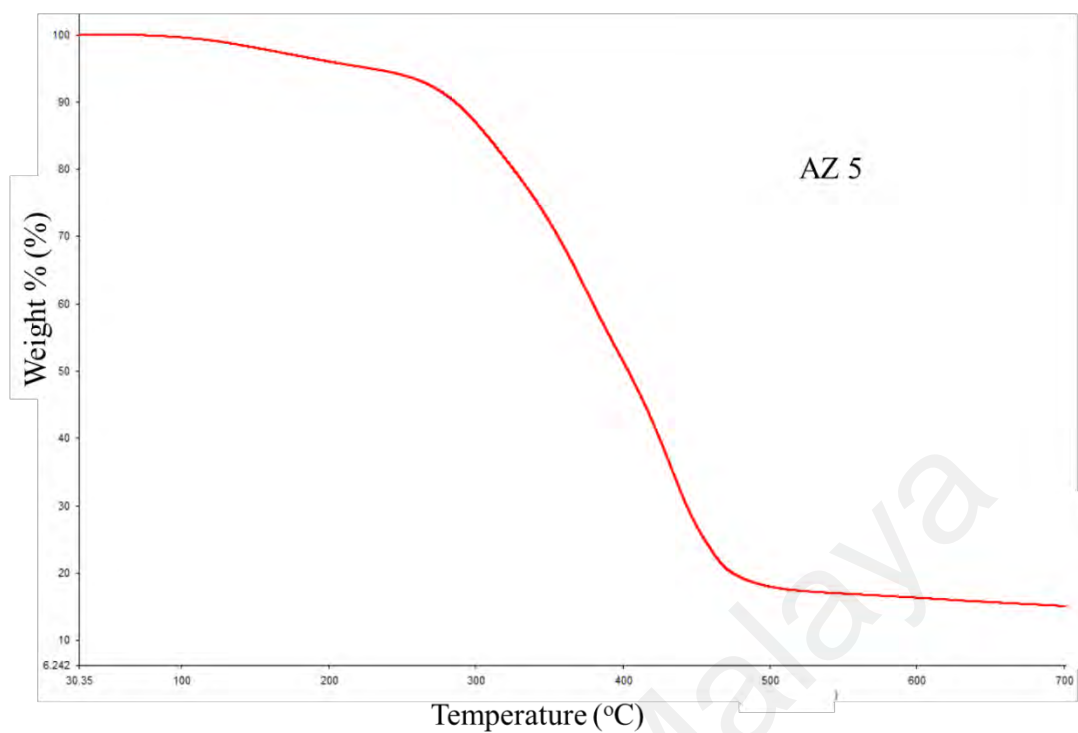


Figure 5.6: TGA thermogram of AZ 5 coating system.

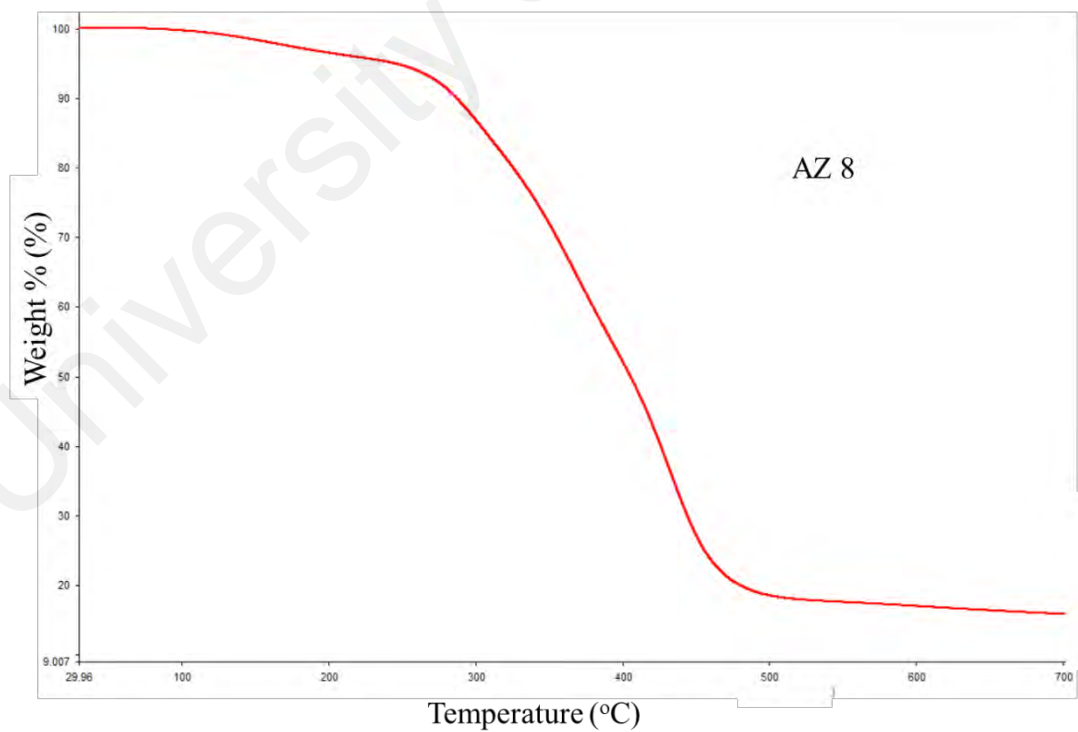


Figure 5.7: TGA thermogram of AZ 8 coating system.

5.7 Electrochemical impedance spectroscopy (EIS)

The EIS technique was employed to investigate the electrochemical response and anti-corrosion properties of the developed ZnO nanocomposite coating systems. EIS measurements were conducted periodically for 60 days after exposing the coated substrates to 3.5 % NaCl solution and the results are shown graphically in Nyquist and Bode plots. In the same manner, as noted in Chapter 4, three different equivalent-circuit models were utilized to obtain the best numerical fitting during the study periods, as shown in Figure 4.11.

To investigate the vital role of the utilized ZnO nanoparticles in enhancing the barrier properties of the fabricated acrylic–silicone polymeric matrix, and to determine the influence of changing the nanoparticles loading rates on the corrosion protection performance of the coating film, EIS results are reported for all the prepared ZnO nanocomposite coating systems after one day, 30 days, and 60 days of immersion. Since as the electrochemical response of the AS 0 coating system was investigated in detail and reported in Chapter 4, only the electrochemical responses of the ZnO nanocomposite coating systems are discussed in this chapter. However, some of the AS 0 coating system results are reported for comparison.

The EIS results for the ZnO nanocomposite coating systems after one day of immersion are shown in the form of a Bode plot in Figure 5.8 and Nyquist plots in Figures 5.9 and 5.10. From these EIS results, we can see the vital role of the embedded ZnO nanoparticles in enhancing the corrosion protection performance of the hybrid acrylic–silicone polymeric matrix after just one day of exposure compared to that of the AS 0 coating system after the same immersion period.

The Bode plot of the AS 0 coating system shows an obvious bend in the low-frequency region in Figure 5.8 and a full semi-circle in the Nyquist plot in Figure 5.9, which is clear evidence that the electrolyte has begun penetrating the coating film and the corrosion

reaction has been initiated. The electrochemical behaviour of the AS 0 system at this level of degradation can be perfectly described with model B of the equivalent circuit. In contrast, at this stage of immersion, the EIS results of the AZ 1, AZ3 and AZ 5 nanocomposite coating systems exhibit a capacitive behaviour in a straight line with a slope of -1 in the Bode plot in Figure 5.8, and one capacitive loop in the Nyquist plot in Figure 5.10, which is clear evidence of the efficiency of these coating systems in preventing any electrolyte penetration and complete isolation of the metal surface from the surrounding corrosion medium. As there was no charge transfer or diffusion of the electrolyte within the coating films, model A of the equivalent circuit was used to fit the EIS diagrams at this stage of immersion.

However, increasing the loading ratio of the ZnO nanoparticles to 8 wt. % did not further enhance the corrosion protection ability of the acrylic–silicone polymeric matrix. As illustrated in Figure 5.8, the Bode plot of the AZ 8 coating system exhibited a bend at the low-frequency range and, as shown in Figure 5.10, there is a full semi-circle in its Nyquist plot. This indicates the initiation of electrolyte permeation into the coating–substrate interface through the polymer coating layer, which leads to the initiation of the corrosion reaction. Therefore, model B of the equivalent circuit was used to explain the electrochemical behaviour of this coating system (Mostafaei & Nasirpour, 2014; Rezaei et al., 2010; Yuan et al., 2015).

The numerical fitting of EIS data was carried out via the employment of the proposed different equivalent circuit models and the obtained values after 1 day of immersion time are tabulated in Tables 5.3 and 5.4.

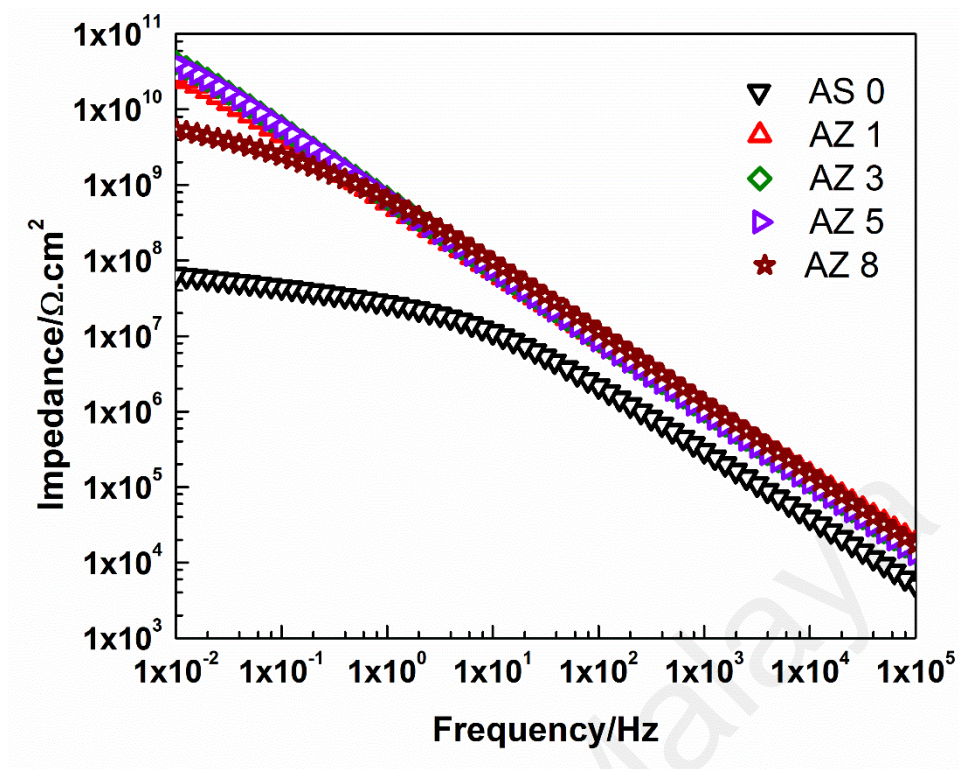


Figure 5.8: Bode plots for AS 0 and all prepared ZnO nanocomposite coating systems after 1 day of immersion time.

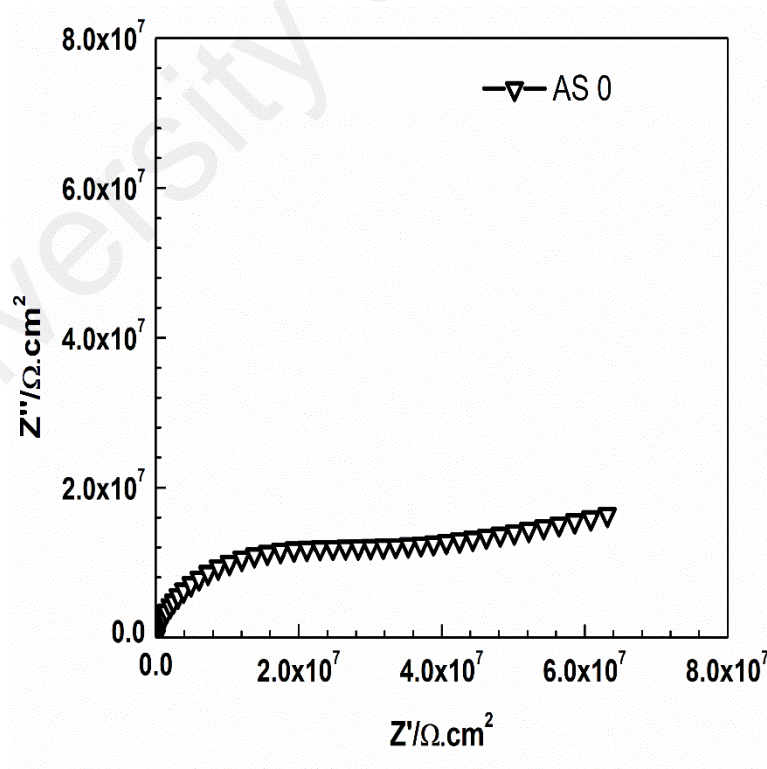


Figure 5.9: Nyquist plot for AS 0 coating system after 1 day of immersion time.

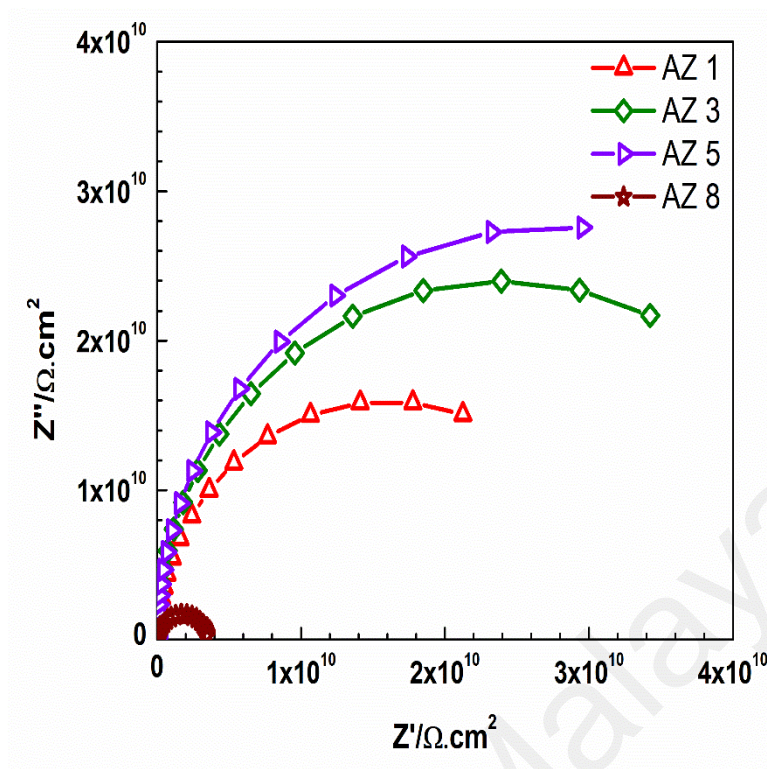


Figure 5.10: Nyquist plots for all prepared ZnO nanocomposite coating systems after 1 day of immersion time.

Table 5.3: The resistance values from EIS studies, along with the equivalent circuit model used to fit the data, of AS 0 and all prepared ZnO nanocomposite coating systems after 1 day of immersion time.

| System | $R_{po} (\Omega \text{ cm}^2)$ | $R_{ct} (\Omega \text{ cm}^2)$ | $R_{diff} (\Omega \text{ cm}^2)$ | Model used |
|--------|----------------------------------|--------------------------------|----------------------------------|------------|
| AS 0 | $(7.94 \pm 0.06) \times 10^6$ | $(2.38 \pm 0.02) \times 10^9$ | - | B |
| AZ 1 | $(4.75 \pm 0.13) \times 10^{10}$ | - | - | A |
| AZ 3 | $(8.2 \pm 0.02) \times 10^{10}$ | - | - | A |
| AZ 5 | $(6.99 \pm 0.01) \times 10^{10}$ | - | - | A |
| AZ 8 | $(2.43 \pm 0.07) \times 10^5$ | $(2.74 \pm 0.09) \times 10^9$ | - | B |

Table 5.4: The constant phase element values from EIS studies of AS 0 and all prepared ZnO nanocomposite coating systems after 1 day of immersion time.

| System | CPR _{po} | | CPE _{dl} | | CPE _{diff} | |
|--------|--|------|--|------|--|---|
| | Y ₀ (Ω ⁻¹ cm ² s ⁿ) | n | Y ₀ (Ω ⁻¹ cm ² s ⁿ) | n | Y ₀ (Ω ⁻¹ cm ² s ⁿ) | n |
| AS 0 | $(1.31 \pm 0.01) \times 10^{-9}$ | 0.89 | $(1.98 \pm 0.10) \times 10^{-8}$ | 0.14 | - | - |
| AZ 1 | $(3.25 \pm 0.02) \times 10^{-10}$ | 0.90 | - | - | - | - |
| AZ 3 | $(2.63 \pm 0.01) \times 10^{-10}$ | 0.94 | - | - | - | - |
| AZ 5 | $(2.58 \pm 0.01) \times 10^{-10}$ | 0.94 | - | - | - | - |
| AZ 8 | $(6.56 \pm 0.08) \times 10^{-10}$ | 0.32 | $(1.88 \pm 0.04) \times 10^{-10}$ | 0.95 | - | - |

As the exposure time elapsed, the EIS graphics of the AS 0 coating system in Figures 5.11 and 5.12 after 30 days of immersion reveal the poor ability of the coating film to withstand corrosion action and the significant degradation of the barrier properties, as discussed in the previous chapter. It is important to note that, in contrast, no significant changes were observed for the acrylic–silicone coating system, AS 0, after 60 days of immersion, as shown in Figures 5.16 and 5.17.

On the other hand, 1 wt. % of ZnO nanoparticles was insufficient to fill all the pores in the polymeric matrix. Therefore, the Bode plot of the AZ 1 coating system, shown in Figure 5.11, shows an obvious bend in the low-frequency region and its Nyquist plot in Figure 5.13 shows a full semi-circle and was fitted to model B of the equivalent circuit. However, of the developed ZnO nanocomposite coating systems, the application of the AZ 3 coating system remarkably enhanced the anti-corrosion performance even after 30 days of immersion, with no significant changes observed in the Bode and Nyquist plots shown in Figures 5.11 and 5.14, respectively. It is also highlighted that, after 30 days of immersion, model A of the equivalent circuit remained suitable for fitting the EIS data of the AZ 3 coating system, which further confirms the durability of this system against corrosive agent penetration.

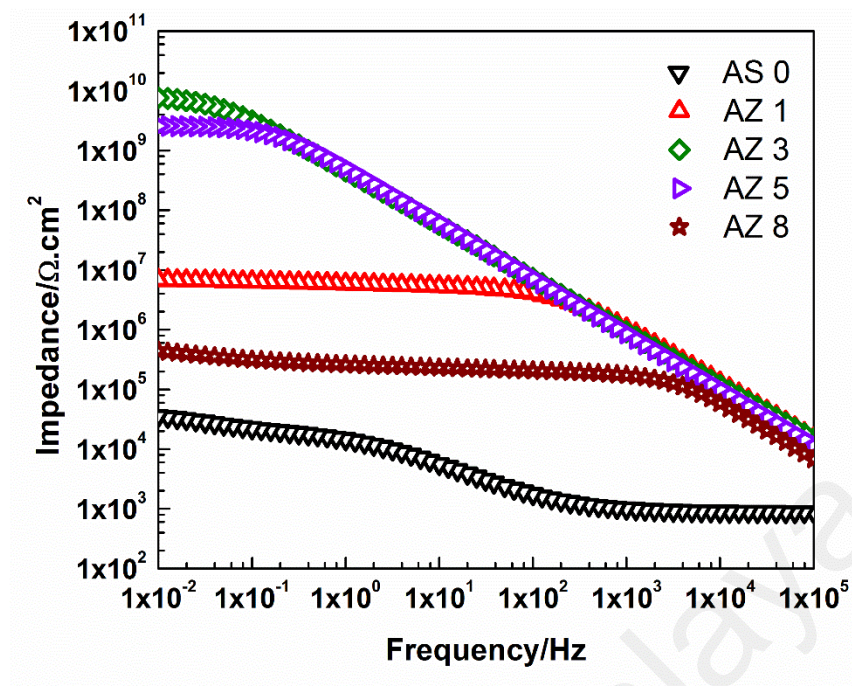


Figure 5.11: Bode plots for AS 0 and all prepared ZnO nanocomposite coating systems after 30 days of immersion time.

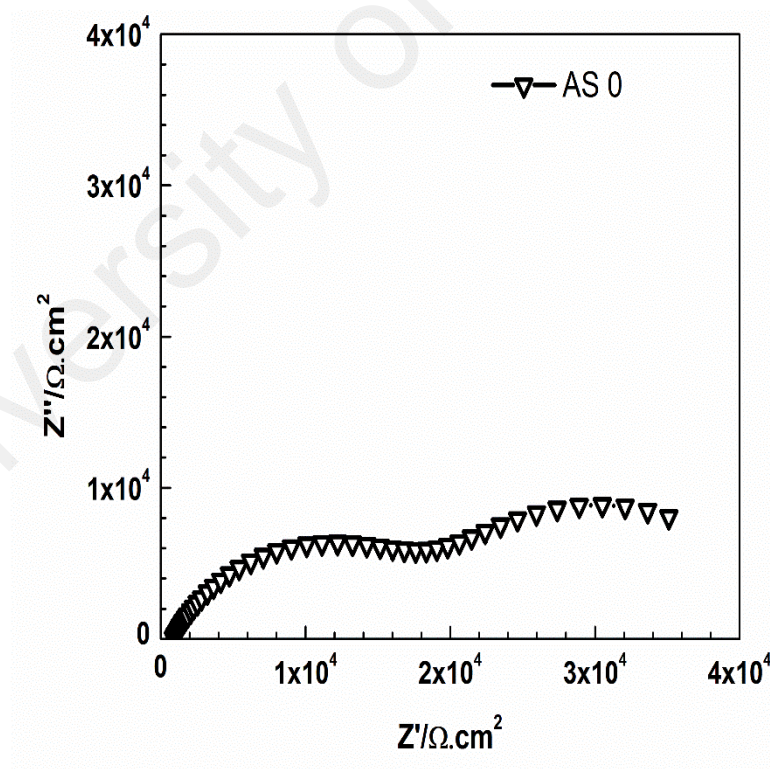


Figure 5.12: Nyquist plot for AS 0 coating system after 30 days of immersion time.

Due to the tendency of the nanoparticles to aggregate at high loading ratios, no further improvement was observed for ZnO nanoparticle loading ratios exceeding 3 wt. %. This was confirmed by the EIS results of the AZ 5 coating system, whose Bode plot in Figure 5.11 shows a slight bend in the low-frequency range, and a full semi-circle in the Nyquist plot in Figure 5.14. Model B of the equivalent circuit was employed to fit the EIS data of the AZ 5 coating system at this stage of immersion. However, the nanoparticles agglomeration effect was more obvious with the utilization of the AZ 8 coating system, as its EIS graphs were fitted with model C of the equivalent circuit and show a Bode plot with two time constants and a Nyquist plot with two full semi-circles, as illustrated in Figures 5.11 and 5.15, respectively. Moreover, the values of all parameters that have been obtained by fitting the EIS data according to the proposed equivalent circuit models after 30 days of immersion time are tabulated in Tables 5.5 and 5.6.

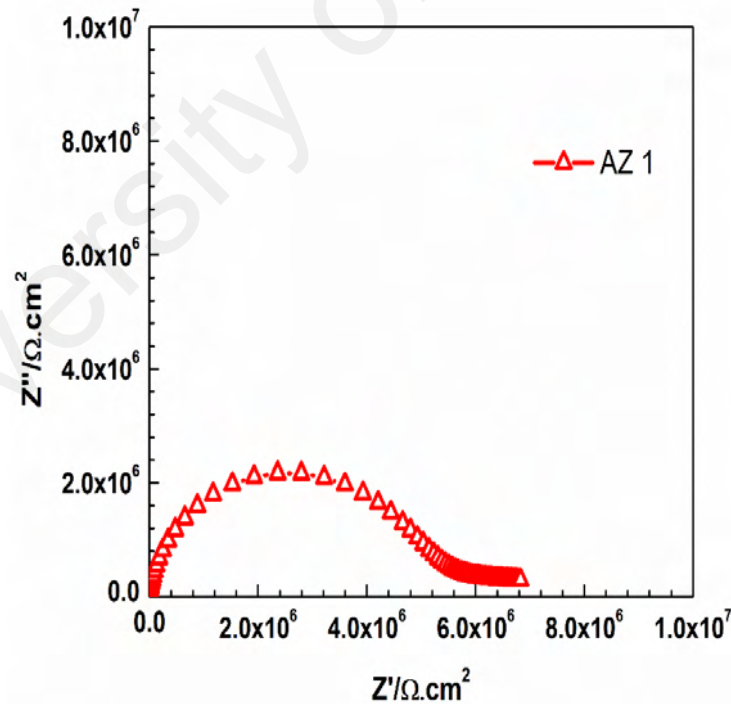


Figure 5.13: Nyquist plot for AZ 1 nanocomposite coating system after 30 days of immersion time.

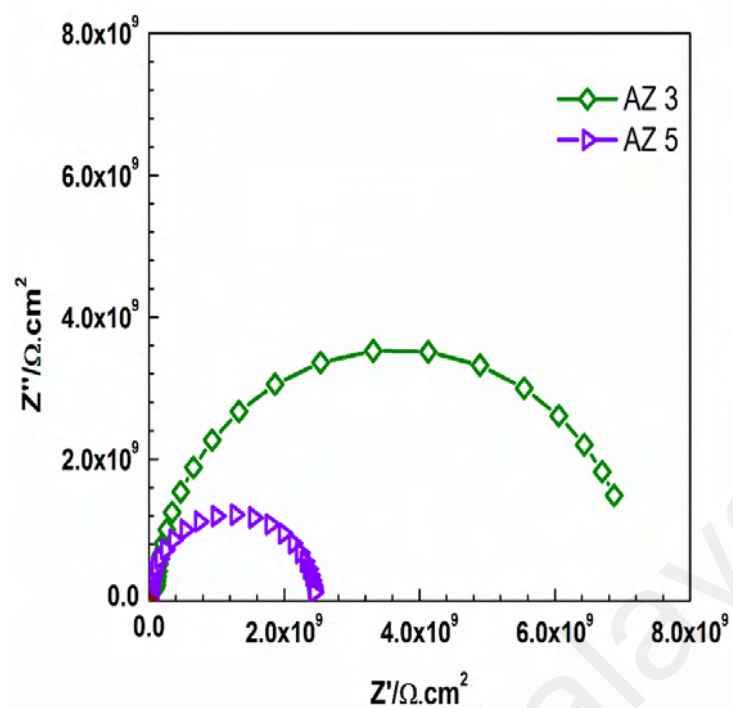


Figure 5.14: Nyquist plots for AZ 3 and AZ 5 nanocomposite coating system after 30 days of immersion time.

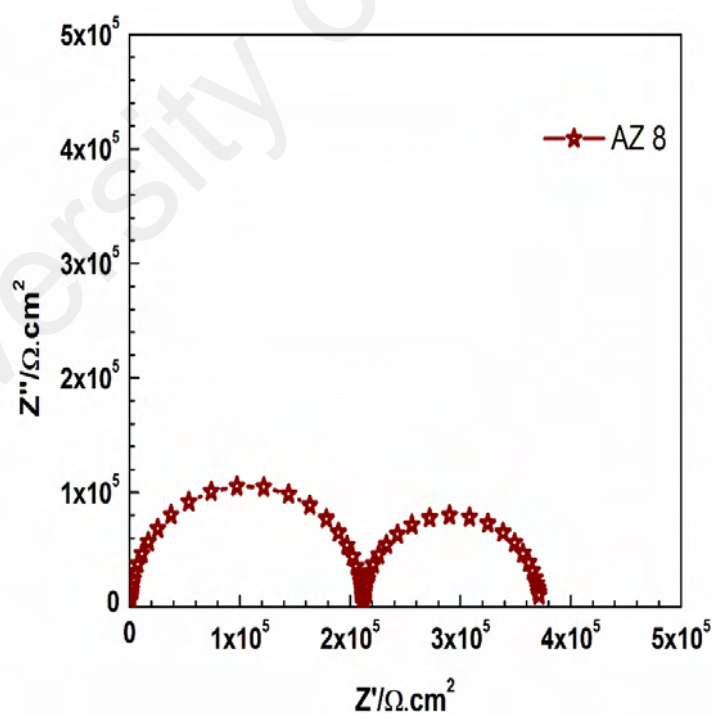


Figure 5.15: Nyquist plot for AZ 8 nanocomposite coating system after 30 days of immersion time.

Table 5.5: The resistance values from EIS studies, along with the equivalent circuit model used to fit the data, of AS 0 and all prepared ZnO nanocomposite coating systems after 30 days of immersion time.

| System | $R_{po} (\Omega \text{ cm}^2)$ | $R_{ct} (\Omega \text{ cm}^2)$ | $R_{diff} (\Omega \text{ cm}^2)$ | Model used |
|--------|--------------------------------|--------------------------------|----------------------------------|------------|
| AS 0 | $(1.37 \pm 0.13) \times 10^3$ | $(1.27 \pm 0.09) \times 10^5$ | $(1.04 \pm 0.06) \times 10^4$ | C |
| AZ 1 | $(2.26 \pm 0.05) \times 10^6$ | $(1.24 \pm 0.07) \times 10^7$ | - | B |
| AZ 3 | $(8.26 \pm 0.01) \times 10^9$ | - | - | A |
| AZ 5 | $(7.33 \pm 0.06) \times 10^7$ | $(2.71 \pm 0.01) \times 10^9$ | - | B |
| AZ 8 | $(1.12 \pm 0.07) \times 10^4$ | $(6.69 \pm 0.06) \times 10^5$ | $(6.32 \pm 0.05) \times 10^6$ | C |

Table 5.6: The constant phase element values from EIS studies of AS 0 and all prepared ZnO nanocomposite coating systems after 30 days of immersion time.

| System | CPR_{po} | | CPE_{dl} | | CPE_{diff} | |
|--------|---|------|---|------|---|------|
| | $Y_0 (\Omega^{-1} \text{ cm}^{-2} \text{ s}^n)$ | n | $Y_0 (\Omega^{-1} \text{ cm}^{-2} \text{ s}^n)$ | n | $Y_0 (\Omega^{-1} \text{ cm}^{-2} \text{ s}^n)$ | n |
| AS 0 | $(3.82 \pm 0.15) \times 10^{-5}$ | 0.20 | $(2.90 \pm 0.09) \times 10^{-6}$ | 0.85 | $(6.40 \pm 0.07) \times 10^{-6}$ | 0.18 |
| AZ 1 | $(2.44 \pm 0.02) \times 10^{-10}$ | 0.93 | $(3.64 \pm 0.09) \times 10^{-9}$ | 0.76 | - | - |
| AZ 3 | $(4.20 \pm 0.02) \times 10^{-10}$ | 0.89 | - | - | - | - |
| AZ 5 | $(2.46 \pm 0.09) \times 10^{-10}$ | 0.96 | $(1.62 \pm 0.08) \times 10^{-10}$ | 0.73 | - | - |
| AZ 8 | $(2.26 \pm 0.04) \times 10^{-6}$ | 0.73 | $(2.83 \pm 0.14) \times 10^{-10}$ | 0.99 | $(4.20 \pm 0.02) \times 10^{-6}$ | 0.67 |

To further confirm the ability of the ZnO nanoparticles to enhance the corrosion protection properties of polymeric coating systems and to determine the best loading ratio for achieving superior barrier properties, the EIS studies were extended to 60 days of exposure to corrosive 3.5 % NaCl solution.

Of the prepared ZnO nanocomposite coating systems, only the AZ 3 coating system showed significant stability over all exposure periods and maintained its capacitive behaviour with a straight line with a slope of -1 in the Bode plot, Figure 5.16, and one

capacitive loop in the Nyquist plot, Figure 5.19. Moreover, it is interesting to note that the EIS results of the AZ 3 coating systems at this stage of immersion could still be fitted with model A of the equivalent circuit, which is clear evidence that the AZ 3 coating film continued to act as a perfect capacitor even after this long-term of exposure.

Many researchers have studied the incorporation of ZnO with different types of polymeric matrices and reached the conclusion that utilizing ZnO nanoparticles leads to remarkable improvements in the anticorrosion properties of the developed coating systems via zigzagging of the diffusion pathways, which forces the corrosive agents to travel longer distances to reach the substrate surface. Thus, a longer lifetime of the coating system is realized before any replacements or maintenance is required (Mostafaei & Nasirpour, 2014; Ramezanzadeh et al., 2011; Shi et al., 2009).

In contrast, all other prepared ZnO nanocomposite coating systems have shown less capability to withstand extended exposure to a corrosive environment. These coating systems exhibited Bode plots with two time constants, as shown in Figure 5.16, and Nyquist plots with two semi-circles, as illustrated in Figures 5.18 and 5.20, respectively, and were best fitted with model C of the equivalent circuit.

Furthermore, the numerical fitting of EIS data after 60 days of immersion time was according to the proposed equivalent circuit models and the obtained values were tabulated in Tables 5.7 and 5.8.

The stability of the developed ZnO coating films over the entire immersion period was investigated via the breakpoint frequency concept, which is defined as the frequency at the -45° phase angle. With this method, the area under the Bode plot (impedance and phase angle as a function of the frequency) can be utilized to classify the state of the coating system as either intact (when the full area under the Bode plot is recognized as a capacitive region) or undergoing corrosion (when the area under Bode plot is a

combination of capacitive and resistive regions). Also, if coating failure occurs, only a resistive region can be observed.

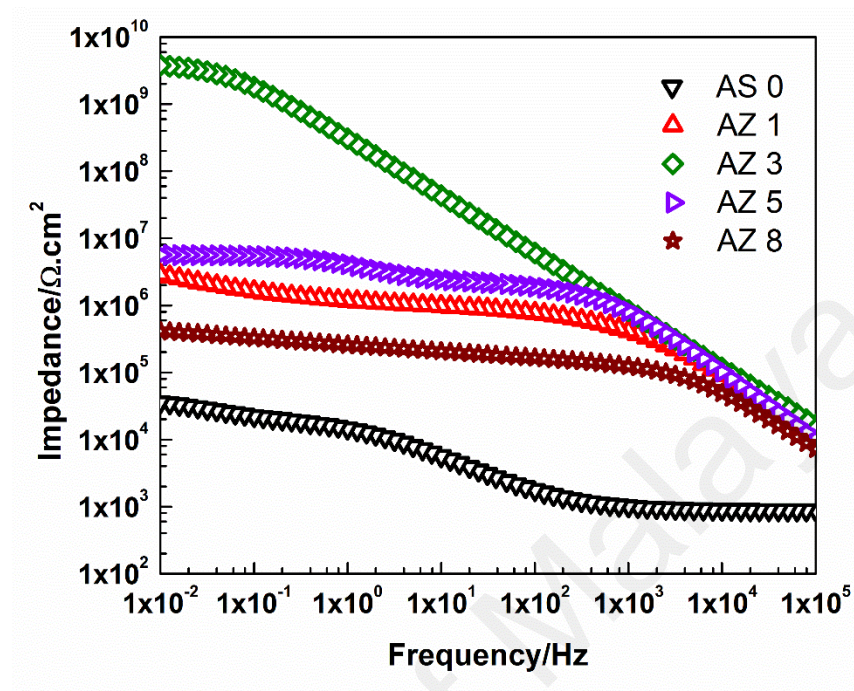


Figure 5.16: Bode plots for AS 0 and all prepared ZnO nanocomposite coating systems after 60 days of immersion time.

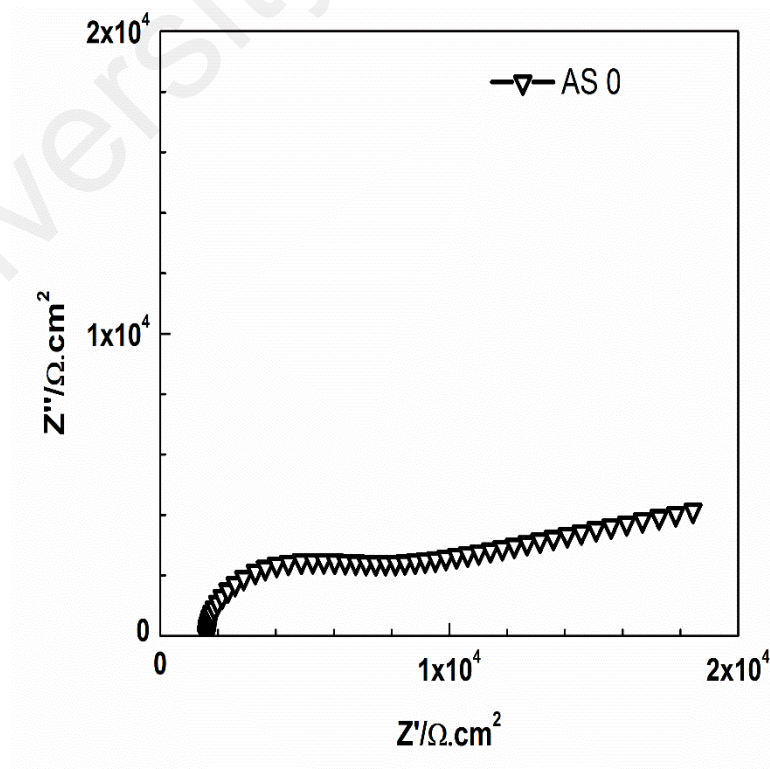


Figure 5.17: Nyquist plot for AS 0 coating system after 60 days of immersion time.

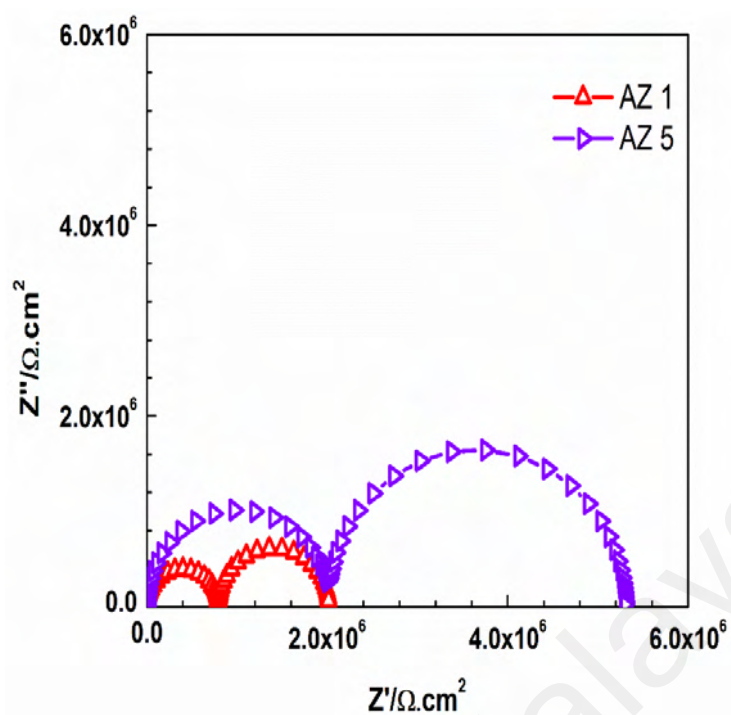


Figure 5.18: Nyquist plots for AZ 1 and AZ 5 nanocomposite coating systems after 60 days of immersion time.

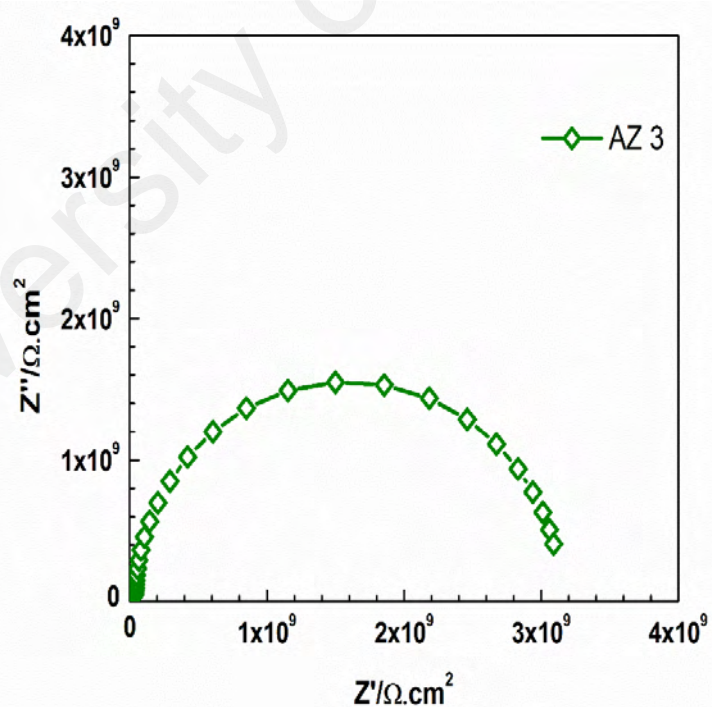


Figure 5.19: Nyquist plot for AZ 3 nanocomposite coating system after 60 days of immersion time.

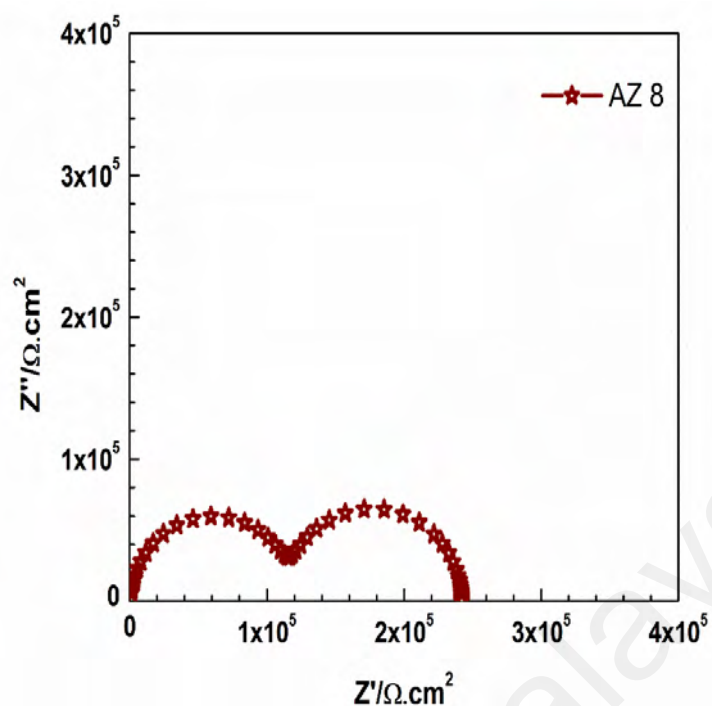


Figure 5.20: Nyquist plot for AZ 8 nanocomposite coating system after 60 days of immersion time.

Table 5.7: The resistance values from EIS studies, along with the equivalent circuit model used to fit the data, of AS 0 and all prepared ZnO nanocomposite coating systems after 60 days of immersion time.

| System | $R_{po} (\Omega \text{ cm}^2)$ | $R_{ct} (\Omega \text{ cm}^2)$ | $R_{diff} (\Omega \text{ cm}^2)$ | Model used |
|--------|--------------------------------|--------------------------------|----------------------------------|------------|
| AS 0 | $(6.38 \pm 0.04) \times 10^3$ | $(7.80 \pm 0.02) \times 10^4$ | $(1.49 \pm 0.05) \times 10^5$ | C |
| AZ 1 | $(2.29 \pm 0.06) \times 10^5$ | $(7.57 \pm 0.03) \times 10^5$ | $(4.40 \pm 0.08) \times 10^7$ | C |
| AZ 3 | $(4.01 \pm 0.01) \times 10^9$ | - | - | A |
| AZ 5 | $(1.37 \pm 0.02) \times 10^6$ | $(1.04 \pm 0.05) \times 10^6$ | $(3.27 \pm 0.03) \times 10^6$ | C |
| AZ 8 | $(8.82 \pm 0.01) \times 10^3$ | $(3.40 \pm 0.12) \times 10^7$ | $(1.01 \pm 0.10) \times 10^7$ | C |

Table 5.8: The constant phase element values from EIS studies of AS 0 and all prepared ZnO nanocomposite coating systems after 60 days of immersion time.

| System | CPR _{po} | | CPE _{dl} | | CPE _{diff} | |
|--------|---|------|---|------|---|------|
| | Y ₀ (Ω ⁻¹ cm ⁻² s ⁿ) | n | Y ₀ (Ω ⁻¹ cm ⁻² s ⁿ) | n | Y ₀ (Ω ⁻¹ cm ⁻² s ⁿ) | n |
| AS 0 | (1.63 ± 0.08) × 10 ⁻⁶ | 0.71 | (5.90 ± 0.03) × 10 ⁻⁷ | 0.94 | (8.33 ± 0.01) × 10 ⁻¹¹ | 0.87 |
| AZ 1 | (1.72 ± 0.01) × 10 ⁻¹⁰ | 0.99 | (2.11 ± 0.08) × 10 ⁻⁸ | 0.53 | (1.58 ± 0.09) × 10 ⁻⁶ | 0.44 |
| AZ 3 | (6.68 ± 0.04) × 10 ⁻¹⁰ | 0.91 | - | - | - | - |
| AZ 5 | (1.52 ± 0.09) × 10 ⁻¹⁰ | 1.00 | (1.06 ± 0.05) × 10 ⁻⁸ | 0.66 | (6.08 ± 0.07) × 10 ⁻⁸ | 0.82 |
| AZ 8 | (3.67 ± 0.01) × 10 ⁻⁶ | 0.95 | (5.37 ± 0.04) × 10 ⁻¹⁰ | 0.95 | (7.32 ± 0.01) × 10 ⁻⁸ | 0.13 |

Therefore, to obtain a full understanding and detailed information about the electrochemical behaviour, barrier properties, coating delamination, and electrolyte diffusion state, it is helpful to observe and analyse the changes to these regions in each coating system over the entire immersion period.

With the incorporation of different loading ratios of ZnO nanoparticles within the acrylic–silicone hybrid polymeric matrix, the AZ 1, AZ 3 and AZ 5 coating systems were observed to be intact, as the whole area under the Bode plot was recognized as a capacitive region after one day of immersion, as shown in the Bode plots of Figures 5.21(a), 5.22(a), and 5.23(a) of the AZ 1, AZ 3 and AZ 5 coating systems, respectively. However, the area under the Bode plot of the AZ 8 coating system, shown in Figure 5.24(a), was divided into capacitive and resistive regions, which reveals the poor barrier properties of the coating layer, and which was in strong agreement with the FESEM and EIS results.

The EIS studies extended to 60 days of immersion, as shown in Figures 5.21(b), 5.22(b), 5.23(b) and 5.24(b), are reported to obtain Bode plots (impedance and phase angle as a function of the frequency) of the AZ 1, AZ 3, AZ 5 and AZ 8 coating systems, respectively, after 60 days of immersion. It is interesting to note that the incorporation of ZnO nanoparticles within the acrylic–silicone polymeric matrix enhanced the barrier

properties, as lower breakpoint frequencies were observed. Therefore, relatively smaller resistive regions at the low-frequency domain were observed and larger capacitive regions in the AS 0 coating system.

However, it is worth mentioning that utilizing the breakpoint frequency method further confirms that AZ 3 coating system could demonstrate the best corrosion protection performance and can provide the best barrier properties among all developed ZnO nanocomposite coatings.

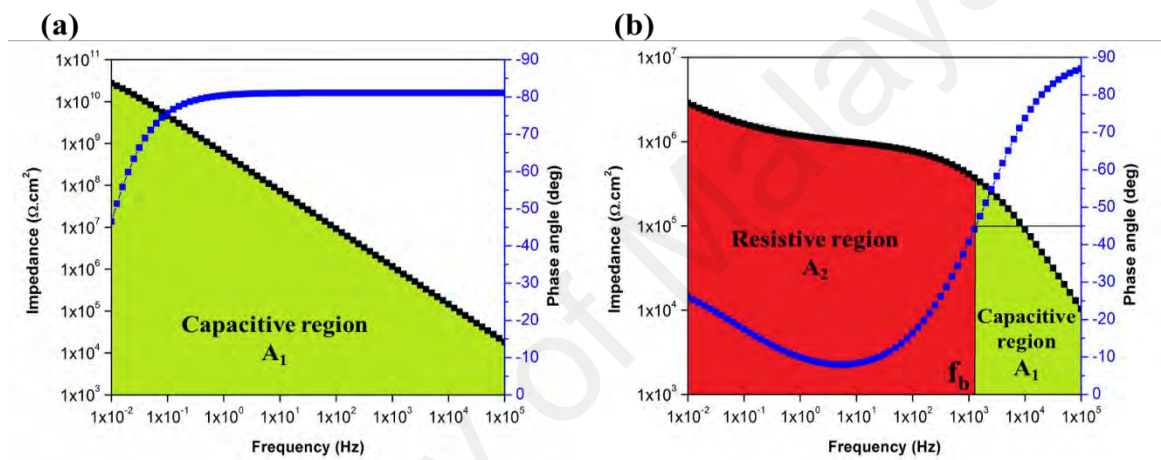


Figure 5.21: Bode plots of AZ 1 coating system after (a) 1 day and (b) 60 days of immersion along with the determining the breakpoint frequency and the corresponding capacitive (A1) and resistive (A2) regions.

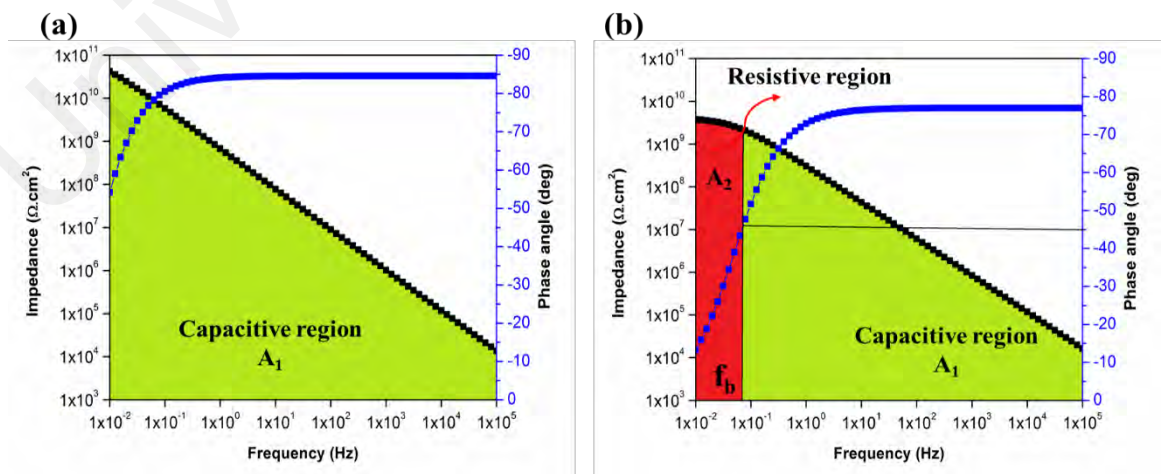


Figure 5.22: Bode plots of AZ 3 coating system after (a) 1 day and (b) 60 days of immersion along with the determining the breakpoint frequency and the corresponding capacitive (A1) and resistive (A2) regions.

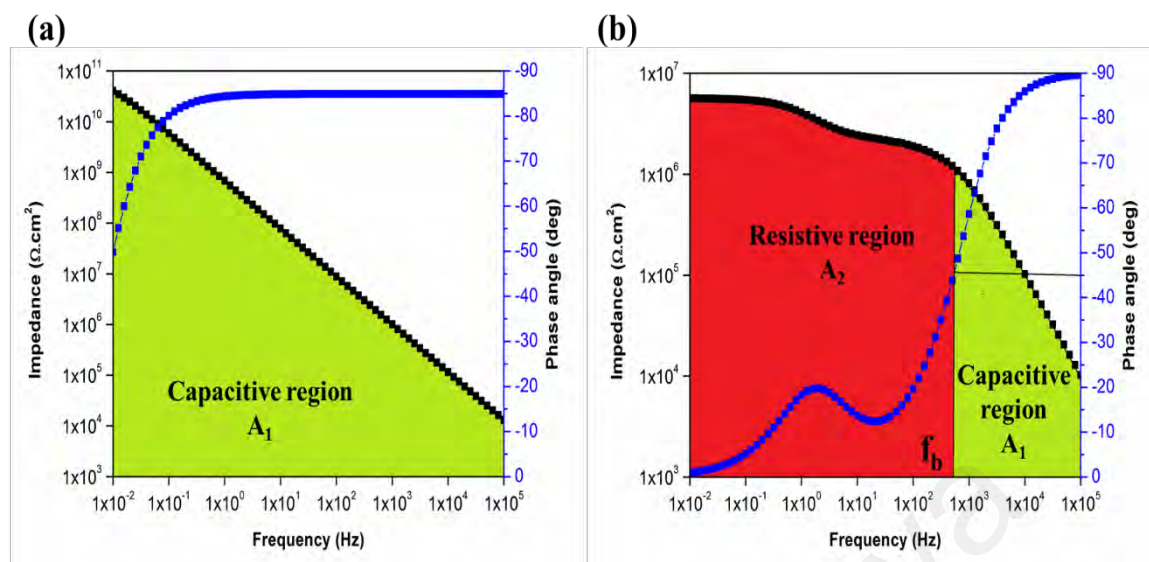


Figure 5.23: Bode plots of AZ 5 coating system after (a) 1 day and (b) 60 days of immersion along with the determining the breakpoint frequency and the corresponding capacitive (A1) and resistive (A2) regions.

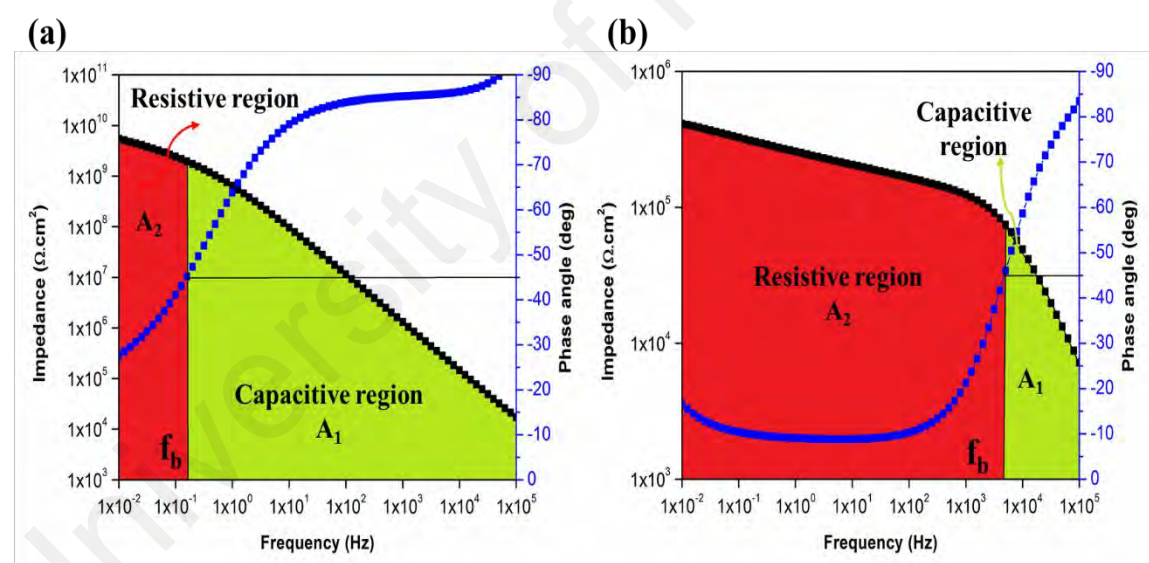


Figure 5.24: Bode plots of AZ 8 coating system after (a) 1 day and (b) 60 days of immersion along with the determining the breakpoint frequency and the corresponding capacitive (A1) and resistive (A2) regions.

5.8 Summary

In this section, the influence of different ZnO nanoparticle loading ratios, specifically 1 wt. %, 3 wt. %, 5 wt. % and 8 wt. %, on the overall performance of the hybrid acrylic silicone polymeric matrix was investigated. Furthermore, to confirm the achievement of multifunctionality with the presence of ZnO nanoparticles, various characterization techniques were conducted to evaluate different properties of the developed nanocomposite coating films.

FESEM was utilized to examine the dispersion state of the ZnO nanoparticles in the polymeric matrix. The wettability of the developed coated surfaces was investigated via the CA measurements, the optical characteristics were determined by UV–Vis spectroscopy and the thermal stability of the developed ZnO nanocomposite coatings was examined by the TGA technique. Moreover, the adhesion properties and the corrosion protection performance of the developed ZnO nanocomposite coating systems were evaluated via CHT and the EIS technique, respectively.

Using the FESEM method, the surface morphology of the developed ZnO nanoparticles was obtained. The obtained micrographs confirm the effectiveness of the sonication process in developing a good level of nanoparticle dispersion in the polymeric matrix. However, increasing the loading ratio of the nanoparticles resulted in increasing the amount of nanoparticles in the unit area. Hence, the attraction of the particles to each other was increased, thereby generating relatively larger agglomerated particles. The best dispersion state of ZnO nanoparticles within the hybrid polymeric matrix was observed in the AZ 3 nanocomposite coating system.

From our investigations of the wettability of developed coated surfaces, it is interesting to note that ZnO nanoparticles at different loading ratios were capable of transforming the wettability of the coated surface from its hydrophilicity characteristic, as observed in the AS 0 coating system, to hydrophilic surfaces for the applied ZnO nanocomposite

coating systems. The most pronounced improvement regarding the surface hydrophobicity was observed with the addition of 3 wt. % of ZnO nanofillers, AZ 3, yielding the highest CA value at 95.6°. It is noted that the CA results are in complete agreement with the FESEM finding, whereby the best dispersion of nanoparticles observed for the AZ 3 coating systems yielded the highest CA.

The optical properties of the developed ZnO nanocomposite coating systems were investigated via UV-Vis measurements. As the AS 0 coating system is characterized by transparency, the influence of embedding different loading ratios of ZnO nanoparticles was studied. The obtained light transmittance spectra reveal a reduction in the transmittance percentage as the loading ratio of ZnO nanoparticles increased. These observations were in complete agreement with the FESEM finding, whereby a high loading ratio of ZnO nanoparticles led to larger agglomerated particles, hence, a lower visible light transmittance of the nanocomposites due to the scattering of agglomerated ZnO nanoparticles. Even so, it was also interesting to note that utilizing ZnO nanoparticles enables the coating film to gain a high-UV shielding efficiency, which increased as the loading ratio of ZnO nanoparticles increased.

The studies were extended to evaluate the adhesion properties of the developed ZnO nanocomposite coating systems via the utilization of CHT. Rather than SiO₂ nanoparticles, the adhesion of the coating film to the steel substrate was altered by the loading ratio of ZnO nanoparticles. When using 1 wt. % and 3 wt. % ZnO nanoparticles, i.e., AZ 1 and AZ 3, respectively, excellent adhesion properties at 5B grade was demonstrated, according to the ASTM D3359 standard. A slight decrease in the adhesion properties was observed for the AZ 5 coating system and a more obvious decrease for the AZ 8 coating system with grades 4B and 3B surfaces were observed after performing the CHT, respectively. This is explained by the fact that ZnO nanoparticles tend to agglomerate at high loading ratios, thereby affecting the bulk properties of the coating

film rather than its surface properties, which is in strong agreement with the FESEM and CA findings.

The thermal stability of all prepared ZnO nanocomposite coatings were determined via TGA. In addition to analysing the resulting thermograms, the IDT, the temperature at which 50 % weight loss occurs ($T_{50 \text{ wt. \%}}$), and the residue yields at 700 °C were utilized as main factors enabling a better understanding of thermal stability.

The ZnO nanocomposite coating systems showed the same four main stages of decomposition as those observed in the AS 0 coating system. This means that reinforcing the hybrid acrylic–silicone polymeric matrix with different loading ratios of ZnO nanoparticles did not significantly alter the good thermal stability obtained by crosslinking the silicone resin to the acrylic resin. Furthermore, it is noted that none of the ZnO nanoparticle loading ratios used resulted in significant changes to the IDT or $T_{50 \text{ wt. \%}}$ values.

EIS technique was utilized to study the corrosion protection performance over a long period of exposing the coated surfaces to 3.5 % NaCl solution up to 60 days. The obtained results in the form of Bode and Nyquist plots, and also the breakpoint frequency concept were utilized and discussed in order to better understand the changes to the coating films after the incorporation with different loading rates of ZnO nanoparticles. Enhancement of the anticorrosion properties was observed from the first day of immersion time, as the AS 0 coating system showed poor barrier properties, whereas the coating films of the ZnO nanocomposite coating systems demonstrated capacitive behaviour. Of the nanocomposite coatings, the AZ 3 coating system, which was loaded with 3 wt. % of ZnO nanoparticles, exhibited the best barrier properties and remained intact even after 60 days of immersion. The intact condition of the AZ 3 coating system was further confirmed by the results of the breakpoint frequency method, in which it exhibited the lowest

breakpoint frequency value, as well as a correspondingly smallest resistive region and largest capacitive region in the Bode plot after 60 days of immersion.

University of Malaya

CHAPTER 6: RESULTS AND DISCUSSIONS OF EPOXY-SOYBEAN OIL MODIFIED ORGANIC COATING SYSTEM

6.1 Introduction

Since organic coatings are characterised by a number of drawbacks that limit their usage in the coating industries, many research attempts have been made to enhance the performance of such systems. The incorporation of a second inorganic phase in the form of metallic base pigments in the nanoscale domain is one such method, which was discussed in the previous chapters. However, the need to develop a totally organic coating system characterized by intact behaviour and superior barrier properties remains an attractive goal.

In that regard, in this section, the potential for achieving a multifunctional coating system with fully organic components was investigated by introducing different loading ratios of E and ESO into the acrylic–silicone polymeric blend. The properties investigated include the chemical structure, wettability, transparency, thermal stability, adhesion, and corrosion protection ability, as well as the multifunctionality of single-layer coating systems.

6.2 Fourier Transform Infrared Spectroscopy (FTIR)

Figure 6.1 shows the FTIR spectra employed to analyse the structure of the developed epoxy–soybean oil modified coating systems. In the figure, a very weak broad peak can be observed at $\sim 3400\text{ cm}^{-1}$, which indicates an overlay of the O-H bond absorption with an N-H stretching vibration absorption. The presence of N-H bonds is due to the association of isocyanate as curing agent. The peaks at 2928 cm^{-1} and 2856 cm^{-1} are attributed to the stretching vibration of the C-H bonds, which vary with the concentration of ESO in the polymeric blend. Moreover, the peaks at 1690 cm^{-1} and 1726 cm^{-1} are attributed to the hydrogen bonded carbonyl group and the stretching vibration absorption

of the free carbonyl group, respectively, due to the presence of the -C=O bond in the isocyanate functional group. The peaks at 1520 cm^{-1} and 1242 cm^{-1} correspond to the -N-O stretching and C-O bond between the isocyanate and epoxide groups, respectively, which clearly show the crosslinking reaction in the polymer matrices. Also, the broad peak from $\sim 1000\text{ cm}^{-1}$ to 1133 cm^{-1} is likely due to the overlaying of the C-O stretching and C-C-O stretching between the acrylate and oxirane groups, respectively. It has been reported that the reduction of oxirane oxygen in the epoxide group is influenced by the acrylate group (Behera & Banthia, 2008). Note that the amount of ESO in the polymeric matrices varied only by up to 10 wt. %. Thus, the intensity frequency of the oxirane group was very weak.

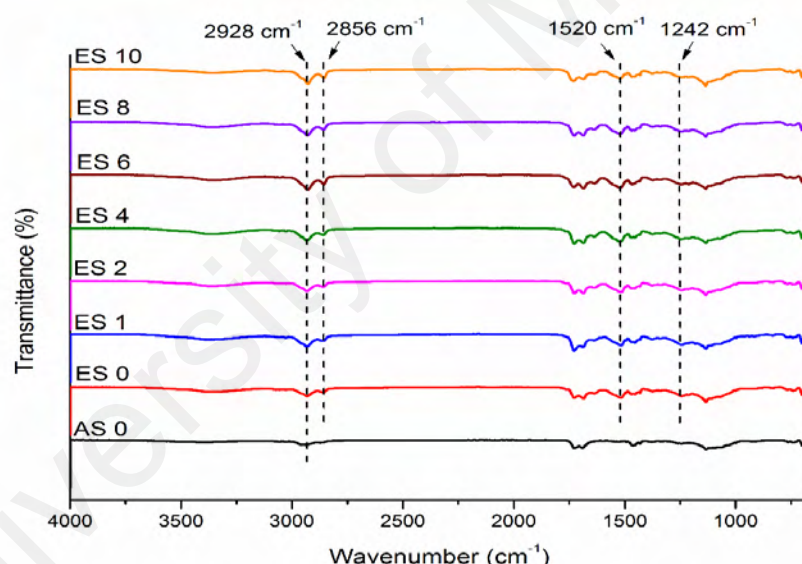


Figure 6.1: FTIR spectra of AS 0 and all prepared epoxy-epoxidized soybean oil hybrid organic coating systems.

6.3 Contact angle measurements (CA)

As the chemical composition of the coating system is considered to be a critical factor that determines the wettability of the resulting coated surface, it is essential to study the influence of the introduction of E and ESO to the hybrid acrylic-silicone polymeric matrix on the wettability of the coating surfaces. In that regard, Table 6.1 shows the CA

values of the A 100 and AS 0 coating systems along with the corresponding CA findings of the modified epoxy–soybean oil modified coating systems. It is also important to report the CA result of the neat epoxy coating system, referred to as the E 100 coating system, to determine the effect of the E on the CA values.

As discussed previously, the incorporation of silicone resin with acrylic resin yielded a significant improvement in the CA values from 52.3° for the A 100 coating system to 78.5° for the AS 0 coating system. However, the CA value of the neat epoxy coating system, E 100, which known for its hydrophilic character, was found to be 65.0°. This can explain the reduction that occurs in the CA value after the introduction of 10 wt. % of E into the acrylic–silicone polymeric matrix, as the CA value of the ES 0 coating system listed in Table 6.1 was 65.0°. It is interesting to note that as the amount of ESO increases, which leads to a decrease in the amount of E, the CA value gradually increases. In addition, the highest CA value of the results in Table 6.1 is 81.7°, with the utilization of ES 10, which contains 10 wt. % of ESO without any E. This can be explained by the hydrophobic nature of soybean oil (Chen et al., 2011).

Table 6.1: Contact angles values of A 100, AS 0 and all epoxy-epoxidized soybean oil hybrid organic coating systems.

| System | Contact angle (θ°) |
|--------|----------------------------------|
| A 100 | 52.3 \pm 0.9 |
| AS 0 | 78.5 \pm 0.7 |
| ES 0 | 65.0 \pm 0.1 |
| ES 1 | 67.8 \pm 0.8 |
| ES 2 | 71.4 \pm 0.4 |
| ES 4 | 73.3 \pm 0.3 |
| ES 6 | 74.9 \pm 0.6 |
| ES 8 | 77.5 \pm 0.4 |
| ES 10 | 81.7 \pm 0.7 |

6.4 UV-Visible Spectroscopy

Figure 6.2 shows the UV-Vis test results for the cured neat acrylic (A100), acrylic/silicone (AS 0), AS/epoxy (ES 0) and ESO composite films. According to these curves, neat acrylic, acrylic/silicone and ES 0 have a high degree of transparency of about 90 % at 550 nm. This shows that the addition of a thermosetting epoxy copolymer does not affect the transparency of the hybrid acrylic/silicon polymer. Meanwhile, the presence of ESO in the polymer matrices decreased the light transmission of the composite films. The composites of ES 1, ES 2 and ES 4 show 84 %, 83 % and 81 % light transmittance, respectively, uniformly in the visible range. At this range, it is suggested that the hybrid acrylic/silicon with epoxy and ESO is suitable for any optical applications. Ni et al. (2010) reported that the presence of soybean oil in polyurethane coating system is promising and meets the requirements of industrial applications. (Ni et al., 2010). Also, Bastürk et al. (2013) reported very interesting properties on a UV-curable acrylated epoxidized-soybean oil based organic-inorganic hybrid coating. (Baştürk et al., 2013).

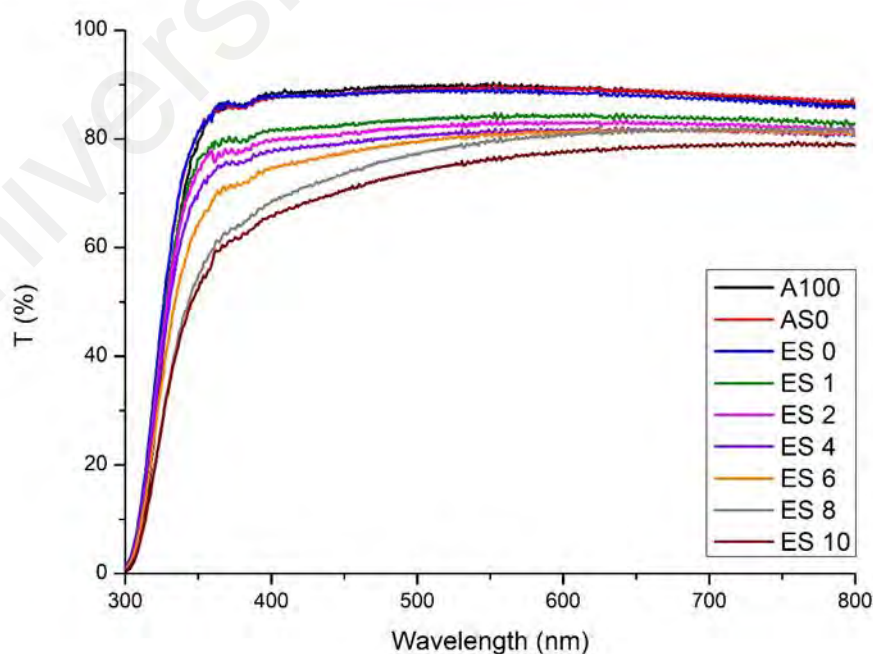


Figure 6.2: UV-Vis spectra for A 100, AS 0 and all prepared epoxy-epoxidized soybean oil hybrid organic coating systems.

As observed in the UV-Vis spectra, the light transmittance of ES 6, ES 8 and ES 10 declined and show an obvious deflation curve starting at ~550 nm. This result shows the loss of homogeneity within the distribution matrices, which leads to a high degree of translucency in the ESO as a co-stabilizer that synergizes the coating system. It can be concluded that the optical properties of the hybrid polymeric coating systems reached an optimum degree of transparency at 4 wt. % of ESO concentration.

6.5 Cross Hatch Test (CHT)

The adhesion properties of the prepared epoxy–soybean oil modified coating systems were investigated by CHT and the obtained results were analysed with respect to the ASTM D3359 method B grade standard.

All the CHT results are presented in the form of images for the reference coating systems, A 100 and AS 0, and the developed modified epoxy–soybean oil modified coating systems, as shown in Figure 6.3. As discussed above, both the A 100 and AS 0 coating systems have shown superior adhesion performance and been given a 5B ranking. For the ES 0 coating system, it was observed that the introduction of 10 wt. % of E in the hybrid polymeric blend of acrylic and silicone resins showed no change regarding the excellent film adherence to the steel substrate. No loss of adhesion was observed in the ES 0 coating system, and an adhesion behaviour of 5B grade was determined. Furthermore, a 5B classification for the adhesion properties was determined for all the epoxy–soybean oil modified coating systems, with no observed loss of adhesion and 0 % coating removal from the steel substrate was recorded. The CHT findings reveal the effectiveness of the coating systems without sacrificing the excellent adhesion properties of the base acrylic–silicone hybrid blend. Also, it further confirms the good curing state of the coating films even after the introduction of various loading ratios of E and ESO at room temperature.

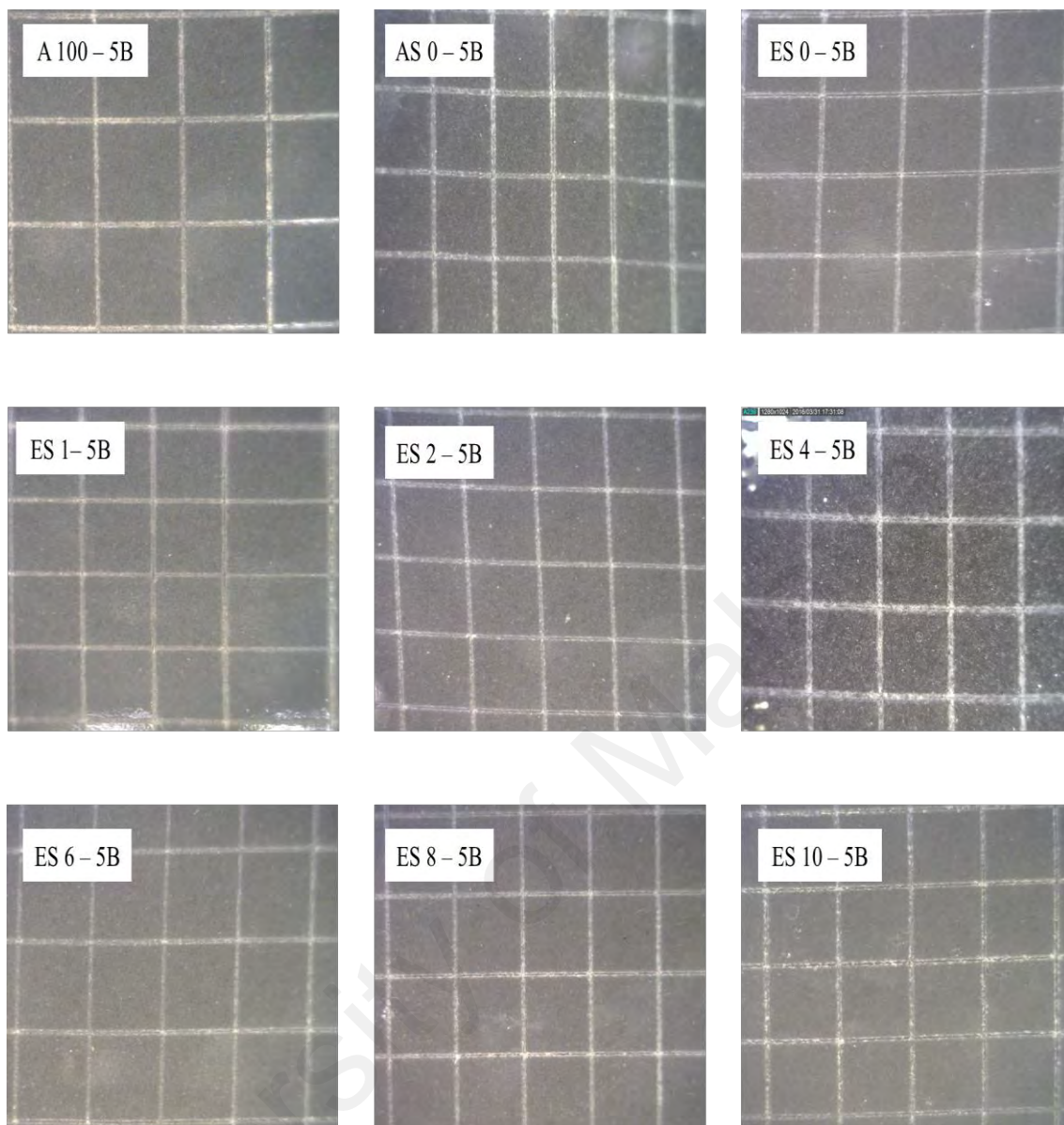


Figure 6.3: Results of cross hatch test for A 100, AS 0 and all epoxy-epoxidized soybean oil hybrid organic coating systems.

6.6 Thermogravimetric Analysis (TGA)

To investigate the thermal stability and decomposition temperatures of the prepared epoxy–soybean oil modified coating systems, TGA was performed and the resulting TGA thermograms are shown in Figures 6.4-6.10. Moreover, the IDT, the temperature at which 50 % weight loss occurred ($T_{50 \text{ wt. \%}}$) and the residue yields at 700 °C were used to determine the influence of the different loading rates of E and ESO on the thermal

properties of the coating films. Table 6.2 presents all the IDT, $T_{50 \text{ wt. \%}}$, and residue values of the A 100, AS 0 and prepared epoxy–soybean oil modified coating systems.

As the effect of silicone resin in enhancing the thermal stability of the neat acrylic coating system was discussed in the previous chapter, only the influence of the E and ESO at different loading ratios is reported in this section.

Figure 6.4 shows the TGA thermogram of the ES 0 coating system, from which it can be observed that thermal degradation occurred in four main stages. The first stage of thermal degradation began at approximately 120 °C and the loss of mass maintained a linear rate up to 250 °C. This can be attributed to the loss of the residual solvent, butyl acetate, which boils, according to the manufacturer's datasheet, in the range of 124–128 °C. Also, at this stage, some of the loss in mass could be related to the loss of xylene solvent present in the E, which boils in the range 135–145 °C, according to the same datasheet.

The second stage of degradation occurred in the temperature range between 280–410 °C, where the loss in mass can be attributed to the loss of NCO resin, which has a boiling point of 280 °C according to the manufacturer's datasheet. Moreover, in this stage, some of the loss of mass can be explained by the degradation of the E, which has a boiling point of 300 °C. Above a temperature of 410 °C, the third stage of degradation was observed, which involves the extensive breakdown of the chemical bonds in the epoxy network, including the phenyl bonds of bisphenol-A and the decomposition of the acrylic resin, which has a boiling point of approximately 370 °C. The fourth stage in the TGA curve is observed when the temperature exceeds 500 °C, which represents the loss of silicone resin, which is known to have ignition temperature above 400 °C. However, it was interesting to note that the addition of E to the hybrid acrylic–silicone polymeric blend did not alter the main stages of decomposition.

Figures 6.5–6.10 show the TGA thermograms of the coating systems that contain different loading ratios of ESO. All four main stages of degradation can be observed in the TGA graphs and can be described in a similar way as the TGA results for the ES 0 coating system. However, the effects of different loading ratios of ESO and of E were investigated via the different observed values of the IDT and the temperature at which 50 % weight loss occurred ($T_{50 \text{ wt. \%}}$), as listed in Table 6.2.

The TGA results reported in Table 6.2 reveal that a higher thermal stability was obtained by the application of the ES 1 coating system. This result is in complete agreement with the results of other experiments, as the ES 1 coating system showed the best overall performance with respect to curing state of all the prepared epoxy–soybean oil modified coating systems. Similar observations have been reported by many researchers for the incorporation of soybean oil in polymeric blends, thereby enhancing thermal stability (Baştürk et al., 2013; Bueno-Ferrer et al., 2010; Habib & Bajpai, 2011).

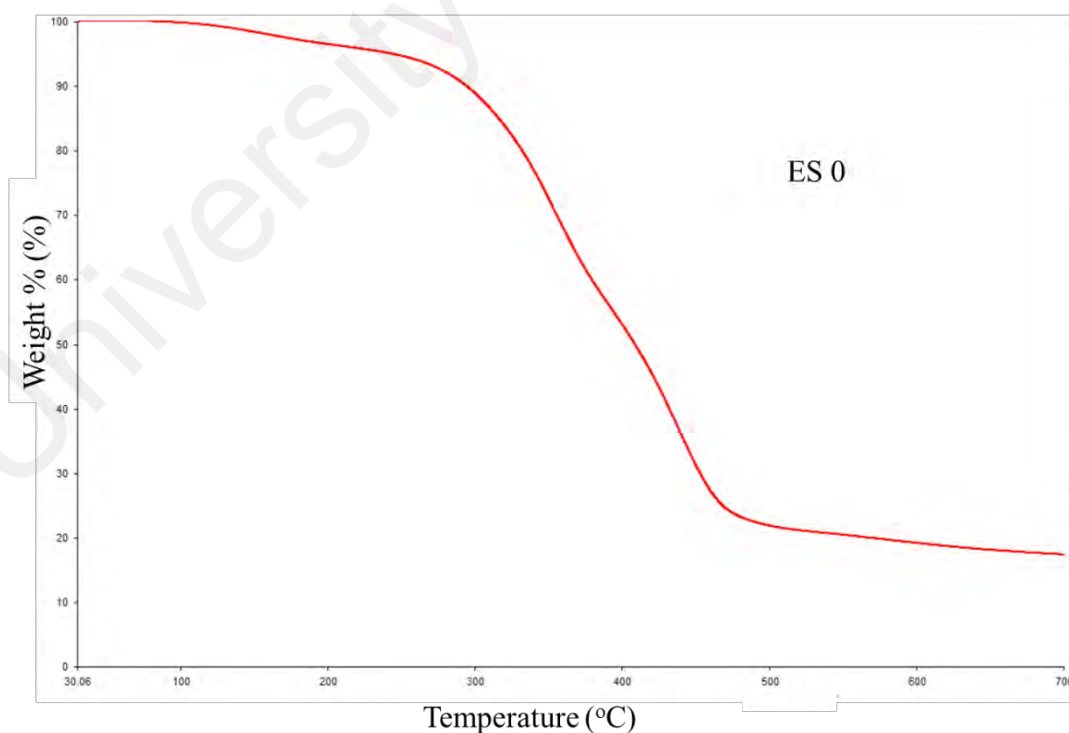


Figure 6.4: TGA thermogram of ES 0 coating system.

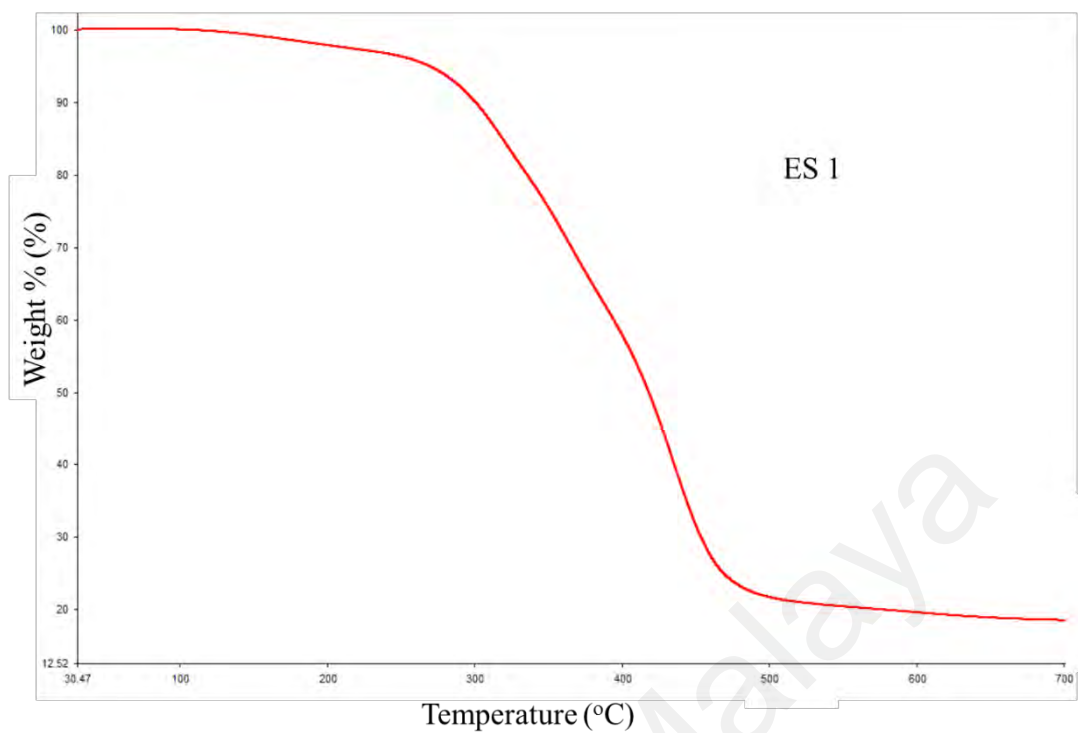


Figure 6.5: TGA thermogram of ES 1 coating system.

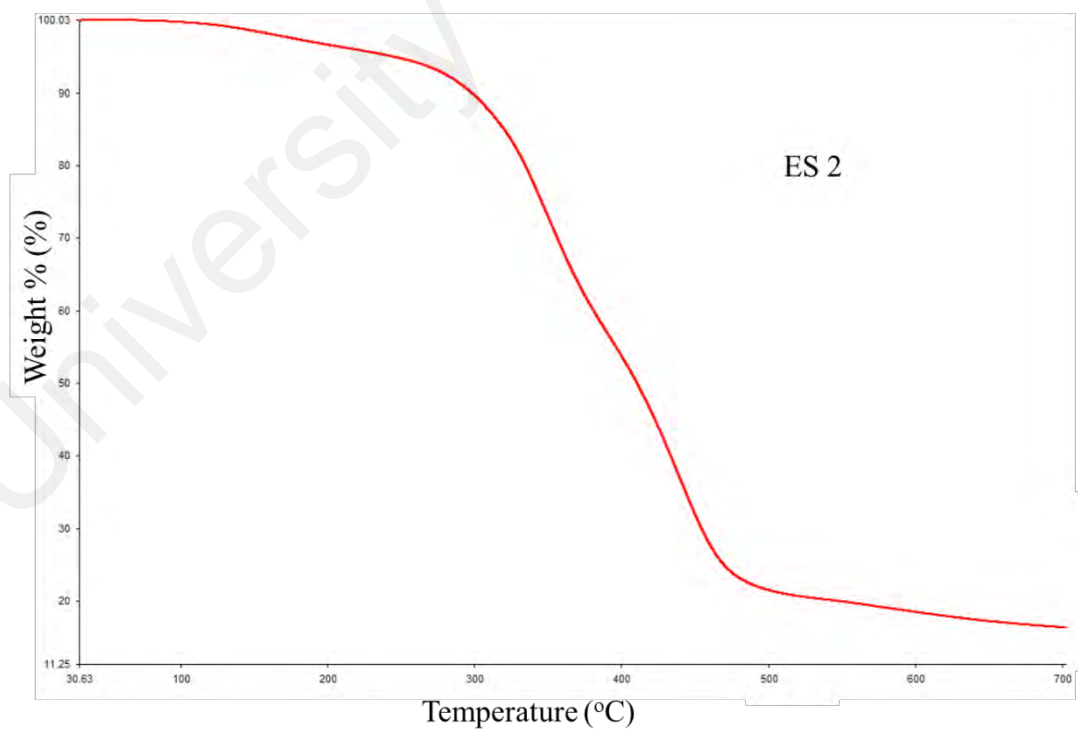


Figure 6.6: TGA thermogram of ES 2 coating system.

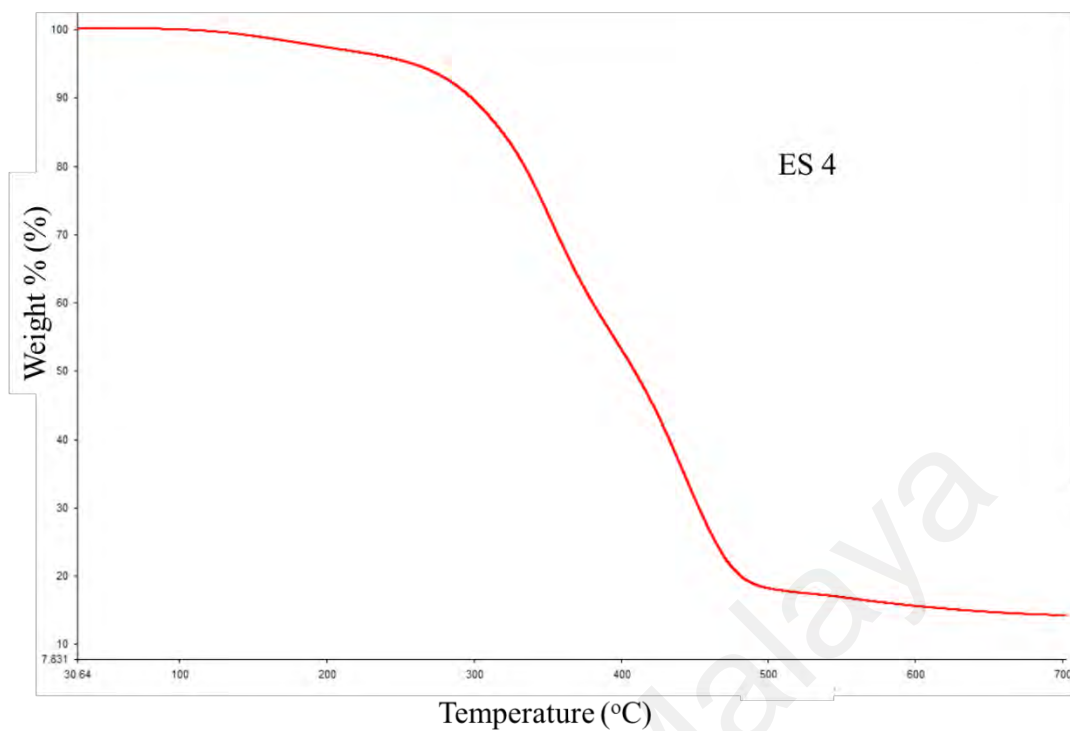


Figure 6.7: TGA thermogram of ES 4 coating system.

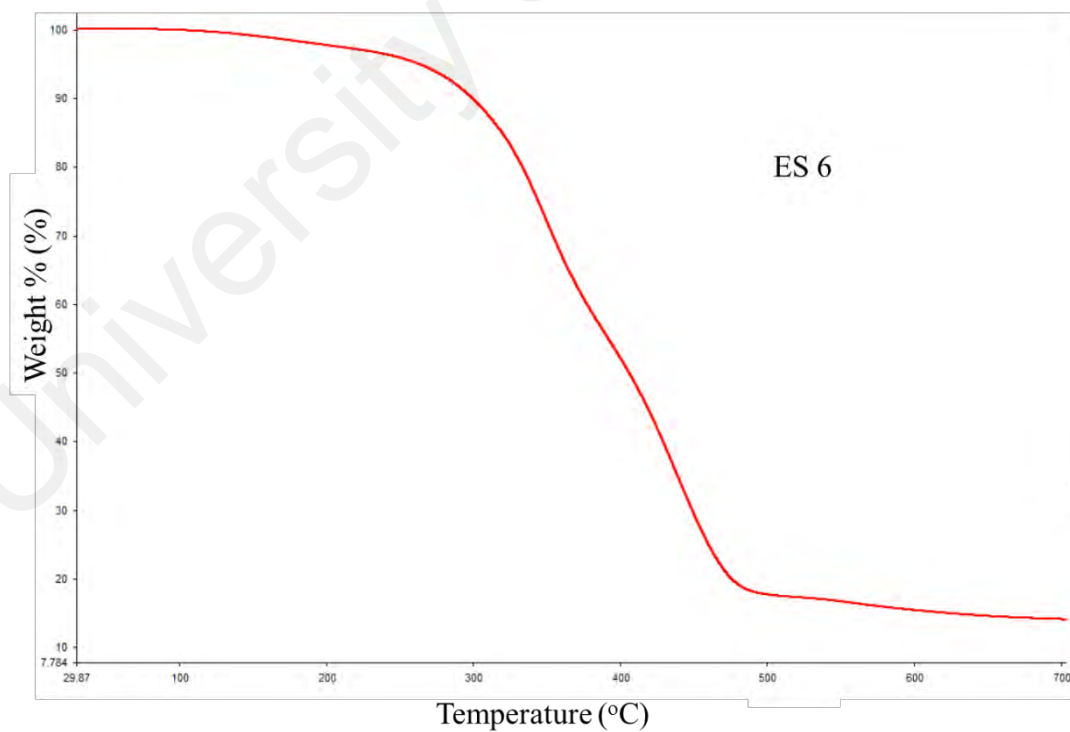


Figure 6.8: TGA thermogram of ES 6 coating system.

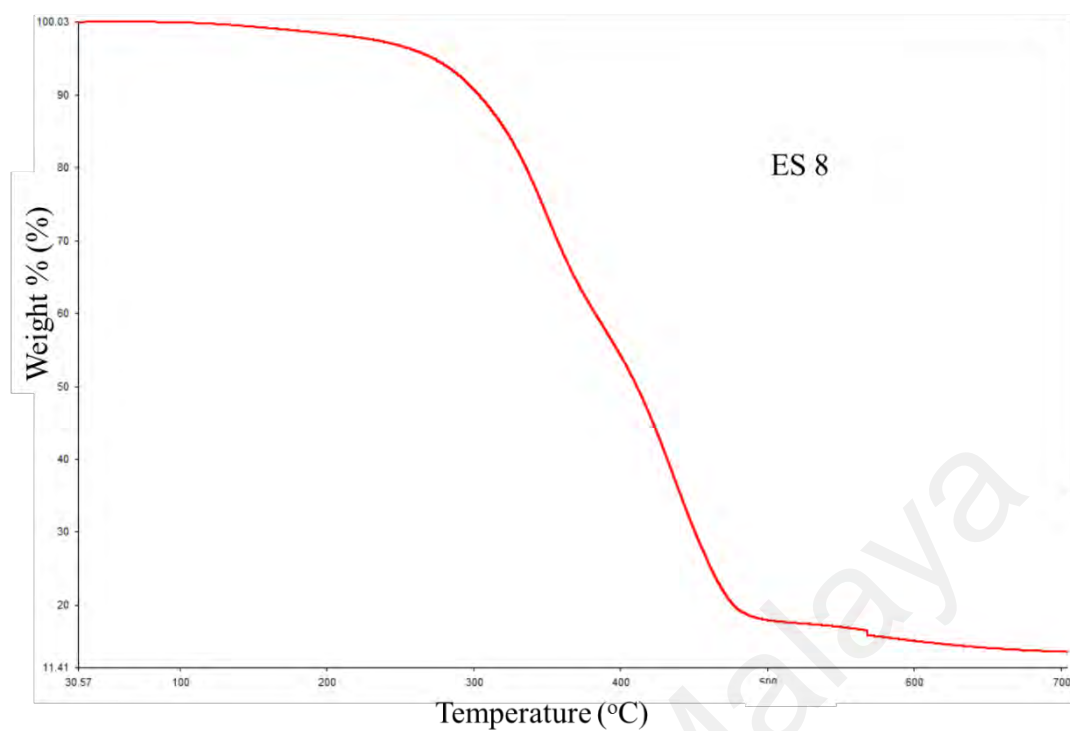


Figure 6.9: TGA thermogram of ES 8 coating system.

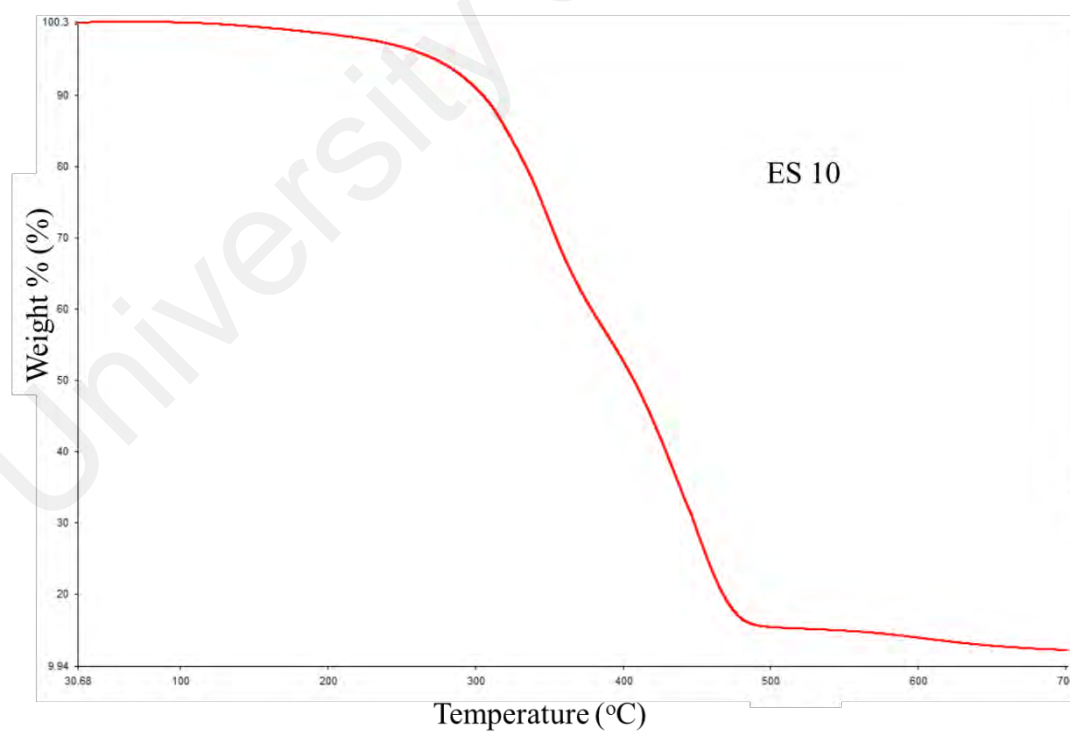


Figure 6.10: TGA thermogram of ES 10 coating system.

Table 6.2: The parameters gained from TGA studies of A 100, AS 0 and all epoxy-epoxidized soybean oil hybrid organic coating systems.

| System | IDT (°C) | T _{50 wt. %} (°C) | Residue at 700 °C |
|--------|----------|----------------------------|-------------------|
| A 100 | 290 | 380 | 1.52 |
| AS 0 | 295 | 411 | 15.28 |
| ES 0 | 295 | 409 | 17.39 |
| ES 1 | 301 | 418 | 18.50 |
| ES 2 | 298 | 411 | 16.31 |
| ES 4 | 298 | 409 | 14.23 |
| ES 6 | 299 | 406 | 14.10 |
| ES 8 | 303 | 411 | 13.55 |
| ES 10 | 305 | 408 | 12.17 |

6.7 Electrochemical impedance spectroscopy (EIS)

The results reported in the previous chapters confirm that the incorporation of nanoparticles in the hybrid polymeric matrix can enhance the overall performance of coating films, and especially their barrier properties and corrosion protection performance. This improvement can be attributed to the vital role of the small nanofiller in filling the organic pores and zigzagging the diffusion pathways to thwart the penetrated ions and corrosive agents, forcing them to travel longer distances to reach the coating–substrate interface, and thereby obtaining a longer period of metal protection against corrosion.

However, this study also investigates the possibility of enhancing the overall performance of the acrylic–silicone hybrid polymeric matrix through the assistance of polymeric resins and a biodegradable vegetable oil, namely epoxy resin and soybean oil, respectively. Nevertheless, it was a challenging task to develop a fully hybrid organic

coating system that could rival the intact behaviour of the achieved SiO₂ and ZnO nanocomposite coatings against corrosion.

In this regard, the EIS technique was employed to investigate the electrochemical response and anti-corrosion properties of the developed epoxy–soybean oil organic coating systems. EIS measurements were conducted periodically for 60 days after exposing the coated substrates to 3.5 % NaCl solution and the results were expressed graphically using Nyquist and Bode plots. In the same manner as described in Chapter 4, three different equivalent circuit models were utilized to obtain the best numerical fitting during the study periods, as shown in Figure 4.11.

Since the EIS results of the AS 0 coating systems were reported in detail in Chapter 4, in this chapter, only the EIS graphs of the above coating systems are included. The effects of the utilization of epoxy resin and ESO at different loading rates in altering the electrochemical response of the coating film for various immersion periods were investigated and the results reported for one day, 30 days and 60 days of immersion.

After one day of immersion, the ES0 coating system, which was developed by introducing 10 wt. % of E to the hybrid acrylic–silicone blend, showed an obvious bend in the low-frequency region in the Bode plot in Figure 6.11 and a full semi-circle in the Nyquist plot in Figure 6.13. This means that, even after this short period of exposure, the electrolyte was able to penetrate the coating film and initiate a corrosion reaction. The electrochemical behaviour of the ES 0 system at this level of degradation can be perfectly described using model B of the equivalent circuit.

However, it was noted that the addition of E resulted in higher pore resistance than that of the AS 0 coating system after the same period of immersion, as listed in Table 6.3. This indicates the good achievement of a crosslinked polymeric structure that is more durable against corrosion.

On the other hand, modifying the acrylic–silicone hybrid polymeric matrix with both E and ESO was more effective, as demonstrated by the capacitive behaviour of the ES 1 and ES 2 coating systems after one day of exposure, as illustrated by the straight line with a slope of -1 in the Bode plot in Figure 6.11, and one capacitive loop in the Nyquist plot in Figure 6.14 for both coating systems. Furthermore, model A of the equivalent circuit was found to perfectly fit the EIS diagrams at this stage of immersion. These observations reveal the ability of ESO to further enhance the barrier properties of the hybrid polymeric blend and confirm the achievement of good curing and a crosslinked structure, which is in strong agreement with the FTIR findings.

No further improvement in the corrosion protection properties was observed with the utilization of more ESO. As illustrated in Figure 5.11, the Bode plots of the other modified organic coating systems, namely, ES 4, ES 6, ES 8 and ES 10, show a bend in the low-frequency range and a full semi-circle in their Nyquist plots, as shown in Figures 6.13 and 6.15, respectively. This indicates an initiation of electrolyte permeation toward the coating–substrate interface through the polymer coating layer, which in turn leads to the initiation of corrosion. Therefore, model B of the equivalent circuit was used to explain the electrochemical behaviour of this particular coating system.

Moreover, the values of all parameters that have been obtained by fitting the EIS data according to the proposed equivalent circuit models after 1 day of immersion time are tabulated in Tables 6.3 and 6.4.

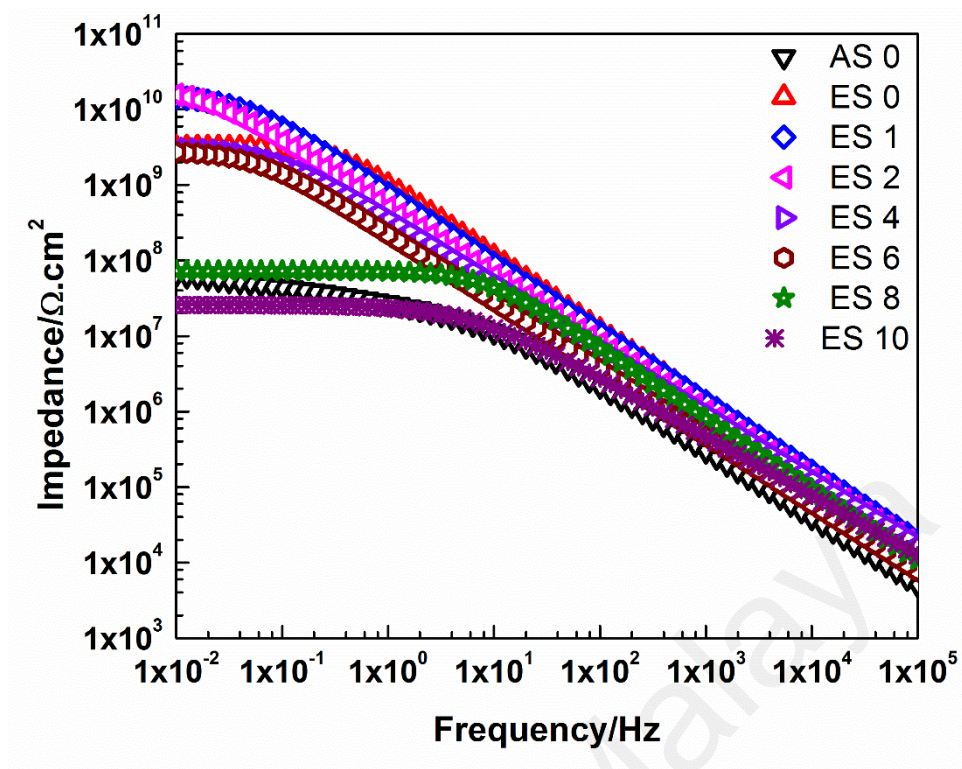


Figure 6.11: Bode plots for AS 0 and all prepared epoxy-epoxidized soybean oil hybrid organic coating systems after 1 day of immersion time.

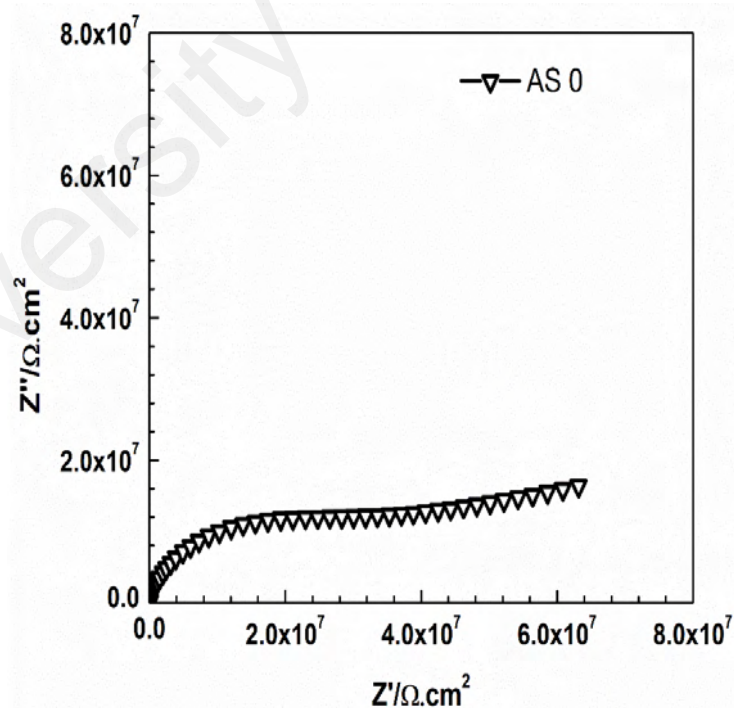


Figure 6.12: Nyquist plot for AS 0 coating system after 1 day of immersion time.

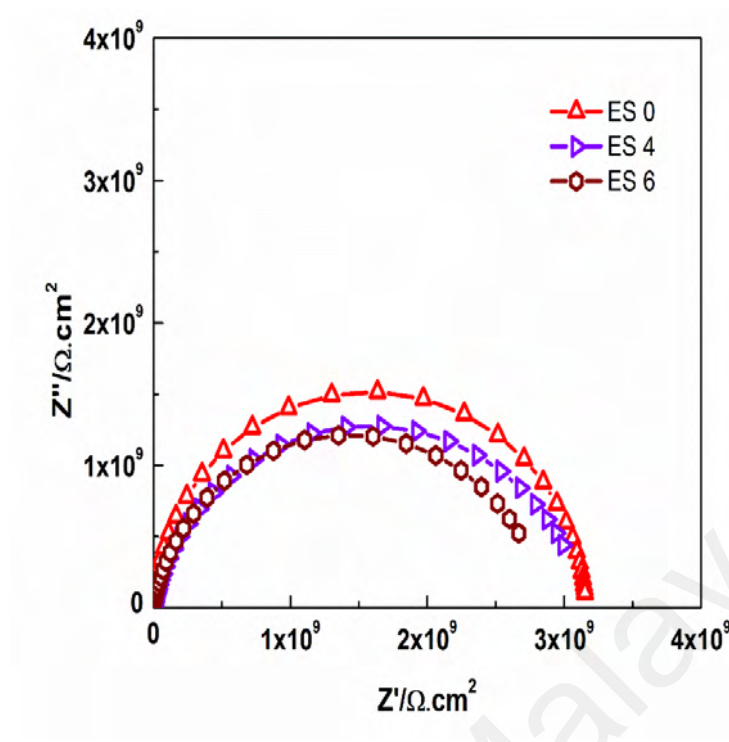


Figure 6.13: Nyquist plots ES 0, ES4 and ES 6 hybrid organic coating systems after 1 day of immersion time.

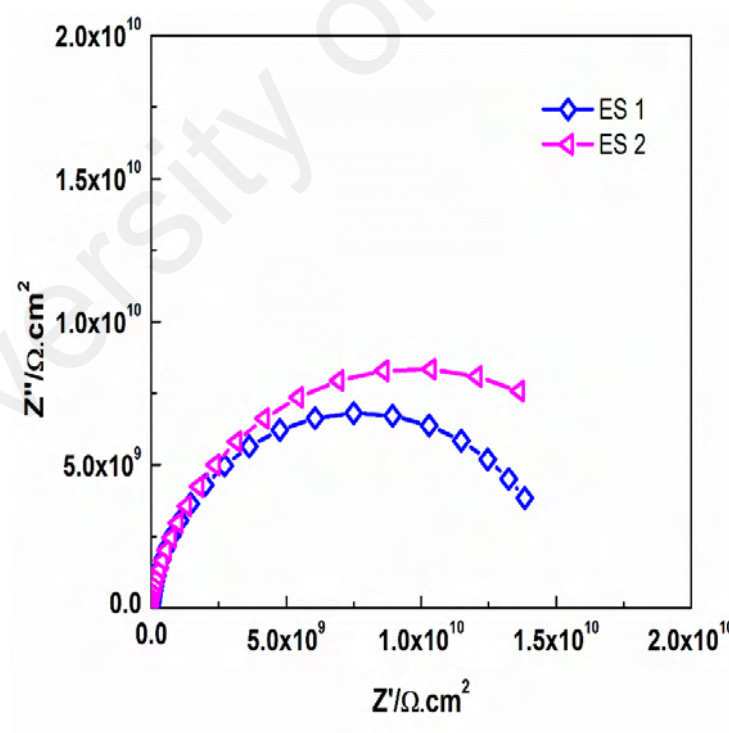


Figure 6.14: Nyquist plots ES 1 and ES 2 hybrid organic coating systems after 1 day of immersion time.

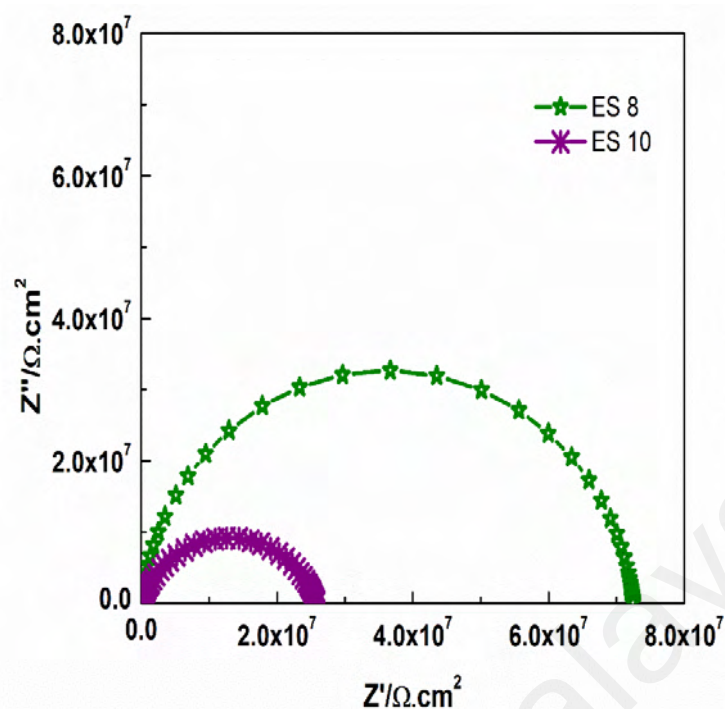


Figure 6.15: Nyquist plots ES 8 and ES 10 hybrid organic coating systems after 1 day of immersion time.

Table 6.3: The resistance values from EIS studies, along with the equivalent circuit model used to fit the data, of AS 0 and all prepared epoxy-epoxidized soybean oil hybrid organic coating systems after 1 day of immersion time.

| System | $R_{po} (\Omega cm^2)$ | $R_{ct} (\Omega cm^2)$ | $R_{diff} (\Omega cm^2)$ | Model used |
|--------|----------------------------------|-------------------------------|--------------------------|------------|
| AS 0 | $(7.94 \pm 0.06) \times 10^6$ | $(2.38 \pm 0.02) \times 10^9$ | - | B |
| ES 0 | $(4.59 \pm 0.03) \times 10^5$ | $(3.16 \pm 0.03) \times 10^9$ | - | B |
| ES 1 | $(1.95 \pm 0.01) \times 10^{10}$ | - | - | A |
| ES 2 | $(1.54 \pm 0.03) \times 10^{10}$ | - | - | A |
| ES 4 | $(8.45 \pm 0.02) \times 10^7$ | $(3.07 \pm 0.06) \times 10^9$ | - | B |
| ES 6 | $(7.86 \pm 0.07) \times 10^7$ | $(2.86 \pm 0.02) \times 10^9$ | - | B |
| ES 8 | $(1.87 \pm 0.03) \times 10^7$ | $(5.37 \pm 0.07) \times 10^7$ | - | B |
| ES 10 | $(2.58 \pm 0.06) \times 10^7$ | $(7.48 \pm 0.04) \times 10^7$ | - | B |

As the exposure time lengthened, the EIS graphics of the AS 0 coating system in Figures 6.16 and 6.17, after 30 days of immersion, reveal the poor ability of this coating

film to withstand corrosion and the significant degradation of the barrier properties, as discussed in the previous chapter. It is important to note that similar observations without significant changes were recorded for the acrylic–silicone coating system, AS 0, after 60 days of exposure, as shown in Figures 6.22 and 6.23.

In contrast, no significant changes were observed in the EIS graphs of the ES 0 coating system after 30 days of immersion. Model B of the equivalent circuit remains the best model for explaining the electrochemical response of the coating film at this stage of immersion.

Table 6.4: The constant phase element values from EIS studies of AS 0 and all prepared epoxy-epoxidized soybean oil hybrid organic coating systems after 1 day of immersion time.

| System | CPR _{po} | | CPE _{dl} | | CPE _{diff} | |
|--------|---|------|---|------|---|---|
| | Y ₀ (Ω ⁻¹ cm ⁻² s ⁿ) | n | Y ₀ (Ω ⁻¹ cm ⁻² s ⁿ) | n | Y ₀ (Ω ⁻¹ cm ⁻² s ⁿ) | n |
| AS 0 | (1.31 ± 0.01) × 10 ⁻⁹ | 0.89 | (1.98 ± 0.10) × 10 ⁻⁸ | 0.14 | - | - |
| ES 0 | (1.98 ± 0.06) × 10 ⁻¹⁰ | 0.97 | (3.12 ± 0.01) × 10 ⁻¹⁰ | 0.91 | - | - |
| ES 1 | (2.39 ± 0.01) × 10 ⁻¹⁰ | 0.91 | - | - | - | - |
| ES 2 | (3.81 ± 0.02) × 10 ⁻¹⁰ | 0.90 | - | - | - | - |
| ES 4 | (5.38 ± 0.05) × 10 ⁻¹⁰ | 0.85 | (3.62 ± 0.05) × 10 ⁻⁹ | 0.76 | - | - |
| ES 6 | (8.53 ± 0.04) × 10 ⁻¹⁰ | 0.89 | (1.39 ± 0.01) × 10 ⁻⁷ | 0.60 | - | - |
| ES 8 | (3.52 ± 0.02) × 10 ⁻¹⁰ | 0.93 | (2.06 ± 0.04) × 10 ⁻⁶ | 0.96 | - | - |
| ES 10 | (2.21 ± 0.08) × 10 ⁻⁹ | 0.78 | (7.86 ± 0.09) × 10 ⁻⁶ | 0.99 | - | - |

It is noted that lower resistance values were recorded for the ES 0 coating system, as shown in Table 6.5, which indicates that the coating film is experiencing corrosion and a low level of substrate protection at this stage of immersion. Moreover, this system, ES 0, continues to show the same level of degradation even after 60 days of immersion, with no significant changes observed in its Bode plot, Figure 6.22, or Nyquist plot, Figure 6.24.

Of all the E-ESO organic coating systems, only the ES 1 coating system exhibited remarkable stability for up to 30 days of immersion and maintained capacitive behaviour, as evidenced by a straight line with a slope of -1 in the Bode plot, Figure 6.16, and one capacitive loop in the Nyquist plot, Figure 6.19. Moreover, it is interesting to note that the EIS results of the ES 1 coating system at this stage of immersion can still be fitted with model A of the equivalent circuit, which is clear evidence that the coating film continues to act as a perfect capacitor even after long-term exposure.

Thirty days of immersion were enough to allow corrosion to start on the substrate coated with the ES 2 coating system, as illustrated in Figures 6.16 and 6.18 of a Bode plot with one time constant and a Nyquist plot with a full semi-circle, respectively. Model B of the equivalent circuit was employed to fit the EIS data at this stage of immersion. However, no further degradation was observed for the ES 2 coating system even after 60 days of immersion, for which similar observations were made, as illustrated in the corresponding Bode plot, Figure 6.12, and Nyquist plot, Figure 6.26.

The EIS results for the other modified organic coating systems, namely, ES 4, ES 6, ES 8 and ES 10, after 30 days of exposure reveal the poor ability of these coating systems to withstand the penetration of corrosive agents into the substrate surface and confirmed the degradation of the coating films.

For these coating systems at this stage of immersion, Bode plots with two time constants, as shown in Figure 6.16, and Nyquist plots with two full semi-circuits, illustrated in Figure 6.20 and Figure 6.21, were recorded. This indicates the poor corrosion resistance of the coating film and reveals the weakness of these coatings in withstanding the penetration of electrolytes to the coating-substrate interface, which leads to the initiation of corrosion and degradation in the barrier properties of the coating film.

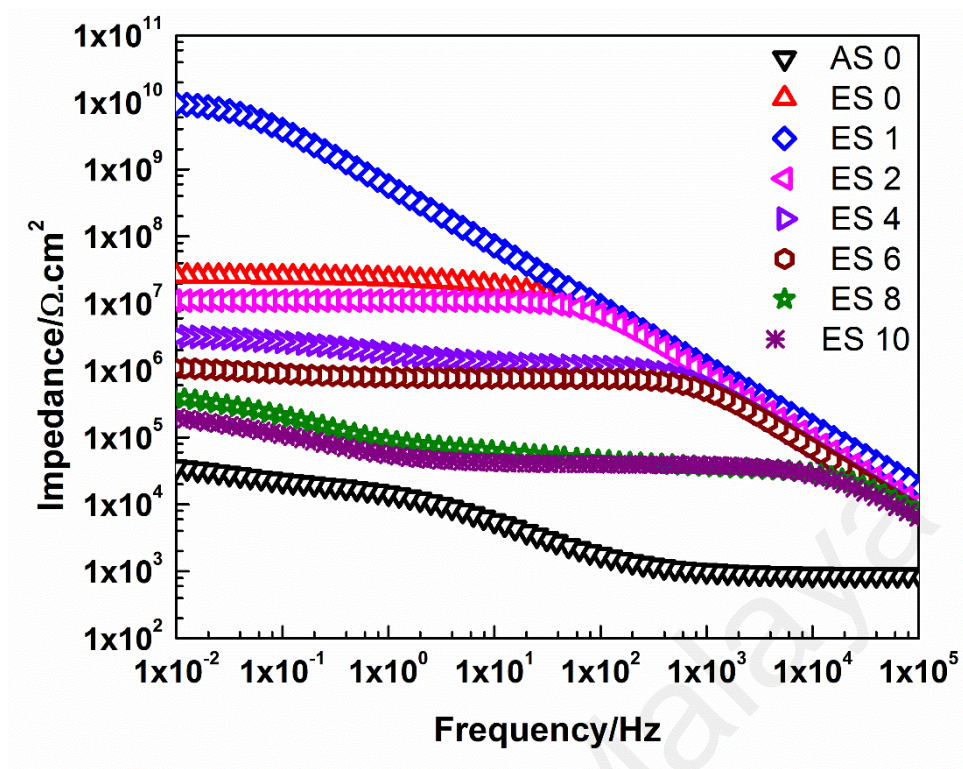


Figure 6.16: Bode plots for AS 0 and all prepared epoxy-epoxidized soybean oil hybrid organic coating systems after 30 days of immersion time.

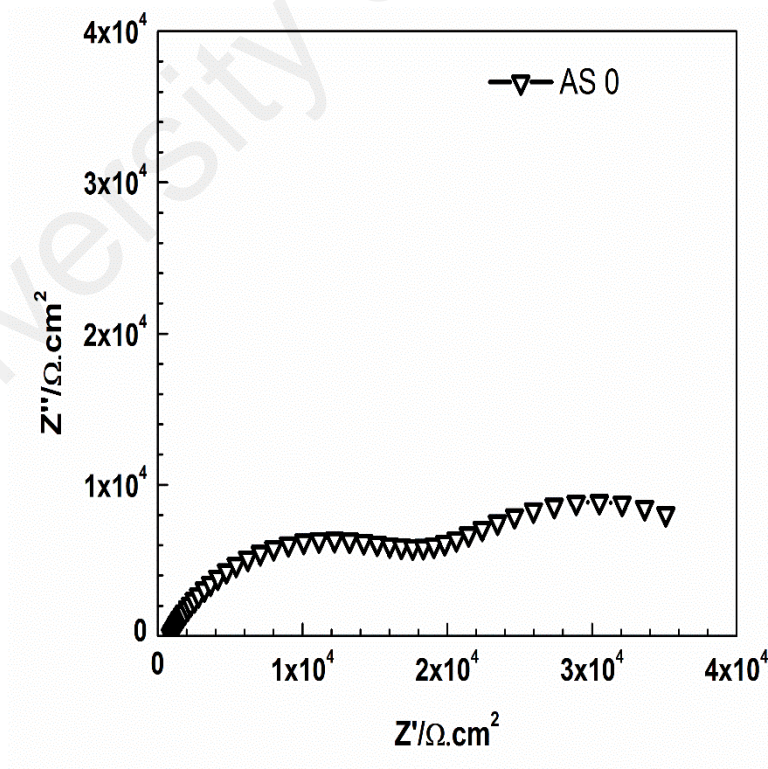


Figure 6.17: Nyquist plot for AS 0 coating system after 30 days of immersion time.

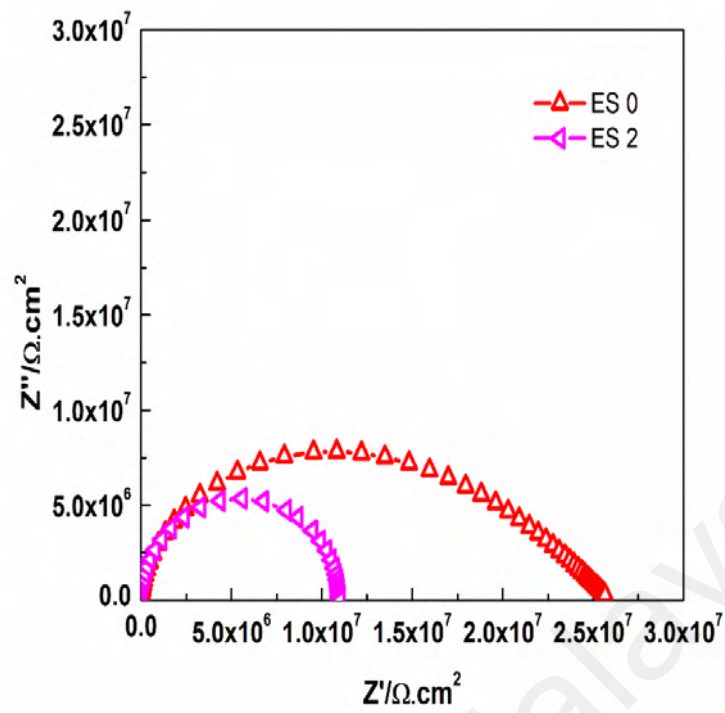


Figure 6.18: Nyquist plots ES 0 and ES 2 hybrid organic coating systems after 30 days of immersion time.

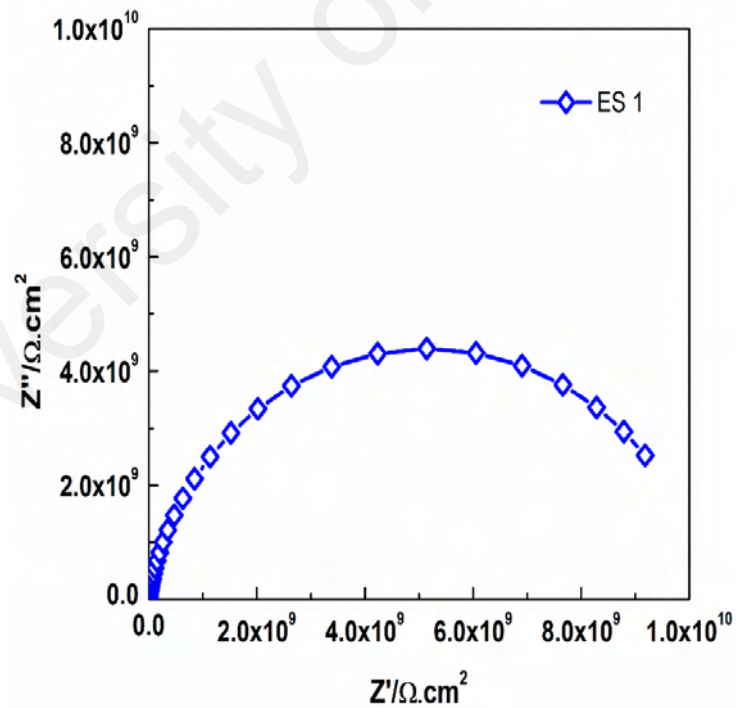


Figure 6.19: Nyquist plots ES 1 hybrid organic coating system after 30 days of immersion time.

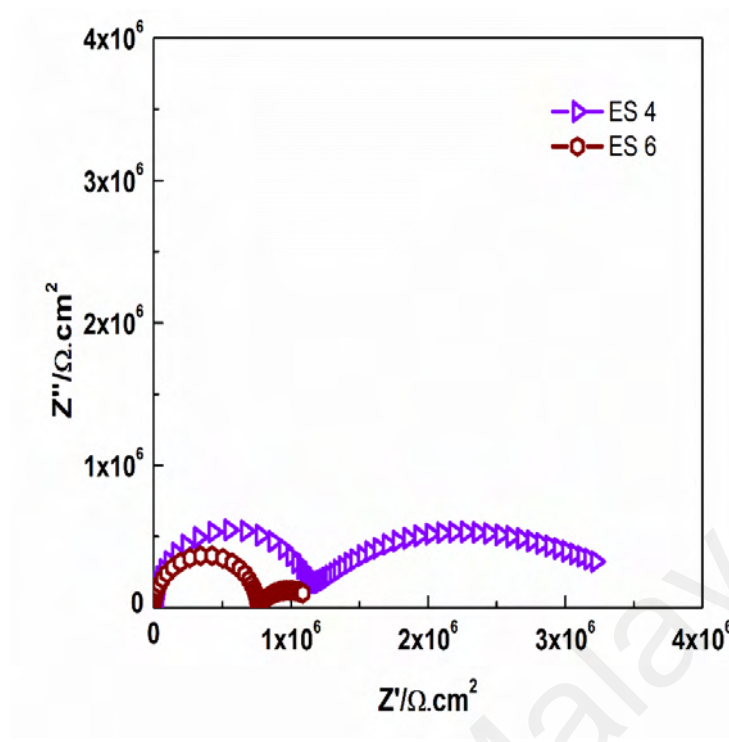


Figure 6.20: Nyquist plots ES 4 and ES 6 hybrid organic coating systems after 30 days of immersion time.

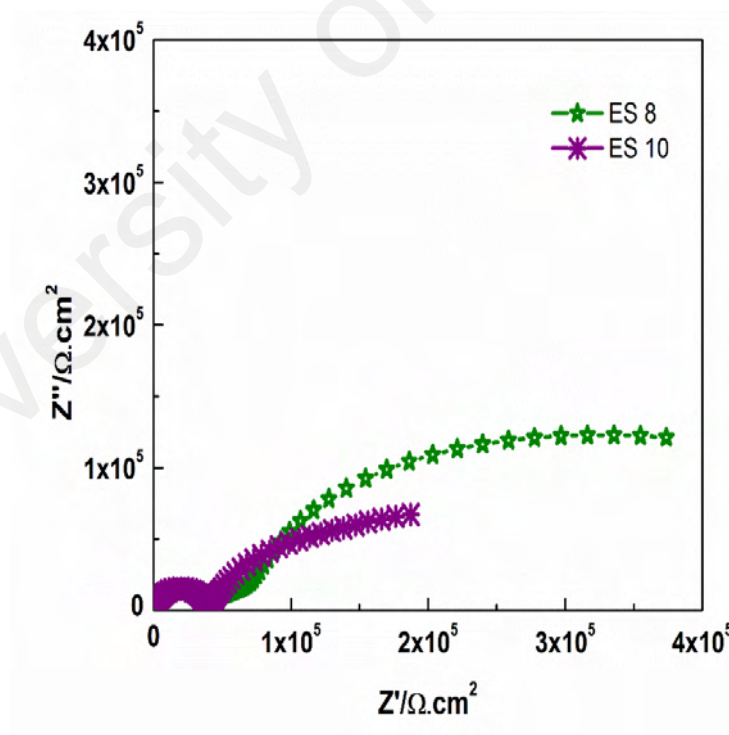


Figure 6.21: Nyquist plots ES 8 and ES 10 hybrid organic coating systems after 30 days of immersion time.

Moreover, the values of all parameters that have been obtained by fitting the EIS data according to the proposed equivalent circuit models after 30 days of immersion time are tabulated in Tables 6.5 and 6.6.

Table 6.5: The resistance values from EIS studies, along with the equivalent circuit model used to fit the data, of AS 0 and all prepared epoxy-epoxidized soybean oil hybrid organic coating systems after 30 days of immersion time.

| System | $R_{po} (\Omega \text{ cm}^2)$ | $R_{ct} (\Omega \text{ cm}^2)$ | $R_{diff} (\Omega \text{ cm}^2)$ | Model used |
|--------|----------------------------------|--------------------------------|----------------------------------|------------|
| AS 0 | $(1.37 \pm 0.13) \times 10^3$ | $(1.27 \pm 0.09) \times 10^5$ | $(1.04 \pm 0.06) \times 10^4$ | C |
| ES 0 | $(8.36 \pm 0.02) \times 10^6$ | $(1.75 \pm 0.02) \times 10^7$ | - | B |
| ES 1 | $(1.03 \pm 0.01) \times 10^{10}$ | - | - | A |
| ES 2 | $(1.10 \pm 0.03) \times 10^6$ | $(1.12 \pm 0.07) \times 10^7$ | - | B |
| ES 4 | $(1.12 \pm 0.03) \times 10^6$ | $(1.68 \pm 0.04) \times 10^6$ | $(1.07 \pm 0.07) \times 10^6$ | C |
| ES 6 | $(3.58 \pm 0.02) \times 10^5$ | $(7.20 \pm 0.04) \times 10^5$ | $(4.58 \pm 0.08) \times 10^5$ | C |
| ES 8 | $(2.97 \pm 0.08) \times 10^4$ | $(9.92 \pm 0.01) \times 10^4$ | $(5.94 \pm 0.07) \times 10^5$ | C |
| ES 10 | $(3.94 \pm 0.05) \times 10^4$ | $(1.47 \pm 0.04) \times 10^5$ | $(1.25 \pm 0.01) \times 10^5$ | C |

Of all the prepared E-ESO organic coating systems, only the ES 1 coating system showed significant stability over the entire exposure period and demonstrated the best anti-corrosion properties after 60 days of immersion. Figures 6.22 and 6.25 show Bode and Nyquist plots of the ES 1 coating system after 60 days of immersion, respectively. A slight bend in the low-frequency region of the Bode plot and almost a full semi-circle in the Nyquist plot were observed and model B of the equivalent circuit was used to fit the EIS diagrams at this stage of immersion.

Table 6.6: The constant phase element values from EIS studies of AS 0 and all prepared epoxy-epoxidized soybean oil hybrid organic coating systems after 30 days of immersion time.

| System | CPR _{po} | | CPE _{dl} | | CPE _{diff} | |
|--------|---|------|---|------|---|------|
| | Y ₀ (Ω ⁻¹ cm ⁻² s ⁿ) | n | Y ₀ (Ω ⁻¹ cm ⁻² s ⁿ) | n | Y ₀ (Ω ⁻¹ cm ⁻² s ⁿ) | n |
| AS 0 | (3.82 ± 0.15) × 10 ⁻⁵ | 0.20 | (2.90 ± 0.24) × 10 ⁻⁶ | 0.85 | (6.40 ± 0.31) × 10 ⁻⁶ | 0.18 |
| ES 0 | (1.87 ± 0.01) × 10 ⁻¹⁰ | 0.96 | (5.06 ± 0.08) × 10 ⁻⁹ | 0.84 | - | - |
| ES 1 | (3.37 ± 0.02) × 10 ⁻¹⁰ | 0.89 | - | - | - | - |
| ES 2 | (2.11 ± 0.04) × 10 ⁻¹⁰ | 0.98 | (5.16 ± 0.02) × 10 ⁻⁶ | 1.00 | - | - |
| ES 4 | (2.72 ± 0.01) × 10 ⁻¹⁰ | 0.97 | (2.73 ± 0.02) × 10 ⁻⁷ | 0.61 | (2.06 ± 0.01) × 10 ⁻⁶ | 0.37 |
| ES 6 | (9.81 ± 0.03) × 10 ⁻⁶ | 0.53 | (1.33 ± 0.09) × 10 ⁻⁹ | 0.98 | (5.92 ± 0.07) × 10 ⁻⁶ | 0.62 |
| ES 8 | (9.68 ± 0.07) × 10 ⁻² | 0.86 | (4.14 ± 0.04) × 10 ⁻⁶ | 0.39 | (2.33 ± 0.07) × 10 ⁻⁶ | 0.94 |
| ES 10 | (8.52 ± 0.01) × 10 ⁻² | 0.68 | (1.19 ± 0.01) × 10 ⁻⁵ | 0.71 | (8.42 ± 0.09) × 10 ⁻⁵ | 0.76 |

Moreover, the values of all parameters that have been obtained by fitting the EIS data according to the proposed equivalent circuit models after 60 days of immersion time are tabulated in Tables 6.7 and 6.8.

A better understanding of the changes that occurred in the coating film during the different periods of immersion can be obtained by the utilization of breakpoint frequency, which is defined as the frequency at a -45° phase angle. With respect to the area under the Bode plot (impedance and phase angle as a function of frequency), a coating film can be classified into one of three categories: an intact coating film where all the areas under the Bode plot are recognized as capacitive regions, a coating film undergoing corrosion where the area under the Bode plot is a combination of capacitive and resistive regions, and coating failure for areas where only resistive regions are observed below the Bode plot.

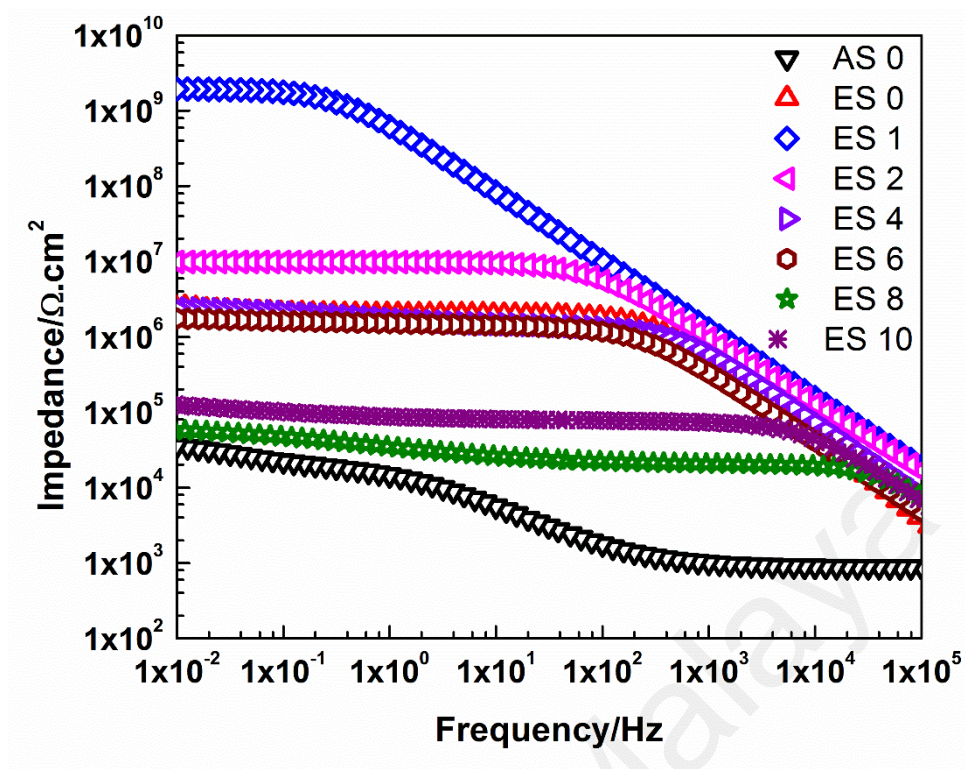


Figure 6.22: Bode plots for AS 0 and all prepared epoxy-epoxidized soybean oil hybrid organic coating systems after 60 days of immersion time.

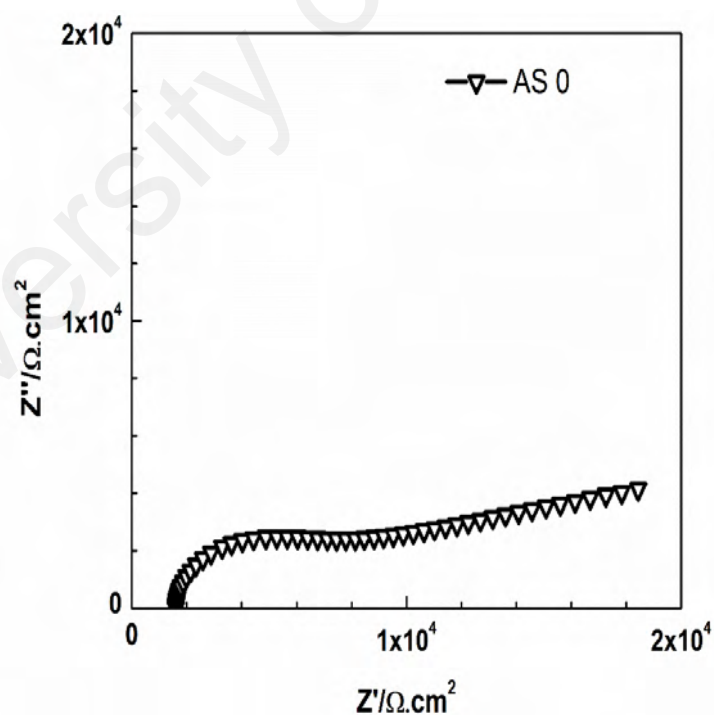


Figure 6.23: Nyquist plot for AS 0 coating system after 60 days of immersion time.

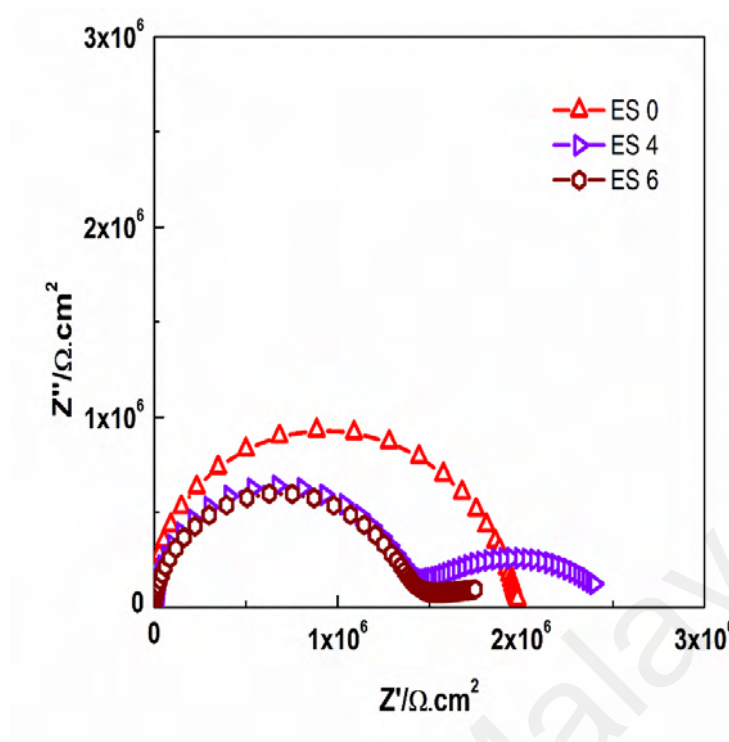


Figure 6.24: Nyquist plots ES 0, ES 4 and ES 6 hybrid organic coating systems after 60 days of immersion time.

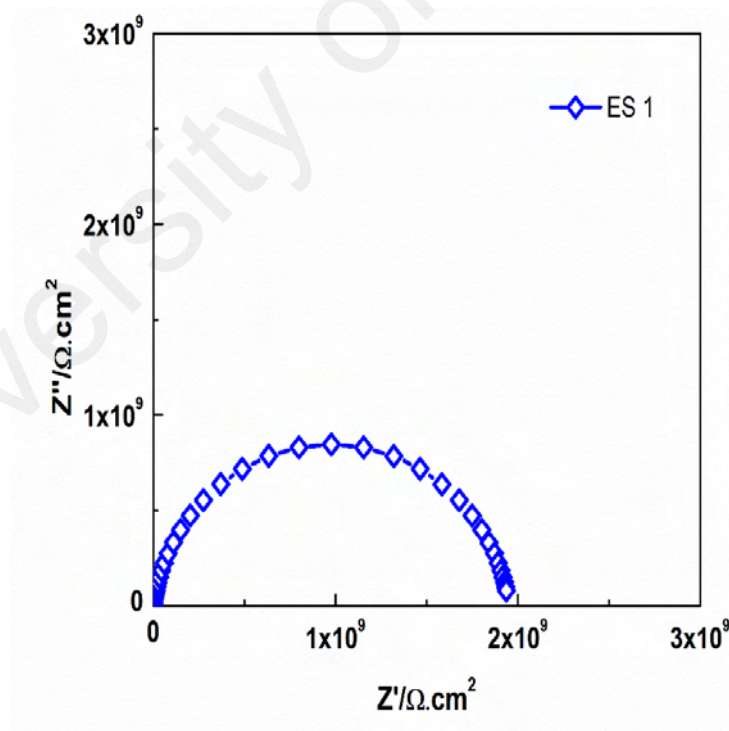


Figure 6.25: Nyquist plots ES 1 hybrid organic coating system after 60 days of immersion time.

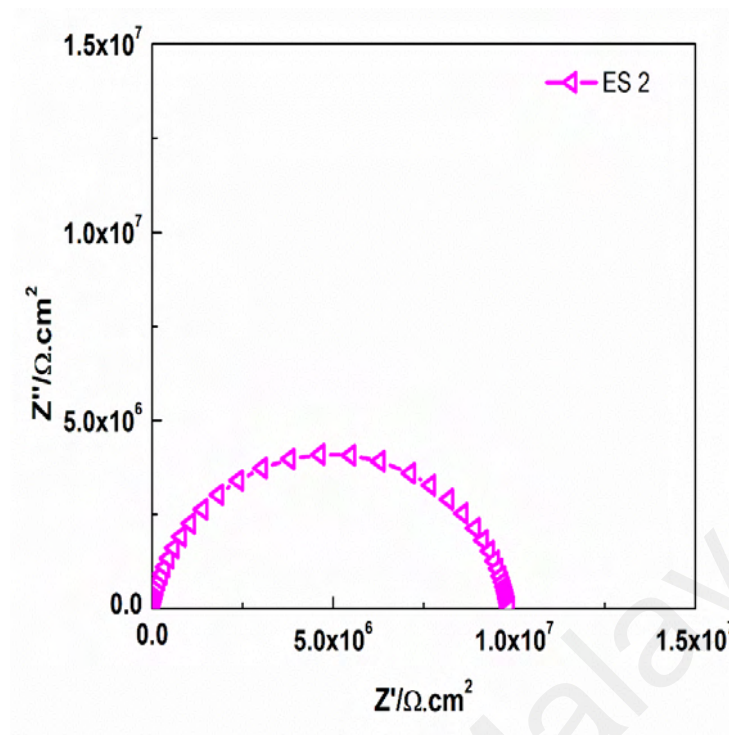


Figure 6.26: Nyquist plots ES 2 hybrid organic coating system after 60 days of immersion time.

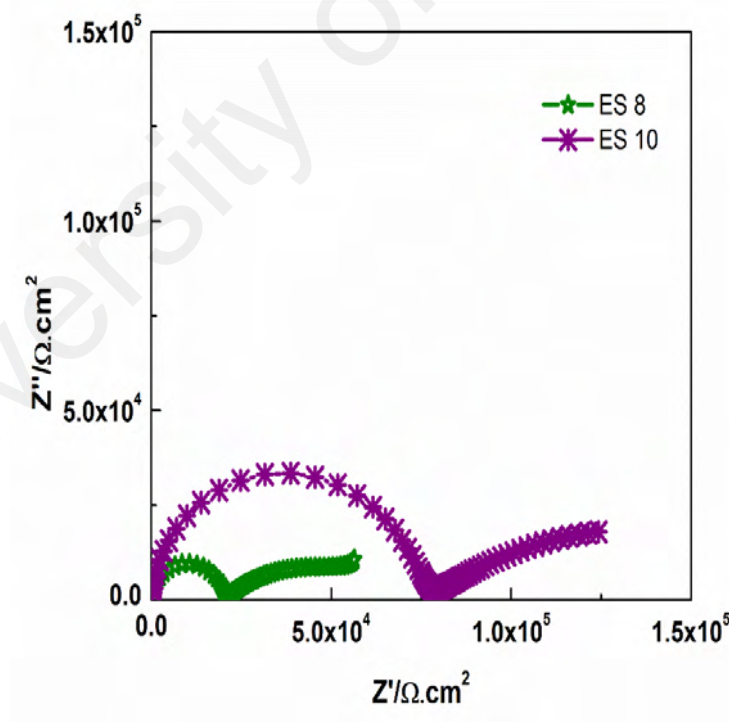


Figure 6.27: Nyquist plots ES 8 and ES 10 hybrid organic coating systems after 60 days of immersion time.

Table 6.7: The resistance values from EIS studies, along with the equivalent circuit model used to fit the data, of AS 0 and all prepared epoxy-epoxidized soybean oil hybrid organic coating systems after 60 days of immersion time.

| System | $R_{po} (\Omega \text{ cm}^2)$ | $R_{ct} (\Omega \text{ cm}^2)$ | $R_{diff} (\Omega \text{ cm}^2)$ | Model used |
|--------|--------------------------------|--------------------------------|----------------------------------|------------|
| AS 0 | $(6.38 \pm 0.04) \times 10^3$ | $(7.80 \pm 0.02) \times 10^4$ | $(1.49 \pm 0.05) \times 10^5$ | C |
| ES 0 | $(1.95 \pm 0.01) \times 10^6$ | $(1.59 \pm 0.03) \times 10^8$ | - | B |
| ES 1 | $(4.88 \pm 0.06) \times 10^7$ | $(2.01 \pm 0.02) \times 10^9$ | - | B |
| ES 2 | $(9.18 \pm 0.09) \times 10^6$ | $(3.43 \pm 0.03) \times 10^7$ | - | B |
| ES 4 | $(1.29 \pm 0.02) \times 10^5$ | $(1.89 \pm 0.07) \times 10^6$ | $(1.05 \pm 0.07) \times 10^6$ | C |
| ES 6 | $(9.40 \pm 0.01) \times 10^5$ | $(5.84 \pm 0.02) \times 10^5$ | $(2.03 \pm 0.03) \times 10^6$ | C |
| ES 8 | $(2.00 \pm 0.03) \times 10^4$ | $(4.33 \pm 0.02) \times 10^4$ | $(8.57 \pm 0.07) \times 10^4$ | C |
| ES 10 | $(1.35 \pm 0.06) \times 10^4$ | $(6.41 \pm 0.05) \times 10^4$ | $(1.14 \pm 0.06) \times 10^5$ | C |

With respect to the EIS results of the AS 0 coating system illustrated in Figure 6.28(a), the obtained EIS data after one day of immersion show significant enhancement of the barrier properties and corrosion protection ability after the application of the ES 0, ES1, ES 2, ES 4 and ES 6 coating systems, as shown in Figures 6.29(a), 6.30(a), 6.31(a), 6.32(a) and 6.33(a), respectively. The application of these coating systems resulted in the observation of lower breakpoint frequency values and, hence, relatively smaller resistive regions in the low-frequency domain and larger capacitive regions. However, as the loading ratio of ESO increased to 8 wt. % and 10 wt. %, no further improvement was observed in the corrosion protection ability of the ES 8 and ES 10 coating systems, as illustrated in Figures 6.34(a) and 6.35(a), respectively.

Table 6.8: The constant phase element values from EIS studies of AS 0 and all prepared epoxy-epoxidized soybean oil hybrid organic coating systems after 60 days of immersion time.

| System | CPR _{po} | | CPE _{dl} | | CPE _{diff} | |
|--------|---|------|---|------|---|------|
| | $Y_0 (\Omega^{-1} \text{ cm}^{-2} \text{ s}^n)$ | n | $Y_0 (\Omega^{-1} \text{ cm}^{-2} \text{ s}^n)$ | n | $Y_0 (\Omega^{-1} \text{ cm}^{-2} \text{ s}^n)$ | n |
| AS 0 | $(1.63 \pm 0.08) \times 10^{-6}$ | 0.71 | $(5.90 \pm 0.03) \times 10^{-7}$ | 0.94 | $(8.33 \pm 0.01) \times 10^{-11}$ | 0.87 |
| ES 0 | $(3.63 \pm 0.01) \times 10^{-10}$ | 1.00 | $(7.08 \pm 0.07) \times 10^{-6}$ | 0.74 | - | - |
| ES 1 | $(1.43 \pm 0.05) \times 10^{-10}$ | 0.97 | $(1.99 \pm 0.08) \times 10^{-10}$ | 0.77 | - | - |
| ES 2 | $(4.33 \pm 0.01) \times 10^{-10}$ | 0.88 | $(7.23 \pm 0.06) \times 10^{-7}$ | 0.57 | - | - |
| ES 4 | $(2.83 \pm 0.02) \times 10^{-10}$ | 0.97 | $(1.03 \pm 0.09) \times 10^{-7}$ | 0.64 | $(7.26 \pm 0.06) \times 10^{-7}$ | 0.53 |
| ES 6 | $(6.02 \pm 0.05) \times 10^{-6}$ | 0.96 | $(1.03 \pm 0.05) \times 10^{-8}$ | 0.74 | $(1.46 \pm 0.04) \times 10^{-5}$ | 0.68 |
| ES 8 | $(3.10 \pm 0.05) \times 10^{-2}$ | 0.96 | $(1.74 \pm 0.05) \times 10^{-5}$ | 0.45 | $(5.87 \pm 0.02) \times 10^{-6}$ | 0.41 |
| ES 10 | $(3.92 \pm 0.02) \times 10^{-2}$ | 0.96 | $(3.71 \pm 0.01) \times 10^{-5}$ | 0.49 | $(3.71 \pm 0.05) \times 10^{-5}$ | 0.39 |

Moreover, as the EIS studies were extended to 60 days of immersion, only the ES1 coating system continued to show remarkable stability against the initiation of corrosion whereby the coating layer successfully prevented the penetration of corrosive agents into the surface of the steel substrate. The lowest breakpoint frequency values with the smallest resistive region in the low-frequency domain and largest capacitive region were observed in Figure 6.30 (b) with the application of ES 1 coating system.

On the other hand, 60 days of immersion revealed the poor barrier properties of all the other E–ESO organic coating systems as high breakpoint frequency values and larger resistive regions were observed in Figures 6.28(b), 6.29(b), 6.31(b), 6.32(b), 6.33(b) 6.34(b) and 6.35(b), which show Bode plots of the AS 0 and the developed E–ESO organic coating systems, except for the ES 1 coating system, after 60 days of immersion.

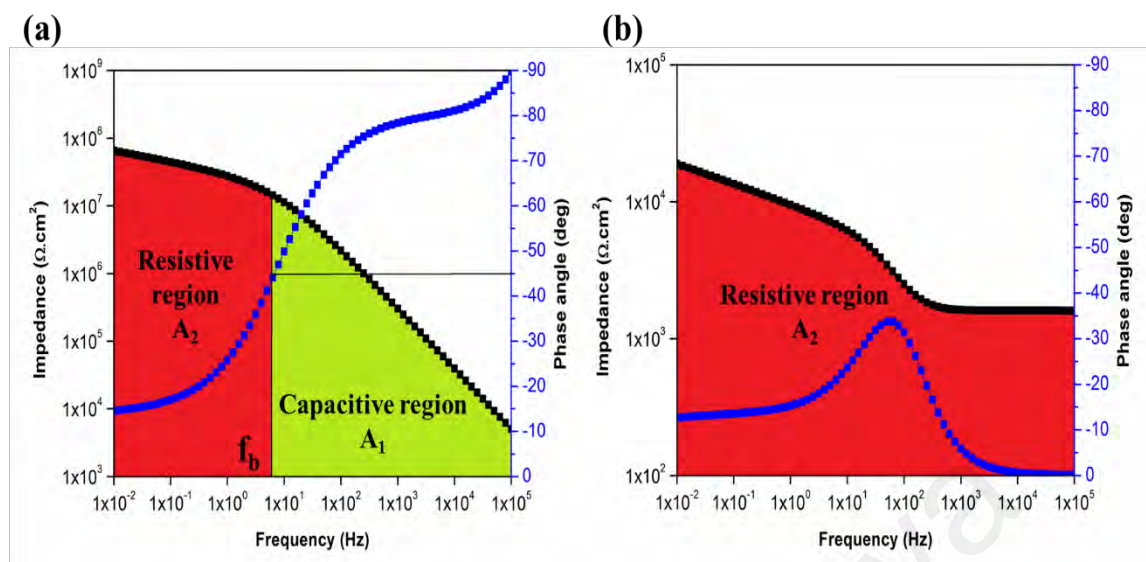


Figure 6.28: Bode plots of AS 0 coating system after (a) 1 day and (b) 60 days of immersion along with the determining the breakpoint frequency and the corresponding capacitive (A_1) and resistive (A_2) regions.

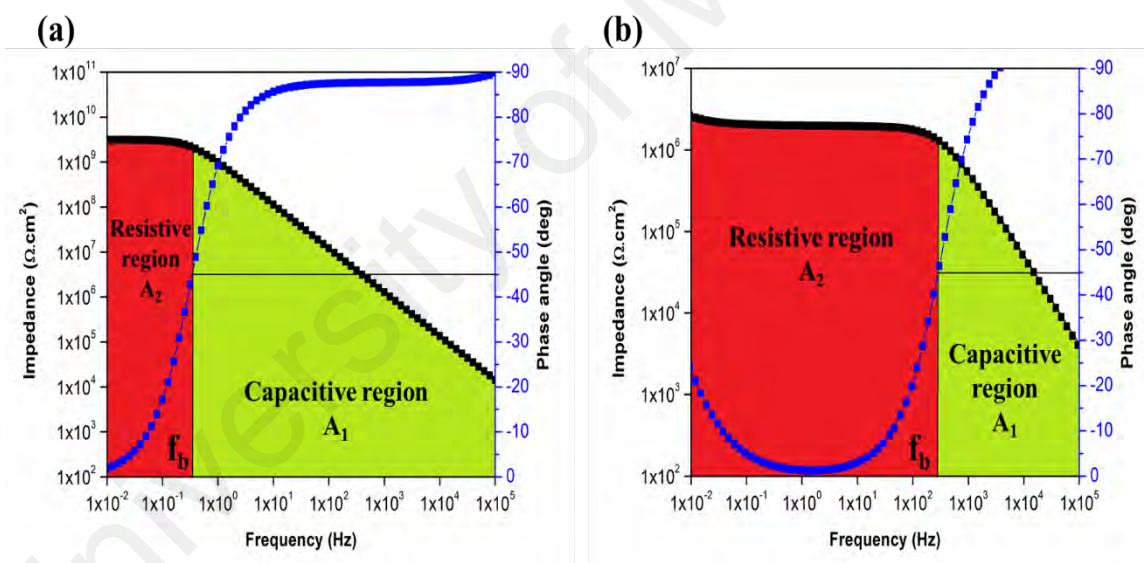


Figure 6.29: Bode plots of ES 0 coating system after (a) 1 day and (b) 60 days of immersion along with the determining the breakpoint frequency and the corresponding capacitive (A_1) and resistive (A_2) regions.

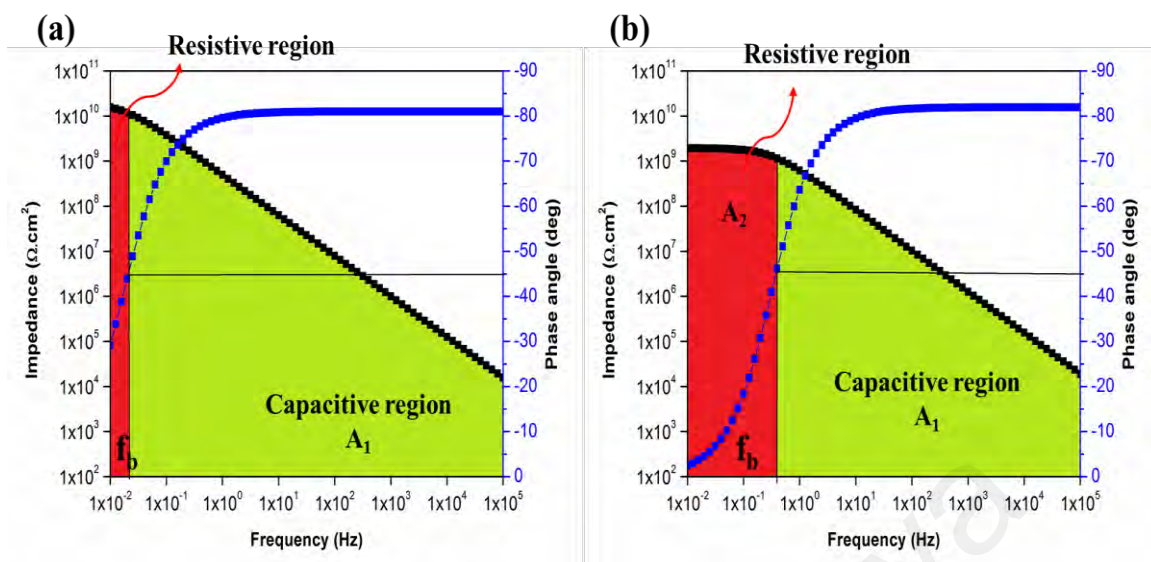


Figure 6.30: Bode plots of ES 1 coating system after (a) 1 day and (b) 60 days of immersion along with the determining the breakpoint frequency and the corresponding capacitive (A1) and resistive (A2) regions.

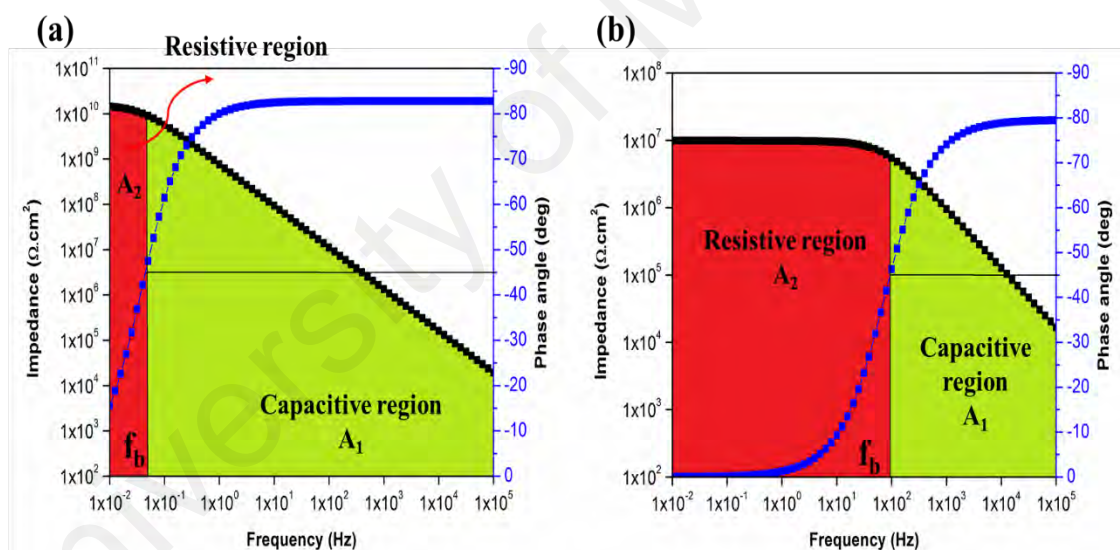


Figure 6.31: Bode plots of ES 2 coating system after (a) 1 day and (b) 60 days of immersion along with the determining the breakpoint frequency and the corresponding capacitive (A1) and resistive (A2) regions.

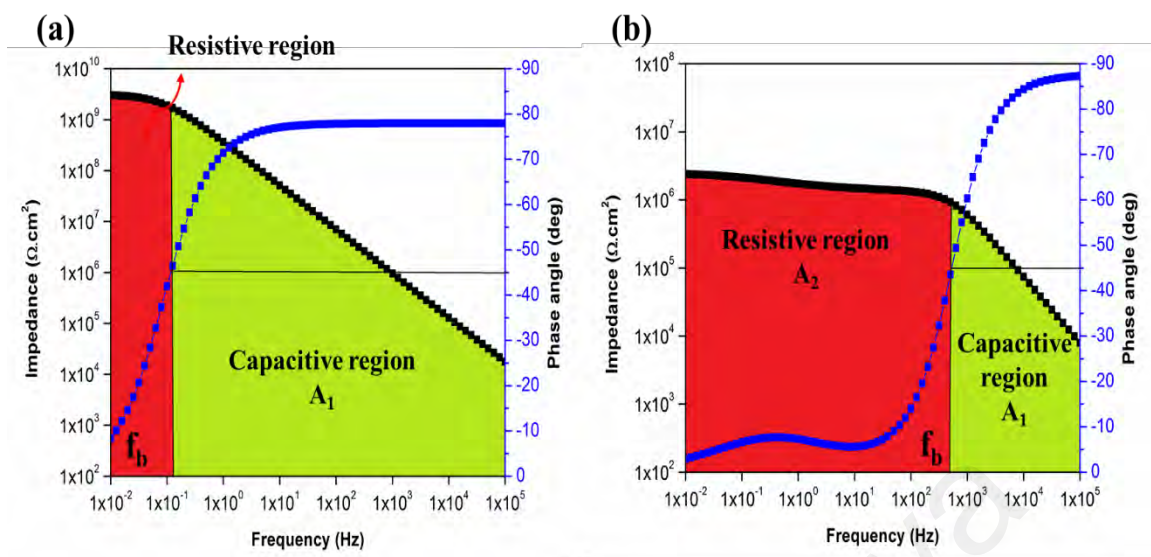


Figure 6.32: Bode plots of ES 4 coating system after (a) 1 day and (b) 60 days of immersion along with the determining the breakpoint frequency and the corresponding capacitive (A1) and resistive (A2) regions.

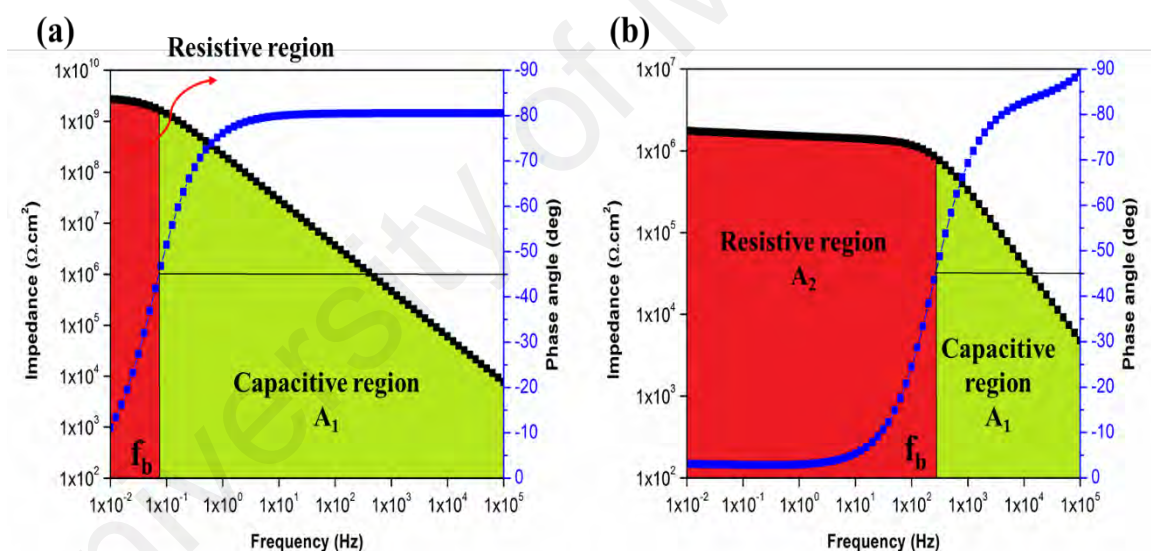


Figure 6.33: Bode plots of ES 6 coating system after (a) 1 day and (b) 60 days of immersion along with the determining the breakpoint frequency and the corresponding capacitive (A1) and resistive (A2) regions.

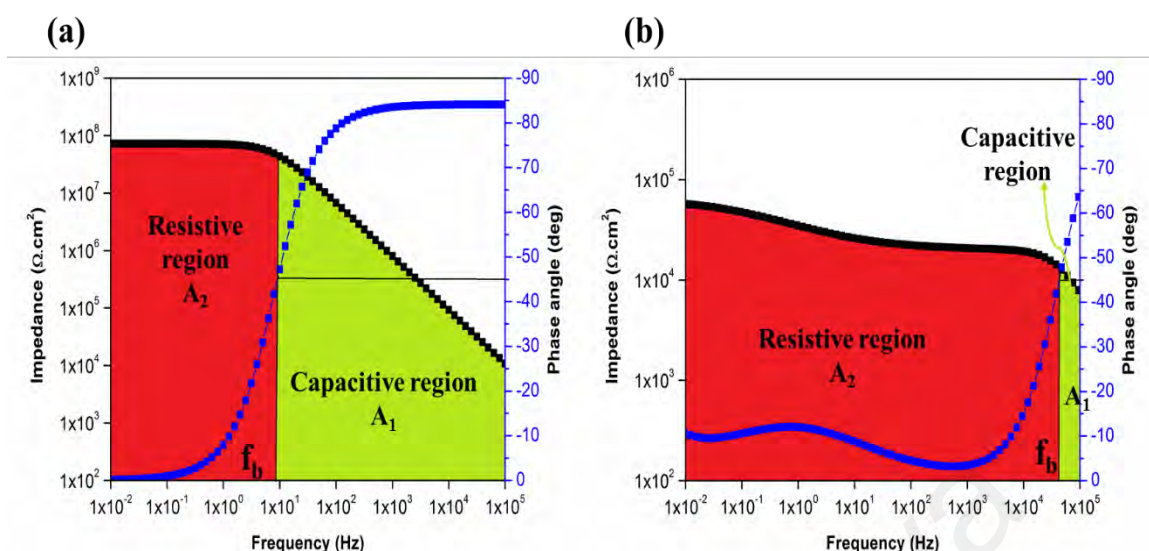


Figure 6.34: Bode plots of ES 8 coating system after (a) 1 day and (b) 60 days of immersion along with the determining the breakpoint frequency and the corresponding capacitive (A_1) and resistive (A_2) regions.

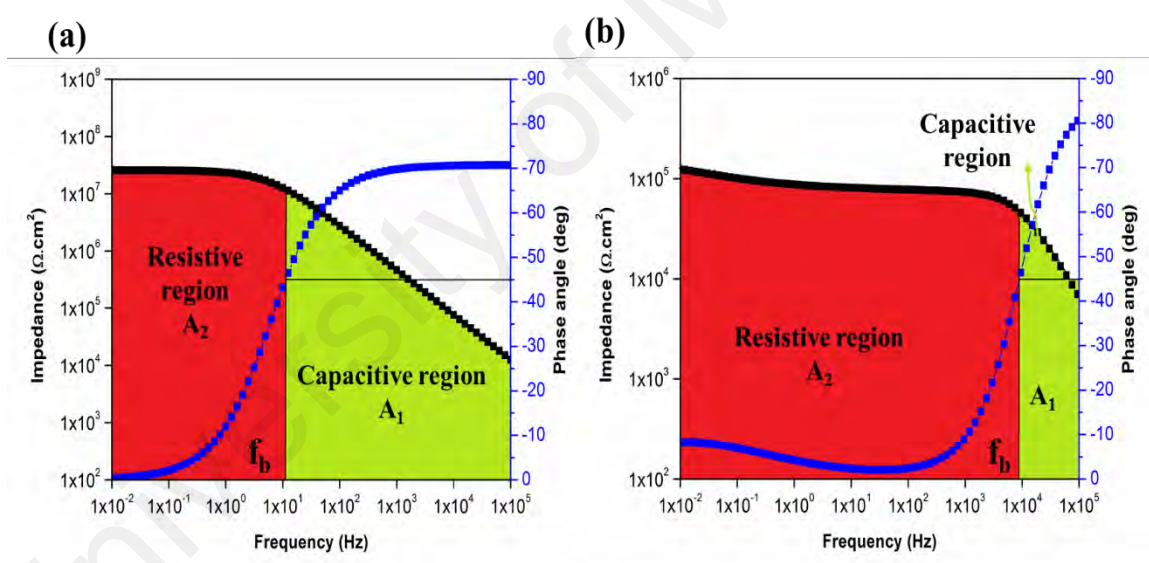


Figure 6.35: Bode plots of ES 10 coating system after (a) 1 day and (b) 60 days of immersion along with the determining the breakpoint frequency and the corresponding capacitive (A_1) and resistive (A_2) regions.

6.8 Summary

In this chapter, the effects of introducing different loading ratios of E and ESO into the acrylic–silicone polymeric blend were investigated. Several characterization techniques were performed to evaluate the different properties of the developed hybrid organic coating films.

FTIR was employed to investigate the chemical structure and to confirm the effectiveness of the curing regimes in crosslinking the different organic components and achieving coating films with good curing levels. The obtained results reveal the existence of crosslinking between all the organic components and confirm the ability of the NCO curing agent to develop an excellent crosslinked structure.

After the application of the developed E–ESO organic coating systems, the wettability of the coated surface was examined using CA measurements. As mentioned in the previous chapter, generally, there are two main factors directly affecting surface wettability, namely, the chemical composition, i.e., the surface energy of the utilized materials, and the surface roughness.

Since no significant changes are believed to have occurred in the surface roughness after the introduction of E and ESO, the chemical composition, as measured by the surface energy, was the main contributor to the altered wettability of the developed coating systems. The hydrophilic nature of E led to the observation of a slight decrease in the CA values with the respect to the AS 0 coating system. However, as the loading amount of ESO increased in the polymeric blend, the resulting coating systems show higher CA values, which is attributed to the hydrophobic character of soybean oil.

The influence of modifying the acrylic–silicone polymeric matrix with different loading rates of E and ESO on the transparency of the resulting coating film was investigated via UV-Vis spectroscopy. The obtained spectra of the ES 0 coating system following the addition of 10 wt. % E, show that E did not alter the transparency of the

coating film in the AS 0 coating system. On the other hand, ESO in the polymer matrices decreased the light transmission of the composite films, although ESO up to a 4 wt. % loading ratio did not significantly alter the transparency of the coating film. As such, the ES1, ES 2 and ES 4 coating systems can still be considered for any optical application. However, when the concentration of ESO exceeded 4 wt. %, up to 10 wt. %, a high degree of translucency was observed.

The adhesion properties of the developed E–ESO organic coating systems were investigated via the CHT method. It was interesting to note that 5B-grade surfaces grade, which indicate superior adhesion properties, according to ASTM D3359 standard, were recorded for the developed coating systems. This further confirms the successful development of multifunctional hybrid organic coating systems.

In TGA studies, the decomposition of the developed E–ESO organic coating systems was investigated. Moreover, the thermal stability and the changes in the IDT, the temperature at which 50 % weight loss occurred (T50 wt. %) and the residue yields at 700 °C were also recorded. It is interesting to note that all the coating films showed thermal degradation in four main stages, which is similar to the degradation of the AS 0 coating system. This further confirms the good crosslinked structure of all the organic components with good thermal stability. Moreover, higher thermal stability was obtained by the addition of ESO, especially with the application of the ES 1 coating system.

In this chapter, the corrosion protection performance and the barrier properties of the developed E–ESO organic coating systems were reported, based on the results of the EIS technique after one day, 30 days and 60 days of immersion. It was interesting to note that modifying the acrylic–silicone polymeric matrix with different loading amounts of E and ESO enhanced the corrosion protection performance. The most pronounced enhancement was gained by the application of the ES 1 coating system. The EIS results for the ES 1 coating system revealed the development of an intact coating film with capacitive

behaviour for up to 60 days of immersion. However, increasing the amount of the ESO resulted in no further enhancement of the corrosion protection ability. Moreover, the EIS results for the breakpoint frequency values further confirm the remarkable stability of the ES1 coating system to withstand corrosion and prevent the penetration of the corrosive agent to the surface of the substrate.

University of Malaya

CHAPTER 7: CONCLUSIONS AND SUGGESTIONS FOR FUTURE WORK

7.1 Conclusions

In this study, an acrylic–silicone polymeric matrix with NCO as the curing agent and butyl acetate as the solvent were prepared and utilized as the base hybrid polymeric matrix for two type of nanocomposite coating systems.

Two types of nanoparticles, SiO₂ and ZnO nanoparticles, were used to individually develop two distinct nanocomposite coating systems. Moreover, different loading ratios of the utilized nanoparticles, 1 wt. %, 3 wt. %, 5 wt. %, and 8 wt. %, were introduced into the hybrid polymeric matrix to obtain a better understanding of the influence of the embedded inorganic nanoparticles and their loading ratios on the overall performance of the developed coating films. Also, the various effects of the hybrid organic polymeric matrix were evaluated. To do so, the solution intercalation method was utilized to effectively introduce the nanoparticles into the polymeric matrix.

The multifunctionality of these fabricated nanocomposite coating systems was discussed and the influence of the incorporation of nanoparticles of different types, sizes and loading rates on the overall coating performance was investigated. However, the need to develop an entirely organic multifunctional coating system remains very attractive. Therefore, these studies were extended to develop and analyse an organic hybrid coating system comprising the same base hybrid acrylic–silicone hybrid blend with the addition of epoxy resin (E) and epoxidized soybean oil (ESO) at different loading rates.

To prove the successful development of a single-layer coating system that could act as a multifunctional coating film, various properties were investigated. As such, several characterization techniques were employed to evaluate the changes that occurred after modifying the hybrid acrylic–silicone polymeric matrix with different types and loading ratios of nanoparticles and after the introduction of a new organic resin and natural oil to the polymeric blend.

FTIR was employed to investigate the chemical structure and to verify the achievement of a good curing level of the prepared acrylic–silicone polymeric blend. The obtained FTIR spectra for the AS 0 coating system clearly indicated the compatibility between acrylic and silicone resins and confirmed the ability of the polyisocyanate (NCO) curing agent to develop an excellent crosslinked structure.

The FTIR technique was also utilized to confirm the crosslinking of the E and ESO to the acrylic and silicone resins and to prove the ability of the NCO curing agent to develop an acceptable level of curing. The obtained results revealed the existence of crosslinking between all the organic components, with all the materials utilized as modifiers - silicone resin, E and ESO - were linked to the acrylic base resin.

On the other hand, reliable information regarding the surface morphology of the developed nanocomposite coating systems, namely the SiO₂ and ZnO nanocomposites, was obtained via the FESEM technique. FESEM micrographs of the surfaces coated with the nanocomposite coating systems revealed the good dispersion of nanoparticles in the polymeric matrix, which is clear evidence of the effectiveness of the solution intercalation method, with the assistance of sonication, in achieving good dispersion of the nanofillers. Furthermore, the FESEM images revealed the coating films to have no microcracks, which proves the optimum curing of the polymeric nanocomposite coatings.

However, it is noted that in the utilization of both SiO₂ and ZnO nanoparticles as reinforcing particles, as the nanoparticles loading ratio increased, the degree of agglomeration increased, especially with the application of the coating system loaded with 8 wt. % of nanoparticles. This was attributed to the increase in the number of the nanoparticles in the unit area, and therefore the increased ability of the nanoparticles to be attracted to each other and form relatively larger agglomerated particles.

In this study, attempts were made to achieve a polymeric base coating system that was multifunctional by the utilization of a single-layer coating film. The hydrophobicity of

the coated surface was one of the main functions investigated. CA measurements were performed to examine the wettability of the developed coating systems. Hydrophobic coated surfaces were realized by the utilization of two types of the nanoparticles and different loading ratios.

For the SiO₂ and ZnO nanocomposites, the highest CA value was recorded when 3 wt. % of nanoparticles were used. These observations were in strong agreement with the FESEM findings, for which the best dispersion of nanoparticles resulted in the highest CA.

However, increasing the nanoparticle loading ratio above 3 wt. % showed no further improvement regarding the surface hydrophobicity. This can be explained by the tendency of nanoparticles at high loading ratios to collect more at the bottom of the coating film than at the surface, therefore tending to affect the bulk properties more than the surface properties.

In contrast, modifying the hybrid polymeric matrix with E and ESO did not result in hydrophobic coated surfaces, even though the wettability of the coating systems shifted to greater hydrophobicity as the amount of ESO was increased.

The optical properties of the developed coating systems were investigated via UV-Vis spectroscopy. First, studies were conducted to evaluate the optical properties of the AS 0 coating system to demonstrate the effects of silicone resin on the optical properties of the coating film fabricated with 100 wt. % of acrylic resin, A 100. The obtained results confirm that the addition of silicone resin to the acrylic matrix does not influence the transparency of the coating film. With respect to the AS 0 light transmittance spectra, the influence of SiO₂ nanoparticle on the optical properties was also investigated. It was observed that as the loading ratio of the SiO₂ nanoparticles increased, the light transmittance values in all the coating films were classified as transparent, with high transmittances values in the visible region. In the utilization of ZnO nanoparticles, greater

reduction in the transmittance percentage was observed as the loading ratio of ZnO nanoparticles was increased. This was attributed to the tendency of the nanoparticles to form larger agglomerated particles at high loading ratios, hence, there was greater suppression of transparency. Moreover, the optical properties of the developed E-ESO organic coating systems were investigated and the results indicated that E did not affect the optical properties of the hybrid acrylic-polymeric blend, whereas the presence of ESO in the polymer matrices decreased the light transmission of composite films. However, the most pronounced effect was observed when loading rates above 4 wt. % were utilized.

Of the developed coating systems, only the ZnO nanocomposite coating systems demonstrated UV shielding, which was more obvious as the loading ratio of the ZnO nanoparticles was increased.

The adhesion properties of the developed coating systems were evaluated via the employment of CHT, with reference to the ASTM D3359 method B standard. It was found that introducing different loading ratios of SiO₂ nanoparticles did not alter the excellent adhesion properties of the hybrid polymeric matrix, for which surfaces with 5B grade were observed for the AS 0 coating system, nor in the developed SiO₂ nanocomposite coating systems. For the ZnO nanocomposite coating systems, the application of AZ 1 and AZ 3 coating systems produced surfaces with superior adhesion properties without any significant change in the AS 0 coating system. However, loss of adhesion was noted as the loading ratio of ZnO nanoparticles exceeded 3 wt. % and a slight decrease in the adhesion properties was observed for surfaces with grades 4B and 3B in the AZ 5 and AZ 8 coating systems, respectively. In the modified E-ESO coating system, no loss of adhesion was observed and there was 0 % removal of the coatings from the steel substrate.

With respect to the TGA results of the AS 0 coating system, the developed coating systems, namely, the SiO₂ and ZnO nanocomposites and modified E-ESO coating

systems, showed no significant changes, and all the coating films demonstrated the same four stages of degradation. These findings reveal that all the modifications enhanced the overall performance of the hybrid acrylic–silicone polymeric matrix and did not reduce the good thermal stability features. In contrast, the TGA results, after introducing 9 wt. % of E and 1 w. % of ESO into the acrylic–silicone polymeric blend (ES 1 coating system) reveal that higher thermal stability was obtained.

To guarantee that the developed coating systems obtain excellent corrosion protection for the surfaces of the metallic substrates, EIS tests were conducted at various intervals for up to 90 days of exposure of the coated samples to 3.5 % NaCl solution. The results were presented in the form of Bode and Nyquist plots after one day, 30 days, 60 days and 90 days of immersion. Three different equivalent circuit models were suggested and utilized to obtain a fuller understanding of the electrochemical behaviour of the coating films and to obtain the best numerical fitting in the study periods. The values of the parameters obtained by fitting the EIS data according to the proposed equivalent circuit models after the different periods of immersion were included. Moreover, the concept of breakpoint frequency was used to further understand the changes to the coating films during the entire exposure period. The EIS findings can be summarized as follows:

- When utilizing SiO₂ nanoparticles as the reinforcing agents, the best corrosion protection performance was observed for the AS 3 coating system with a loading ratio of 3 wt. % in the hybrid polymeric matrix. The intact behaviour of the coating film was observed over the entire immersion period without significant changes in the shapes of the Bode and Nyquist plots. Furthermore, this system showed the lowest breakpoint frequency value, and therefore a relatively smaller resistive region in the low-frequency domain and a larger capacitive region. It is worth noting that of all the developed coating systems, only the SiO₂ nanocomposite coating systems exhibited significant stability in their electrochemical

performance after 60 days of immersion. Hence, the EIS studies were conducted for up to 90 days of immersion. Moreover, the intact behaviour and the excellent barrier properties of the AS 3 coating system were in complete agreement with the FESEM and CA results, in which the best dispersion of SiO₂ and the highest CA value were recorded, respectively.

- Similar observations were recorded for the utilization of ZnO nanoparticles, for which a 3 wt. % loading ratio yielded the best nanocomposite coating system, namely, AZ 3. Even after 60 days of immersion, the coating film of the AZ 3 coating system maintained effective isolation of the substrate surface with remarkable barrier properties. The intact behaviour of the AZ 3 coating system was further confirmed by the results of the breakpoint frequency method, achieving the lowest breakpoint frequency value, and therefore the smallest resistive region and largest capacitive region in the Bode plot after 60 days of immersion. Again, the results of all the other characterization technique support the EIS findings, with the surface coated with the AZ 3 coating systems demonstrating good dispersion of the nanoparticles, as confirmed by FESEM, and the greatest hydrophobicity, as evidenced by the highest CA value.
- The potential for achieving a multifunctional coating system with fully organic components was also investigated in this study. The EIS results obtained after adding various loading ratios of E and ESO revealed the possibility of these systems obtaining an acceptable level of corrosion protection with good barrier properties. Of the prepared modified organic coating systems, the ES 1 coating system exhibited remarkable stability for up to 60 days of immersion and maintained capacitive behaviour without significant changes in the shape of its Bode and Nyquist plots throughout the exposure periods. The results obtained regarding breakpoint frequency further confirm the good performance of the ES

1 coating system and gave solid evidence of the ability of certain amounts of E and ESO, specifically 9 wt. % and 1 wt. %, respectively, to develop an intact organic coating layer with optimum barrier properties that can withstand corrosion for up to 60 days of immersion.

7.2 Suggestions for Future Work

In future work, investigations could address the possibility of developing more eco-friendly coating systems that could be fabricated by replacing the solvent-based resin with one that is water-based. However, detailed studies must be undertaken to determine the appropriate curing regimes. Furthermore, as the study results reported here on the modified E-ESO organic coating systems are promising, more research regarding the development of nanocomposite coating systems that utilize such hybrid polymeric blends as a matrix must be considered. However, challenges remain regarding the compatibility of the utilized nanoparticle and soybeans, which are hydrophilic in nature.

On the other hand, adding more functions to the developed coating systems could be considered. For instance, demand is increasing for a self-healing feature in today's coating industries. Also, through a social-marketplace and acceptance study, we could strengthen the economics associated with developing coating systems by ensuring their technical efficiencies as well as their marketability and social acceptance. Based on the social marketplace, this model could identify the optimal type of materials used in different markets. This would be a step toward the commercialization of research output by proposing an optimal solution for the design and marketing of developed coating systems.

REFERENCES

- Ahmed, N., El-Gawad, W. A., Mohamed, M., & Elshami, A. (2016). Introducing rice husk after utilizing new technology as anticorrosive pigments in organic coatings. *Progress in Organic Coatings*, 101, 309-321.
- Ahn, B. K., Kraft, S., Wang, D., & Sun, X. S. (2011). Thermally stable, transparent, pressure-sensitive adhesives from epoxidized and dihydroxyl soybean oil. *Biomacromolecules*, 12(5), 1839-1843.
- Amerio, E., Fabbri, P., Malucelli, G., Messori, M., Sangermano, M., & Taurino, R. (2008). Scratch resistance of nano-silica reinforced acrylic coatings. *Progress in Organic Coatings*, 62(2), 129-133.
- Ananda Kumar, S., & Sankara Narayanan, T. (2002). Thermal properties of siliconized epoxy interpenetrating coatings. *Progress in Organic Coatings*, 45(4), 323-330.
- Andriot, M., Chao, S., Colas, A., Cray, S., DeBuyl, F., DeGroot, J., . . . Gerlach, E. (2007). *Silicones in industrial applications: Inorganic polymers* (1st ed, pp. 61-161). Nova Science Publishers.
- Aneja, K. S., Bohm, S., Khanna, A., & Bohm, H. M. (2015). Graphene based anticorrosive coatings for Cr (VI) replacement. *Nanoscale*, 7(42), 17879-17888.
- Balaskas, A., Kartsonakis, I., Snihirova, D., Montemor, M., & Kordas, G. (2011). Improving the corrosion protection properties of organically modified silicate-epoxy coatings by incorporation of organic and inorganic inhibitors. *Progress in Organic Coatings*, 72(4), 653-662.
- Baştürk, E., Inan, T., & Güngör, A. (2013). Flame retardant UV-curable acrylated epoxidized soybean oil based organic-inorganic hybrid coating. *Progress in Organic Coatings*, 76(6), 985-992.
- Baştürk, E., Inan, T., & Güngör, A. (2013). Flame retardant UV-curable acrylated epoxidized soybean oil based organic-inorganic hybrid coating. *Progress in Organic Coatings*, 76(6), 985-992.
- Behera, D., & Banthia, A. (2008). Synthesis, characterization, and kinetics study of thermal decomposition of epoxidized soybean oil acrylate. *Journal of Applied Polymer Science*, 109(4), 2583-2590.
- Bravo, J., Zhai, L., Wu, Z., Cohen, R. E., & Rubner, M. F. (2007). Transparent superhydrophobic films based on silica nanoparticles. *Langmuir*, 23(13), 7293-7298.
- Bueno-Ferrer, C., Garrigós, M., & Jiménez, A. (2010). Characterization and thermal stability of poly (vinyl chloride) plasticized with epoxidized soybean oil for food packaging. *Polymer Degradation and Stability*, 95(11), 2207-2212.
- Chen, L., Song, R., Li, X., Guo, Y., Wang, C., & Jiang, Y. (2015). The improvement of corrosion resistance of fluoropolymer coatings by SiO₂/poly (styrene-co-butyl acrylate) nanocomposite particles. *Applied Surface Science*, 353, 254-262.

- Chen, Z., Wu, J. F., Fernando, S., & Jagodzinski, K. (2011). Soy-based, high biorenewable content UV curable coatings. *Progress in Organic Coatings*, 71(1), 98-109.
- Dolatzadeh, F., Moradian, S., & Jalili, M. M. (2011a). Influence of various surface treated silica nanoparticles on the electrochemical properties of SiO₂/polyurethane nanocoatings. *Corrosion Science*, 53(12), 4248-4257.
- Dolatzadeh, F., Moradian, S., & Jalili, M. M. (2011b). Influence of various surface treated silica nanoparticles on the electrochemical properties of SiO₂/polyurethane nanocoatings. *Corrosion Science*, 53(12), 4248-4257.
- Duo, S., Li, M., Zhu, M., & Zhou, Y. (2008). Polydimethylsiloxane/silica hybrid coatings protecting Kapton from atomic oxygen attack. *Materials Chemistry and Physics*, 112(3), 1093-1098.
- El Rayes, M. M., Abdo, H. S., & Khalil, K. A. (2013). Erosion-corrosion of cermet coating. *International Journal of Electrochemical Science*, 8(1), 1117-1137.
- Freitag, W., & Stoye, D. (2008). *Paints, coatings and solvents* (2nd ed, pp. 101-159). John Wiley & Sons.
- Gangloff, R. P. (1995). Environmental cracking-corrosion fatigue. *ASTM MANUAL SERIES MNL*, 253-271. Retrieved from [http:// www.psu.edu](http://www.psu.edu)
- Ghasemi, E., Ramezanzadeh, B., Saket, S., & Ashhari, S. (2016). Electrochemical investigation of the epoxy nanocomposites containing MnAl₂O₄ and CoAl₂O₄ nanopigments applied on the aluminum alloy 1050. *Journal of Coatings Technology and Research*, 13(1), 97-114.
- Habib, F., & Bajpai, M. (2011). Synthesis and characterization of acrylated epoxidized soybean oil for UV cured coatings. *Chemistry & Chemical Technology*, 5(3), 317-326.
- Heidarian, M., Shishesaz, M., Kassiriha, S., & Nematollahi, M. (2010). Characterization of structure and corrosion resistivity of polyurethane/organoclay nanocomposite coatings prepared through an ultrasonication assisted process. *Progress in Organic Coatings*, 68(3), 180-188.
- Hirschorn, B., Orazem, M. E., Tribollet, B., Vivier, V., Frateur, I., & Musiani, M. (2010). Determination of effective capacitance and film thickness from constant-phase-element parameters. *Electrochimica Acta*, 55(21), 6218-6227.
- Hong, J., Luo, Q., Wan, X., Petrović, Z. S., & Shah, B. K. (2011). Biopolymers from vegetable oils via catalyst-and solvent-free “Click” chemistry: effects of cross-linking density. *Biomacromolecules*, 13(1), 261-266.
- Hou, B., Li, X., Ma, X., Du, C., Zhang, D., Zheng, M., . . . Ma, F. (2017). The cost of corrosion in China. *npj Materials Degradation*, 1(1), 4.
- Hou, S.-S., Chung, Y.-P., Chan, C.-K., & Kuo, P.-L. (2000). Function and performance of silicone copolymer. Part IV. Curing behavior and characterization of epoxy-siloxane copolymers blended with diglycidyl ether of bisphenol-A. *Polymer*, 41(9), 3263-3272.

- Huang, H.-C., & Hsieh, T.-E. (2010). Preparation and characterizations of highly transparent UV-curable ZnO-acrylic nanocomposites. *Ceramics International*, 36(4), 1245-1251.
- Huttunen-Saarivirta, E., Vaganov, G., Yudin, V., & Vuorinen, J. (2013). Characterization and corrosion protection properties of epoxy powder coatings containing nanoclays. *Progress in Organic Coatings*, 76(4), 757-767.
- Islam, M., Azhar, M. R., Fredj, N., Burleigh, T. D., Oloyede, O. R., Almajid, A. A., & Shah, S. I. (2015). Influence of SiO₂ nanoparticles on hardness and corrosion resistance of electroless Ni-P coatings. *Surface and Coatings Technology*, 261, 141-148.
- Jie, L., Xiang-Bo, L., Jia, W., Tian-Yuan, L., & Xiao-Ming, W. (2013). Studies of impedance models and water transport behaviours of epoxy coating at hydrostatic pressure of seawater. *Progress in Organic Coatings*, 76(7), 1075-1081.
- John, S., Joseph, A., Jose, A. J., & Narayana, B. (2015). Enhancement of corrosion protection of mild steel by chitosan/ZnO nanoparticle composite membranes. *Progress in Organic Coatings*, 84, 28-34.
- Jones, F. N., Nichols, M. E., & Pappas, S. P. (2017). *Organic coatings: Science and technology* (3rd ed.). John Wiley & Sons.
- Kalendová, A., Veselý, D., Kohl, M., & Stejskal, J. (2014). Effect of surface treatment of pigment particles with polypyrrole and polyaniline phosphate on their corrosion inhibiting properties in organic coatings. *Progress in Organic Coatings*, 77(9), 1465-1483.
- Kalendová, A., Veselý, D., & Stejskal, J. (2008). Organic coatings containing polyaniline and inorganic pigments as corrosion inhibitors. *Progress in Organic Coatings*, 62(1), 105-116.
- Kapridaki, C., & Maravelaki-Kalaitzaki, P. (2013). TiO₂-SiO₂-PDMS nano-composite hydrophobic coating with self-cleaning properties for marble protection. *Progress in Organic Coatings*, 76(2), 400-410.
- Kasturibai, S., & Kalaignan, G. P. (2013). Physical and electrochemical characterizations of Ni-SiO₂ nanocomposite coatings. *Ionics*, 19(5), 763-770.
- Khan, R., Azhar, M. R., Anis, A., Alam, M. A., Boumaza, M., & Al-Zahrani, S. M. (2016). Facile synthesis of epoxy nanocomposite coatings using inorganic nanoparticles for enhanced thermo-mechanical properties: a comparative study. *Journal of Coatings Technology and Research*, 13(1), 159-169.
- Knudsen, O. Ø., & Forsgren, A. (2017). *Corrosion control through organic coatings* (2nd ed.). CRC Press.
- Krasowska, M., Zawala, J., & Malysa, K. (2009). Air at hydrophobic surfaces and kinetics of three phase contact formation. *Advances in Colloid and Interface Science*, 147, 155-169.

- Lakshmi, R., Bera, P., Anandan, C., & Basu, B. J. (2014). Effect of the size of silica nanoparticles on wettability and surface chemistry of sol-gel superhydrophobic and oleophobic nanocomposite coatings. *Applied Surface Science*, 320, 780-786.
- Landolt, D. (2007). *Corrosion and surface chemistry of metals* (1st ed.). CRC Press.
- Lang, E. (2012). *The role of active elements in the oxidation behaviour of high temperature metals and alloys*: Springer Science & Business Media.
- Li, Y.-Q., Fu, S.-Y., & Mai, Y.-W. (2006). Preparation and characterization of transparent ZnO/epoxy nanocomposites with high-UV shielding efficiency. *Polymer*, 47(6), 2127-2132.
- Lyon, S. B., Bingham, R., & Mills, D. J. (2017). Advances in corrosion protection by organic coatings: What we know and what we would like to know. *Progress in Organic Coatings*, 102, 2-7.
- Ma, X.-Y., & Zhang, W.-D. (2009). Effects of flower-like ZnO nanowhiskers on the mechanical, thermal and antibacterial properties of waterborne polyurethane. *Polymer Degradation and Stability*, 94(7), 1103-1109.
- Marcus, P. (2011). *Corrosion mechanisms in theory and practice* (3rd ed.). CRC press.
- McMurray, H., Holder, A., Williams, G., Scamans, G., & Coleman, A. (2010). The kinetics and mechanisms of filiform corrosion on aluminium alloy AA6111. *Electrochimica Acta*, 55(27), 7843-7852.
- Meng, F., Liu, L., Tian, W., Wu, H., Li, Y., Zhang, T., & Wang, F. (2015). The influence of the chemically bonded interface between fillers and binder on the failure behaviour of an epoxy coating under marine alternating hydrostatic pressure. *Corrosion Science*, 101, 139-154.
- Mohamed, A. M., Abdullah, A. M., & Younan, N. A. (2015). Corrosion behavior of superhydrophobic surfaces: A review. *Arabian Journal of Chemistry*, 8(6), 749-765.
- Montemor, M. (2014). Functional and smart coatings for corrosion protection: a review of recent advances. *Surface and Coatings Technology*, 258, 17-37.
- Montemor, M., & Ferreira, M. (2007). Electrochemical study of modified bis-[triethoxysilylpropyl] tetrasulfide silane films applied on the AZ31 Mg alloy. *Electrochimica Acta*, 52(27), 7486-7495.
- Mostafaei, A., & Nasirpour, F. (2014). Epoxy/polyaniline-ZnO nanorods hybrid nanocomposite coatings: Synthesis, characterization and corrosion protection performance of conducting paints. *Progress in Organic Coatings*, 77(1), 146-159.
- Ni, B., Yang, L., Wang, C., Wang, L., & Finlow, D. E. (2010). Synthesis and thermal properties of soybean oil-based waterborne polyurethane coatings. *Journal of Thermal Analysis and Calorimetry*, 100(1), 239-246.
- Ogihara, H., Xie, J., Okagaki, J., & Saji, T. (2012). Simple method for preparing superhydrophobic paper: Spray-deposited hydrophobic silica nanoparticle

- coatings exhibit high water-repellency and transparency. *Langmuir*, 28(10), 4605-4608.
- Ou, C. F., & Shiu, M. C. (2010). Epoxy composites reinforced by different size silica nanoparticles. *Journal of Applied Polymer Science*, 115(5), 2648-2653.
- Patel, C. J., & Mannari, V. (2014). Air-drying bio-based polyurethane dispersion from cardanol: Synthesis and characterization of coatings. *Progress in Organic Coatings*, 77(5), 997-1006.
- Pouget, E., Tonnar, J., Lucas, P., Lacroix-Desmazes, P., Ganachaud, F. o., & Boutevin, B. (2009). Well-architected poly (dimethylsiloxane)-containing copolymers obtained by radical chemistry. *Chemical Reviews*, 110(3), 1233-1277.
- Pourhashem, S., Vaezi, M. R., & Rashidi, A. (2017). Investigating the effect of SiO₂-graphene oxide hybrid as inorganic nanofiller on corrosion protection properties of epoxy coatings. *Surface and Coatings Technology*, 311, 282-294.
- Quadri, T. W., Olasunkanmi, L. O., Fayemi, O. E., Solomon, M. M., & Ebenso, E. E. (2017). Zinc Oxide Nanocomposites of Selected Polymers: Synthesis, Characterization, and Corrosion Inhibition Studies on Mild Steel in HCl Solution. *ACS Omega*, 2(11), 8421-8437.
- Ramesh, K., Nor, N., Ramesh, S., Vengadaesvaran, B., & Arof, A. (2013). Studies on Electrochemical Properties and FTIR analysis of Epoxy Polyester Hybrid Coating System. *International Journal of Electrochemical Science*, 8, 8422-8432.
- Ramesh, K., Osman, Z., Arof, A., Vengadaeswaran, B., & Basirun, W. (2008). Structural and corrosion protection analyses of coatings containing silicone-polyester resins. *Pigment & Resin Technology*, 37(1), 37-41.
- Ramezanzadeh, B., Attar, M., & Farzam, M. (2011). A study on the anticorrosion performance of the epoxy-polyamide nanocomposites containing ZnO nanoparticles. *Progress in Organic Coatings*, 72(3), 410-422.
- Ramezanzadeh, B., Niroumandrad, S., Ahmadi, A., Mahdavian, M., & Moghadam, M. M. (2016). Enhancement of barrier and corrosion protection performance of an epoxy coating through wet transfer of amino functionalized graphene oxide. *Corrosion Science*, 103, 283-304.
- Ramis Rao, S. (2016). *Development of an anti corrosion coating using organic resins hybrid system*. (Published doctoral thesis). University of Malaya, Kuala Lumpur, Malaysia.
- Ramis Rau, S., Vengadaesvaran, B., Naziron, N., & Arof, A. (2013). Strength and adhesion properties of acrylic polyol-epoxy polyol resin protective coating on mild steel substrate. *Pigment & Resin Technology*, 42(2), 111-116.
- Rashidi, N., Alavi-Soltani, S. R., & Asmatulu, R. (2007). Crevice corrosion theory, mechanisms and prevention methods. Retrieved from [http:// www.wichita.edu](http://www.wichita.edu)
- Rau, S. R., Vengadaesvaran, B., Ramesh, K., & Arof, A. (2012). Studies on the Adhesion and Corrosion Performance of an Acrylic-Epoxy Hybrid Coating. *The Journal of Adhesion*, 88(4-6), 282-293.

- Ray, S. S., & Okamoto, M. (2003). Polymer/layered silicate nanocomposites: a review from preparation to processing. *Progress in Polymer Science*, 28(11), 1539-1641.
- Reddy, B. (2011). *Advances in diverse industrial applications of nanocomposites* (1st ed.). Intech.
- Revie, R. W. (2008). *Corrosion and corrosion control: an introduction to corrosion science and engineering*: John Wiley & Sons.
- Rezaei, F., Sharif, F., Sarabi, A., Kasiriha, S., Rahmanian, M., & Akbarinezhad, E. (2010). Evaluating water transport through high solid polyurethane coating using the EIS method. *Journal of Coatings Technology and Research*, 7(2), 209-217.
- Ribeiro, T., Baleizão, C., & Farinha, J. P. S. (2014). Functional films from silica/polymer nanoparticles. *Materials*, 7(5), 3881-3900.
- Saji, V. S., & Cook, R. (2012). *Corrosion protection and control using nanomaterials* (1st ed.). Elsevier.
- Salihoglu, G., & Salihoglu, N. K. (2016). A review on paint sludge from automotive industries: Generation, characteristics and management. *Journal of Environmental Management*, 169, 223-235.
- Selvaganapathi, A. (2013). Synthesis and characterization of organic inorganic hybrid epoxy layered silicate CNT Nanocomposites.
- Sharma, B. K., Adhvaryu, A., & Erhan, S. (2006). Synthesis of hydroxy thio-ether derivatives of vegetable oil. *Journal of Agricultural and Food Chemistry*, 54(26), 9866-9872.
- Sharmin, E., Imo, L., Ashraf, S., & Ahmad, S. (2004). Acrylic-melamine modified DGEBA-epoxy coatings and their anticorrosive behavior. *Progress in Organic Coatings*, 50(1), 47-54.
- Shen, S., & Zuo, Y. (2014). The improved performance of Mg-rich epoxy primer on AZ91D magnesium alloy by addition of ZnO. *Corrosion Science*, 87, 167-178.
- Shi, X., Nguyen, T. A., Suo, Z., Liu, Y., & Avci, R. (2009). Effect of nanoparticles on the anticorrosion and mechanical properties of epoxy coating. *Surface and Coatings Technology*, 204(3), 237-245.
- Sriharsha, P., Kumar, S., Reddy, B. R. H., & Reddy, R. S. (2017). A Review on Corrosion Resistance of Ceramic Coated Materials. *International Journal of Science and Research*, 3(2), 557-560.
- Su, C., Li, J., Geng, H., Wang, Q., & Chen, Q. (2006). Fabrication of an optically transparent super-hydrophobic surface via embedding nano-silica. *Applied Surface Science*, 253(5), 2633-2636.
- Tao, Q., Pinter, G., & Krivec, T. (2017). Influence of cooling rate and annealing on the DSC Tg of an epoxy resin. *Microelectronics Reliability*, 78, 396-400.

- Tehfe, M.-A., Lalevée, J., Gigmes, D., & Fouassier, J. P. (2010). Green chemistry: sunlight-induced cationic polymerization of renewable epoxy monomers under air. *Macromolecules*, 43(3), 1364-1370.
- Tomić, M. D., Dunjić, B., Likić, V., Bajat, J., Rogan, J., & Djonlagić, J. (2014). The use of nanoclay in preparation of epoxy anticorrosive coatings. *Progress in Organic Coatings*, 77(2), 518-527.
- Vengadaesvaran, B., Ramis Rau, S., Kasi, R., & Arof, A. (2013). Evaluation of heat resistant properties of silicone-acrylic polyol coating by electrochemical methods. *Pigment & Resin Technology*, 42(2), 117-122.
- Vengadaesvaran, B., Rau, S., Ramesh, K., Puteh, R., & Arof, A. (2010). Preparation and characterisation of phenyl silicone-acrylic polyol coatings. *Pigment & Resin Technology*, 39(5), 283-287.
- Wang, G., Zeng, Z., Chen, J., Xu, M., Zhu, J., Liu, S., . . . Xue, Q. (2016). Ultra low water adhesive metal surface for enhanced corrosion protection. *RSC Advances*, 6(47), 40641-40649.
- Wang, S., Li, Y., Fei, X., Sun, M., Zhang, C., Li, Y., . . . Hong, X. (2011). Preparation of a durable superhydrophobic membrane by electrospinning poly (vinylidene fluoride)(PVDF) mixed with epoxy-siloxane modified SiO₂ nanoparticles: a possible route to superhydrophobic surfaces with low water sliding angle and high water contact angle. *Journal of Colloid and Interface Science*, 359(2), 380-388.
- Wicks, Z. W., Jones, F. N., Pappas, S. P., & Wicks, D. A. (2007). Binders based on polyisocyanates: polyurethanes. *Organic Coatings: Science and Technology*, 3, 231-270.
- Wika, S. F. (2012). *Pitting and crevice corrosion of stainless steel under offshore conditions*. (Published master thesis), Institutt for materialteknologi, Trondheim, Norway.
- Xu, J., Sun, C., Yan, M., & Wang, F. (2012). Effects of sulfate reducing bacteria on corrosion of carbon steel Q235 in soil-extract solution. *International Journal of Electrochemical Science*, 7(11), 11281-11296.
- Yuan, X., Yue, Z., Chen, X., Wen, S., Li, L., & Feng, T. (2015). EIS study of effective capacitance and water uptake behaviors of silicone-epoxy hybrid coatings on mild steel. *Progress in Organic Coatings*, 86, 41-48.
- Zhang, D., Wang, L., Qian, H., & Li, X. (2016). Superhydrophobic surfaces for corrosion protection: a review of recent progresses and future directions. *Journal of Coatings Technology and Research*, 13(1), 11-29.
- Zhao, M., Zuo, X., Wang, C., Xiao, X., Liu, J., & Nan, J. (2016). Preparation and performance of the polyethylene-supported polyvinylidene fluoride/cellulose acetate butyrate/nano-SiO₂ particles blended gel polymer electrolyte. *Ionics*, 22(11), 2123-2132.
- Zhou, C., Lu, X., Xin, Z., Liu, J., & Zhang, Y. (2014). Polybenzoxazine/SiO₂ nanocomposite coatings for corrosion protection of mild steel. *Corrosion Science*, 80, 269-275.

- Zhou, S., Wu, L., Sun, J., & Shen, W. (2002). The change of the properties of acrylic-based polyurethane via addition of nano-silica. *Progress in Organic Coatings*, 45(1), 33-42.
- Ziegler, A., McNaney, J., Hoffmann, M., & Ritchie, R. (2005). On the Effect of Local Grain-Boundary Chemistry on the Macroscopic Mechanical Properties of a High-Purity $\text{Y}_2\text{O}_3\text{-Al}_2\text{O}_3$ -Containing Silicon Nitride Ceramic: Role of Oxygen. *Journal of the American Ceramic Society*, 88(7), 1900-1908.
- Zvonkina, I., & Soucek, M. (2016). Inorganic–organic hybrid coatings: common and new approaches. *Current Opinion in Chemical Engineering*, 11, 123-127.

University of Malaya

LIST OF PUBLICATIONS AND PAPERS PRESENTED

- Ammar, S.,** Ramesh, K., Vengadaesvaran, B., Ramesh, S., & Arof, A. (2016). A novel coating material that uses nano-sized SiO₂ particles to intensify hydrophobicity and corrosion protection properties. *Electrochimica Acta*, 220, 417-426.
- Ammar, S.,** Ramesh, K., Vengadaesvaran, B., Ramesh, S., & Arof, A. (2016). Formulation and characterization of hybrid polymeric/ZnO nanocomposite coatings with remarkable anti-corrosion and hydrophobic characteristics. *Journal of Coatings Technology and Research*, 13(5), 921-930.
- Ammar, S.,** Ramesh, K., Ma, I., Farah, Z., Vengadaesvaran, B., Ramesh, S., & Arof, A. (2017). Studies on SiO₂-hybrid polymeric nanocomposite coatings with superior corrosion protection and hydrophobicity. *Surface and Coatings Technology*, 324, 536-545.
- Ammar, S.,** Ramesh, K., Azman, N., Vengadaesvaran, B., Ramesh, S., & Arof, A. (2016). Comparison studies on the anticorrosion and overall performance of solvent/water based epoxy-copper reinforced composite coatings. *Materials Express*, 6(5), 403-413.
- Ammar, S.,** Ramesh, K., Vengadaesvaran, B., Ramesh, S., & Arof, A. (2016). Amelioration of anticorrosion and hydrophobic properties of epoxy/PDMS composite coatings containing nano ZnO particles. *Progress in Organic Coatings*, 92, 54-65.
- Basiru, Y. A., **Ammar, S.,** Ramesh, K., Vengadaesvaran, B., Ramesh, S., & Arof, A. (2018). Corrosion protection performance of nanocomposite coatings under static, UV, and dynamic conditions. *Journal of Coatings Technology and Research*, 1-13.
- Ma, I. A. W., **Ammar, S.,** Ramesh, K., Zaini, F. N., Vengadaesvaran, B., Ramesh, S., & Arof, A. (2017). Anticorrosion properties of epoxy/nanocellulose nanocomposite coating. *BioResources*, 12(2), 2912-2929.
- Ma, I. A. W., **Ammar, S.,** Ramesh, K., Vengadaesvaran, B., Ramesh, S., & Arof, A. (2017). Anticorrosion properties of epoxy-nanochitosan nanocomposite coating. *Progress in Organic Coatings*, 113, 74-81.

CONFERENCES

Ammar, S., Ramesh, K., Vengadaesvaran, B., Ramesh, S., & Arof. A. Fabrication and characterization of multifunctional nanocomposite coating system. 6th International Conference on Functional Material and Devices 2017 (ICFMD-2017), Melaka, Malaysia, 15th – 18th August 2017: **Oral Presentation.**

Ammar, S., Ramesh, K., Vengadaesvaran, B., Ramesh, S., & Gan, N. S. Formulation and characterization of epoxy - rubber hybrid polymeric composite coatings with remarkable anticorrosion and hydrophobic characteristics. The 1st Asian Researcher Symposium 2016, Universitas Indonesia, Jakarta, Indonesia, 24th – 28th April 2016: **Oral Presentation.**

WORKSHOP

Ammar, S., Workshop on Impedance Spectroscopy Theory, Applications and Laboratory Instruction, Centre for Ionics University of Malaya (CIUM), University of Malaya, 12th – 14th April 2016: **Oral Presentation.**

INDUSTRIAL PROJECT

Ammar, S., Vengadaesvaran, B., Ramesh, K., Kufian, D., Ramesh, S., & Arof. A. Preparation and investigation of novel composite coating system with superior corrosion protection for aluminium micro-channel heat exchanger. Daikin Research and Development Sdn. Bhd & Centre for Ionics University of Malaya, Department of Physics, Faculty of Science, University of Malaya, October 2016-February 2018. **Executive researcher.**